Titre: Title:	Aerodynamic Simulations of Helicopter Rotors through the Actuator Line Method
Auteur: Author:	Réda Mérabet
Date:	2021
Type:	Mémoire ou thèse / Dissertation or Thesis
Référence: Citation:	Mérabet, R. (2021). Aerodynamic Simulations of Helicopter Rotors through the Actuator Line Method [Thèse de doctorat, Polytechnique Montréal]. PolyPublie. https://publications.polymtl.ca/9095/

URL de PolyPublie: PolyPublie URL:	https://publications.polymtl.ca/9095/
Directeurs de recherche: Advisors:	Éric Laurendeau
Programme: Program:	Génie mécanique

POLYTECHNIQUE MONTRÉAL
affiliée à l'Université de Montréal

Aerodynamic Simulations of Helicopter Rotors through the Actuator Line Method

RÉDA MÉRABET
Département de Génie Mécanique

Thèse présentée en vue de l'obtention du diplôme de *Philosophiæ Doctor*
Génie Mécanique

Juillet 2021

POLYTECHNIQUE MONTRÉAL
affiliée à l'Université de Montréal

Cette thèse intitulée :

Aerodynamic Simulations of Helicopter Rotors through the Actuator Line Method

présentée par **Réda MÉRABET**
en vue de l'obtention du diplôme de *Philosophiæ Doctor*
a été dûment acceptée par le jury d'examen constitué de :

Marcelo REGGIO, président
Éric LAURENDEAU, membre et directeur de recherche
Hachimi FELLOUAH, membre
Daniele ZAGAGLIA, membre externe

ACKNOWLEDGEMENTS

First and foremost, I would like to thank my research director, Professor Éric Laurendeau for entrusting me with this research project along with the autonomy and trust you have given me. Your support, guidance, and overall contagious enthusiasm have been gratefully appreciated. The opportunities you work so hard in creating for all of us are truly fantastic.

I would also like to thank CAE inc. and the *Natural Sciences and Engineering Research Council of Canada* (NSERC) for the financial support in this collaborative project. To Mike Theophanides, and other CAE staff who have participated, thank you for the support and technical input. The generous computational resources provided by Compute Canada and Calcul Québec are also gratefully acknowledged.

I would like to thank Professor Michon and Dr. Prothin and my colleagues Claudia and Anaïs for their warm welcome for my stay at ISAE-SupAero in Toulouse. Sadly shortened by the pandemic, it was nevertheless an amazing experience for which I am grateful.

To my colleagues in the lab, you are *all* some of the brightest and hardest working individuals I have met. I am grateful to have been part of this fantastic environment that has allowed me to grow immensely on a professional level. In particular, I would like to thank Hélène for holding the fort with me for the past year, your presence brought some sense of normality in this otherwise zoom-dominated pandemic year. And Pablo, even though not in the lab, thank you for the multiple laughs, music taste, and the advanced Spanish lessons.

To the past and present members of "Team Helicos", Carlo, Tuan, and Vincent, thank you for sharing the joys and woes of this new field and our respective methods. Vincent, it has been a pleasure to work with you for the past four years and I can't thank you enough for the numerous technically related (or not) talks, feedback and ideas. In particular one evening over dinner in Toulouse where you so candidly suggested to "just cut the Gaussian". Your suggestion worked brilliantly.

I would like to thank my close friends Charles, Mike and Minh for encouraging me throughout the years and allowing me to keep some kind of balance through our weekend outdoor activities that, more often than not, tend to be Type-2 fun. In particular, the last-minute winter powder-hunting ski days in the middle of the week, thank you for making your schedule as "flexible" as mine Charles.

Finally, I would like to thank my family who has always supported and believed in me, in particular my sister Leïla and my mother Sylvie who have always been there for me.

RÉSUMÉ

Les hélicoptères se distinguent des autres aéronefs par leur polyvalence inégalée dans leur capacité de vol vertical efficace leur permettant d'accéder facilement à des zones reculées. Bien que les capacités de vol vertical et leurs performances soient d'une importance primordiale, l'hélicoptère d'aujourd'hui doit encore fonctionner efficacement dans tous les régimes de vol, comme le vol vers l'avant, la descente et en interaction étroite avec les obstacles environnants sur des terrains difficiles. Ces défis, en particulier le dernier, s'étendent également à un champ plus large de véhicules à décollage/atterrissage vertical plus généraux tels que les drones sous la forme de micro-véhicules aériens et l'avènement de la mobilité aérienne urbaine.

Toutefois, en raison de la grande polyvalence et de l'applicabilité de l'aéronef, il serait impossible pour les concepteurs d'envisager tous les cas de vol et les configurations hors design dans lesquels les opérateurs utilisent l'aéronef. Pour certaines de ces applications spécifiques, il est nécessaire d'évaluer les performances de vol des hélicoptères dans des conditions de vol difficiles.

L'objectif principal de cette thèse est d'étudier les calculs aérodynamiques haute-fidélité des rotors d'hélicoptères dans diverses conditions de vol. Des conditions telles que le vol stationnaire, le vol avant, l'effet de sol et l'interaction avec un bâtiment de faible hauteur sont évaluées. Les simulations traditionnelles de haute fidélité basées sur les méthodes Navier-Stokes par Moyennage de Reynolds Instationnaire (U-RANS) peuvent prendre jusqu'à plusieurs semaines sur des centaines de cœurs de CPU pour compléter un calcul pour une configuration, ce qui les rend intensives en temps et en calcul. Pour tenter d'enrayer ce problème, un modèle, toujours basé sur un cadre U-RANS haute fidélité, est exploré. La méthode développée doit simuler et prédire avec précision les principaux paramètres de performance du rotor tels que la poussée, le couple, le facteur de mérite et le sillage général du rotor.

Le modèle retenu est la méthode de la ligne actuatrice (ALM). Cette méthode, qui est largement utilisée pour les simulations d'éoliennes, remplace les pales du rotor par des termes sources de quantité de mouvement dans les équations U-RANS. La suppression du maillage des pales réduit considérablement la taille du maillage de calcul, ce qui diminue le coût de calcul.

Tout d'abord, afin d'adapter l'ALM aux écoulements de rotor d'hélicoptère, une étude paramétrique est réalisée dans un cadre simplifié. Dans un cadre bidimensionnel, différentes méthodologies d'échantillonnage de la vitesse sont testées avec l'échantillonnage intégral de la vitesse s'avérant supérieur. D'autres sensibilités du modèle liées à la modélisation et à l'écoulement sont évaluées et caractérisées. Ensuite, une simple extension en 3D pour une application d'aile fixe montre l'adéquation de la méthode dans le traitement des écoulements 3D.

Ensuite, l'ALM est appliquée à un rotor en vol stationnaire. Un kernel Gaussien tronqué-normalisé correctement ajusté donne des résultats supérieurs en termes de capacités de prédiction des coefficients du rotor. L'ALM produit également un sillage tourbillonnaire similaire à celui d'une simulation avec les pales pleinement résolues.

Troisièmement, la méthode est appliquée à un cas de vol axial où les capacités de prédiction du modèle ALM sont presque identiques par rapport à la simulation de référence avec pales entièrement résolue. L'ALM est également capable de prédire la diminution linéaire du facteur de mérite pour un rotor en montée avec une grande précision. En descente, l'accord est moins bon en raison de l'absence de régime d'anneau tourbillonnaire sensé être présent tel qu'observé dans les résultats expérimentaux.

Enfin, l'ALM est testée dans des conditions d'écoulement de plus en plus complexes, y compris le vol stationnaire en effet de sol, le vol avant en effet de sol, en effet de sol en interaction avec un obstacle en forme de boîte, avec et sans vent incident. Dans tous les cas, l'ALM est capable de prédire les tendances globales de l'écoulement avec une petite erreur de prédiction de la poussée dans les états d'effet de sol les plus extrêmes. La méthode est également capable de prédire la magnitude relative et le changement d'orientation du coefficient de moment. L'ALM est par ailleurs en bon accord avec les simulations de référence avec les pales pleinement résolues.

La concordance globale de l'ALM avec les simulations à pales entièrement résolues et les données expérimentales démontre ses capacités à prédire avec précision l'écoulement autour d'un rotor ainsi que ses performances dans des conditions difficiles. La méthode est donc jugée apte à remplacer les simulations à pales entièrement résolues qui sont plus coûteuses en temps de calcul.

ABSTRACT

Helicopters distinguish themselves from other aircraft by their unparalleled versatility in their capacity of efficient vertical flight allowing them to access remote areas easily. Although vertical flight capabilities and their performance are of primordial importance, today's helicopter must still operate in all flight regimes efficiently such as forward flight, descent and in close interaction with surrounding obstacles over challenging terrain. These challenges, in particular the latter, also extend to a widening field of more general vertical take off/landing vehicles such as drones in the form of Micro Air Vehicles and the advent of urban air mobility.

However, due to the wide versatility and applicability of the aircraft, it would be impossible for designers to consider all flight cases and off-design configurations that third parties use or operate the aircraft in. For some of these specific applications, there remains a need to evaluate the aerodynamic performances of helicopters in possibly challenging conditions.

The main objective of this thesis is to study the high fidelity aerodynamic computations of helicopter rotors in various flight conditions. Conditions such as hover, forward flight, ground effect and in interaction with a low-rise building are assessed. Traditional high fidelity simulations based on Unsteady Reynolds Averaged Navier Stokes (U-RANS) methods can take up to several weeks on hundreds of CPU cores to complete a computation for one configuration, making them time and computationally intensive. In an attempt to curtail this issue, a model, still based on a high fidelity U-RANS framework, is explored. The developed method needs to accurately simulate and predict the main rotor performance metrics such as thrust, torque, figure of merit and general rotor wake.

The Actuator Line Method is the selected model. This method, which is widely used for wind turbine simulations, replaces the rotor blades by momentum source terms in the U-RANS equations. The removal of the blade mesh significantly reduces the computational mesh size thus lowering the computational cost.

First, in order to adapt the ALM for helicopter rotor flows, a parametric study is performed in a simplified framework. In a two-dimensional setting, different velocity sampling methodologies are tested with the integral velocity sampling proving superior. Other model sensibilities related to the modelling and the flowfield are assessed and characterized. Then, a simple extension in 3D for a fixed wing application shows the appropriateness of the method in handling 3D flows.

Second, the ALM is applied to a rotor in hover. A properly tuned truncated-normalized

Gaussian kernel showed superior results in terms of integrated coefficient prediction capabilities. The ALM also produces a similar tip vortex wake when compared to an equivalent blade resolved simulation.

Third, the method is applied to an axial flight case where the predictive capabilities of the ALM model are near identical when compared to the fully resolved reference. The ALM is also capable of predicting the linear decrease in figure of merit for a rotor in climb with great accuracy. In descent, less agreement is found due to the mispredicted absence of vortex ring state present in the experimental results.

Finally, the ALM is tested in increasingly difficult flow conditions including hovering in ground effect, forward flight in ground effect, in ground effect in interaction with a box-shaped obstacle both with and without incoming wind. In all cases, the ALM is capable of predicting global flow trends with a small misprediction of thrust in the most extreme ground effect states. The method is also capable of predicting the relative magnitude and orientation change of the moment coefficient. The ALM otherwise agrees well with the reference blade resolved simulations.

The overall agreement of the ALM with both the fully blade resolved simulations and the experimental data demonstrates its capabilities in accurately predicting rotor flows in challenging conditions and its appropriateness to replace more costly fully blade resolved simulations.

TABLE OF CONTENTS

LIST OF TABLES

LIST OF FIGURES

LIST OF SYMBOLS AND ACRONYMS

Latin Symbols

A_{disk}	Area of the rotor disk	m^2
AR	Aspect Ratio, R/c_{ref}	-
c	Local chord	m
c_e	Thrust weighted equivalent chord, $3\int_0^1 cr^2\,dr$	m
c_{ref}	Reference chord	m
C_d	2D Blade section drag coefficient, $\frac{d}{0.5\rho_\infty U_\infty^2 c}$	-
C_D	3D Wing drag coefficient, $\frac{D}{0.5\rho_\infty U_\infty^2 S}$	-
C_D'	3D Wing sectional drag coefficient, $\frac{D'}{0.5\rho_\infty U_\infty^2 c}$	-
C_l	2D Blade section lift coefficient, $\frac{l}{0.5\rho_\infty U_\infty^2 c}$	-
C_L	3D Wing lift coefficient, $\frac{L}{0.5\rho_\infty U_\infty^2 S}$	-
C_L'	3D Wing sectional lift coefficient, $\frac{L'}{0.5\rho_\infty U_\infty^2 c}$	-
C_{Mx}, C_{My}	Rotor in plane moment coefficients, $\frac{M}{\rho_\infty V_{tip}^2 A_{disk} R}$	-
C_p	Pressure coefficient, $\frac{p-p_\infty}{0.5\rho_\infty U_\infty^2}$	-
$\overline{C_P}$	Average pressure coefficient, $\frac{\overline{p}-p_\infty}{0.5\rho_\infty V_{ind}^2}$	-
C_Q	Rotor torque coefficient, $\frac{Q}{\rho_\infty V_{\mathrm{tip}}^2 A_{\mathrm{disk}} R}$	-
C_T	Rotor thrust coefficient, $\frac{T}{\rho_\infty V_{\mathrm{tip}}^2 A_{\mathrm{disk}}}$	-
$\mathbf{f_{alm}}$	Volumetric body force of the ALM	-
FoM	Figure of merit, $\frac{{C_T}^{1.5}}{\sqrt{2}C_Q}$	-
g	Gaussian kernel	-
M	Mach number	-
N_b	Number of blades	-
r, r' and z, z'	Radial and axial rotor coordinate normalized by R	-
r_c	Vortex core size	m
r_s	Sampling radius	m
r_v	Vortex core radial coordinate	m
R	Rotor radius	m
Re	Reynolds number	-
$\mathbf{U_P}$	Perpendicular velocity to the rotor disk	m/s
$\mathbf{U_{rel}}$	Relative velocity a blade section sees	m/s
$\mathbf{U_s}$	Sampled velocity at kernel centre	m/s
$\mathbf{U_T}$	Tangential velocity to the rotor disk	m/s

U_∞	Freestream velocity	m/s
V_c	Rotor climb or descent speed	m/s
V_{ind}	Hover induced velocity, $V_{tip}\sqrt{C_T/2}$	m/s
V_tan	Tangential velocity of vortex core	m/s
$\bar{V}_\mathrm{tan}$	Average tangential velocity across vortex core	m/s
V_tip	Velocity of the blade tip	m/s
(x_0, y_0, z_0)	ALM node location	m
(x, y, z)	Rotor reference coordinate system	m
(X, Y, Z)	Absolute reference coordinate system	m

Greek Symbols

α	Freestream Angle of attack	degree
α_eff, α_rel	Effective/Relative angle of attack of an airfoil section	degree
α_s	Sampled angle of attack	degree
β_norm	Volumetric normalization factor	-
Γ	Circulation of a vortex core	m^2/s
ΔD	Blade segment drag force	N
Δ_g	Grid spacing	m
ΔL	Blade segment lift force	N
ΔR	Blade segment radial length	m
ϵ	Gaussian smearing width parameter	m
Θ_{75}	Collective pitch at 75% blade span	degree
μ	Advance ratio, $\frac{U_\infty}{V_{tip}}$	-
ρ	Air density	kg/m^3
σ	Rotor solidity, $\frac{N_b c_\mathrm{ref}}{\pi R}$	-
ϕ, ϕ_i	Inflow angle	degree
$\Psi_{C_{Mtot}}$	Orientation of the total in plane moment coefficient	deg
Ω	Rotor rotational speed	rad/s

Subscripts and Superscripts

hov	In hovering condition
i	ALM node index on the rotor blades
ige	Inside ground effect
ind	Denoting an induced value
iso	Denoting an isometric kernel
max	Denoting a maximum value before stall

$Mtot$	Total moment coefficient
oge	Outside of ground effect
$root$	Denoting a value at the blade root
tip	Denoting a value at the blade tip
tr	Denoting a truncated kernel
∞	Denoting a freestream condition

Abbreviations

AD	Actuator Disk
ALM	Actuator Line Method
AMR	Adaptive Mesh Refinement
ASM	Actuator Surface Method
BEMT	Blade Element Momentum Theory
BET	Blade Element Theory
BL	Boundary Layer
B-R	Blade Resolved
BVI	Blade Vortex Interaction
CFD	Computational Fluid Dynamics
CPU	Central Processing Unit
HAWT	Horizontal Axis Wind Turbine
HPW	Hover Prediction Workshop
IGE	Inside of Ground Effect
LES	Large Eddy Simulation
MAV	Micor Air Vehicle
OGE	Outside of Ground Effect
PIV	Particle Image Velocimetry
PM	Panel Method
RANS	Reynolds-Averaged-Navier-Stokes
SHOL	Ship-Helicopter Operational Limitation
UAD	Unsteady Actuator Disk
U-RANS	Unsteady Reynolds-Averaged-Navier-Stokes
VLM	Vortex Lattice Method
VPM	Vortex Particle Method
VRS	Vortex Ring State
VTOL	Vertical Take Off/Landing
(W)ENO	(Weighted) Essentially Non Oscillatory

CHAPTER 1 INTRODUCTION

1.1 Context

Helicopters distinguish themselves from other aircraft by their unparalleled versatility. They may not be able to transport a large number of passengers across oceans, but their capacity of efficient vertical flight allows them to access remote areas easily. It is this feature that defines the true value of a helicopter and is the reason why this type of aircraft is used by emergency/medical intervention crews, coast guards and the military in a number of difficult operations. Although vertical flight capabilities and their performance are of primordial importance, today's helicopter must still operate in all flight regimes efficiently such as forward flight, descent and in close interaction with surrounding obstacles over challenging terrain. These challenges, in particular the latter, also extend to a widening field of more general vertical take off/landing (VTOL) vehicles such as drones in the form of Micro Air Vehicles (MAV) and the advent of urban air mobility.

With the continuous evolution of more traditional helicopter and the rapid rise and surge in interest of newer VTOL vehicles, there is a need for engineers to be able to predict the flight performances of these rotor-operated aircraft. At the core of the challenges associated with the flight performances of a helicopter are the aerodynamics of the rotor blades and their wake. Although the modelling methods to compute the aerodynamic loading of the helicopter blade are on par with their fixed wing counterparts, there can still be some notable discrepancies in the calculated performances that are still, to this day, difficult to explain. A good part of the problem can be attributed to the wake of the blades. Similar to fixed wings, there is a tip vortex that forms at the end of the individual blades due to the strong pressure difference between the suction and pressure side of the airfoil in that region. But instead of being quickly advected downstream perpendicular to the wing as it does for an airplane, these tip vortices have a helicoidal shape and linger in the vicinity of the rotor, strongly affecting its performances. A strong emphasis is put on correctly capturing or modelling these vortices in today's numerical codes.

In hover, vertical descent and in proximity to the ground, these tip vortices dominate the flowfield. In hovering conditions, the vortices can only be advected by the induced flow made by the rotor and stay directly beneath it, slightly inwards with respect to the rotor disk as the wake contracts. In vertical descent, and to some extent in hover too, the blades can interact strongly with these vortices and completely change the loading of the blade, possibly causing unsteadiness and vibrations of the rotorcraft [3].

When considering forward flight, a rotor faces additional challenges. In hover, each spanwise blade section experiences a constant axisymmetric velocity consisting of the sum of the rotation rate of the rotor and the inflow velocity coming from above the rotor disk. In forward flight, there is the addition of the aircraft forward velocity that needs to be taken into account. This causes the advancing side of the blade (side of the rotor disk where the blade advances into the wind) to see a higher velocity than the retreating side. If a rigid rotor with a constant geometric angle of attack is assumed for the blade, the additional dynamic pressure on the advancing side will create a lift imbalance between a blade that is in the advancing or retreating position thus creating a rolling moment. To re-balance this moment, it is possible to either vary the angle of attack cyclically so the blade sees a higher angle of attack on the retreating side and a smaller one on the advancing side or to let the blade freely flap so it can rotate around a hinge up and down. The first method increases the lift coefficient on the retreating side to offset the added dynamic pressure on the advancing side and should yield equal lift on both sides. The second method relieves the root of the blade and the hub from moments and stresses due to the lift distribution along the blade span. Doing so, the blade can freely flap and the motion is driven by a balance in the aerodynamic lift, blade inertia and centrifugal force. On the advancing side, because of the added dynamic pressure, the lift is higher and the blade would naturally want to go up. This motion effectively decreases the angle of attack seen by the blade, thus reducing its lift. The opposite is happening on the retreating side. Overall, it helps alleviate the moment imbalance between the two sides. Another movement in the lead-lag direction can help with the unequal drag in a similar fashion. These motions are illustrated in Fig. 1.1. In addition to that unequal lift distribution, the advancing side is subject to a higher velocity which can result in compressible transonic effects and even reach sonic speeds at the tip. These effects limit the flight envelope of the helicopter due to the added drag and excessive noise generation. The retreating side on the other hand can undergo dynamic stall due to the high angles of attack it experiences and reduced velocity (i.e. lower Reynolds number). Near the root, where the rotational velocity is at its lowest, the freesteam velocity can be higher and acts in the opposite direction of the

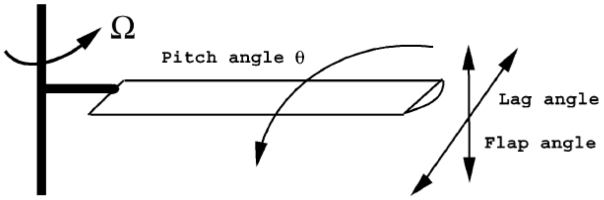

Figure 1.1 Articulated rotor blade motions taken from Conlisk [1]

rotational velocity which results in reverse flow over the blade in that section. Since the tip vortices can be convected by the freesteam faster than the induced flow of the rotor, they can easily be hit by the following blade and Blade Vortex Interaction (BVI) can occur causing vibrations and significant noise. Finally, the tip vortices can interact with the fuselage, empennage and tail rotor again causing vibrations and unsteady loads on these surfaces. Most of these phenomena are illustrated in Fig. 1.2.

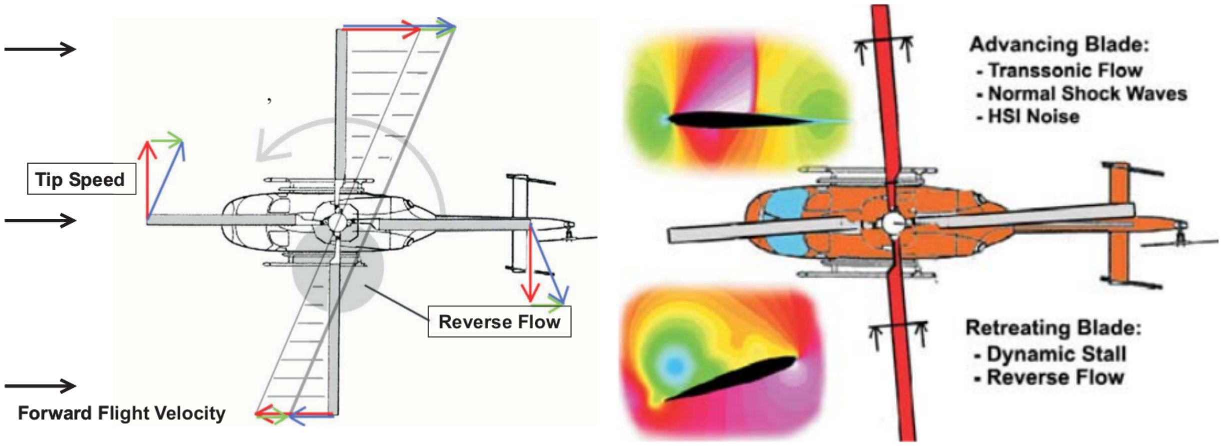

Figure 1.2 Forward flight flow phenomena taken from Wagner [2]

The operation of helicopters around other objects gives rise to interactional aerodynamics problems that see the rotor flowfield interacting with the surrounding obstacles whether it be the fuselage, the tail rotor, the ground or some other generic obstacle. This interaction modifies the flowfield around the rotor, thus modifying its performances and handling qualities, sometimes significantly. One notorious example is the interaction of a helicopter trying to land on a naval vessel at sea. The wake shed from the ship superstructure in addition to rotor-induced wake makes it challenging for helicopter pilots to land the aircraft in certain conditions. This problem introduces the concept of Ship-Helicopter Operational Limitation (SHOL) which evaluates the acceptable envelope of wind speed and direction in which it is acceptable for a pilot to land [13]. Another interactional aerodynamics problem of notable interest is the flight of rotor in confined areas (i.e. when a rotorcraft sees its displacement restricted in at least one direction) where asymmetrical flow re-circulation patterns appear around the rotor altering its thrust and torque and greatly modifying the pitching and rolling moments. These phenomena strongly affect the controllability of the helicopter and produce an increased workload on the pilot. They are, however, not isolated to helicopters only, as there is growing interest from other rotor-propelled VTOL vehicles mentioned hereinabove. It is expected for urban air vehicles to operate near city sky-rises, whereas MAVs be used in confined areas and accurate physics-based control laws are needed provided they be flown in partial of full autonomy [14].

As we can see, the flow around a helicopter rotor is quite complex due to the wide range of physical phenomena it involves and the wide range of operational conditions they operate in. To simulate helicopter flight, different numerical methods exist ranging from low to high fidelity models that may or may not take into account all these flow-dominated phenomena. Typically, lower fidelity models will have strong modelling assumptions that will make their range of usability limited but are much cheaper to run than high fidelity models.

1.2 Problem Statement

Being the versatile and most efficient hovering aircraft [3] there is, the helicopter is a highly efficient machine that designers and aerodynamicists try to optimize for various flight conditions. A heavy focus on hover is nevertheless present as this flight condition defines the true value of a helicopter and designs are often being judged on 0.5% difference of Figure of Merit [15]. However, due to the wide versatility and applicability of the aircraft, it would be impossible for designers to consider all flight cases and off-design configurations that third parties use or operate the aircraft in.

The interactional aerodynamics overview presented in Sec. 1.1 lists some of these off-design flight conditions. Notoriously, the SHOL evaluation is one of the most challenging cases which is typically done by real pilots in expensive at-sea trials. Given the limits of the safety envelope need to be found, these trials necessitate pilots to fly in dangerous situations. Once established, pilots would typically fly within the limits, but coming near them still produces challenging and dangerous flight conditions. In recent years there has been active research that aims at quantifying the SHOL limits through high fidelity aerodynamic simulations alone [16–18].

Another consideration is the use of aircraft flight simulators which offer an efficient way to procure training to pilots while both reducing the costs and risks associated to real-life test flights. Furthermore, flight simulators allow pilots to train on particularly hard manoeuvres that could possibly be dangerous to both the aircraft's integrity and even the pilot's life. To provide effective training, the simulators themselves need to recreate actual flight conditions and physical response of the helicopter with accuracy. Therefore, the flight simulator must be able to account for the effects of the flowfield encountered by the helicopter in all flight conditions, including the most complex ones. However, since simulators have the constraint to run in real-time, the embedded aerodynamic solver cannot run high fidelity aerodynamic simulations in a time-true fashion in order to predict the correct flow physics. The solvers in the simulator are therefore corrected/augmented from either empirical or pre-computed data coming from higher fidelity simulations in order to correctly portray the challenging flow physics and flight conditions. Note that, contrary to designers, flight simulators do not require extreme accuracy in terms of absolute value provided the global trends are well-captured.

This thesis focuses on the high fidelity aerodynamic computations of helicopter rotors in various flight conditions. Conditions such as hover, forward flight, ground effect and in interaction with a low-rise building are assessed. Traditional high fidelity simulations based on Unsteady Reynolds Averaged Navier Stokes (U-RANS) methods can take up to several weeks on hundreds of CPU cores to complete a computation for one configuration, making them time and computationally intensive. In an attempt to curtail this issue, a model, still based on a high fidelity U-RANS framework, is explored.

1.3 Background on Rotor Aerodynamic Modelling

This section presents an overview of the different modelling methodologies used through the years to represent rotor aerodynamics. The general ideas and arrangement are largely based on the books of Johnson [3] and Seddon [19] and the excellent review articles of Conlisk [1], Strawn et al. [20], Komerath et al. [21] and Hariharan et al. [22, 23] which the reader is invited to consult for further details. Although the subject of this research focuses more on high fidelity simulations, it is essential to review some elementary concepts coming from momentum and vortex theory as these notions are used throughout the thesis.

1.3.1 Grid-Less Methods

Generally, grid-less methodologies can be considered as of lower order or fidelity than grid-based solutions such as the Navier-Stokes (N-S) based simulations. But they are much cheaper in terms of computational speeds. Blade Element and Lifting Line methods are used in comprehensive rotor codes such as CAMRAD/JA [24] that are still well in use today. Given sufficient modelling and empirical corrections, these codes can predict the performances of a rotor in flight with an adequate level of accuracy. Also their fast turnaround time allows them to be used in advanced design phases of a new rotor development cycle as well as coupling them with more complex CFD code for more advanced computations of complex multi-physics problems such as aeroelasticity. Momentum theory, due to its simple formulation and multitude of analytical results, allows the engineer to have a more fundamental understanding of the flow around a helicopter. Even if the method seems old or obsolete by today's standards, there are still advances being made in recent research that try to clarify or expand on assumptions made by the method [25].

Momentum and Blade Element Theory

One of the simplest models to idealize a rotor by a disk of zero thickness that carries a pressure difference from one side to the other that represents the thrust distributed equally over the circular surface [3]. Assuming incompressible, irrotational and inviscid flow and by using Bernoulli's equation on both sides of the disk along overall mass conservation, we can find important features of the flow as represented in Fig. 1.3. We can assume the flow far upstream from the disk as being motionless with a pressure of p_0. The flow accelerates downwards up to the upper surface of the rotor disk. At this stage, station 1, the flow experiences a lowering in pressure that is translated in a downward velocity v_{ind}.

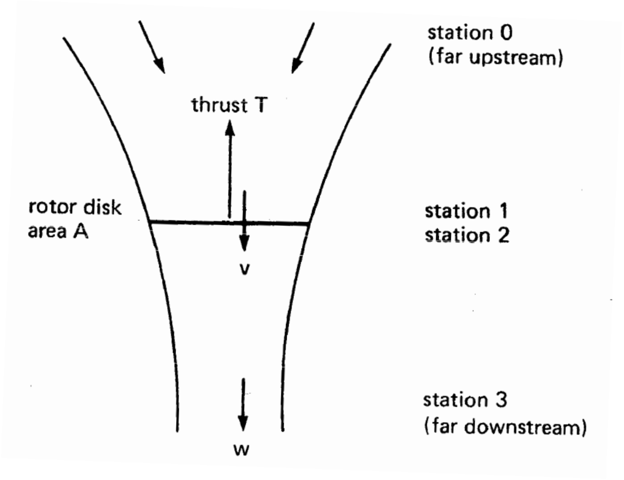

Figure 1.3 Momentum theory for a rotor in hover taken from Jonhson [3]

$$p_0 = p_1 + \frac{1}{2}\rho v_{ind}^2 \tag{1.1}$$

Crossing the disk surface at station 3, the pressure discontinuity $\Delta p = p_2 - p_1 = T/A_{disk}$ representing the rotor thrust, makes the pressure just below the disk sharply increase whereas the velocity is continuous with a value of v_{ind}. Far downstream, the pressure recovers and lowers to the original p_0 value causing the velocity to increase in the wake to a value of w.

$$p_2 + \frac{1}{2}\rho v_{ind}^2 = p_0 + \frac{1}{2}\rho w^2 \tag{1.2}$$

Rearranging and subtracting Eqs 1.1 and 1.2, we find $\Delta p = T/A_{disk} = \frac{1}{2}\rho w^2$. Given the total thrust can be calculated by the change in fluid momentum between sections 0 and 3, we have to evaluate the momentum at station 3 as it is zero at station 0 because the fluid is at rest. Therefore at station 3, the thrust is given by the mass flow rate $\dot{m}$ multiplied by the local velocity w. The mass flow rate can be evaluated at the disk directly as $\dot{m} = \rho A_{disk} v_{ind}$.

$$T = \dot{m}w = \rho A_{disk} v_{ind} w \tag{1.3}$$

We substitute Eqn 1.3 in T/A_{disk} and simplify:

$$\frac{\rho A_{disk} v_{ind} w}{A_{disk}} = \frac{1}{2}\rho w^2 \tag{1.4}$$

$$2v_{ind} = w \tag{1.5}$$

We find that the velocity in the far wake downstream is twice the thrust induced velocity in hover v_{ind} found at the rotor disk. The axial change in velocity from the station upstream at rest to the far downstream station mandates the stream-tube around the rotor to contract through conservation of mass. This contraction is a defining characteristic of helicopter rotor flows. From the equations above, we can find other useful relations and equations. Substituting Eq. 1.5 into $T/A_{disk} = \frac{1}{2}\rho w^2 = \frac{1}{2}\rho(2v_{ind})^2$ relates the hover induced velocity to the thrust:

$$v_{ind} = \sqrt{\frac{T}{2\rho A_{disk}}} = V_{tip}\sqrt{C_T/2} \tag{1.6}$$

The flow induced power is evaluated as the product of the rotor thrust multiplied by the hover induced velocity $P = Tv_{ind}$. It can be shown that the most effective induced velocity distribution that gives the lowest and ideal induced power is a constant value of v_{ind} as already predicted by momentum theory through the event of a pressure jump across the disk. However, real rotors do not produce this constant velocity across the rotor disk. This introduced the concept of Figure of Merit (FoM) which compares the actual rotor power to the ideal rotor power

$$C_{P,ideal} = \frac{C_T^{3/2}}{\sqrt{2}} \tag{1.7}$$

$$FoM = \frac{C_{P,ideal}}{C_{P,real}} = \frac{C_T^{3/2}}{\sqrt{2}C_{P,real}} \tag{1.8}$$

More elaborate models of Momentum Theory consider the rotor in vertical climb, the swirl in the flow, which is generally negligible in helicopter applications, and even a forward flight model. But Momentum Theory alone contains no information about the actual number of blades or blade profiles. The rotor blade geometrical features are considered in Blade Element Theory (BET). The method assumes that every blade section is independent of each other and flow effects and forces act only in the plane defined by each section. The blade section is illustrated in Fig. 1.4 where U_P corresponds to the local induced velocity v_{ind} and U_T corresponds to the rotational velocity Ωr, Θ is the geometric angle of attack, α_{eff} is the effective angle of attack and ϕ is the inflow angle.

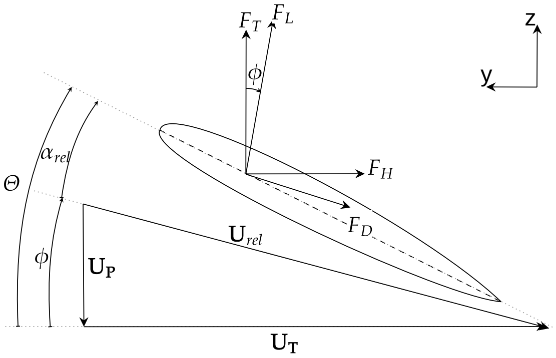

Figure 1.4 Blade element representation of a blade section

$$\phi = \arctan(\frac{v_{ind}}{\Omega r}) \tag{1.9}$$

$$\alpha_{eff} = \Theta - \phi \tag{1.10}$$

$$U_{rel} = \sqrt{v_{ind}^2 + \Omega r^2} \tag{1.11}$$

With the blade sectional properties in terms of relative velocity and effective angle of attack, we can relate these values to equivalent free-stream two-dimensional airfoil aerodynamic properties. The evaluation of the airfoil properties, in terms of lift and drag coefficients, can be done with a multitude of methods ranging from a simple theoretical lift curve, to empirical data/functions and finally to tabulated 2D sectional data coming from high fidelity CFD simulations. The coefficients are then re-dimensionalized for every blade section and then rotated in the correct rotor referential.

$$\Delta L = \frac{1}{2}\rho U_{rel}^2 C_l c \Delta R \tag{1.12}$$

$$\Delta D = \frac{1}{2}\rho U_{rel}^2 C_d c \Delta R \tag{1.13}$$

$$\Delta F_T = \Delta L \cos(\phi) - \Delta D \sin(\phi) \tag{1.14}$$

$$\Delta F_H = \Delta L \sin(\phi) + \Delta D \cos(\phi) \tag{1.15}$$

From this theory and with some simplifications, many analytical closed form formulas can be obtained, describing the optimal twist or chord length a rotor should have and even the power and thrust of a given analytically defined geometry. Now, the geometrical information of the blade is included in the model. However, by itself, BET cannot produce meaningful results as v_{ind} is to be determined. If we couple the Momentum Theory to the Blade Element Theory by assuming the inflow at the disk as being non-constant across the span of the blade (essentially applying momentum theory in stream-tubes associated with the correct airfoil section) we can obtain a much better solution. This coupling also gives birth to closed formed equations that can predict the performance coefficients of the rotor. Finally, as one can expect, the Blade Element Momentum Theory (BEMT) has a major flaw as it does not consider the finite amount of blades and the tip vortex system that comes with it. Inflow approximations from momentum theory are azimuthally averaged and typically tend to grossly over-predict the blade loading in the tip region. From vortex theory, some closed form approximations of the effect of a helix shaped sheet of vorticity can be derived and act as a correction factor applied on the force of the individual stream-tubes of momentum and makes the local Thrust near the tip decay to zero. Different versions exist such as Prandtl's approximate solutions as in Eq. 1.16 and Goldstein exact solution for propellers.

$$F_{loss}(r_i) = \frac{2}{\pi} \arccos(\exp((r_i - 1)N_{blade}/2\lambda_i)) \tag{1.16}$$

If a more general approach is considered by using airfoil properties from tabulated data and varying airfoil profiles, an iterative numerical solution becomes mandatory due to non-linear effects. This is one of the most basic numerical implementations for computing a rotor in hover or vertical flight. It is also easy to implement corrections to consider effects such as dynamic stall, blade flapping/lagging and compressibility.

Singularity Based Methods

In vortex theory, the flow created by a rotor is typically represented by features present in Fig. 1.5. Two distinctive features are present; the tip vortex and the vortex sheet. Both of these entities move at a different speed in the wake due to different local inflow of the rotor. If the blade is idealized as a lifting line and observes a bound circulation along its span as in Fig. 1.6, the strong negative circulation gradient in the tip region gives birth to a strong tip vortex whereas the more gradual loading along most if the inner span gives the shed vortex sheet. In typical lifting line methodology, the wake behind the blade is represented as a continuous vortex sheet that spans from root to tip. The sheet is formed of the trailing and shed vortices due to the change in bound circulation on the blade. In the present case, since the gradient is strong in the tip region, the sheet near the tip quickly rolls up on itself and forms the tip vortex. As such, some computational methods completely neglect the effect of the inner vortex sheet and only consider the effect of the tip vortex as it dominates the response on the flowfield [26].

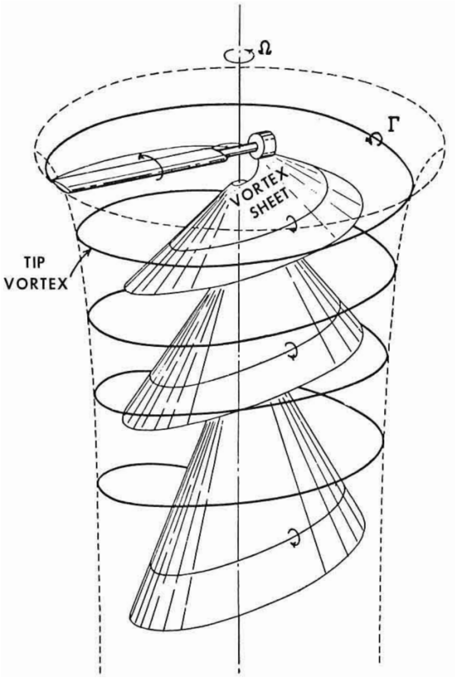

Figure 1.5 Wake representation of a rotor adapted from Gray [4]

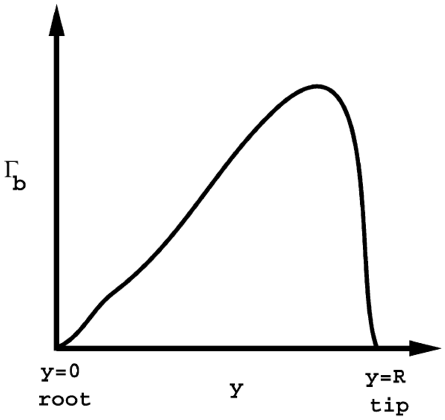

Figure 1.6 Representation of the bound circulation over a blade taken from Conlisk [1]

The fundamental equation used in vortex theory is the Biot-Savart equation which computes the induced flow a vortex has on a point in the field. Numerical vortex methods typically discretize the vortices as a sum of smaller straight line vortex elements of finite lengths. The induced flow of one such element is:

$$\Delta\vec{v} = \frac{\Gamma}{4\pi}\vec{r}_1 \times \vec{r}_2(\frac{1}{r_1} + \frac{1}{r_2})\frac{1}{r_1 r_2 + \vec{r}_1 \cdot \vec{r}_2} \tag{1.17}$$

Where $\vec{r}_1$ and $\vec{r}_2$ are the vectors pointing from the rear and the front of the straight line vortex element to the point it is being computed on as represented in Fig. 1.7. Γ is the vortex strength. This formula becomes singular as the point is getting close to the vortex element. This is an issue in rotorcraft wakes as blades rotate in close proximity the trailing tip vortices from the preceding blade. The problem is also present in the wake roll-up procedure where panels from the vortex sheet become entangled and interact in close proximity to each other. To solve this issue, vortex cores can be used. They limit the induction a vortex element has on a point when they are near each other. Instead of rising to infinity when they are superposed, the vortex core smooths it down to zero induced velocity. Different core models exist such as Rankine, Scully, Lamb-Oseen or Vatistas [27] and they all necessitate a different Biot-Savart kernel to compute the induced velocity on a point as represented in Fig. 1.8. These different kernels have been tested and compared within a vortex lattice method framework in the works of Ferlisi [5]. Another extension of vortex theory is to consider the rotor as a lifting surface. Instead of a simple line of bound circulation, the planform of the blade is discretized as multiple panels in the span-wise and chord-wise directions. In typical VLM implementation, the vorticity on the panels themselves is not known *a priori* and is solved as a whole with the flowfield by imposing a no penetration boundary condition on the panels. This produces a system of linear equations that can be solved for both the wake and the forces on the blades at the same time but relies on the inviscid lift characteristics. Corrections can be added to take into account viscous and compressibility effects [28].

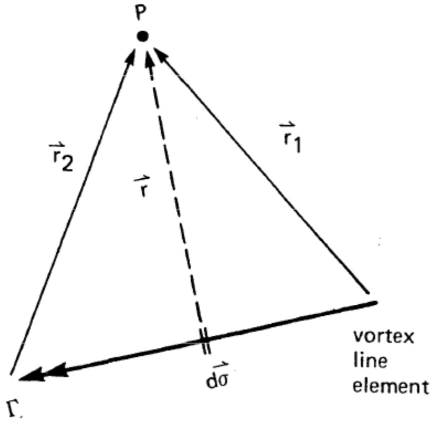

Figure 1.7 Induction of a finite length vortex-element on a point taken from Johnson [3]

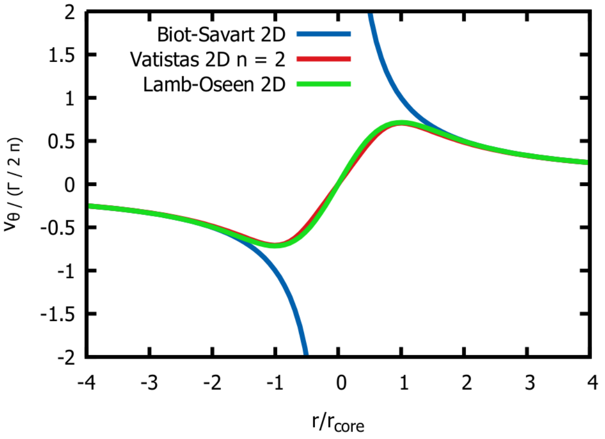

Figure 1.8 Viscous core models induction from Ferlisi [5]

Prescribed Wake

Prescribing a wake sets the geometry of the wake before the calculation starts. Models range from simplistic cylinders to more complex ones such as Landgrebe [29] or Kocurek and Tangler [30] which are based on experimental data and describe the positions of the tip vortices and vortex sheets in function of the rotor geometry and operating conditions. Different rotor sizes, aspect ratios, twist distributions have been used in order to generate the most general formula that can take into account a diverse set of rotor geometries. Different thrusts settings are also computed. The equations that prescribe the wake give the spatial positions of the tip vortices and vortex sheets as a function of the wake age azimuth angle Ψ. With their positions known, it is possible to discretize the wake with wake markers that lie on the prescribed tip vortex/sheet path and link the markers together with straight line vortex elements. Then, using a Biot-Savart induction formula, the induced flow at the different radial points on the rotor blade can be computed. Prescribed wakes can be coupled to a Blade Element Theory and find a good approximation for the loads on the blade such as in Landgrebe et al. [31]. Models also exist for forwards flight conditions [32].

Free Wake

The next step is to let the wake evolve and stabilize itself. To that end, different methodologies exist. A prescribed or approximate wake geometry can be used to initialize a solution and then let it deform it until convergence such as in [33]. An other possibility is time marching starting from a rotor at rest. The rotor is put into motion and the wake develops by itself to a stabilized regime. Here, since the bound circulation varies in time, the shed vorticity is taken into account by being shed into the vortex sheet wake at every time-step (usually equivalent to about $\Delta\Psi = 5^o$ to 15^o). The effect of the wake on itself is of great importance as the strong vorticity near the root and tip sections of the vortex sheet in addition to the starting vortex tend to roll up the vortex sheet such as in Fig. 1.9. One important limitation of free wakes is the increase in compute time, as the wake grows in size, which scales quadratically with the number of panels. Furthermore, these simulations are prone to encounter nonphysical panel stretching due to their mutual interaction in close proximity. A viscous core model therefore becomes mandatory. A further evolution of the method is to transform the wake into viscous vortex particles [34, 35] that are showing great promise for rotor flows. They are based on the velocity-vorticity form of the Navier-Stokes equations in a Lagrangian formulation, which conserves the vorticity, as well as being well suited for the simulation of complex environments with interaction.

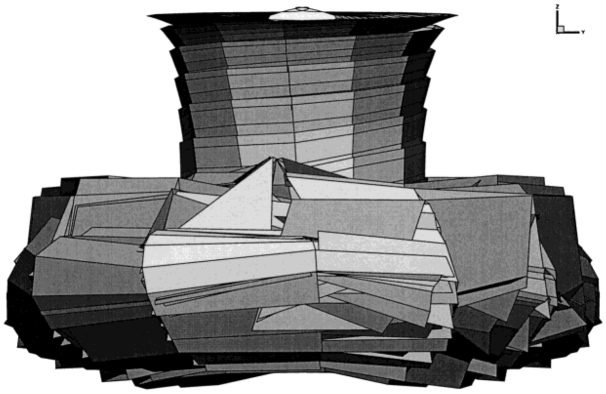

Figure 1.9 Vortex lattice method free wake simulation with roll-up taken from Wagner [6]

1.3.2 Grid-Based Methods

Using grids to represent the flowfield of a rotor enables a better representation of the true geometry of the rotor blades/helicopter which is essential for design purposes. This explicit geometry definition implemented as boundary conditions easily allow the definition of other geometrical objects in the flow domain such as fuselage, ground or obstacles which are not always as straightforward to implement in grid-less methods. Also, it allows the user to obtain more detailed information about the overall flowfield variables. The first types of grid-based solvers are the Transonic Small Disturbance and Full Potential equations. They are simplified versions of the Navier-Stokes equations and are much less intensive in terms of computational time as there is only one equation that needs to be solved. They were the first methods capable of predicting the transonic flow near the tip of rotors which gave great insight to engineers at the time, both in terms of rotor performances in that regime and noise generation [1, 20].

With the tremendous computational speed increase seen in the late 1980s and early 1990s, came the first developments of Euler and compressible Navier-Stokes solvers applied to rotor blades. Today, it has become the standard technique to compute the flowfield of a helicopter rotor. These methods can compute accurate pressure distributions and resolve shocks over the blade surface quite well. Reynolds-Averaged Navier-Stokes (RANS) equations have an advantage over Euler equations as they take into account the viscous effects and turbulence seen by the blade which can greatly affect the loads on the blade. One major flaw of these methods is the treatment of the vortical wake. In the previous section, the vortex methods were perfectly preserving the vortical nature of the wake with Lagrangian markers being moved around in time. Grid-based computations on the other hand suffer from numerical diffusion or insufficient grid resolution, especially in the early days where grid sizes were capped to a few hundred of thousands cells, yielding a loss of the tip vortex geometry. Most of the subsequent developments in these methods were aimed at improving the capture of the tip vortex wake.

The numerical dissipation of the early codes pushed the researchers to develop ways to alleviate this effect. The most notable one is the use of high order numerical schemes [36]. There are many different spatial discretization techniques for compressible finite volume Navier-Stokes/Euler equations for the convective term. It is this term that has the most impact on the quality and stability of the solution. One of the most used schemes is to use a central difference and to damp the oscillations by adding artificial dissipation (scalar or matrix) [37]. Due to the added dissipation, the solutions near shocks and in boundary layers may be a bit smeared and degrade the conservation of the velocity profile of a tip vortex over time. Another popular scheme is the Roe Flux Difference Splitting [38]. This scheme evaluates the convective fluxes on each side (Left and Right) of every cell face. In evaluating these fluxes, we need to take the primitive variable vector and evaluate it on both sides of the interface. High order methods are constructed by changing how these Left and Right states of primitive variable vector are evaluated. This is how (W)ENO , (Weighted) Essentially Non Oscillatory, schemes are constructed. The evaluation of the Left and Right quantities rely on a reconstruction stencil involving 5-7 grid cells and can yield schemes that are 5-7th order accurate in space. By carefully choosing the weights associated with every point, the schemes do not show oscillations [39].

The use of high order schemes is quite widespread in the helicopter community as it is a great way to increase the resolution and lower the dissipation of tip vortices in the wake. But as noted by Min and Sankar [11], these schemes have excellent accuracy on fine or uniform grids, but unfortunately loose much of their advantages on highly stretches or deformed grids, which is typically the case for a 3-D curvilinear mesh away from the blade surface. Also, the order of accuracy of the scheme must gradually diminish as it gets closer to the boundaries of the domain to facilitate the implementation of boundary conditions. Even if uniform grids resolve the velocity profile inside the core of a tip vortex very accurately, it might not be necessary. As it was noticed by some researchers [32], even if lower order schemes might seem more diffusive and not capture the correct vortex core profile, the vorticity is still essentially conserved and effect on the rotor inflow is adequate which gives correct integrated performance coefficients. This can be observed in today's codes as some 2nd order schemes tend to be more stable and predict essentially, if not better, the same performance figures as high order methods at the cost of having the tip vortex wake structure not as clearly defined as observed in Hariharan et al. [40]. The use of high order schemes on uniform Cartesian high density meshes have also the tendency to break down the helicoidal wake for simulations above 10 rotor revolutions as observed in Fig. 1.10. This breakdown pattern has been observed in recent years and marginally affects integrated performances coefficients, but an explanation has yet to be confirmed [15].

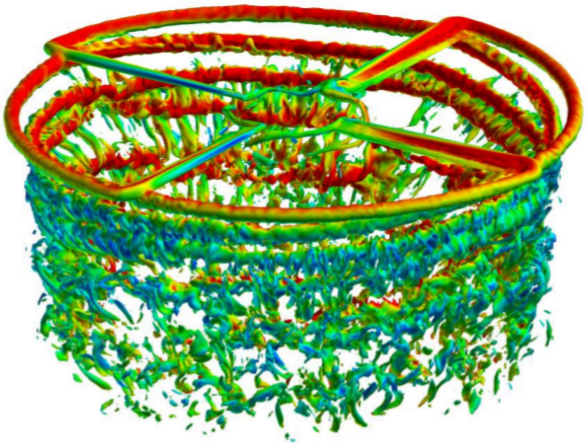

Figure 1.10 Wake breakdown due to high order scheme on a fine grid taken from Coder [7]

Another method used to prevent the numerical diffusion of vorticity developed by Steinhoff and Underhill [41] adds a body force (momentum source terms) to the N-S equations. This force is is applied to high vorticity regions, such as the vortex sheet or more importantly the tip vortex, and constrains the vorticity to be artificially contained within a few grid cells.

Meshing Methodologies

The evolution of meshing methodologies has yielded notable improvements in the simulations of helicopter rotors over the years. Starting with one of the simplest grid representations would be a structured Cartesian grid. However, this topology by itself can't represent correctly the complex geometry of a rotor in a body conforming way. To that end, a lot of solvers use curvilinear coordinates that map a rectangular structured domain around the geometry. A Jacobian of the geometric transformation is used to correct the N-S equations. For complex geometries, such as a full helicopter fuselage, multi-block meshes, that assemble together different sets of curvilinear grids, are needed [42].

To simulate a rotor in rotation, two methods are typically used. Either the whole domain is set in rotation by adding momentum source terms to the N-S equations to simulate the effect of a rotating flowfield with a stationary geometry. Or the geometry and mesh are set into motion within a stationary flowfield. The former is employed when only the rotor geometry is being considered as the whole geometry contained within the flow domain is considered rotating. In that case, exploiting the axisymmetric geometry of the rotor blades is possible and can reduce the grid size significantly [43]. The latter is needed when two or more geometries are in relative movement such as the fuselage and the rotor. To consider a moving mesh, the usual methodology is to use a Chimera/Overset mesh technique which embeds a smaller mesh within an other. Usually, there is a mesh around the rotor that is inserted in a larger background mesh which contains the fuselage and the rest of the flow domain as illustrated in Fig. 1.11. Cells of the background mesh that overlap within the rotor mesh are blanked and do no participate in the computation of the flow. There needs to be an exchange of information between the two meshes that is typically done through interpolation at the boundary of the inner (rotor) mesh. For rotor computation, this inner mesh needs to be put in movement and the connectivity/computation of blanked cells needs to be rerun at every time-step which can dramatically slow down the computation and has poor parallel computational scalability. Another similar approach, that is computationally cheaper, is to implement a Sliding Plane methodology [44]. The rotating mesh has a pre-defined shape, such as a cylinder, and the background mesh has a hole carved at the centre with the exact geometry of the rotor-containing cylinder mesh. The two meshes are body conforming and there is no need to recompute the blanking cells ans the interpolation becomes simpler to manage.

Unstructured meshes are also widely used in helicopter computation as they are much easier and quicker to implement than multi-block grids. Moreover, unstructured meshes can cover much more complex geometries. However, they typically tend to run slower in terms of computational performances when compared to structured meshes. Also, it becomes much harder to implement high order schemes with this kind of mesh. A structured mesh knows its neighbours through ordered indexes with flow variables readily available for stencil construction. It is not the case for unstructured meshes that typically only know their immediate neighbour and rely on gradient information in order to reconstruct higher order schemes.

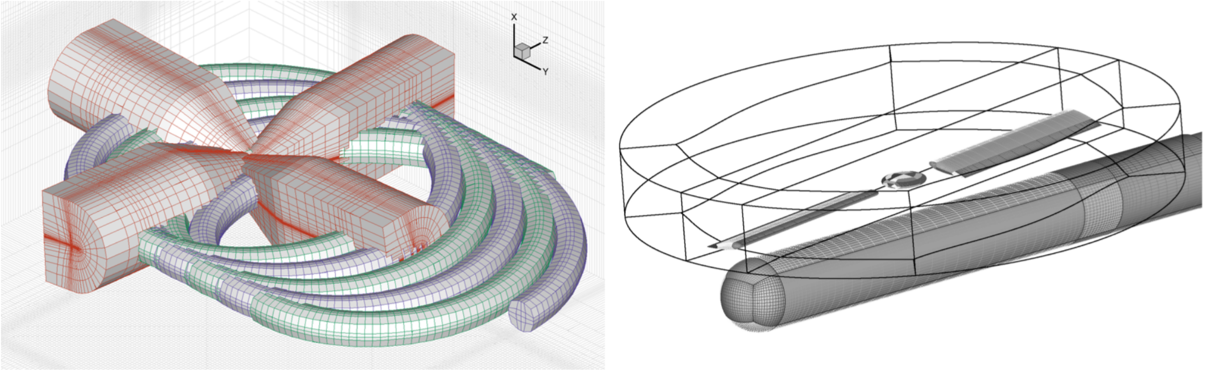

Figure 1.11 Overset mesh or rotor and wake from Dietz et al. [8] and sliding mesh taken from Steijl et al. [9]

Adaptive Mesh Refinement (AMR) is a technique that refines the mesh dynamically in an area based of some criterion such as the vorticity. Therefore, in the case of rotor flows, the refined areas would be centred around the tip vortices. AMR can be implemented in an unstructured mesh quite easily. Overset grids can also be generated and used to refine the area around a tip vortex such as in Refs. [8,45] and depicted in Fig. 1.11. The challenge here is to be able to clearly identify the tip vortices with good criteria.

Overset/Chimera meshes are also employed to embed different types of meshes/solvers together. Hariharan et al. [10] used an unstructured mesh for the near body of the helicopter fuselage and the rotor blades whereas the wake used an off body structured Cartesian grid as shown in Fig. 1.12. In this particular implementation, the unstructured mesh solver has a lower order of accuracy than the solver used in the Cartesian grid wake. A diminution of the order of the scheme of the Cartesian wake is needed near the unstructured mesh/Chimera boundary and near the boundaries of the domain. This setup allows simpler mesh generation around the rotor and fuselage in addition to the increased accuracy from the high order scheme used in the rotor wake.

Aeroelastic and Blade Dynamics Considerations

In order to simulate a realistic fully articulated rotor, in particular in forward flight, it is necessary to consider the aeroelastic/blade dynamics effects needed to balance the unequal lift moment caused by advancing/retreating side of the rotor. Implementing these models in grid-less techniques is relatively straightforward as everything is defined in a Lagrangian framework and thus free to move. Blade movements are easy to implement as velocity corrections such as in Ref. [24]. However, within an Eulerian framework, which has a grid attached to it, these straightforward velocity corrections are not possible. Therefore the

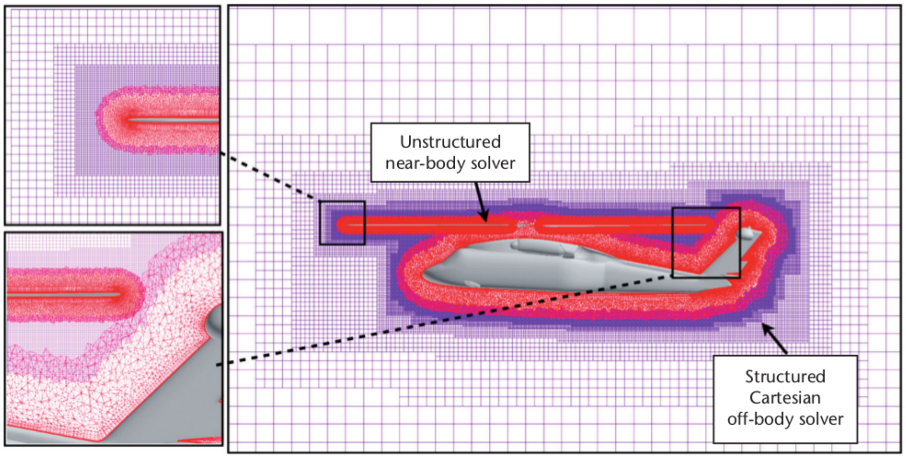

Figure 1.12 Dual mesh solver taken from Hariharan et al. [10]

mesh has to deform to comply with the new blade geometry which changes at every timestep. However, grid deformation often needs to be supported by a Geometric Conservation Law (GCL) which takes into account the time dependant variation of volume of every cell. Min and Sankar [11] noted that adding a GCL did not improve the integrated results by a lot, but it solved the un-physical non conservation of mass at the farfield boundaries.

To compute the elastic deformation/dynamic movement of a blade, a coupling is typically made with a standalone Comprehensive rotor code such as CAMRAD/JA [24] or by programming a dynamic/finite element solver within the CFD code. To gain in computation speeds, different coupling methodologies can be used with a varying level of accuracy as observed in Dietz et al. [8]. Loosely coupling the CFD code to the comprehensive code will let the comprehensive code trim and find the deformed blade geometry with vortex methods representing the wake. Then, the updated geometry will be fed back to the CFD code for an update of the geometry/grid which might not occur at every time step, even once per rotor revolution. Strong coupling will interchange information between a structural and CFD solver in a time-true manner. At every iteration, the structure code will compute the deformed blade geometry and send it to the CFD code that will deform the mesh accordingly.

Hybrid Methods

Typical hybrid methodologies model split the computation in two parts. The near-field of the blade is computed with CFD on a grid whereas the wake is modelled with straight-line vortex elements as represented in Fig. 1.13. The straight line vortex elements are used in a similar fashion as in vortex methods. Their influence is computed on the farfield as boundary conditions of the flow domain so the effect of the wake is felt by the blade. Only vortex elements outside the CFD domain are considered as the ones passing inside are already considered by the CFD flow solver. Different versions exist about the number or span-wise trailing vortex stations and displacement of the wake. Typically, only the tip vortex is considered with a strength equal to the peak circulation on the blade. The displacement of the Lagrangian markers is typically done in a Vortex Free Wake fashion. Prescribed wake geometries with additional span-wise sections are also possible such as in Marpu et al. [46]. These methods solve the problem of the dissipation of vorticity by considering it directly in a Lagrangian framework and are much cheaper to run than full CFD.

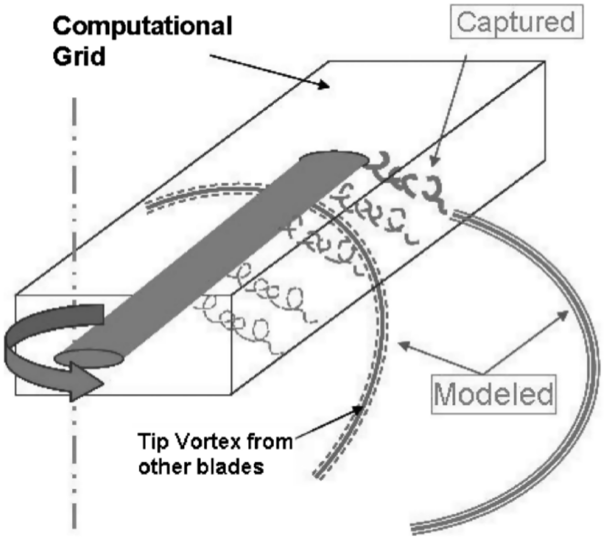

Figure 1.13 Hybrid rotor computation methodology taken from Min and Sankar [11]

Rotor Replacement Techniques

Hybrid methods are good for detailed solutions on the blades and can help in detailed design to obtain accurate performance figures. These methods model the far wake and accurately solve the near wake to obtain accurate blade surface pressure and wall shear stress distributions. By opposition, if the overall flowfield is of greater interest, the opposite methodology is possible: model the rotor blades through a lower order methodology and accurately solve the rest of the wake through CFD. This approach is useful when studying average coefficients or interactional aerodynamics problems (ground, fuselage) when computational resources are limited. Methods such as the Actuator Disk [47] and Actuating Blade [48] have been proposed with the former being one of the most popular in complex rotor-obstacle interaction cases [49–51]. These methods are usually based on a BET representation of the blade and coupled to a CFD flow solver for the resolution of the wake instead of momentum theory. A more detailed overview is presented in Sec. 1.4.3

Current State of Helicopter High Fidelity Flow Modelling

The current level of accuracy of the solvers present at the AIAA Rotorcraft Simulation working group [23] is around 1-4% error in terms of Figure of Merit for hover simulations. But rotor designs are being judged and decided upon on a 0.5% difference of FoM in the industry [15]. Although high order methods with significant mesh resolutions would appear to perform in a far superior fashion, more traditional and modest second order CFD schemes can produce excellent results with a modest computational cost [43, 52]. Also, some unexplained phenomena such as the wake blow-up have yet to be addressed for higher order models.

When considering the performances of a helicopter in forward flight with the interactions between the rotor and fuselage, an extensive program recently took place in Europe. The GOAHEAD project [9] provided the participating European entities with new and extensive wind tunnel data including unsteady balance, unsteady pressure taps all around the body and several locations for flow visualization [53] to allow the participants to validate their codes and models. A great number of participants [54–61] managed to obtain good results in terms of pressure profiles on the blades at different span-wise sections on their CFD codes. The comparison of unsteady pressure taps on the body agreed fairly well in terms of frequency (corresponding blade passage harmonics) but not so much in terms of amplitude. Most of the participants used a rotating Chimera mesh assembly in order to represent the motion of the rotor. This had for effect to increase the total cell count and add computation time due to the overset treatment of the cells which has to be recomputed at every time-step due to the rotation of the mesh. Therefore the computations costs were significant and could attain up to 80 hrs for 1 rotor revolution and up to a month for a full simulation on a cluster. Other hybrid methodologies which combine 3D RANS for the near fuselage and Potential/Vortex methods for the wake [62] can be used to achieve a similar level of accuracy at a fraction of the computation cost. But these methods require more modelling of the potential part of the flow thus making them less suitable if more general test cases need to be run.

More applied applications such as the interaction of a helicopter with the ground [55, 63] are also being investigated. A parent application is the study of the interaction of a helicopter trying to land on a ship. This problem is of particular interest for the flight simulation industry as it needs to verify/calibrate their models on higher accuracy simulations in order to make the flight simulator as realistic as possible. An aerodynamic database in the form of a table lookup can also be built to link to the simulator in real time to account for the effects of the ship's flow. Considering this, Crozon et al. [64] stresses the emphasis put on the coupling of the rotor-ship as 2 way coupled simulations (ship interacts on the rotor and rotor interacts on the ship) are necessary to obtain good results. The unsteady Chimera mesh approach yielded much better results than a steady Actuator Disk approach.

1.4 Background on Rotor Replacement Techniques

Rotor replacement techniques are not unique to helicopter rotors. In fact, they are found in many rotor or propeller based applications such as boat propellers [65], aircraft propellers [66–68], tidal turbines [69], vertical axis wind turbines [70] and most notably horizontal axis wind turbines (HAWT). The latter, being the most common and enjoying sustained interest on the research side.

1.4.1 Actuator Methods for Wind Turbines

Wind turbines face some of the same computational challenges as rotorcrafts since they are both rotating rotor systems. But in opposition to helicopters, an area of great interest for wind turbines resides in solving for the influence a rotor has on the far wake in order to assess the effect of wake interactions between multiple wind turbines in wind farms [71]. Solving a flow on a scale as large as a wind farm requires a massive amount of grid cells. If in addition multiple rotating overset mesh grid assemblies are used to represent all the rotors and the blades boundary layer's are solved correctly, the computational expenses quickly become unrealistic. Therefore, most of far wake computation of wind turbines are done with reduced fidelity rotor models which project the effect the blades would have on the flow. These so-called Actuator Methods regroup the Actuator Disk, Actuator Line and Actuator Surface methods. Two families of implementations are possible to account for the forces a wind turbine exerts on the flow: a direct modification of primitive flow variables and modification of the momentum equations by addition of source terms.

Primitive Variable Modification Methods

A way to represent a wind turbine is to consider it as an Actuator Disk which is an infinitely thin surface through which either the velocity and/or the pressure are discontinuous. The discontinuity magnitude should be representative of the force the wind turbine exerts on the flow. This concept has been explored by Leclerc and Masson [72] in an axisymmetric flow solver. The loading of the disk was found through Blade Element Theory, then transformed to azimuthally averaged circulation to then define a velocity jump between the two sides of the surface. Numerical results were compared to four sets of experimental data and were in good agreement until peak power due to the onset of blade-sections stall.

An evolution of this method to account for 3D flow and discrete blades was developed by Sibuet-Watters and Masson [73–76]. The Actuator Surface concept now accounts for the remaining spatial dimension and can model the effects of a finite number of blades. The same methodology of applying a primitive variable jump across a surface is used. In this case, the surface is represented by the blade planform oriented perpendicular to the incoming flow. The velocity discontinuity in the chordwise direction is distributed in a parabolic way to limit possible instabilities in the flow that a constant velocity discontinuity would cause due to the strong gradients at the leading and trailing edges. The model has been verified against a Prandtl Lifting Line solution and compared well in terms of force and flow characteristics. The model was also validated against different experimental wind turbine measurements and agreed well except in stalled conditions.

A slightly different approach was used by [77] to model an Actuator Surface. A simple pressure jump across a surface (airfoil chord in a 2D version or blade planform in 3D) was implemented through the use of a fan boundary condition in a commercial flow solver with user defined functions. The distribution of the pressure discontinuity along the chord resembled a typical inviscid pressure distribution. The 2D model produced a similar flowfield around the model when compared to a fully resolved airfoil. In 3D, the model reproduced well the power curve for a wind turbine at low speed. The method is however only capable of representing the force normal to the surface thus making it hard to take into account drag forces.

Source Terms Methods

Actuator Disk methods with body force terms were originally used in 2D axisymmetric codes. Similar to the primitive variable case, the method finds the loading on the blades by averaging the forces given by Blade Element Theory. Then the forces would be considered directly as momentum source terms in the flow equations. The first installments of the method had solutions that were subject to oscillations near the force application nodes that were later removed by smearing the solutions with a Gaussian function (1D and 3D smoothing) that distributed the force on multiple adjacent points [78]. Three dimensional versions of the AD are still in use today [79] but are less accurate than ALM or ASM due to the non-representation of discrete blade.

The next step in wind turbine modelling is the introduction of the Actuator Line by Sørensen and Shen [80]. This three-dimensional method discretizes the individual blades in sections on which the forces and source terms are computed. Their strengths correspond to the local loading of the blade and are then distributed on the adjacent grid nodes by the means of a 3D Gaussian function. The loading is determined by local flow condition by sampling the velocity at the closest grid cell to a control point on the actuator line and then finding the 2D airfoil lift and drag values from tabulated data. Flow features such as blade tip vortices are captured by the method. The Actuator Line is still well in use today and has been used to study Wind Turbine performances, the effects of atmospheric boundary layer and turbulence by Troldborg [81], near wake analysis by Sarmast et al. [82], tip vortex tracking and comparison from Ivanell et al. [83] and wind farm interaction study by Jha [84]. At the time of writing, the original Actuator Line is still widely used in different codes with some minor changes and improvements regarding the velocity sampling and application of a tip loss function to better match the experimental results [85].

A potential further evolution of the ALM is the Actuator Surface (with source terms) [70]. This method was originally only implemented in two dimensions. Instead of a line, a surface is used as the support from which the force is projected from. The shape of the force projection follows the shape of the pressure profile in the chordwise direction. A 2D Gaussian smoothing function is again added for stability reasons. The velocity sampling is performed some distance in front of the leading edge and is corrected from self induction of the bound circulation with a Biot-Savart law. The method was used to study vertical axis wind turbines and isolated airfoil profiles.

1.4.2 Recent Advances in Actuator Methods

Although the original ALM is a capable tool, there is still some problems with the model. The velocity sampling at the actuator points is inconsistent, the recommended smoothing parameter relies on a rule of thumb and the solutions can be greatly affected by a change in grid size and smoothing parameter as observed by Martínez-Tossas et al. [86]. The integrated Power and Thrust coefficients can often be either over or under estimated depending on the grid spacing or smoothing length choice. Consequently, some implementations also rely on Prandtl type tip loss functions to correct the spanwise loads which are often over-estimated in blade tip regions. Such corrections should not be needed as the 3D Navier-Stokes already take into account the effects of discrete tip vortices. In recent years, there have been different approaches to try and solve some of these problems.

Wimshurst and Willden [87] proposed to use airfoil properties extracted from full 3D resolved simulations of the wind turbine in associated wind flow conditions. Actuator Line simulations with these section properties were in good agreement to blade resolved simulations and were better than simulations that used 2D blade polars with a Tip Loss correction factor. However, running full blade resolved simulations to then apply them to a lower order model seems redundant and lacks flexibility in terms of other possible flow conditions or configurations.

To sample an accurate velocity from the flowfield around a wind turbine blade section and correlate it to an equivalent free-stream velocity, it must reflect only the effect of the free-stream and the induced velocity in the area of the blade section (negative for a wind turbine). However, the velocity in the vicinity of the blade is disturbed by the local circulation around the profile. To counter this effect Shen et al. [88] proposed to correct the sampling location (typically 1-4 chords in front of the leading edge) by subtracting the influence of the bound vorticity on the sampling point. The correction thus only considers the local induction and global flow velocity which allows proper use of 2D airfoil tables. The two methods suggested by the authors subtracted the influence of either a point vortex of strength equal to the local lift located the profile quarter chord or the influence of distributed vorticity on the airfoil surface reconstructed through the pressure coefficient profile and the Bernoulli equations. Both techniques used the Biot-Savart law of either the point vortex or distributed vorticity acting on an arbitrary located point. The distributed vorticity method performed better than the point vortex method to recover an equivalent free-stream velocity. However, the procedure requires an iterative procedure to converge as the Biot-Savart law requires a circulation value which in itself is the result of the proper velocity sampling.

Shives and Crawford [89] showed that by superposing a Gaussian smoothed force perpendicular to an incoming flow, the velocity profile within the force affected region is similar to a Scully vortex with a viscous core. Therefore the velocity in the vicinity of an actuator line could be sampled directly in its centre, on the line itself as a vortex velocity induction on itself is zero provided the mesh is fine enough. Would a coarse mesh be used, important errors can be present. The authors also suggest that the Gaussian smoothing parameter be at least 4x larger than the local mesh size to not be affected by numerical oscillations. The value could be code dependent. The Gaussian smoothing parameter was also scaled with the local chord of an elliptical wing and showed better results than a constant smearing parameter along the span of the wing.

Schluntz and Willden [90] proposed a way of sampling the velocity around an actuator line by considering the location of application of the force (typically the quarter chord) as being a point vortex and taking three sampling points around the centre (on a same radius, a point directly above, in front and under). With these three sampled velocities, the three unknowns consisting of the bound circulation the two in-plane velocities (yielding the velocity magnitude and angle of attack) can be identified. A new distribution function was used instead of a Gaussian function with reported mixed results.

Kim et al. [91] proposed to couple a numerical lifting line method to an actuator surface method. The actuator surface method models the blade planform interface and applies a source term directly on the interface. The forces are not smeared by a Gaussian. The velocity is sampled on a line in front of the blade planform and corrected from the induction of the bound circulation with the help of the bound circulation of the lifting line. The trailing vortex lines are also considered and are said to help with the prediction of the velocities at the tip thus eliminating the need of a tip loss function.

Mittal et al. [92] tested different ways of obtaining the velocity at actuator line control points by using an average of a few nodes around the point of application and by using gradient information to extrapolate the velocity of the nearest nodes. Both methods reduced the “noise”/standard deviation a direct sampling method at the closest node would have, however results in terms of coefficients did not show improvements. A new 3D Gaussian smoothing function that had two different smoothing lengths based on the local chord and on the size of the blade element was also tested with marginal improvements.

In Martínez-Tossas et al. [93], the authors conducted an extensive test campaign to qualify and quantify the effects of using Gaussian force smoothing that represents an airfoil. Every computation was performed with linearized Euler equations in order to derive analytical expressions. The velocity sampling is explored with the presence of only a lift force, sampling the velocity in the middle of the Gaussian kernel is correct, but has to be corrected if an additional drag force is considered. Flowfields between a Joukowski airfoil and a Gaussian function of equal lift were compared and the error of velocities in the flowfield minimized in order to find which smoothing parameter and position resulted in the best flowfield. The same procedure was used to compare a Gaussian distribution which had a smearing parameter in the chord and thickness direction. Overall the optimal location tends to be slightly in front of the 1/4 chord line and the optimal values did not change with the angle of attack. However, they changed with airfoil camber change.

In Jha et al. [94] some of the main problems of the ALM are exposed such as the mesh and smearing length sensitivity of the method. The authors suggest a new way of scaling the Gaussian function. The 3D smearing parameter is scaled with an equivalent local elliptic chord. The aspect ratio of the actual blade is evaluated and an equivalent elliptical blade, with similar aspect ratio, is calculated. The results give an “equivalent" blade with variable chord length that is elliptic. The smearing parameter is then scaled according to it. The method shows improved results compared to a constant coefficient scaling.

Based on some of the articles reviewed hereinbefore, Churchfield et al. [95] proposed to project the force by a non-isotropic Gaussian function with smearing parameters in three directions: profile-chord, profile-thickness and blade-radial. These three parameters would then be tied to geometric blade dimensions for scaling. For the velocity sampling, an integral of the velocity multiplied by the value of Gaussian function at every grid point is performed. The development of this method comes from theoretical derivation of 2D incompressible steady Navier-Stokes formulas upon which a force is projected by an arbitrary function that integrates to unity. Therefore, this way of sampling velocity should be applicable to other functions than solely Gaussian-based kernels.

1.4.3 Actuator Methods Applied to Helicopter Flows

Actuator Disks have been used to model helicopter rotor flow for some time now and are still in use today [96] even when more powerful tools exist such as overset meshes. Steady and unsteady versions exist with the latter being somewhat similar to an Actuator Surface [97] and sometimes called Actuator Blade. Different types of Actuator Disk boundary conditions have been studied by Le Chuiton [98] in a compressible Navier-Stokes solver. The source terms approach proved to be the most robust and stable compared to direct modifications of flow variables or characteristics across the disk. Since the energy equation is also solved, a work term of the force times the velocity appears. O'Brien and Smith [99] explored different loading patterns for an actuator disk and found the BET loading to be the more physically representative and that the constant loading should be avoided. Compared to overset methods, actuator disk and actuator blade methods are more diffusive in terms of tip vortices but still predict the average pressure coefficient well on the surface of a fuselage [48].

Although the Actuator Blade of the previous author is a reduced order method that should be faster than full computations, a non-optimized search algorithm made the code slower than overset simulations thus nullifying its performance advantage. Lynch et al. [100] optimized the search algorithm by implementing an efficient k-d tree search algorithm to detect the closest cells to the source cells which is said to be 5x faster than overset blade resolved simulation. Kim et al. [101] have also experienced interesting speed-ups (3x) when compared to overset simulation at a similar level of accuracy. Inflow models were used in the last one to correct under-predicted tip losses.

The aforementioned Actuator Blade method usually distributes the loading evenly in the chord direction. Kim and Park [102] proposed to distribute the force along the chord following an inviscid pressure distribution over a symmetric airfoil. In order to find the velocities and angle of attack an integral average of the last 80% of the chord was considered. Kim et al. [103] expanded on previous work on wind turbines actuator surface to include the lifting line correction of the bound circulation in Actuator Surfaces for helicopter applications with encouraging results. A slightly different approach by Linton et al. [104] used a tip vortex wake with only one vortex line to account for the induced bound vorticity and tip effects. These last authors also developed an unsteady coupling algorithm for their lifting surface that takes into account the time history force response of the profile in an event of parallel Blade Vortex Interaction event as well as a pitch oscillating airfoil [105]. Their ASM model was used to simulate different helicopter configuration and in interaction with a ship with the aim of evaluating the dynamic interface [17, 106, 107].

The actuator line with Gaussian smeared forces is seldom used in the rotorcraft community. Alpman et al. [108] combined a helicopter flight dynamic model to a modified ALM in order to compute rotor load time histories for a rotor placed behind a hangar with incoming wind. A rotor placed behind a ship frigate was also used to evaluate different coupling procedures between the different solvers. Schmitz et al. [109] used it to model a rotor hub considering only drag forces. In a showcase of complex interaction problems Forsythe et al. [110] used a modified version of the original Actuator Line to study a full moving helicopter landing on a ship coupled with a pilot model from a flight simulator program. The integral velocity sampling discussed previously was used. The Gaussian was modified to take into account larger azimuthal steps which effectively swept the force source term. Delorme et al. [111, 112] used the ALM to compute the noise generated by a rotor in a Large Eddy Simulation (LES) framework through the use of a Ffowcs Williams-Hawkings acoustics model.

In an interesting adaptation of the actuator line method Caprace et al. [113, 114] transformed a vortex-theory-based lifting line representation of a rotor blade into a model analogous to an ALM through the mollification of the lifting line equations. The new model was coupled to a vortex particle method free-wake for a non-diffusive representation of the wake.

1.5 Thesis Objectives

The goal of this project is to develop a high fidelity aerodynamic model that is capable of accurately simulating a rotor flow in challenging and diverse flight conditions at a lower computational cost than blade-resolved U-RANS models. As observed in the previous sections, actuator methods are widely used to that effect. These methods procure a substantial advantage in terms of computational time when compared to fully blade-resolved simulations. This advantage however comes at the cost of some accuracy. In the context of interactional aerodynamics or in confined areas, this loss of absolute accuracy over a single simulation is balanced by the possibility of running parametric sweeps more efficiently, provided these actuator methods still correctly predict the global trends in terms of thrust, torque and moment coefficients in addition to global flowfield characteristics.

Specific Objectives

1. Develop a rotor replacement technique based on unsteady momentum source terms approach in order to model the force a rotor exerts on a flowfield. The method would run faster than a fully blade resolved overset method with the speed-up on the order of the mesh ratio between the two methods.
2. Identify and examine model parameters that produce accurate Thrust, Power and Moment figures compared to equivalent blade resolved simulations and/or experimental data and ensure global trends are captured.
3. Validate the method on a wide range of experimental data setups in increasing level of complexity including hover, axial flight, ground effect, fuselage assessment, forward flight and in interaction with a generic obstacles.

The developed method will be implemented within a commercial CFD flow solver as a constraint. StarCCM+ is selected because of its ability to handle user-coded field functions through which the model will be developed. The software also includes a complete suite of CFD models such as overset mesh capabilities. A direct comparison of the developed model and more traditional fully blade resolved simulation on the same mesh and solver basis can therefore be performed in order to focus on the rotor modelling instead of the flow solver itself.

1.5.1 Thesis Scope and Methodology Overview

Flowfields in some of the considered applications, including behind a ship, can be highly unsteady with large separated surfaces [115]. Ship simulations fully coupled with a rotor model in an unsteady framework showed significantly improved results compared to models ran separately or in a time averaged way [64]. Furthermore, when considering the fuselage, time accurate simulations can predict the unsteady loads and the interaction between individual blade passages over the fuselage resulting on possible unsteady loads on control surfaces and fuselage [9, 62]. Steady or azimuthally averaged methods such as the actuator disk would not account correctly for these interactions. Unsteady momentum source terms techniques such as the Actuator Blade [116] are starting to gain popularity but their implementation are usually done on cylindrical/disk shaped meshes. These meshes tend to need to be conformal with the rest of the domain in order to have a clearly defined interface and do not handle the geometric movement of the blade and possible coning angle and blade motion. On the other hand, methods such as the Actuator Line [80] handle well arbitrary blade positions and unsteady flow effects associated to rotors. Their source terms spreading through the summation of Gaussian functions is easily implemented in any flow solver. The method is widely adopted and used in the wind energy sector with active developments made on the research side. Using the method for helicopter applications would therefore benefit from convergent research efforts from both wind and aerospace rotor applications. The ALM is therefore selected as the rotor replacement technique.

Although widely used today, the actuator line has some problems and ambiguities that could prove critical in helicopter applications. In wind turbine applications the method is typically used to study the far wake, large scale turbulence effects, global flowfield and wake expansion, turbine performances and interactions. This project aims at studying the near field of a helicopter rotor and its performance. The interaction of the blade with the fuselage is only a few chords below the rotor and the ground effect starts to be noticeable at around 1-3 rotor diameter below. Rotor performances are also extremely sensitive to the location and intensity of tip vortices. In conditions such as in hover, these vortices will be advected solely by the induced flow of the rotor. Therefore the “rule of thumb” usually employed for scaling the isotropic Gaussian smearing parameter with a fixed amount of cells to prevent numerical oscillations has to be revisited. Too much smearing can cause the solution to be too diffuse and no flow acceleration/deceleration will be observed above or under the profile. Integral velocity sampling [95] will also be validated as it has not been done before. The effect of spanwise force distribution and smearing needs addressing. As it is now, a smearing parameter too large could disrupt the position and strength of the tip vortex. Helicopter blades find the majority of their loading at the tip. If the Gaussian smears this force peak past the blade tip, the vortex could be too much outboard and not affect the blade loading correctly. Furthermore, a Gaussian smoothing too large can smear the loading peak and the strong gradient in that region will be diminished causing incorrect trailing vortex strength according to lifting line theory. The developed model is believed to be a gateway towards an actuator line where the span loading solution would not need to be corrected by tip functions or lifting lines coupled to the solver. Proper tip vortex representation in Navier-Stokes based simulations should be sufficient to get the appropriate loading.

In the literature, a wide selection of experimental data is available. Many of which are based on real rotor aeromechanics. As such, to represent a real helicopter, rotors are often articulated and trimmed. This adds to the complexity of the rotor performance evaluation as the additional motions of the blades (other than the main rotation) have a significant impact on the aerodynamics which need to be accounted for with additional models [117]. For running trimmed simulations, a blade aeromechanic model with a trim algorithm needs to be coupled in addition. In an attempt to simplify the present study to solely aerodynamic effects, the selection of test cases is made in consequence with rotors showing no blade motions or with fixed geometries. It can be argued that such a simplification is not really representative of a real helicopter in operation, but all the main flow features and typical characteristics are nevertheless present. The ALM and fully blade resolved model will therefore be compared to each other from a purely aerodynamic standpoint without a possible discrepancy from a possible mismatch in a secondary model.

1.6 Thesis Outline

This thesis is arranged in an article-based fashion and is presented as follows:

- **Chapter 1 - Introduction**
  The problem is presented along with a review of the literature of various rotor modelling techniques and an in-depth look at rotor replacement techniques applied to both wind turbines and helicopter rotors. Research objectives are then stated.
- **Chapter 2 - Parametric study on the ALM velocity sampling and fixed wing performances assessment**
  A two-dimensional ALM model is introduced to explore diverse flow features and model settings. The main velocity sampling techniques for ALM simulations are benchmarked and compared to actual free-stream conditions. Limitations in terms of flow regime, model calibration coefficients and mesh requirements are observed. Then, an extension to a three-dimensional finite wing is presented. The effect of different Gaussian widths is explored in addition to an assessment of the model subject to an angle of attack sweep and aspect ratio variation.
- **Chapter 3 - Article 1: Hovering Helicopter Rotors Modelling Using the Actuator Line Method**
  A three-dimensional ALM implementation with a novel spanwise distribution is presented. The effects of the Gaussian smearing parameter is explored over a full collective sweep. Then an in-depth analysis of the rotor performances in terms of integrated performance coefficients, blade loading, tip vortex positions, strength and core radius. A computational efficiency assessment of the ALM and blade resolved overset solution is performed.
- **Chapter 4 - Axial flight: Vertical climb and descent**
  The model is placed in an axial flow scenario consisting of climb and descent at different

rates. Comparing to the numerical results, good agreement is found with the ever so important linear trend in figure of merit being properly captured.

- **Chapter 5 - Article 2: Numerical simulations of a rotor in confined areas including the presence of wind**
  The ALM is benchmarked against blade resolved simulations in multiple flight conditions including Hover, with the presence of fuselage, forward flight, in ground effect and in the presence of a box-shaped obstacle. The performances of the two methods are compared to the integrated load coefficients from experimental data.

- **Chapter 6 - General Discussion**
  The current modelling capabilities of the method are assessed with an in depth discussion of the current limitations observed through the different thesis chapters. Then an assessment of the method in terms of physical representation of the flow is performed. Followed by a comprehensive computational time and speed-up comparison.

- **Chapter 7 - Conclusion**
  Results from the thesis are synthesized and the objectives assessed. Limitations are summarized and future research paths and recommendations are explored.

CHAPTER 2 PARAMETRIC STUDY ON THE ALM VELOCITY SAMPLING AND FIXED WING PERFORMANCES ASSESSMENT

2.1 Context

The Actuator Line Method typically relies on tabulated 2D airfoil data in order to apply an equivalent force on the flowfield. To find the appropriate force, the method samples the velocity in the flowfield to relate it to the freestream value needed by the 2D airfoil tables. Several velocity sampling techniques exist, and there is still no consensus on which one to choose for optimal performances. In an attempt to judge the different sampling methods purely on a velocity sampling performance basis, this chapter first compares the performances of the main sampling techniques in a 2D framework thus comparing them directly against the real freestream imposed on the farfield boundaries and void of any three-dimensional effects. Then an extension towards a 3D wing is performed to assess the performances of the best sampling method against a fully resolved CFD wing in order to validate the ALM in an equivalent and simplistic scenario.

The two steps of evaluating the velocity and projecting the force onto the field can be ambiguous and have been at the centre of much of the proposed improvements to the method through the years. The sampled velocity must be able to include the effects of rotor inflow, blade rotational speed and tip vortex influence, but must not include the self-induction the local body force has on itself. This sampled velocity is then translated in freestream velocity U_∞ and angle of attack α_∞ needed by the 2D airfoil database. Once the force of an element is retrieved, it can be projected on the mesh through a smoothing kernel, with the isometric Gaussian being the most widely used. In multiple wind turbine applications, the size ϵ of the Gaussian kernel has become a tunable parameter in order to achieve a better representation of global rotor performance coefficients or to stabilize the solution. Even if some Gaussian smearing lengths might seem to improve the solution in terms of global performance coefficients, the resulting flowfield in the close vicinity of the rotor-blade is often inaccurate and too diffuse which could prove even more critical for helicopter applications. A recent in-depth look at these issues is presented in Churchfield et al. [95].

To sample the velocity that will be used to interpolate the 2D airfoil database, a zone that feels the local inflow due to the effects of the wake, in particular the tip vortices, needs to be identified. This zone also needs to be insensitive to the up/downwash that the source

---

Parts of this chapter have been presented in Ref. [118]

term produces on the surrounding flow. In essence, a Gaussian smeared ALM blade can be idealized as a vortex singularity-based lifting line and produces similar up/downwash patterns in the close vicinity of the line-like representation of the blade bound vorticity, i.e. a point vortex flowfield that is related to the local section circulation through the Kutta-Joukowski theorem.

Martinez-Tossas et al. [93] developed a 2D analytical solution of a flowfield affected by a Gaussian shaped source term and observed that the velocity sampled directly at the centre of the Gaussian yielded exactly the freestream velocity $\vec{U}_\infty$ when only the lift force was considered. Some corrections were needed to take into account the effects of a drag force. Shives and Crawford [89] showed numerically that the effect of smearing a lift force by a Gaussian in a 2D flow resulted in a velocity profile around the centre of application of the force that resembled a point vortex with a Scully type viscous core, thus zero self-induction at the centre. With these observations in mind, it becomes clear why most of the velocity sampling techniques try to sample as close as possible to the centre of the Gaussian smeared force: the flow passing through this point is not affected by its own circulation self-induction and is thus a good representation of the freestream. This is only true for an isotropic Gaussian smearing kernel, however.

In their original article, Sørensen and Shen [80] do not explicitly mention how or where the velocity sampling should be done. One of the simplest techniques could be to use the cell-centred value of the closest cell. In the literature, this technique is seldom used, but it was the one employed by Mittal et al. [92] before new development presented in their paper. In his thesis, Mikkelsen [78] points out that even if the discretization of the line matches with the mesh discretization, when it is put into motion, the sampling points on the line do not necessarily match with the grid centroid anymore. Therefore a linear interpolation of the cell centred velocity values onto the sampling point has to be performed. This mismatch between the sampling point and cell centred values is even more evident when the discretization of the line does not match with the grid when coning angle is introduced and if an irregular/unstructured grid is used. Mittal et al. [92] proposed additional ways to correct the sampled velocity. An average of the 7 to 21 closest nodes, extrapolation to the sampling point using velocity gradient information from the closest node and a combination of both. The average of 7 nodes and extrapolation of the closest cell improved the Power Coefficient prediction, but most importantly reduced the standard deviation of the performance coefficients. Due to the similarities of the flowfield around the actuator line and potential flow, Schluntz and Willden [90] proposed to sample the velocity around the point of application of the force and correct it by subtracting the effect of a point vortex. A similar approach by Shen et al. presented in [88, 119] was applied on fully blade resolved Wind Turbine simulations in order to obtain the equivalent 2D angle of attack and velocity. Finally, in [95, 110] an Integral Velocity Sampling method is proposed which consists in a weighted average of the velocity field where the weights are the values of the projection kernel. This last method should also be valid for any projection function, not only isometric Gaussian, as long as it integrates to unity.

All these methods have been introduced in order to improve the velocity prediction of the ALM, but most of the time, only the global performance coefficients (Thrust and Power) are considered. Sometimes, the sampled angle of attack is compared to the results of BEMT or theoretical lifting line results of a simple wing section. Furthermore, these comparisons are often performed on similar types of grids and solvers which are well suited for the study of the far wake behind a wind turbine rotor. It is therefore difficult to conclude over the merit or performance benefits of a velocity sampling method on such specific settings, especially in a 3D framework where inaccurate representation of a Gaussian smeared force can have substantial effects over the solution, in particular on the tip vortex structure which is essential in obtaining an accurate solution.

2.2 Methodology for Two Dimensional Velocity Sampling

For the results to be considered as general as possible, different flow solvers combinations and meshes are presented and tested. Then the formulation of the ALM in a 2D framework is described followed by the different velocity sampling techniques. Finally, two Base Cases are defined and the different variable parameters are outlined.

2.2.1 Flow Solver

The implementation of this 2D ALM is performed in Star-CCM+ 12.06 [120]. It is a general purpose, finite-volume, unstructured, cell-centred, multi-physics flow solver. Different solvers are available depending on the physics of the flow being considered. Different solver combinations are considered ranging from segregated algorithms to density based coupled approach along with a wide range of turbulent closure models. All have been tested with the 2D ALM resulting in no, or negligible differences. Mode details are found in [118]. A coupled, compressible and inviscid flow solver running at low Mach numbers is ultimately selected for the majority of the simulations herein. The goal of using such a simplistic flow model is to be as close as possible to the theoretical developments of Martinez-Tossas et al. [93] and Churchfield et al. [95] which do not include the effects of viscosity, compressibility, turbulence and the energy equation. The use of an incompressible segregated flow solver without the energy equation was also considered, but the coupled solver converged in about 10x less iterations with proper solver settings.

2.2.2 Meshes

The mesher within Star-CCM+ offers three main types of mesh in 2D: Trimmed cell mesh, Triangular mesh and Polygonal mesh. The first one is very regular as it generates square cells where each level of refinement is exactly half of the previous coarser one such as an octree type mesh. The other two types of meshes are typical unstructured grids with irregular shapes and arrangements, but still respect the overall imposed grid size Δ_g. All three mesh types are investigated since the trimmed cell mesh represents the type of mesh that is currently being used in Large Eddy Simulations for wind turbines and the other 2 are more suitable for generic and complex 3D geometries for RANS simulations such as helicopters.

The basic template for the mesh generation is presented in Fig. 2.1 along with an example of a Polygonal Mesh used. The mesh is built around a fictitious airfoil profile of $c = 1\,\mathrm{m}$ roughly centred in the middle of the domain. The outer part of the domain is a square with a minimum distance of 40 chords to the profile. The inner refinement zone is also a square with a distance of 5 chords away from the profile. This dimension is set in order to have the Gaussian function decay to 0 before it leaves the inner refinement zone, thus having the whole Gaussian on a single mesh size without coarsening. The target grid size Δ_g/c is imposed in the refinement zone and the cells on the boundaries of the domain have a size of 1.0 meter (i.e. one chord). A low volumetric growth rate is used to ensure a smooth transition between the two zones. Table 2.1 gives an overview of the meshes used and their sizes.

Table 2.1 2D Mesh sizes

	Nb. cells		
Δ_g/c	Trimmed	Triangular	Polygonal
2	1600	2278	1208
1	6400	9180	4727
0.5	6832	14418	5624
0.25	9052	20398	10334
0.125	16120	43872	22071
0.0625	39568	114436	57353

2.2.3 Actuator Line in 2D

As the ALM is a 3D model, modifications are in order for the model to be studied in 2D. Essentially, a cross-section of a blade is studied in order to relate it to 2D flow making the

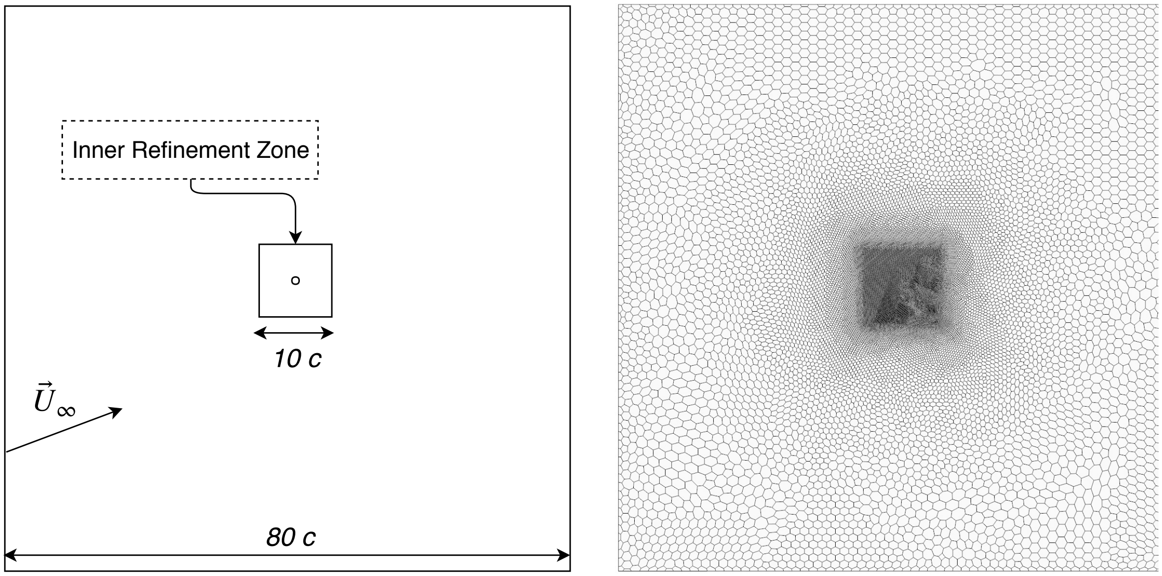

(a) Mesh Domain Template (b) Polygonal Mesh $\Delta_g/c = 0.125$

Figure 2.1 2D Mesh representation

method more of an "Actuator Point" than a line. To simulate an airfoil with the ALM in 2D, the appropriate forces need to be applied on the flowfield as in Eqs. (2.1) and (2.2).

$$L' = \frac{1}{2}\rho U_\infty^2 c C_l(\alpha_\infty, Re, M) \tag{2.1}$$

$$D' = \frac{1}{2}\rho U_\infty^2 c C_d(\alpha_\infty, Re, M) \tag{2.2}$$

Usually U_∞ and α_∞ are the values sampled from the flowfield in order to get the force and proper coefficients from pre-computed airfoil tables. In this case, they are taken directly as an input thus representing the *real freestream.* C_l and C_d are also imposed values. This allows a constant force projection independent of the various errors encountered by the different sampling techniques. Since the freestream angle is set at the inlet (i.e. the fictitious airfoil profile chord remains horizontal), the resulting force vector is oriented so the lift is perpendicular to the inlet freestream and the drag parallel. The force projection is done through an isotropic Gaussian function Eq. (2.3) which is taken as a product with the force vector and therefore distributed in the surrounding cells as a body force per unit volume Eq. (2.4) as needed by Star-CCM+. When the energy equation is solved, there is the possibility to add a volumetric energy source term Eq. (2.5) corresponding to the rate of work done by the momentum source term:

$$g(x,y) = \frac{1}{\epsilon^2 \pi} \exp\left(-\frac{(x-x_0)^2 + (y-y_0)^2}{\epsilon^2}\right) \tag{2.3}$$

$$\vec{s}_m = g(x,y) \times \vec{F} \tag{2.4}$$

$$s_e = \vec{s}_m \cdot \vec{U} \tag{2.5}$$

where x_0 and y_0 are the coordinates for the centre of application of the force, ϵ the smearing parameter, and $\vec{U}$ the velocity vector.

2.2.4 Velocity Sampling

Closest Cell

The minimum distance between every cell centroid and the force application centre (x_0, y_0) is computed. The velocity vector is then extracted from the cell centre value with U_s and α_s computed which represent the sampled velocity and angle of attack. All the results presented are done with a Gaussian force centred exactly on a cell centroid near $(x, y) = (0, 0)$. According to the theory presented earlier, it should yield directly the freesteam values without the need for correction.

If the centre of the Gaussian force is not aligned with a cell centroid, the assumption of zero self-induction at the centre of the force will not be verified and the sampled velocity will need to be corrected in order to reflect the freestream as illustrated in Fig.2.2 when $d \neq 0$. Furthermore, when used on a regular grid (such as the Trimmed cell mesh), there are possibilities to have multiple cells with an equal distance to the query point which could cause numerical problems due to noisy velocity sampling.

Average (N cells)

A component-wise average ($\bar{U}_x$ and $\bar{U}_y$) of the velocity vectors $\vec{U}$ from the N nearest cell centroids is computed to obtain U_s and α_s. The goal of this technique is to average out the sampled velocities near the centre of application of the Gaussian, thus correcting the possible errors occurring when the closest cell is not centred on a cell centroid which would typically be the case in a real rotating 3D ALM implementation. An average over $N = [1, 1000]$ cells has been performed with $N = 6$ yielding the lowest error overall on the selected Polygonal mesh of $\Delta_g/c = 0.125$. It should be noted that even for $N = 1$ (which is equivalent to the closest cell directly centred on a centroid), a small error in sampling is present in the order of 0.02% and -0.8% of the velocity magnitude and angle of attack respectively. At $N = 6$, these errors drop to 0.01% and 0.2% with respect to the freestream values. Increasing the amount of averaging cells up to 1000 shows some resemblance of convergence towards the $N = 1$ value, but the behaviour is erratic and non-monotonic. It is therefore fortuitous that $N = 6$ yields better results and is only valid on the present mesh and particular setup. Different mesh arrangements and sampling locations will produce different results. Regardless of this limitation, $N = 6$ is used for the rest of the study.

Integral Velocity Sampling

This technique suggests a weighted average of the velocity field by the projection function as defined in Eq. (2.6). In the present case, the projection function is the Gaussian defined in Eq. (2.3), but could be any function that integrates to one. Numerically, this translates to Eq. (2.7). This implementation is consistent with what is used internally in Star-CCM+ to evaluate volumetric integrals such as momentum source terms.

$$\vec{U}_\infty = \iint g(x,y)\vec{U}(x,y)\,dx\,dy \tag{2.6}$$

$$\vec{U}_s = \sum_{i=1}^{Nbcells} g(x_i,y_i)\vec{U}(x_i,y_i)dA_i \tag{2.7}$$

In opposition to the methods presented above, the Integral Velocity Sampling does not rely on the fact that there is no self-induction at the centre of the Gaussian. It considers the whole span of the projection function and, in the case of an isotropic Gaussian, it has a certain bias towards the centre of the function. Therefore the method is not as local as the ones presented above which will cause incoming flow perturbations to be felt before and after they pass through the centre of application the force. But with the typical range of smearing lengths ϵ of the order of the chord, it should not cause a major issue in rotor type applications.

Point Vortex Correction

When not sampling at the middle of the Gaussian, the velocity needs to be corrected due to a non-zero induction at the sampling point caused by the circulation. Due to the similarities of a Gaussian smeared lift force to the potential flow of a point vortex in freestream, it becomes natural to correct the sampled velocity by the effect of a point vortex (in 2D). A Scully type vortex with a viscous core is considered with an azimuthal velocity induction presented by Eq. (2.8).

$$V_{\theta_{visc}} = -\frac{\Gamma}{2\pi}\frac{r_s}{{r_s}^2 + {r_c}^2} \tag{2.8}$$

This equation contains the circulation $\Gamma = \frac{1}{2}U_\infty C_l c$ which in turn depends on U_∞ and $C_l(\alpha_\infty)$ which are the two variables that are the end result of the velocity sampling. An approach similar to Schluntz and Willden [90] or an iterative method could be employed to solve this circular dependency. In the present simplified 2D case, there is no such issue since U_∞ and C_l are imposed. The sampling radius r_s is taken in front of the point application of the force in line with the fictitious chord. The velocity reading is taken at the closest cell centorid to the target r_s then the actual radius and angle are computed so the velocity induction corrections can be properly applied. The Scully core radius was taken as $r_c = 0.75\epsilon$ as suggested by Shives and Crawford [89] and matched well with the induced velocities observed especially at small ϵ. Finally, after testing multiple sampling radii, a value of $r_s = 1.75c$ in front of the force application yields the best agreement whilst retaining some locality of the sampling position. Although the dependence between the viscous core size r_c and Gaussian smearing parameter could also cause another unaccounted dependency for the sampling length r_s as larger kernel width would have this sampling length within the viscous core.

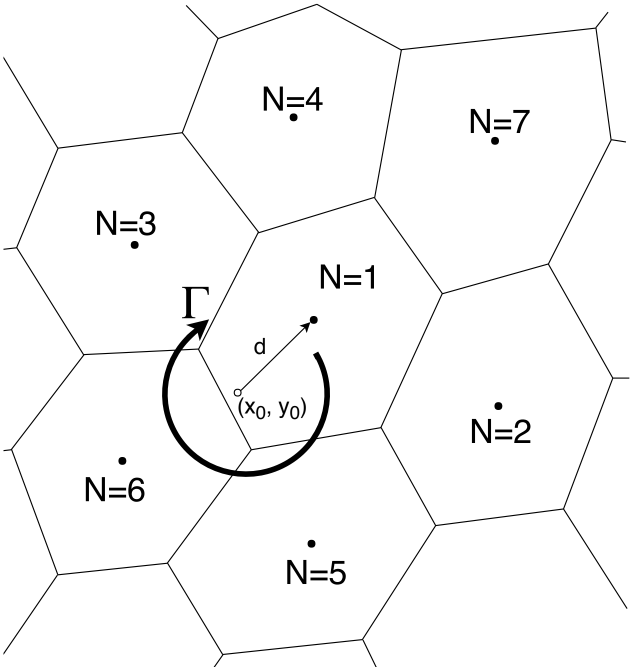

Figure 2.2 Discrete grid representation and general induced flow on unstructured mesh

2.2.5 Parametric Study Overview

This parametric study tries to consider parameters that could affect the performance of the Actuator Line in regards to velocity sampling. Therefore, variables of interest are the sampled angle of attack $\Delta\alpha_s$ and velocity magnitude ΔU_s relative difference compared to the freestream values (α_∞ and U_∞). To evaluate the ability of the Gaussian to project its force on the flowfield, the volumetric integral of $g(x, y)$ is evaluated in a similar way as Eq. (2.7), but without the velocity term. The integral should be equal to one.

Table 2.2 presents the two Base Cases considered herein. The first is an ideal case that can be tested against the theoretical developments discussed earlier and the second represents a more realistic case of an airfoil with a smaller Gaussian projection length thus a more realistic flowfield. Base Case 1 is used as the default case whereas Case 2 is used to test the different solvers and flow regimes.

Table 2.2 2D Base cases definition

	Base Case 1	Base Case 2
α_∞	5 deg	5 deg
C_l	1.0	1.0
C_d	0	0.02
ϵ/c	1.5	0.5
M_∞	0.2	0.2
Re	-	1E6
Δ_g/c	0.125	0.125
Mesh Type	Polygonal	Polygonal

The different parameters studied in the following section can be split into three different categories:

- *Mesh and Gaussian Size*: A mesh convergence study is performed on the three types of meshes described in Table 2.1. Then, on the default Polygonal mesh with $\Delta_g/c = 0.125$, ϵ/c is varied.
- *Airfoil Characteristics*: The effect of changing the freestream angle of attack is investigated. Then, the amount of force projected on the flow is varied by the means of changing the imposed C_l. Finally, drag is added to the flow for two different Gaussian sizes.
- *Flow Regime*: Considering Base Case 2 in order to have more realistic and challenging flow conditions and a more complete solver that considers viscosity and turbulence, the effects of different flow regimes are studied.

2.3 Results

2.3.1 Mesh and Gaussian Size

With a constant Gaussian size $\epsilon/c = 1.5$, the mesh size is varied in the range Δ_g/c=[0.0625, 2.0] with a refinement factor of two between the different levels. The mesh convergence based on ΔC_P and U_s sampling for the Closest Cell are presented in Fig. 2.3 for the three different families of meshes. For lack of a better integrated coefficient convergence metric, ΔC_P, defined as the difference in maximum and minimum C_P value in the field, is used for assessing flow convergence. Every velocity sampling technique converges in a similar fashion, towards a non-zero error value, regardless of mesh type. The different sampling techniques are presented in Fig. 2.4 for the Polygonal mesh. The flowfield is considered fully converged on all meshes at a value of $\epsilon/\Delta_g \approx 6$ in the present 2D framework. The different velocity sampling techniques also stabilize around $\epsilon/\Delta_g \approx 6$ except for the Average which behaves erratically due to the change in the local mesh size and cell arrangement near the centre of application of the force.

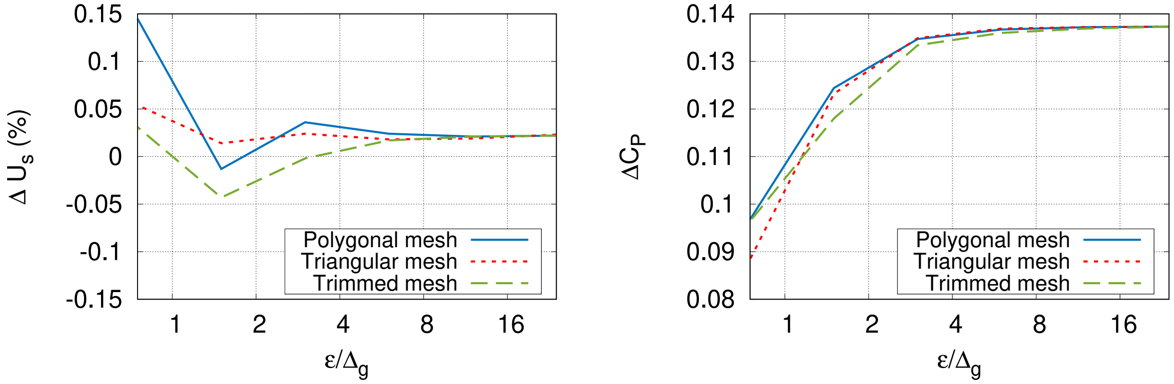

(a) $\Delta U_s\%$ (b) ΔC_P

Figure 2.3 Mesh convergence for $\Delta_g/c = [0.0625, 2.0]$ with closest cell sampling at $\epsilon/c = 1.5$

On the Polygonal mesh with a constant $\Delta_g/c = 0.125$, the size of the Gaussian ϵ is varied. Figure 2.5 presents the results for the different velocity sampling techniques. Similar to what has been observed for the different mesh sizes, the sampling methods converge to a low error for values of $\epsilon/\Delta_g \geq 6$ with some, most notably the integral velocity sampling, showing good flow and sampling convergence as early as $\epsilon/\Delta_g \approx 3$. This time, since the mesh is static, the Average is much more well behaved and the point vortex correction is not since the induced velocity profile changes with ϵ and the sampling radius r_s is kept constant.

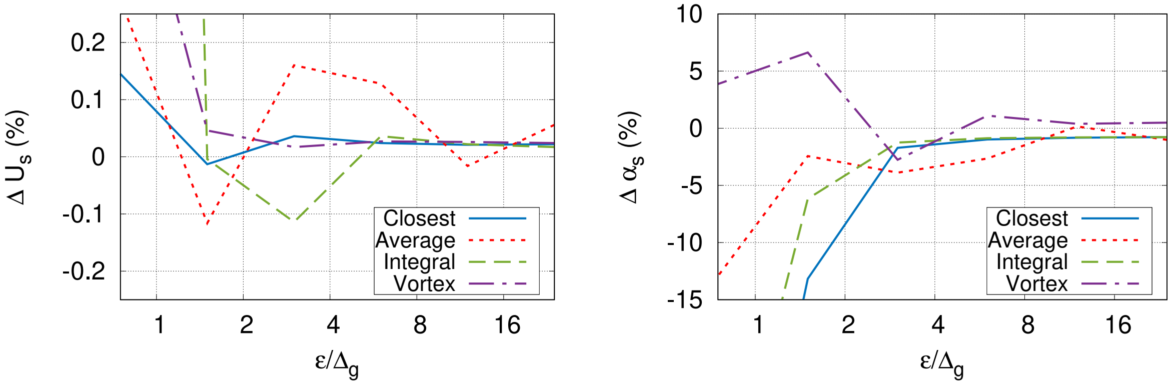

(a) $\Delta U_s\%$ (b) $\Delta\alpha_s\%$

Figure 2.4 Sampling error for different $\Delta_g/c = [0.0625, 2.0]$ at $\epsilon/c = 1.5$

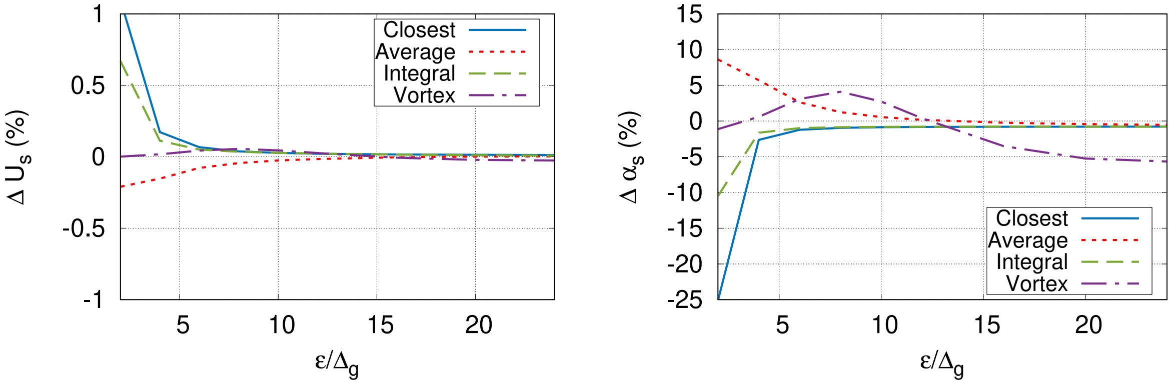

(a) $\Delta U_s\%$ (b) $\Delta\alpha_s\%$

Figure 2.5 Sampling error for different $\epsilon/c = [0.2, 3.0]$ with $\Delta_g/c = 0.125$

Changing the Gaussian size significantly alters the flowfield. Reducing ϵ/c towards the optimal value of 0.2-0.25, as suggested by Martinez-Tossas et al. [93], improves the flowfield compared to a real NACA 0012 airfoil at a similar C_l as shown in Fig. 2.6. But such a low value is not reachable on the present grid as the velocity sampling errors would be too large. Furthermore, as ϵ/c is lowered, the amount of cells supporting the force projection diminishes. At $\epsilon/c = 0.1$ ($\epsilon/\Delta_g = 0.8$) only 7 cells have a non-zero value for the momentum source term. This number falls to one for $\epsilon/c = 0.04$ as the Gaussian used in Eq. (2.3) decays to zero in approximately 3ϵ. At this point, with only one cell to support the force projection and the value of the Gaussian increasing at (x_0, y_0), more than 100% of the force will be projected in the field. If the Gaussian is not centred on a cell centroid, it could decay to zero before it meets a cell centroid thus projecting no force to the field.

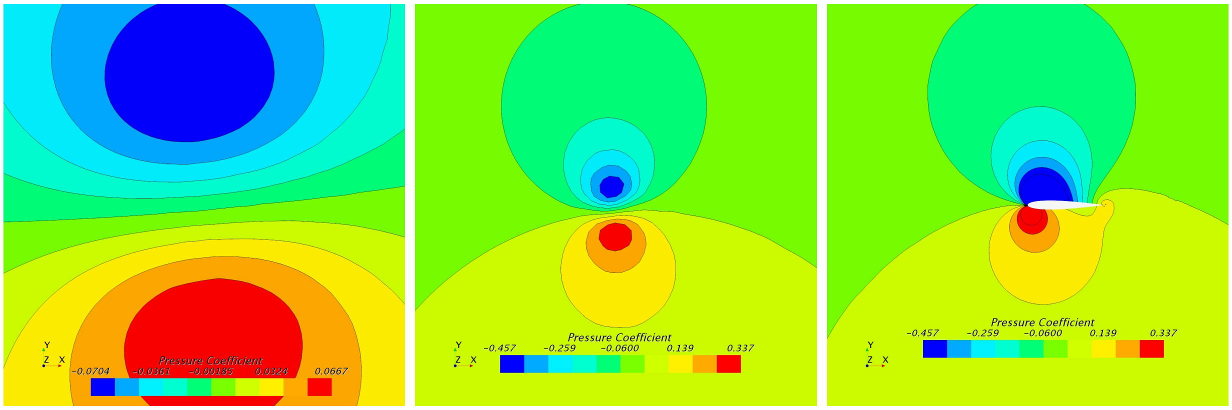

(a) $\epsilon/c = 1.5$ (b) $\epsilon/c = 0.25$ (c) NACA0012 at $C_l = 0.983$

Figure 2.6 Pressure coefficient field for different Gaussian sizes

This shows the importance of properly scaling the Gaussian to *both* the local chord and the grid as mentioned in Shives and Crawford [89] . The former allows the flowfield to be correctly represented compared to the flow around a real airfoil given a proper tuning of ϵ/c. The latter is needed in order to accurately represent the flowfield numerically allowing it to converge which in turn will yield a better sampling of the velocity. The values of $\epsilon/\Delta_g \geq 6$ suggested above will result in a higher cell count especially as ϵ/c is decreased towards its optimum value. This might cause unrealistic simulation sizes in typical LES Wind Turbines applications in wind farms but are easily achievable for helicopter rotor simulations with a proper local grid refinement for U-RANS modelling.

2.3.2 Airfoil Characteristics

Figure 2.7 presents the effects of changing the α_∞ on the velocity sampling. For U_s all the methods behave in a similar fashion but have a different offset and slope. They all have a small error of below 0.1% across the range tested. On the other hand, the absolute error of α_s is roughly constant at less than 0.05 deg across the whole span of α_∞ tested. The spike in relative error near 0 deg is due to the denominator getting smaller.

The effects of variation of the C_l are presented in Fig. 2.8. The error for U_s all follow a similar quadratic trend with different amplitudes and offsets. The error values are small at less than 0.15% for the different methods and C_l tested. The α_s error follows a linear trend for all the methods.

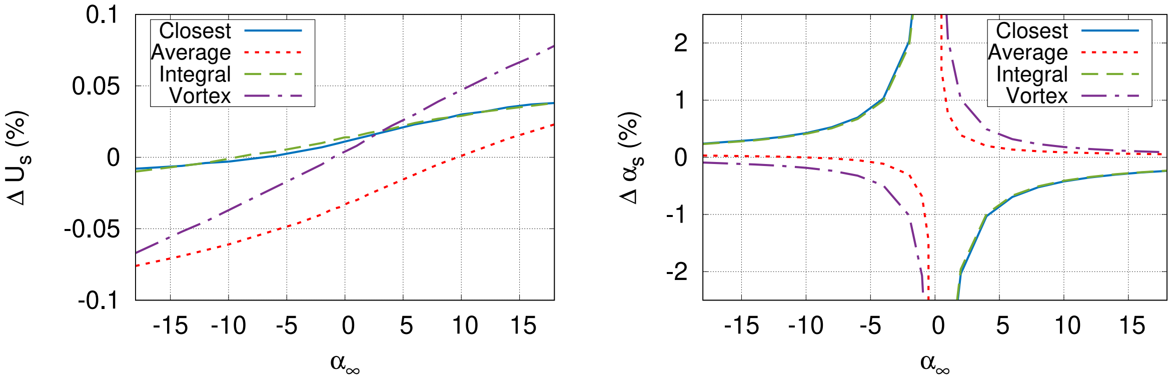

(a) $\Delta U_s\%$ (b) $\Delta\alpha_s\%$

Figure 2.7 Sampling error for different $\alpha_\infty = [-20, 20]$

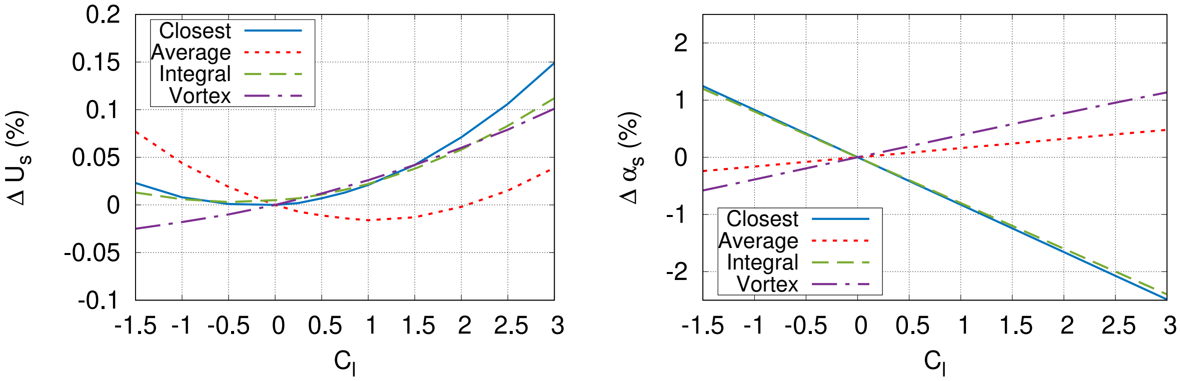

(a) $\Delta U_s\%$ (b) $\Delta\alpha_s\%$

Figure 2.8 Sampling error for different $C_l = [-1.5, 3.0]$

Adding a drag force parallel to the freestream alters the flow by creating a velocity deficit downstream from the point of application of the force as depicted in Figs. 2.9 and 2.12. The results for the velocity sampling are presented in Fig. 2.10 for $\epsilon/c = 0.5$ and 1.5.

Martinez-Tossas et al. [93] define $\frac{1}{4\sqrt{\pi}}C_d\frac{c}{\epsilon}$ as a correction term to the velocity magnitude sampled at the centre of a Gaussian with a drag force. The correction term is directly plotted on Fig. 2.10. They limit the range of validity of this correction term to $\frac{1}{4\sqrt{\pi}}C_d\frac{c}{\epsilon} \approx 0.28$ as, above this limit, the velocity deficit becomes non-linear. For our cases, this correction term at $C_d = 1.0$ with $\epsilon/c = 1.5$ and 0.5 evaluates to 0.094 and 0.282 respectively. Thus, the non-linear behaviour discussed above can be observed at high drag values with $\epsilon/c = 0.5$

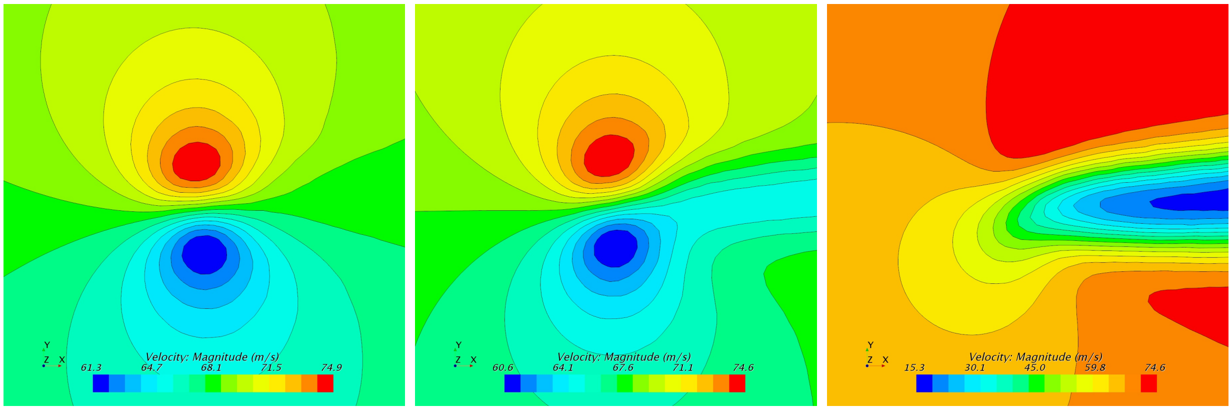

(a) $C_d = 0.0$ (b) $C_d = 0.1$ (c) $C_d = 1.0$

Figure 2.9 Velocity magnitude field with addition of a drag force at $\epsilon/c = 0.5$

which start to appear at $\frac{1}{4\sqrt{\pi}}C_d\frac{c}{\epsilon} \approx 0.14$ or at $C_d = 0.5$. In the linear region, this term is an excellent correction for the velocities sampled directly at the centre of the Gaussian. Since the point vortex correction is sampled upstream and the Integral Velocity Sampling is an integral average of the velocity field, this correction would not be applicable for these two methods as it stands. Fortunately, these methods are not as affected by the drag for the sampling of U_s. The sampling of α_s is much less sensitive to the drag as it remains roughly constant in the linear region of $\frac{1}{4\sqrt{\pi}}C_d\frac{c}{\epsilon}$. The exception is the point vortex correction due to the velocity induction upstream of the Gaussian being different from the Scully core model used for the correction term. On the other hand, since it is located upstream, the method does not feel much of the flow deceleration the other methods detect.

2.3.3 Flow Regime

Changing to Base Case 2, the effect of the Reynolds number is assessed by changing the viscosity of the flow. The error of the different sampling methods are presented in Fig. 2.11. At moderate to high Re, there is no effect. For low Reynolds numbers, viscous effects start to be noticeable and change the velocity field induced by the Gaussian smeared force as depicted in Fig. 2.12. For practical Reynolds number ranges used for wind turbines or helicopter blades applications it is a non-issue, however, it could impact the performances of velocity sampling for micro-rotor/drone applications. The only method not affected by this is the vortex sampling since the sampling point sits further upstream and is not affected by the change in local flow induction for this ϵ/c.

Finally, to investigate the effect of compressibility, the results for different M_∞ are presented

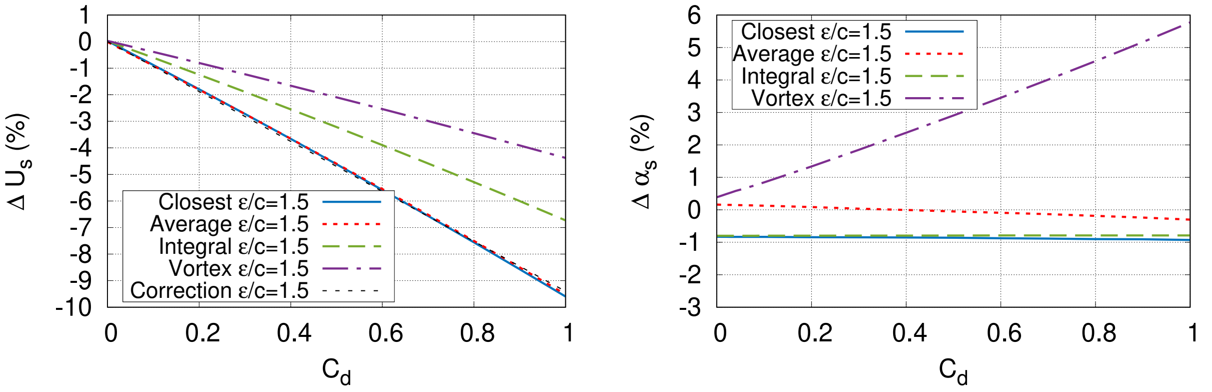

(a) $\Delta U_s\%$ at $\epsilon/c = 1.5$ (b) $\Delta\alpha_s\%$ at $\epsilon/c = 1.5$

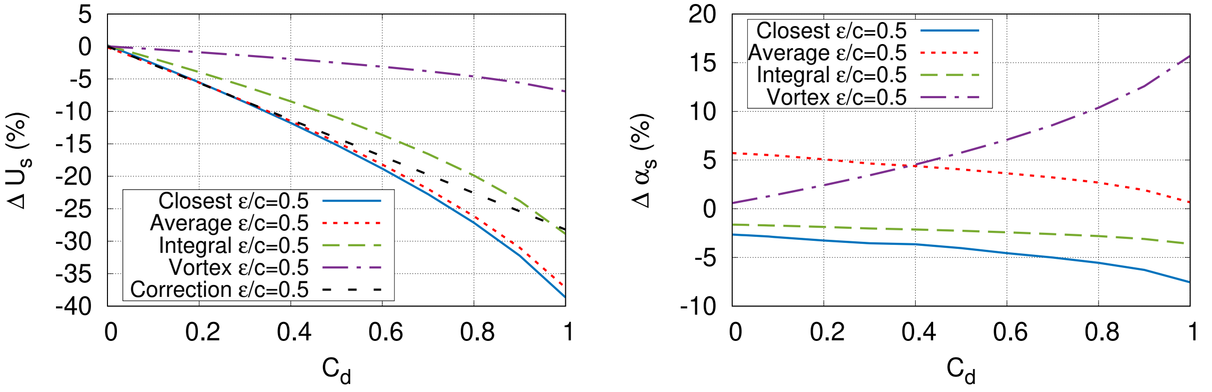

(c) $\Delta U_s\%$ at $\epsilon/c = 0.5$ (d) $\Delta\alpha_s\%$ at $\epsilon/c = 0.5$

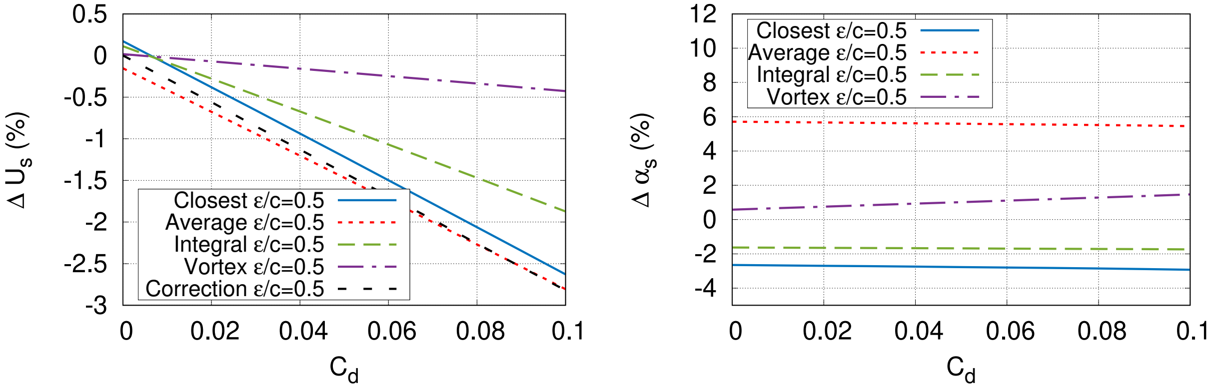

(e) $\Delta U_s\%$ at $\epsilon/c = 0.5$ zoom (f) $\Delta\alpha_s\%$ at $\epsilon/c = 0.5$ zoom

Figure 2.10 Sampling error for different $C_d = [0.0, 1.0]$

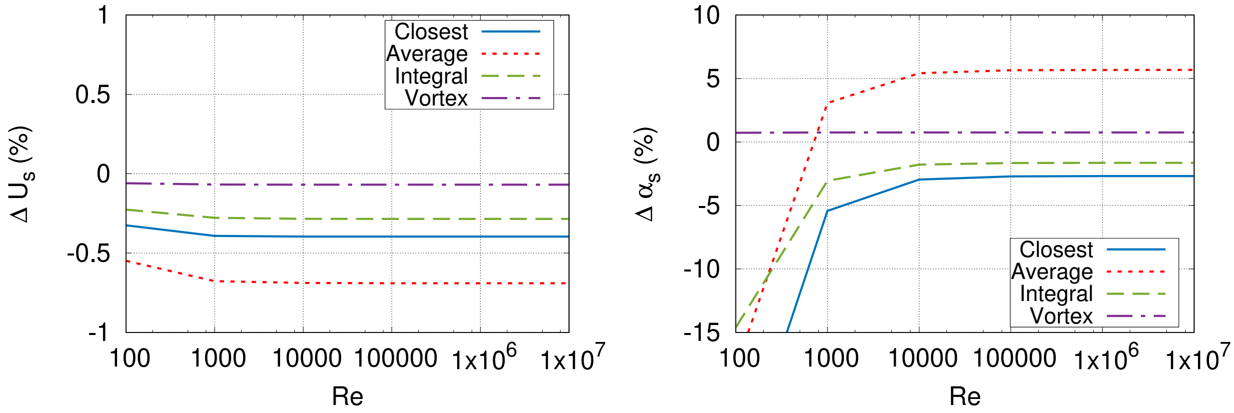

(a) $\Delta U_s\%$ (b) $\Delta \alpha_s \%$

Figure 2.11 Sampling error for different $Re = [10^2, 10^7]$

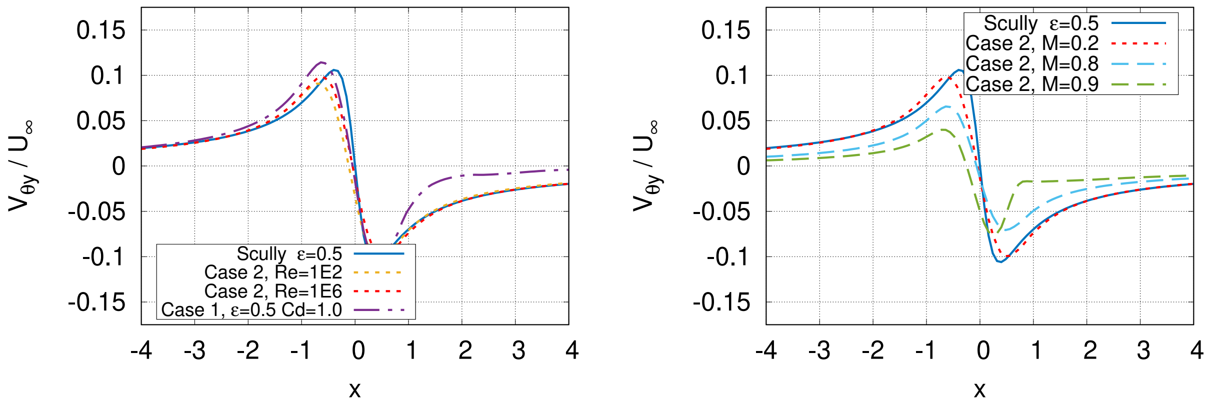

(a) Viscosity and drag variations (b) Compressibility variations

Figure 2.12 Induced velocity profile V_θ with $\epsilon/c = 0.5$ for different flow regimes

in Fig. 2.13. The sampling errors of both U_s and α_s grow as the compressibility effects start to appear. Relative to their respective low Mach error values, the velocity magnitude is more sensitive to the change of density occurring near the centre of the Gaussian force up to $M_\infty = 0.8$. At $M_\infty = 0.9$ the formation of a stationary shock changes the velocity induction of the Gaussian force in the region thus significantly impacting the angle of attack. The lower sensitivity of the vortex sampling is due to the fact that at $r_s = 1.75c$, the sampling is done some distance upstream where the density fluctuation is not as important as in the centre of the Gaussian. The change in the induced velocity profile is still enough to cause a significant error in the angle of attack.

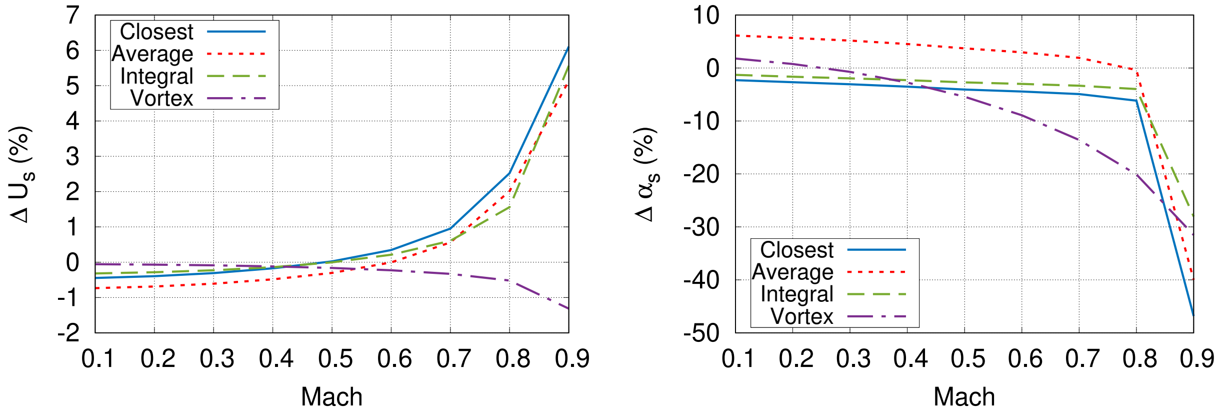

(a) $\Delta U_s\%$

(b) $\Delta \alpha_s\%$

Figure 2.13 Sampling error for different $M_\infty = [0.1, 0.9]$

2.4 Takeaways from 2D Analysis

The parameters that have the largest impact on the different velocity sampling techniques are the ones that make the model stray away from potential flow conditions. Poor mesh resolution for a given Gaussian size marginally resolves the flowfield thus changing it and yielding larger errors and erratic behaviour for the velocity sampling. The addition of a drag force creates a velocity deficit in the stream-wise direction that significantly impacts the velocity magnitude sampling. Different flow regimes where viscous or compressibility effects start being important also alter the flowfield. The error increases for all the velocity sampling techniques as they are all loosely based on inviscid incompressible flow theory.

Overall, the Integral Velocity Sampling consistently yields the lowest or second lowest error for the considered cases for both the velocity magnitude and angle of attack. It is on par and even out-performs the closest cell sampling which is, in this simplified case, directly located on a cell centroid therefore representing a theoretically ideal condition for Gaussian kernel centre sampling. This ideal location is however not always observed in practice with complex 3D meshes and moving blades. Due to its integral formulation and therefore averaging/smoothing characteristics, the integral velocity sampling is better suited to be applied on a rotating rotor where the velocity sampling point moves around on the grid thereby potentially causing noise or unsteadiness for the other sampling techniques.

In addition to the lower errors and consistency, the Integral Velocity Sampling does not rely on parameter tuning or a dependency on the circulation Γ to retrieve the sampled velocity. The implementation is straightforward and directly applicable on unstructured grids. As the general tendency is leaning towards more precise projection functions that are not isometric Gaussians, the property of zero self-induction at the centre of the force projection function could be voided. The Integral Velocity Sampling does not have this problem as it only requires the projection function integrates to unity over the domain. For all these reasons, it is therefore judged superior to the other velocity sampling techniques.

2.5 Extension to a Three Dimensional Wing

Now that the velocity sampling has been thoroughly investigated in a two-dimensional framework, with the important takeaways summarized hereinabove, the ALM framework is ready to be expanded in three dimensions with the integral velocity sampling being selected. The framework will consider a simplistic fixed wing application that is representative of a helicopter blade geometry with all results being compared to an equivalent fully resolved CFD wing on near identical meshes and flow solvers. A first investigation of the effect of the Gaussian size is performed as it was the sole tuning parameter of the ALM model which had a significant impact on the flowfield. A lift and drag polar is simulated with these two values compared in addition to the blade loading distribution. Then, at a constant angle of attack, different wing aspect ratios are tested.

2.5.1 Methodology

Test Case & Geometry

The selected test case for this section is a simple straight, un-twisted, non-tapered wing based on a NACA0012 profile and summarized in Table 2.3. The wing geometry is based on a rotor blade geometry later used in Chapter 5. The baseline setup consists of a half-wing aspect ratio of 10, numerically modelled through a symmetry plane, at a 5° angle of attack. Both of these baseline values are varied individually with the other one kept constant to study their effects separately.

Numerical Setup

The selected flow solver is again the density-based coupled algorithm with second order accuracy and inviscid fluxes evaluated by a Weiss-Smith preconditioned Roe flux-difference-splitting scheme [121] implemented in Star-CCM+. The turbulence closure is done through the $k - \omega$ SST turbulence model [122]. In order to save grid points and to exploit the symmetry of the setup, only half of the wing is modelled with a symmetry plane placed at

Table 2.3 3D Wing characteristics

Wing Geometry	
Airfoil Profile, constant	NACA0012
Chord, constant (c)	0.032 m
Linear Twist	0°
Velocity (U_∞)	101 m/s
Mach number (M_{wing})	0.3
Reynolds number (Re_{wing})	220000
Half Wing Aspect Ratio (AR)	2.5, 5, 7.5, **10**, 15
Angle of attack, (α)	2.5°, **5°**, 7.5°, 10°, 12.5°

the would-be full wing half span. However, Star-CCM+ does not handle well the symmetry boundary conditions with the added user-defined functions source terms. ALM simulations therefore present a small oscillation near the symmetry plane when compared with the fully resolved loading. It should be noted that the reported Aspect Ratios in this section pertain to the half wings only.

Meshes have farfield boundaries located 50 chord-lengths away from the half wing geometry with progressive mesh refinement towards the wing. Both the fully resolved and ALM grid have refinement regions for the near wake and wing-tip vortex, spanning ten chord lengths downstream with the latter having a grid refinement level of 6.25%c (1/16c). A further refinement region along the wingspan axis with a value of 3.125%c (1/32c) ensures that the minimal grid criteria of $\epsilon/\Delta_g = 6$ is met for the considered Gaussian lengths as discussed in Sec. 2.3.1. Although the integral velocity sampling showed superior mesh convergence characteristics in terms of flowfield resolution and sampling accuracy with $\epsilon/\Delta_g = 3$ proving sufficient. The fully resolved CFD wing has its boundary layer meshed with a near wall spacing equivalent to $5.0e-5$ along with 35 prismatic boundary layer cells normal to the surface ensuring a $y^+_{wall} \leq 1$. Further refinements are placed along the wing tip as well as the leading and trailing edges. For reference, the baseline fully resolved half-wing has 7.8M cells whereas the corresponding ALM simulation only has 2M cells. This showcases the potential economy in mesh size the ALM provides by eliminating the boundary layer mesh and additional geometry-related refinement present for fully resolved simulations.

The ALM is extended in the third dimension in a fully coupled fashion using a Blade Element approach with a detailed description given in the following chapter in Sec.3.3.3 with some modifications to adapt the method for fixed wing application, notably the removal of the rotational speed and movement. The ALM is discretized with 100 sections and uses a hyperbolic tangent spanwise distribution that allows clustering of ALM control points near the wing tip which is useful in fixed wing applications and critical for rotor blades. The hyperbolic tangent is not as aggressive as a cosine distribution and allows a more gradual refinement distribution thereby retaining adequate spacing near the blade root, and in the present case near the fixed wing centre close to the symmetry plane. In addition to the regular isometric Gaussian typically used and investigated in the two dimensional framework, a new span-truncated Gaussian is proposed as later presented in Sec.3.3.3. Truncating the Gaussian in the spanwise direction allows a more consistent projection of the force onto the flowfield that respects the geometrical dimensions of the wing. Otherwise, the force projection near the tip would overflow past the wing-tip thus potentially creating weaker tip vortices that sit too far outboard therefore modifying the induced velocity profile along the wing.

2.5.2 Results

Gaussian Width Influence

For a given mesh refinement level, changing the value of the Gaussian width has a significant effect on the flowfield convergence and velocity sampling as explored earlier in two dimensions. Provided the mesh is fine enough, varying ϵ/c also has a significant impact on the flowfield with larger values of ϵ producing diffuse flowfield whereas values in the area of $\epsilon/c = 0.25$ produced similar flow characteristics when compared to the 2D fully resolved airfoil reference. The ALM behaves similarly in a 3D setting.

First, Fig. 2.14 presents the vertical induced velocity flowfield over a plane parallel to the freestream passing by the quarter chord of the wing. Tip and bound vortices are represented by green iso-surfaces of Q-criterion. The different Gaussian smearing lengths are presented. When comparing to the fully resolved case, we can observe that Gaussian widths in the range $\epsilon/c = [0.125, 0.5]$ produce similar vertically induced velocity in the mid to far-wake region. Moving closer to the wing or the trailing tip vortex, only $\epsilon/c = 0.125$ and $\epsilon/c = 0.25$ (both regular and truncated) appear to accurately reproduce the velocity fluctuations. The value of $\epsilon/c = 1.5$ produces a much larger and diffuse bound & tip vortex pair not accurately represented at the selected relatively low Q-criterion level. This weak vortex structure in turn results in a more diffuse velocity field that is in no shape or form similar to the fully resolved wing reference. As suggested earlier, the regular isometric Gaussian kernel projects some force past the geometrical limits of the actual wing geometry. This behaviour is manifested here through the "rounded corners" appearance at the junction of the bound and trailing vorticity. This over-projection also produces slight changes in the location of the tip vortex sitting slightly more outboard, a trend which is exacerbated at the larger ϵ values. This issue is solved by truncating the Gaussian kernel which creates a much more realistic tip vortex structure, in particular with the rapid vortex core expansion just behind the wing (from the vortex formation onset until one chord downstream).

Looking into more details at the wing lift loading presented in Fig. 2.15, the effects of the weaker tip vortex structure are again observable with larger ϵ values being too weak to create appropriate downwash near the tip. All Gaussian smearing lengths otherwise create an appropriate loading along most of the span with an over-estimation present near the tips. However, the kernel with $\epsilon/c = 0.125$ does predict a somewhat lower lift distribution compared to the other kernel widths. This wing tip loading over-prediction is somewhat common in similar rotor replacement techniques with Caprace et al. [113] observing the behaviour in lifting line-based analytical ALM model whereas Linton [17] observed it in an actuator surface framework.

Truncating the Gaussian at the tip creates identical lift distributions for most of the blade span for a given ϵ. The behaviour at the tip is much more well behaved with a marked decrease in sectional lift in this region. It is however not sufficient to recover the reference fully resolved wing loading in that region. The use of the truncated Gaussian is only enabled by the utilization of the integral velocity sampling in the present framework as this sampling method theoretically accurately samples any projection function that integrates to unity, which is the current case through normalization. Other sampling methods have not been tested with this kernel variation as it offers no guarantee the velocity in the centre sees no self-induction and is an appropriate equivalent freestream representation.

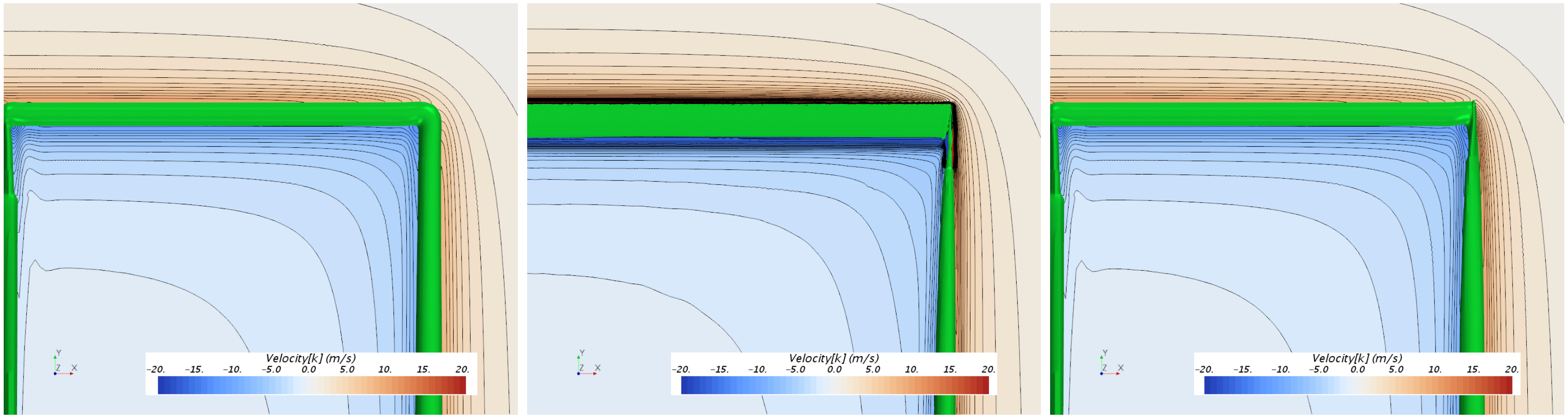

(a) ALM $\epsilon/c = 0.25$

(b) Fully Resolved

(c) ALM truncated $\epsilon_{tr}/c = 0.25$

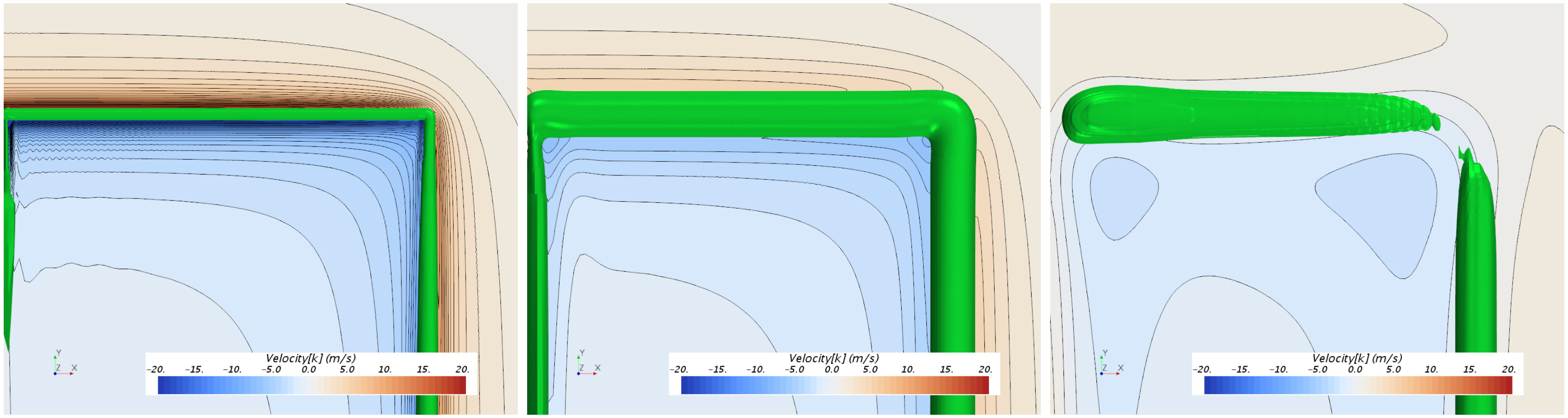

(d) ALM $\epsilon/c = 0.125$

(e) ALM $\epsilon/c = 0.5$

(f) ALM $\epsilon/c = 1.5$

Figure 2.14 Induced flow Velocity plane and Q-Criterion tip vortices at Q-crit=2500

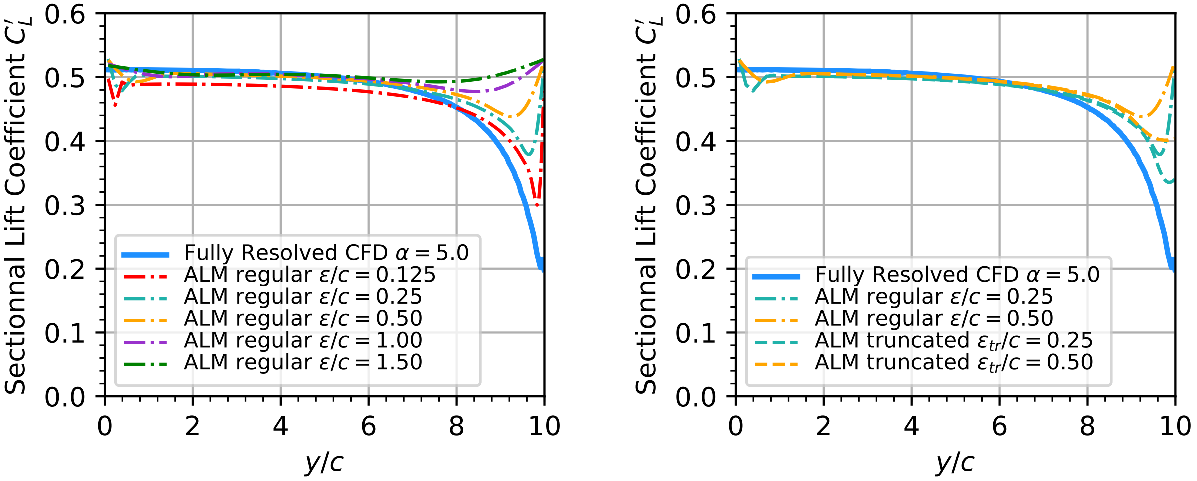

(a) Regular Gaussian

(b) Truncated Gaussian

Figure 2.15 Wing lift distribution for different Gaussian kernel sizes and types

Wing Polar

Simulating the fully resolved wing and both the regular and truncated Gaussian kernels at a width of $\epsilon/c = 0.25$ for an angle of attack sweep, the lift and drag polars of Fig. 2.16 are obtained. Both the fully resolved wing and the two ALM simulations produce near identical results in terms of total lift and drag coefficient. The regular Gaussian ever so slightly produced more lift than the other two. One remarkable feat is the accurate prediction of near identical C_L^{max} values and post-stall lift coefficient and drag. Upon inspection of the 2D section polar, a consistent trend is also found with a C_L^{max} located at an $\alpha^{max} \approx 10^o$ and similar post-stall values. Three-dimensional results are however ever so slightly lower than the 2D polar due to the finite aspect ratio of the wing. Figure 2.17 presents the corresponding wing loading in the pre-stall region. Again, a similar loading and tip behaviour is observed with the two ALM smearing accurately predicting the sectional lift coefficient along most of the blade span. Due to the growing tip vortex strength and produced downwash as the angle of attack is increased, the discrepancy of the ALM loading prediction also increases near the tip. The truncated Gaussian still outperforms the regular kernel.

Effect of Different Aspect Ratios

At a constant angle of attack, the half wing aspect ratio is varied. Figure 2.18 presents the total wing lift coefficient variation. As expected, reducing the aspect ratio of the wing

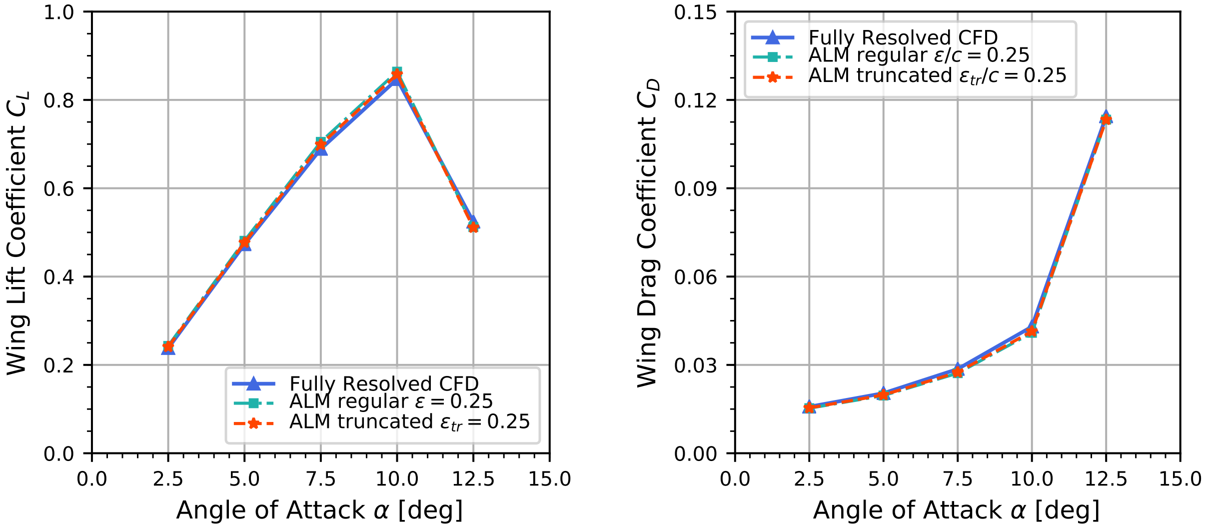

(a) Lift polar

(b) Drag polar

Figure 2.16 Wing lift and drag polar plots

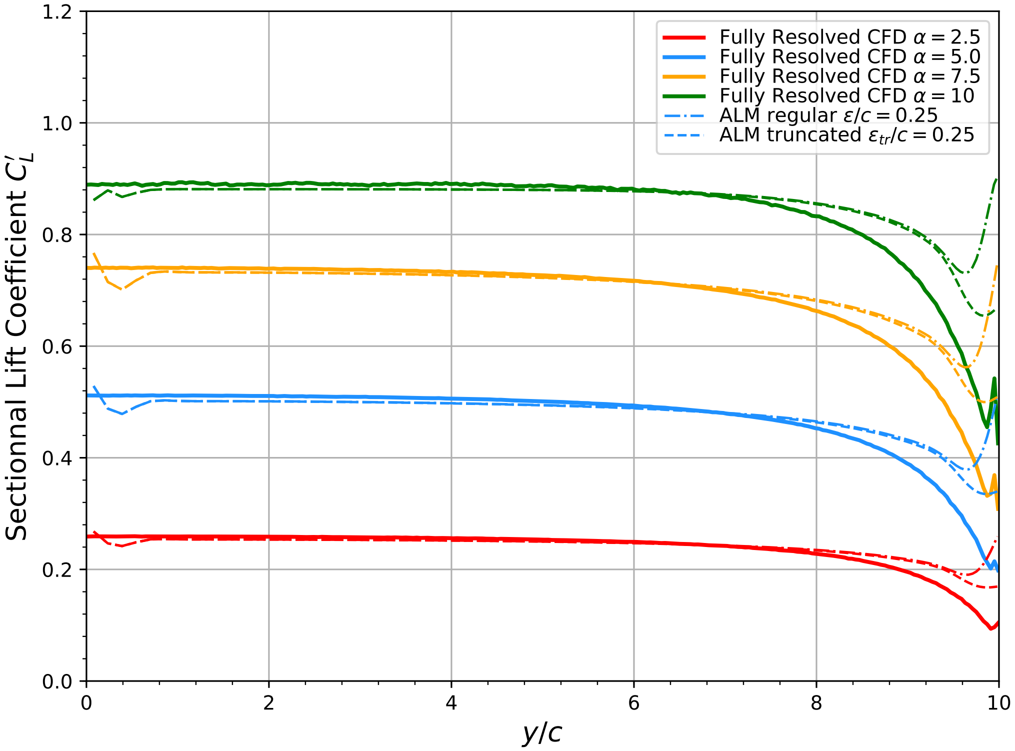

Figure 2.17 Wing lift distribution for $\alpha = [2.5, 10.0]$

reduces the lift coefficient as the tip vortex downwash affects a greater proportion of the wind span as per elementary finite wing theory. Both ALM kernels capture the trend, but not in sufficient amplitude. With the wing tips having consistent overloading thus far, it explains the progressively larger discrepancy between the ALM and fully resolved simulations as the aspect ratio is reduced. The wing loading is presented in Fig. 2.19 with the expected trend of wing tip lift over-prediction. From the figure, it also appears that the over-predictions might be limited to only the last two and a half chord lengths in span. This value might be case-specific in terms of geometry and Gaussian width.

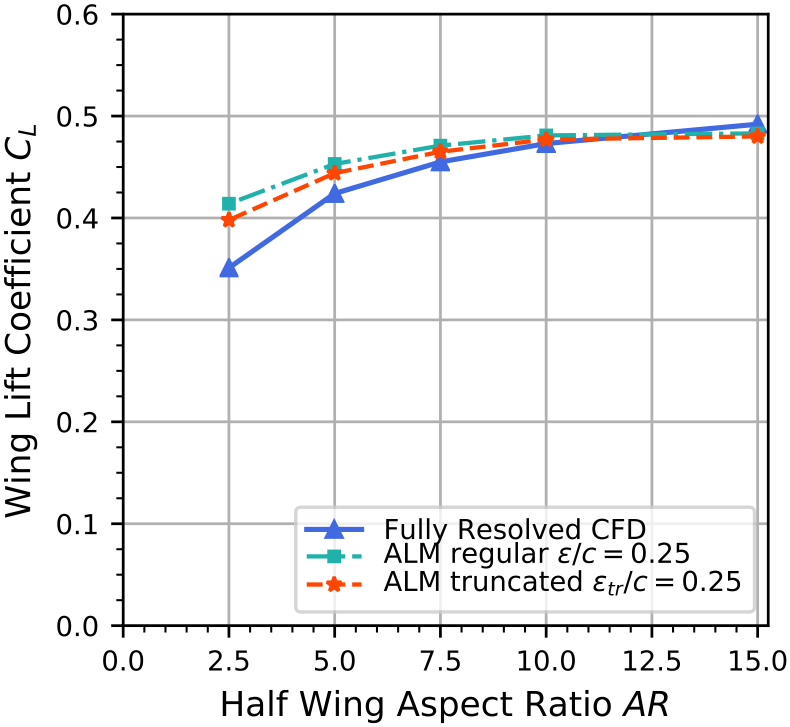

Figure 2.18 Wing lift coefficient for $AR = [2.5, 15.0]$

2.6 Conclusion

Different velocity sampling techniques for the Actuator Line Method are implemented in a 2D framework thus making the comparison to the real freestream and theoretical developments direct. The implementation is tested on different flow solvers and meshes that pertain to both LES and RANS type simulations with only marginal differences on the considered test cases. This makes the observations herein pertinent to all types of rotor modelled by an ALM as the technique is gaining attention, especially for helicopter rotors.

As recent ALM theoretical developments are based on potential flow, setups that stray too far away from this idealized condition make the model perform poorly in terms of velocity sampling. The ALM and associated Gaussian kernel need to be properly resolved on a fine enough grid that should be scaled with the Gaussian width. This Gaussian width also has a physical meaning with values near the optimal $\epsilon/c = 0.25$ producing more realistic flowfields. In terms of velocity sampling, the integral velocity sampling showed its superior accuracy,

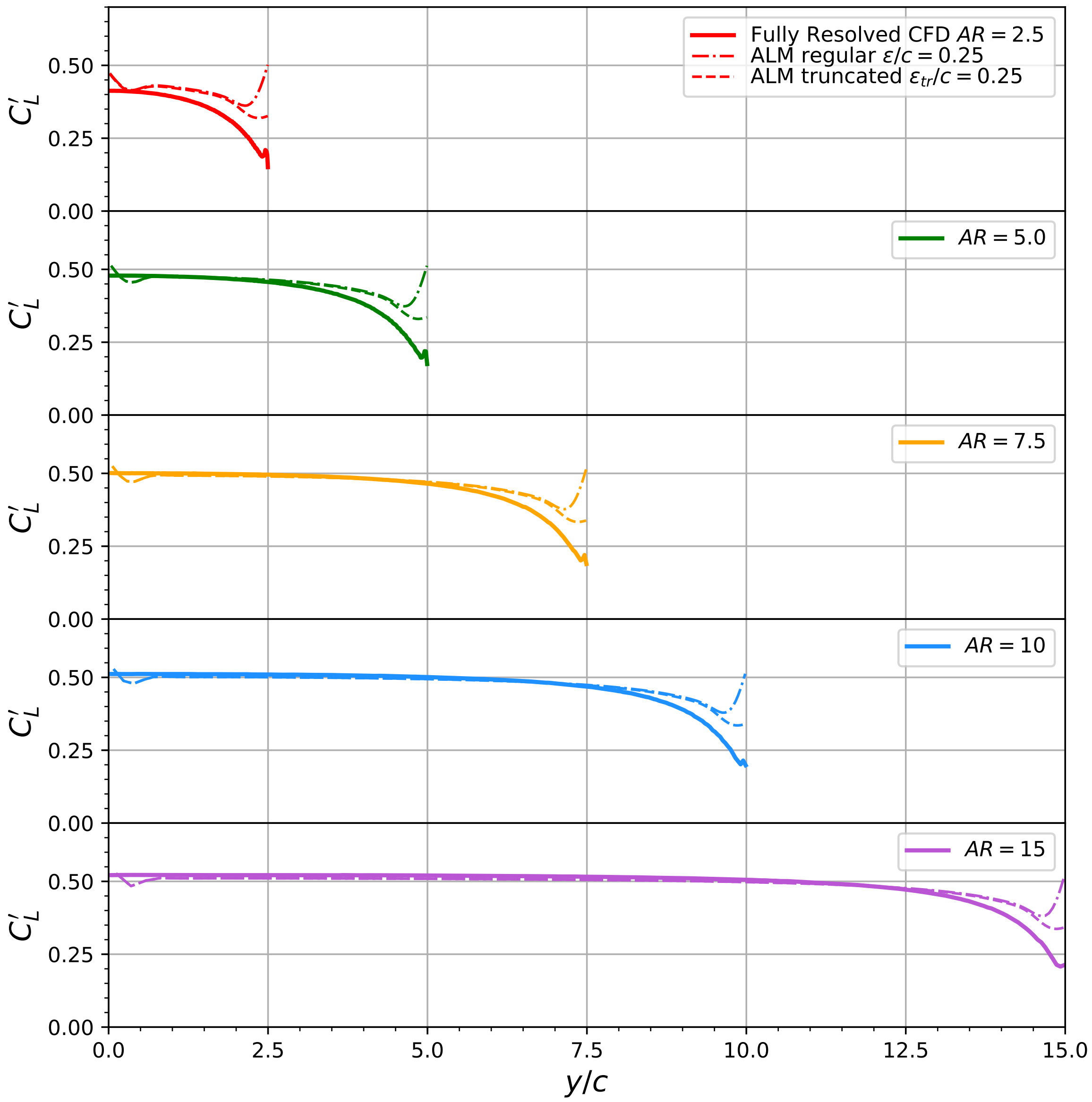

Figure 2.19 Wing lift distribution for $AR = [2.5, 15.0]$

consistency and greater flexibility in both two and three-dimensional framework integration as well as potential expandability to other smoothing kernels.

These conclusions are echoed in a three dimensional framework expansion as the integral velocity sampling is also used. Using Gaussian widths of the order of the quarter chord produced superior results by more accurately representing the bound vorticity and associated wing tip vortex structure and size thereby creating more realistic induced velocity. Introducing a truncated Gaussian variation also helped better preserve the wing loading and stabilize the location of the tip vortex. However, in all cases, the ALM with an isometric Gaussian appears to be unable to accurately represent the tip loading that might be caused by an improper tip vortex-induced velocity. Nevertheless, this over-prediction is local to the tip and for typical rotor blades application with aspect ratios in the order of 15-20, this over-prediction will be small once the full wing loading integrated.

CHAPTER 3 ARTICLE 1: HOVERING HELICOPTER ROTORS MODELING USING THE ACTUATOR LINE METHOD

Merabet, R., and Laurendeau, E., Hovering Helicopter Rotors Modeling Using the Actuator Line Method, *Under Review by* AIAA Journal of Aircraft, Dec. 2020.

Abstract

An implementation of the Actuator Line Method (ALM) is applied to an hovering helicopter rotor. This method, which is widely used for wind turbine simulations, replaces the rotor blades by momentum source terms in the Unsteady Reynolds-Averaged-Navier-Stokes equations. The removal of the blade mesh significantly reduces the computational mesh size thus lowering the computational cost. The ALM is presented along with some improvements, notably the choice and treatment of the projection kernel. A parameter sweep is performed showcasing the importance of proper selection of the Gaussian smearing coefficient ϵ for accurate rotor performance predictions with a value of ϵ scaled around a quarter chord in size. With this value, a new set of simulations on a refined mesh is performed and analyzed covering global rotor performance coefficients, sectional blade loading, tip vortex characteristics in terms of positions, circulation and core radius. The ALM is benchmarked against an equivalent Blade Resolved case on the well known S-76 rotor. Results confirm the appropriateness of the ALM model for a hovering rotor for main flow features and performance metrics, albeit a small loss of accuracy on the tip blade loading in the presence of a Blade Vortex Interaction. Finally, computational performances indicate an elapsed-time speed-up between 3 and 4x in addition to a greater parallel efficiency in favor of the ALM.

3.1 Introduction

Helicopters are used to access hard to reach destinations and operate in the close vicinity of complex terrain and obstacles. In addition, the geometry of these obstacles can be the source of complex three dimensional flow conditions which pose an added challenge to the workload of the pilot. One such example is the landing of an helicopter on the deck of a ship at sea which is particularly difficult for the pilots especially in high crosswind conditions [13]. To help in the training of pilots in such situations, helicopter aircraft simulators must be able to recreate these challenging conditions which necessitate a high level of realism and comprehensive physical models. High fidelity numerical simulations are typically used to augment the physical modeling of the aircraft simulator through calibration or by using wind maps extracted from the flowfield in some coupling procedures [16, 64, 123, 124].

Different methods exist for simulating the aerodynamic performances of helicopter rotors. These techniques vary in terms of level of fidelity along with their respective computational cost having orders of magnitude difference between them. Simple models such as Blade Element Theory (BET) and Blade Element Momentum Theory (BEMT) [3] are extremely fast in terms of computational time and are often at the core of real time flight simulator systems, but often lack accuracy in challenging flow conditions such as in ground effect or in interaction with walls where flow recirculation can exist and affect the performance of the rotor [125]. Extensive and specific modeling would be needed to increase the accuracy of the models and they would still need to be fine tuned and benchmarked against higher fidelity models or experimental data. Medium fidelity models, most notably singularity based vortex methods [5, 126, 127] offer an increased level of fidelity at a still reasonable compute time. By modeling a subset of the fluid flow equations, a reasonable level of accuracy can be obtained in hovering conditions or in interaction with simple walls or floor geometries. These methods become less than ideal as the interacting geometries become more complex and are often plagued by numerical instabilities caused by their singular nature. Finally, high fidelity meshed-based Navier-Stokes/Euler simulations [23, 43, 59] that model the exact geometry of the rotor and the surrounding obstacles using body fitted grids yield more accurate results as the equations are more complete and the geometry is explicitly included in the numerical models. Their main drawback is the setup and computational time that can take weeks to compute on large computer clusters which is orders of magnitude more when compared to other lower fidelity techniques mentioned earlier.

This article focuses on the Actuator Line Method (ALM) introduced by Sørensen and Shen [80] in the Wind Energy sector as an evolution of the steady Actuator Disk (AD) technique which has been present in rotor flow simulations for the past 30 years [47, 99, 128]. The ALM, along other "Actuator Type" methods, is an alternative to traditional fully blade resolved Unsteady Reynolds-Averaged-Navier-Stokes (U-RANS) simulations that eliminates the blades geometries and thus their associated body-fitted meshes. This significantly reduces the mesh size of the flow domain and eliminates the possible Chimera/Overset mesh overhead which further reduces computational time. The effect of the rotor blades is replaced by momentum source terms that exert forces on the flowfield resulting in similar flow characteristics. The integrated performance coefficients are recovered along with the blade loading and the full wake details of the discrete set of tip vortices.

The ALM is seldom used in the helicopter community. Forsythe et al. [110] introduced a slightly modified version from the original model by sweeping the force source term to achieve larger time steps towards applying it to a helicopter landing on a ship. Schmitz et al. [109] used it as a pure drag device to model an isolated rotor hub. Stanly et al. [111] recently showed preliminary results using the ALM with the aim of computing rotor noise. Alpman et al. [108] coupled a helicopter flight dynamic model to a modified ALM model for the computation of rotor load time histories for a rotor placed behind a hangar with incoming wind as well as a rotor behind a ship frigate to evaluate different coupling procedures. Other similar rotor replacement techniques exist and are being used and researched in the helicopter community in recent years. The Unsteady Actuator Disk (UAD) was used to study rotor-fuselage interaction by Boyd [97], the interaction between a rotor and a Ship Frigate in a simulation coupled with a flight dynamic model by Oruc et al. [16] whereas Chirico et al. [129] used it to investigate the interaction between a rotor and a generic box shaped obstacle. An Actuating Blade introduced by O'Brien and Smith [48] was used to study rotor-fuselage interaction and was benchmarked against Actuator Disk and Chimera Blade Resolved solutions. The Actuator Surface Method (ASM) was used by Kim and Park [101, 102] to study the interaction between a rotor and a simple fuselage geometry as well as a test case in hover. Wood et al. [130] used a simplified ASM model with a constant loading to study wake breakdown in high resolution hovering simulations on the S-76 geometry. Kim et al. [103] proposed an improved ASM which couples the model to vortex panels to obtain a more accurate induced velocity at the blade and validated their results on a rotor in a hovering condition and in forward flight with a fuselage. Linton et al. further developed the method [104] and later incorporated an unsteady aerodynamic model [105] to take into account the time history in the force response for the case of a parallel Blade Vortex Interaction (BVI) and of an oscillating airfoil.

For helicopters, the motivation behind these new rotor replacement techniques is to have a more computationally efficient approach than the traditional blade resolved simulations making them an ideal tool for complex rotor interaction studies such as with fuselages or obstacles. This efficiency comes at the cost of some accuracy which can be an acceptable trade-off when only main flow features and their interactions are of interest and not the fine details of the flowfield and blade surface coefficients. The majority of the rotor replacement techniques discussed above are often used directly on complex interactional cases and sometimes validated succinctly on hovering cases. Furthermore, in recent years, a substantial effort was made in the helicopter community to validate the predictive performances of various Computational Fluid Dynamics (CFD) codes for a rotor in hovering conditions through the AIAA Hover Prediction Workshop (HPW) [23].

To better understand the current predictive capabilities of this class of methods, this work explores an in depth validation of the ALM in hovering conditions. This method is chosen in favor of the others because of its simplicity attributed to its line-like representation of the force and to less stringent mesh requirements compared to an ASM. Furthermore, it is the most popular method used in the wind energy sector for horizontal axis wind turbines which gives an additional wealth of information and advancements through recent research in that sector. The method is presented along with a set of modifications performed with respect to the original method for more consistent, robust and accurate results. The analysis and performance metrics are also in tune with what was done during the HPW. The first part of the results explores the effect of the proper selection of the force smearing coefficient ϵ and its effects on the integrated performance plots, blade loading and tip vortex positions for a full collective sweep. Then the second part of the results compares an ALM solution to a Blade Resolved (B-R) solution on these same metrics and performs a more detailed analysis of the tip vortex properties at an equal trim level. Finally, the computational efficiency of the two methods is compared.

3.2 Test Case & Rotor Geometry

The selected geometry for this paper is the 1/4.71 model scale of the S-76 rotor used in the experimental study of Balch and Lombardi [131, 132]. This geometry has been used as the central test case of the HPW due to its public availability and now offers a wide variety of numerical comparative studies. The characteristics of the rotor are listed in Table 3.1. The geometry of the different sections along the span is defined at specific breakpoints presented in the table. Between the breakpoints the geometry is linearly interpolated for the B-R simulations whereas the blade section properties are linearly interpolated for the ALM. The airfoil geometries are taken form Bousman [133]. The SC1094-R8 airfoil is manually scaled to 13% and 10.09% thickness to obtain the airfoil profiles of the first two radial sections respectively. The last 5% of the span towards the tip is where the different tip shapes usually differ, but this work focuses only on the rectangular tip variant of the S-76.

On this geometry, one tip Mach number of $M_{\text{tip}} = 0.60$ is considered in this work with an associated Reynolds number of $\text{Re}_{\text{tip}} = 1.1 \times 10^6$. This corresponds to the Test Run 54 in the experimental reports of Balch and Lombardi. The ALM simulations are run at collective angles $\Theta_{75} = 4.5^o$ through 9.5^o by increments of one degree which gives the most direct comparison points with the experimental data. The B-R simulations are limited to collectives of $\Theta_{75} = \{6.5^o, 7.5^o, 9.5^o\}$ due to their higher computational costs. An additional set of B-R and ALM simulations are run on a finer mesh at a trimmed state of $C_T/\sigma = 0.09$

for a more accurate comparison of blade loading and wake characteristics.

Table 3.1 S-76 Model rotor characteristics

Rotor Definition		**Blade sections definition**			
	value	Section	Twist	Thickness	Airfoil
		(r/R)	(deg)	(t/c %)	
Nb. Blades (N_b)	4	0.189	4.01	13	SC1013-R8
Rotor Radius (R)	56.04 in	0.285	4.5	10.09	Blend
Reference Chord (c_{ref})	3.1 in	0.400	3.5	9.4	SC1094-R8
Aspect Ratio (AR)	18.077	0.750	0	9.4	SC1094-R8
Solidity (σ)	0.07043	0.800	-0.5	9.4	SC1094-R8
Linear Twist	-10°	0.840	-0.9	9.5	SC1095
		0.950	-2	9.5	SC1095
		1.000	-2.5	9.5	SC1095

3.3 Numerical Modelling

3.3.1 Flow Solver

The software used in this work is Star-CCM+ 12.06 [120] which is a general purpose finite volume, unstructured, cell centered, multi physics flow solver. All computations are done with a coupled flow solver (density based, compressible) with an unsteady dual time stepping approach with a 2^{nd} order accuracy in time. Spatial discretization uses a 2^{nd} order upwind scheme with inviscid fluxes evaluated by a Weiss-Smith preconditioned Roe flux-difference-splitting scheme [121]. The U-RANS equations are solved with the $k-\omega$ SST turbulence model [122] as a closure. The ALM is implemented through the User Coding framework and loaded as a shared library into Star-CCM+ which applies the resulting field function as a momentum body force source term in the flow equations. The library is written in C and parallelized with the same MPI implementation as the base flow solver for communications. For faster convergence and reduced domain size a source-sink type boundary condition is adapted from Mohd and Barakos [134] and Vieira et al. [135] for the Velocity Inlet and Outlet boundary conditions used in Star-CCM+.

3.3.2 Blade Resolved Simulations

The B-R simulations model the four rotating blades as four different overset mesh regions interfaced with a static background mesh. No rotor hub or linkages are considered nor modeled. The interpolation between the different overset mesh levels is done with an inverse distance weighted approach. These rotating mesh regions are cylinder shaped and encompass their respective blades, which are then put into motion by applying a rotational velocity on the geometry that then moves the blade meshes at every completion of the flow solver time step. The chosen time step corresponds to 1^o of azimuthal rotation. The only exception is the B-R simulation at a trimmed state of $C_T/\sigma = 0.09$ which required the time step to be reduced to 0.25^o due to its refined mesh. The dual time stepping approach uses 15-20 sub-iterations per time steps for the flow residuals to drop approximately three orders of magnitude or more at the end of each physical time step.

3.3.3 ALM Modeling

The ALM is a model that allows the computation of the flow around rotors by removing the blades geometries from the computations therefore only leaving the background mesh for resolving the wake. Thus, a substantial amount of grid points can be eliminated in addition to the removal of overset mesh overhead resulting in faster computation and setup time. The rotor forces are computed by the model and applied to the flowfield through momentum source terms in the fluid flow equations. These equations are summarized in their generic integral form, omitting any turbulence model, by Eqs. (3.1-3.3), as per Ref. [120]:

$$\frac{\partial}{\partial t}\int_V \rho \, dV + \oint_A \rho \mathbf{v} \cdot d\mathbf{a} = 0 \tag{3.1}$$

$$\frac{\partial}{\partial t}\int_V \rho \mathbf{v} \, dV + \oint_A \rho \mathbf{v} \otimes \mathbf{v} \cdot d\mathbf{a} + \oint_A p\mathbf{I} \cdot d\mathbf{a} = \oint_A \mathbf{T} \cdot d\mathbf{a} + \int_V \mathbf{f_b} \, dV - \int_V \mathbf{f_{alm}} \, dV \tag{3.2}$$

$$\frac{\partial}{\partial t}\int_V \rho E \, dV + \oint_A \rho H \mathbf{v} \cdot d\mathbf{a} + \oint_A \mathbf{q} \cdot d\mathbf{a} = \oint_A \mathbf{T} \cdot \mathbf{v} \, d\mathbf{a} + \int_V \mathbf{f_b} \cdot \mathbf{v} \, dV - \int_V \mathbf{f_{alm}} \cdot \mathbf{v} \, dV \tag{3.3}$$

where V is the control volume of a cell and $\mathbf{a}$ its outward area vector of a given face. Flow properties are represented by ρ the density, $\mathbf{v}$ the velocity vector, p the pressure, $\mathbf{T}$ the viscous stress tensor, $\mathbf{q}$ the heat flux vector, E and H the total energy and enthalpy , respectively. The term $\mathbf{f_b}$ represents a generic body force such as gravity or centrifugal force and is taken into account in the energy equation through the scalar product with the velocity vector. The volumetric body force needed for the modeling of the ALM is represented by the $\mathbf{f_{alm}}$ term which is treated as any other body force. The negative signs indicate that the force to be applied on the flowfield is of equal strength, but opposite direction of the rotor forces. In this work, the energy source term in Eq. (3.3) is omitted as it has only a minor impact on the results and saves computational time (results not shown for the sake of brevity). The energy equation is more often than not neglected in wind turbine simulation as a result of the incompressible flow equations that are solved. In [118], it was also shown that this term had no significant impact on the results for sub-critical cases.

To model the $\mathbf{f_{alm}}$ source term, a BET approach is taken and the process is illustrated in Figure 3.2. The different blades are treated as lines and discretized by points along their span axis corresponding to the local quarter chord point of the profile. The points form line segments with the flow properties evaluated at the center of each line segments and form an ALM control point. The velocity is sampled at this point, denoted by $\mathbf{U_s}$, and represents the wake induced velocity void of any bound circulation induced velocity. More details on the velocity sampling will follow. With the velocity known, the local equivalent freestream angle of attack α_{rel} and velocity $\mathbf{U_{rel}}$ are reconstructed as per Eqs. (3.4-3.7) and illustrated in Fig.3.1. The identification of these two properties allows the interpolation in a 2D viscous database generated in Star-CCM+.

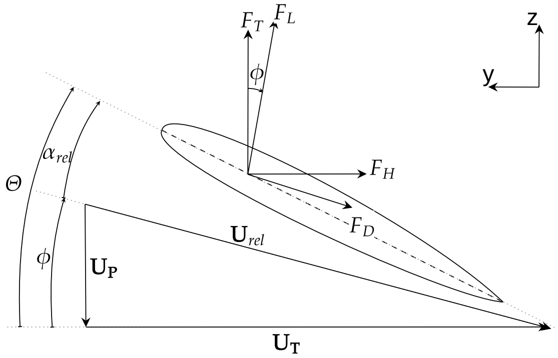

Figure 3.1 Blade element representation of a blade section

$$\mathbf{U_T} = \Omega(r \cdot R) - \mathbf{U_{s,y}} \tag{3.4}$$

$$\mathbf{U_P} = -\mathbf{U_{s,z}} \tag{3.5}$$

$$\mathbf{U_{rel}} = \mathbf{U_P} + \mathbf{U_T} \tag{3.6}$$

$$\phi = \arctan\left(U_P/U_T\right) \tag{3.7}$$

The database in this work comprises 10 sections along the span where lift, drag and moment polars are evaluated at angles of attack ranging from -10^o to 17^o. This wide angle of attack range ensures that all the simulations in this work have their effective angle of attack well within the database range. Otherwise, the values of the coefficients at the end of the range would be used and extrapolated. The geometry and flow properties, such as Mach and Reynolds numbers, change according to their respective radial positions along the span. With the information about the local effective velocity and the known force coefficients, the force of every sections can be re-dimensionalized as per Eqs. (3.8) and (3.9) and projected onto the flowfield.

$$\Delta L = \frac{1}{2}\rho \|\mathbf{U_{rel}}\|^2 C_l(\alpha_{\text{rel}}, \text{Re}, M) c\Delta R \tag{3.8}$$

$$\Delta D = \frac{1}{2}\rho \|\mathbf{U_{rel}}\|^2 C_d(\alpha_{\text{rel}}, \text{Re}, M) c\Delta R \tag{3.9}$$

The force is then spread over several grid cells through a projection kernel. The one used in this work is a modified version of the isometric Gaussian kernel typically used in ALM simulations shown by Eq. (3.10). Every ALM control point is centered on the section quarter chord point (x_0, y_0, z_0) and has its own kernel associated to it as shown in Fig. 3.2 on Blade *(ii)*. Then, $\mathbf{f_{alm}}$ is constructed by summing all the products of the kernels multiplied by their associated force vectors as illustrated on Blade *(iii)* and shown in Eq. (3.13) where $\mathbf{e_L}$ and $\mathbf{e_D}$ are the unit vectors representing the direction of application of the sectional lift and drag force respectively. These forces are later converted to a global coordinate system taking into account the induced flow and angle of attack.

$$g_{\text{iso}}(x, y, z) = \frac{1}{\epsilon^3 \pi^{\frac{3}{2}}} \exp\left(-\frac{(x - x_0)^2 + (y - y_0)^2 + (z - z_0)^2}{\epsilon^2}\right) \tag{3.10}$$

$$g_{\text{tr}} = \begin{cases} g_{\text{iso}}, & \text{if } R_{\text{root}} \leq \sqrt{(X)^2 + (Y)^2} \leq R_{\text{tip}} \\ 0, & \text{otherwise} \end{cases} \tag{3.11}$$

$$\beta_{\text{norm}} = \frac{1}{\int_V g_{\text{tr}}} \, dV \tag{3.12}$$

$$\mathbf{f_{alm}} = \sum_i \beta_{\text{norm,i}} \cdot g_{\text{tr, i}} \cdot (\Delta L_i \mathbf{e_{L,i}} + \Delta D_i \mathbf{e_{D,i}}) \tag{3.13}$$

Some improvements to the traditional ALM are performed and detailed as follows. The kernel is truncated at both the tip and the root and normalized as shown in Eqs. (3.11) and (3.12) and illustrated in Fig. 3.2 on Blade *(iv)*. Truncating the kernel constrains the source term to respect the geometrical limits of the blade in the spanwise direction as no force is projected past the root or tip of the blade. If the Gaussian projection is not truncated, the source terms would project force past the root and tip of the blade whereas varying the smearing parameter ϵ would modify the distance at which this over-projection would end.

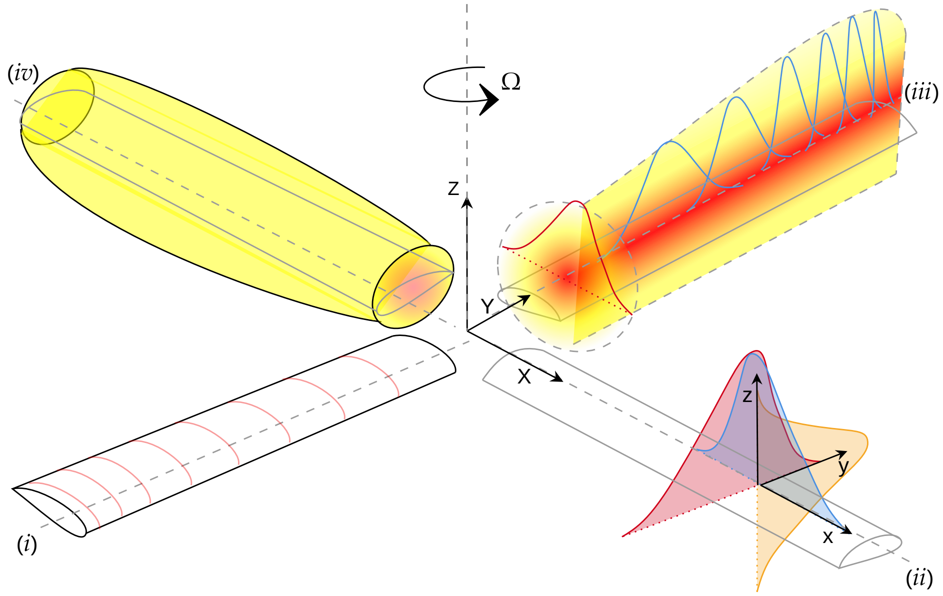

Figure 3.2 ALM representation with different blades representing different steps in the process. *(i)* Blade element section discretization, *(ii)* Gaussian smoothing in three spatial dimensions, *(iii)* Chordwise and spanwise cut planes of the body force, *(iv)* Body force isosurface.

Both the over-projection past the root and tip and its variable distance would modify the force distribution which results in an inconsistent tip vortex position and strength. The normalization allows to conserve the property of the kernel to integrate to unity which is not the case when truncating it or when using a coarser mesh. It is to be noted that although the truncation and normalization are applied to every kernel for every ALM control points, only the ones close to the root and tip are considerably affected because a typical simulation has its smearing parameter scaled at $\epsilon \sim 25\%$ of the local chord c and the kernel decays quickly to ~ 0 within 3ϵ. For reference, integrating the Gaussian spread force over a 3ϵ span corresponds to 99.9934% of the total projected force.

For a better force representation along the span of the blade, the ALM control points follow an hyperbolic tangent distribution. This distribution allows a much finer ALM discretization near the tip, which sees the greatest variation of blade loading, while keeping the overall number of ALM points low. Other distributions were tried, most notably the cosine distribution, but it was deemed too aggressive in its refinement ratio. The hyperbolic tangent allows a more gradual and controllable refinement as per Eq. (3.14) where χ is the normalized $[0, 1]$ coordinate, x is an array of equally spaced coordinate that spans the range $[0, \zeta]$ and ζ is the tuning parameter:

$$\chi = \frac{\tanh(x)}{\tanh(\zeta)} \tag{3.14}$$

In the present work, the rotor is modeled with 65 ALM control points per blade and $\zeta = 1.375$. This discretization ensures the convergence of the ALM model for the present geometry and test cases.

Different approaches exist to evaluate the velocities at the ALM control points. Merabet and Laurendeau [118] identified the integral velocity sampling proposed in Forsythe et al. [110] and Churchfield et al. [95] as being the most robust and overall most accurate method in a 2D framework. Caprace et al. [113] further generalized the sampling technique to a three dimensional lifting line. The technique relies on the same kernel projection function used to project the force and essentially acts as a weighted average of the velocity field multiplied by the kernel times the volumes of the cells as shown in Eq. (3.15).The analytical developments of the integral velocity sampling ensure that any kernel that integrates to unity can be used, hence it is surmised that this method, developed in 2D, is well suited for the present truncated-normalized Gaussian kernel for most of the span with possible exceptions near the tip and root where 3D effects are stronger caused by the tip and root vortices. The method thus samples the wake induced velocity $\mathbf{U_{s,i}}$ directly at the ALM control point located at the quarter chord point. No correction for bound circulation is needed and all the information about the wake induced velocity is present. It then becomes straightforward to reconstruct a velocity triangle and recover $\mathbf{U_{rel}}$ and α_{rel} from the measured induced velocity, blade rotational speed and blade geometry as per BET.

$$\mathbf{U_{s,i}} = \int_V \beta_{\text{norm,i}} \cdot g_{\text{tr, i}} \cdot \mathbf{v} \, dV \tag{3.15}$$

In most ALM implementations, the model uses a tip-loss function as it was noticed that the blade loading near the tip would grow to abnormally high values thus resembling an uncorrected BEMT solution. But this correction should not be needed in a 3D U-RANS framework as the tip vortices are resolved as noted in [95]. Given proper shed vorticity and tip vortex structures, the ALM should not need to be corrected artificially because the induction of the wake is correctly captured by the method. The value of the smearing parameter ϵ greatly affects the tip vortices which in turn affects the blade loading and performance coefficients. The general tendency in wind turbine simulations is to use higher values of ϵ as it allows a coarser mesh resolution. Several researchers [89,93,136] identified an optimal value of the smearing coefficient to be in the area of $\epsilon/c = 0.25$ as this value produced the best results and does not need a tip-loss function to produce accurate blade loading distributions. An in-depth look at this issue can be found in Martinez-Tossas and Meneveu [136]. Other Gaussian smearing coefficient guidelines exist [94, 137], but they pertain to more coarsely resolved wind turbine simulations. Therefore, this paper considers the aforementioned value of the Gaussian smearing parameter as the de facto value along with no tip-loss function. Different values of ϵ are still used on a coarse mesh to assess the effects of the parameter.

Finally, more implementation specific improvements are used in this work. For an improved conditioning of the startup revolutions and faster thrust convergence, the force is ramped up from zero to its nominal value over the first two revolutions. An under-relaxation of the applied force is also implemented for the intra timestep sub-iterations. This under-relaxation ensures an increased convergence of the method that tends to be noisy on coarse meshes or as small values of ϵ are used. An under-relaxation factor of 0.75 typically produces a normalized convergence of the thrust and torque coefficients of at least four orders of magnitude on the last sub-iteration of the timestep.

3.3.4 Computational Meshes and Refinement

For a fair comparison between the B-R and the ALM, the two methods share similar background meshes. The difference lies with the B-R needing every blade to be meshed individually and the ALM needing a finer mesh around the rotor disk for proper resolution of the source terms especially at lower ϵ values. Flow domains are meshed with cubic hexahedron cells in a oct-tree type mesh.

Every simulation is run in a cylindrical background mesh that extends $4R$ above the rotor origin whereas the outflow and radial boundaries are $8R$ from the origin. Successive cylindrical refinement zones are placed near the rotor disk region to better capture the near wake. The finest refinement zone of the mesh i.e. "Near Wake" is a cylinder slightly larger than the rotor radius R and spans 0.25m and 0.6m above and below the rotor disk respectively. A background mesh for an ALM simulation is displayed in Fig. 3.3b. These dimensions ensure at least one revolution of the wake is captured at the highest collective setting. The ALM has a further refinement zone i.e. "ALM Near Field" that spans one chord above and below the rotor disk as shown in Fig. 3.3c. The sizes of the cells in all the meshes used are reported in Table 3.2.

The B-R simulations have their four blades individually meshed and interfaced with the background mesh through the overset module. The blade mesh is a cylinder around the blade geometry with a radius of 0.15m and extends 0.1m further than the tip and root as displayed in Fig. 3.3a. The cell size at the boundary of the cylinder matches the background grid cell size. The blade surfaces have their default mesh size used presented in Table 3.2 and local refinement near the tips, leading and trailing edges refined down to 0.5-1%c_{ref}. The boundary layer height is fixed at 4%c_{ref} and the amount of cells contained within it are also present in the table.

For the simulations at the trimmed state of $C_T = 0.09$, the tip vortices and their characteristics are looked in more depth and a finer mesh is used in their vicinity. The tip vortex "T.V." refinement zone consists of an annulus. The inner and outer diameters capture the radial position of the tip vortex while its depth is enough to capture these tip vortices for 300 degrees of wake age. This additional mesh refinement results in total mesh size of 54.0 and 73.45 million cells for the ALM and B-R meshes respectively which is significantly higher than their respective Medium mesh template upon which they are based on.

Table 3.2 Mesh cell sizes

	Refinement zone			Blade Mesh	
Grid	Near Wake	ALM Near Field	T.V.	Nb. Prism layers	Surface size
B-R Coarse	25.0% c_{ref}	-	-	20	4.0% c_{ref}
B-R Medium	17.5% c_{ref}	-	-	30	4.0% c_{ref}
B-R T.V.	17.5% c_{ref}	-	4.0% c_{ref}	30	4.0% c_{ref}
B-R Fine	12.5% c_{ref}	-	-	30	2.5% c_{ref}
ALM Coarse I	25.0% c_{ref}	12.5% c_{ref}	-	-	-
ALM Coarse II	30.0% c_{ref}	7.5% c_{ref}	-	-	-
ALM Medium	16.0% c_{ref}	8.0% c_{ref}	-	-	-
ALM T.V.	16.0% c_{ref}	8.0% c_{ref}	4.0% c_{ref}	-	-
ALM Fine	11.7% c_{ref}	5.8% c_{ref}	-	-	-

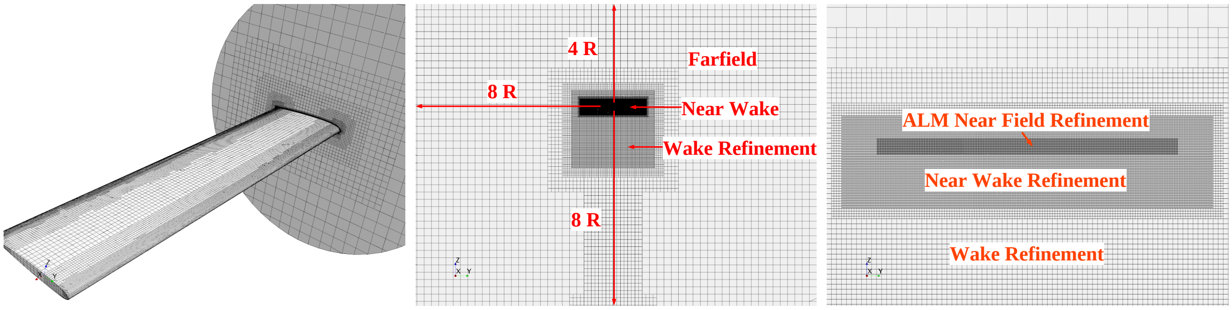

(a) Blade Surface Mesh (b) Far Field (c) Near Field

Figure 3.3 Computational mesh template

Table 3.3 presents the results of a mesh refinement study on the three key integrated performance coefficients on the $\Theta_{75} = 7.5^o$ case along with their relative error compared to the experimental value. The errors decrease as the B-R meshes are refined. Both the Medium and Fine grids have a FoM error of less than 0.5% whereas the Fine mesh results also have excellent agreement for both the thrust and torque coefficients. The ALM on the other hand has a more constant error for all integrated performance coefficients with only a small improvement between the Coarse and Fine grids. Despite this slightly larger error, the method shows robustness in regards to the mesh density as the goal is to ultimately use the least amount of cells as possible. The error range for the thrust coefficient is within 2.90% accuracy whereas the torque coefficient is at most 3.81% and are considered reasonable for the type of method employed. The FoM error range is higher with an error within 7.83% because the thrust is under-predicted and the torque is over-predicted.

Table 3.3 Mesh convergence study at $\Theta_{75} = 7.5^o$

	Cell count (millions)			**Coefficients**					
Grid	Back.	Blade	Total	C_T/σ	$\Delta[\%]$	C_Q/σ	$\Delta[\%]$	FoM	$\Delta[\%]$
B-R Coarse	4.0	3.5	17.9	0.07255	0.35%	0.00573	2.85%	0.63991	-2.26%
B-R Medium	9.1	4.9	28.7	0.07311	1.12%	0.00569	2.18%	0.65162	-0.47%
B-R Fine	24.2	8.1	56.6	0.07213	-0.24%	0.00558	0.14%	0.65147	-0.50%
ALM Coarse I	3.9	-	3.9	0.07020	-2.90.%	0.00578	3.81%	0.60343	-7.83%
ALM Medium	10.1	-	10.1	0.07042	-2.60%	0.00576	3.41%	0.60857	-7.05%
ALM Fine	25.6	-	25.6	0.07048	-2.52%	0.00577	3.55%	0.60856	-7.05%
Exp.	-	-	-	0.07230	-	0.00557	-	0.65472	-

3.4 Tip Vortex Analysis

As the near wake of helicopter rotors is of great importance for its performance predictions, the helical tip vortex wake is analyzed. The process of post processing data from tip vortices is typically done manually which can be both time consuming and error prone as noted by Jain [138, 139]. The tip vortex analysis in this work is automated for both the extraction of the data from the flowfield and the subsequent post-processing. The present methodology is based on the works of Goerttler et al. [140] and Linton et al. [105]. The extraction of tip vortices positions and properties is done by extracting constrained 2D planes of the flow properties around the tip vortices. Because the position is not known beforehand, it is first approximated by the Kocurek and Tangler prescribed wake model [30]. With a thrust coefficient and a desired wake age, a plane is placed in the wake with its center on the guessed vortex position. Its orientation is determined by the wake age where the plane is rotated at this angle relative to the blade from which the tip vortex originates as illustrated in Fig. 3.4. Through interpolation from the background mesh, flow properties of interest are interpolated on a $N \times N$ evenly spaced grid and exported as a *.csv* file.

The solution is reconstructed in a Python script which changes the referential frame to one local to the cut plane. Its axes are aligned with the radial direction given by the rotor disk radius, the rotor disk vertical axis oriented in the thrust direction and the direction opposite to the rotation of the blade. This referential represents the radial-azimuthal-vertical ordinates (r, Ψ, z) which makes it easy to extract the position of the tip vortices as every cut plane lies in a 2D (r, z) plane. From there, the center of the tip vortex is identified through the maximum Q-criterion. With the center identified, radial lines are traced around the vortex core and the velocities are sampled along these lines. The velocities are further transformed to a vortex tangential-radial-axial reference frame for the identification of the core properties. These lines, typically 90 in this work, are then averaged to obtain an averaged tangential velocity profile $\bar{V}_{\text{tan}}$ across a particular vortex core from which the core size is extracted at the location of the highest ($\bar{V}_{\text{tan}}$) and the circulation is given by Eq. 3.16. As the value of the circulation Γ varies through the viscous vortex core, a suitable location needs to be identified for its evaluation. Because the core resembles a Vatistas [27] vortex core of power $n = 2$ as per Eq. (3.17), the circulation of the core is evaluated at $2.5r_c$. As shown in Fig. 3.5, the empirical core model fits the extracted core model well from the Blade Resolved simulations at $\theta_{75} = 7.5^o$ on the Medium mesh that is displayed. The circulation along the viscous core shown in Fig. 3.5b, varies substantially along the core radius. The Vatistas model tends asymptotically to an equivalent inviscid vortex circulation Γ_∞ whereas the B-R extracted data behave similarly until $2.5r_c$. Past this point, the interaction between the tip vortex, the vortex sheet and the region outside the contracting wake make the sampled circulation increase further and deviate from the theoretical model. By sampling the circulation at this location, it avoids this problem and recovers 98.7% of the Γ_∞ from the Vatistas model. This method allows a more consistent evaluation of the circulation especially as the wake age gets older where the vortex core diffuses. Sampling at a fixed radius could yield an incorrect circulation by either being too small and measuring the circulation inside the viscous core, or too far and have the effects of the helical vortex wake present.

$$\Gamma = \oint v\, ds = \sum V_{\text{tan}} r d\theta = 2\pi \bar{V}_{\text{tan}} r \tag{3.16}$$

$$V_{\text{tan}} = \frac{\Gamma_\infty}{2\pi r_c} \frac{r/r_c}{(1 + (r/r_c)^{2n})^{1/n}} \tag{3.17}$$

For most of the cases in this work, the meshes used are too coarse to properly resolve the tip vortices which further adds the drawback of quickly diffusing the viscous core of the vortices. Nonetheless, the position can still be accurately extracted for wake ages under one revolution. Because the background meshes of both the ALM and B-R simulations closely match, the results can be compared together, but are not representative of the real evolution of a tip vortex that would be measured experimentally or computed on a very fine grid as done in [140]. Hence, only the near wake is considered and the comparisons are to be made in between the two methods on similar meshes only. The simulations at the trimmed condition of $C_T/\sigma = 0.09$ in Section 3.5.2 have a finer mesh for a more in depth quantitative analysis

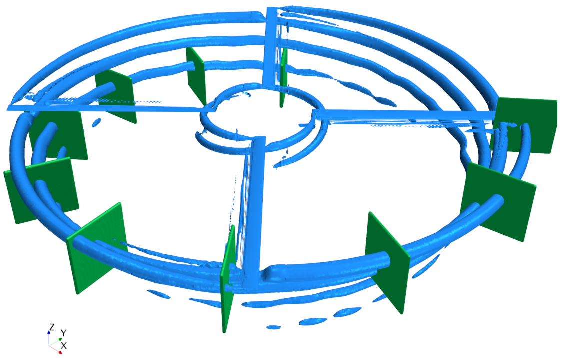

Figure 3.4 Tip vortex extraction planes with Q-criterion contour representing the vortices

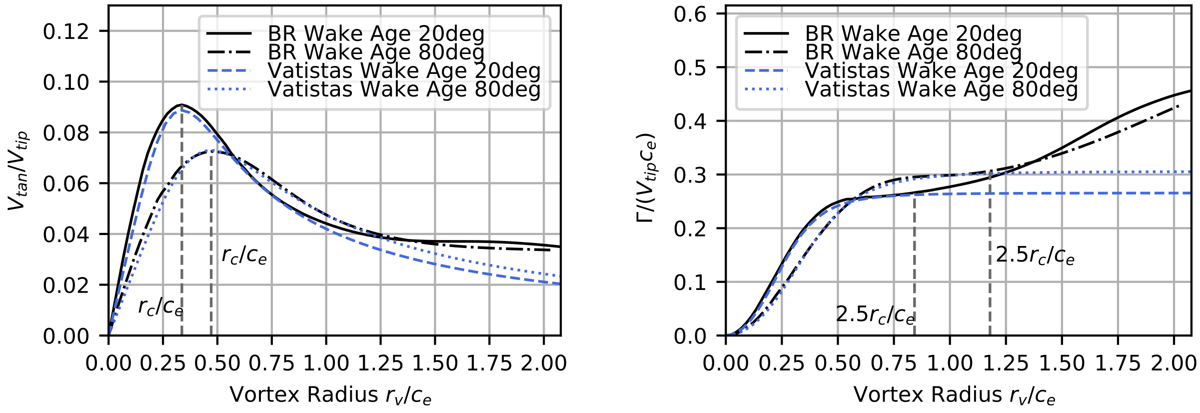

(a) Tangential velocity profile

(b) Circulation along vortex core

Figure 3.5 Vortex core comparison of B-R extracted data and empirical model

of the tip vortex properties.

3.5 Results and Discussion

3.5.1 Gaussian Smearing Width Sensitivity

The effects of using different Gaussian smearing parameter ϵ are evaluated in this section with values in the range $\epsilon/c = [0.2, 1.0]$. Because of the large amount of simulations, the Coarse II mesh is used for the ALM simulations. The results are compared on the basis of their integrated coefficients, blade loading and tip vortex characteristics.

Integrated Performance Coefficients

The integrated performance coefficients for the thrust, torque and Figure of Merit are presented in Fig. 3.6. For a given ϵ, the curves show consistent trends with the experimental data albeit some offset. A smaller value of ϵ produces an under-prediction of thrust and over-prediction of the torque for given thrust level especially at higher collectives. These two errors combined yield an even larger offset for the figure of merit which is under-predicted. This trend is reversed at the highest values of ϵ as the thrust is over-predicted whereas the torque is under-predicted at higher collective values yielding an over-prediction of the FoM. From the present figures, $\epsilon/c = 0.35$ produces the best integrated coefficients compared to the experimental data across the whole range of collectives. Then $\epsilon/c = 0.25$ is more accurate for the thrust coefficient across the simulated collective range, especially at the lower to mid-range values, but slightly over-predicts the torque resulting in a lower Figure of Merit.

Blade Loading

To explain the integrated results, the blade sectional thrust and torque loading are presented in Fig. 3.7. The ALM simulations are presented at a trimmed thrust of $C_T/\sigma = 0.0723$ which corresponds to the experimental value at $\Theta_{75} = 7.5^o$ whereas the B-R is presented at its nominal collective angle of $\Theta_{75} = 7.5^o$. The ALM simulations are compared to B-R simulation on the Medium mesh because the experimental data did not provide blade loading data. The thrust loading is well approximated from the root until 80% of the span of the blade for all the ϵ values. Although a small constant offset is observed across the range of kernel width with a trend that sees the lower values of ϵ have a marginally higher thrust loading in the first 80% blade span. From $r = 0.80$ to $r = 1.00$, the ALM simulations differ quite substantially from their B-R reference. This difference is attributed to the helical vortex wake of this particular rotor geometry which sees the tip vortex of the preceding blade hitting the next blade thus causing a perpendicular blade vortex interaction at around 93% blade span. This encounter sees the viscous core interacting closely with the blade and induces high velocities as it passes through. The induced velocities are in the plane of the rotor disk and significantly impact the effective angle of attack which in turn changes the local blade loading. Such a close encounter is not well captured by the method compared to the B-R simulation which has a solid geometry cutting through the previous blade tip vortex thus creating different flow physics. The force projected by the ALM is porous and, because of its line-like representation, has no way to enforce a non-penetrating boundary condition as is done in other higher fidelity methods that rely on source terms such as Immersed Boundary Methods. Towards the tip of the blade, the discrepancies between the various

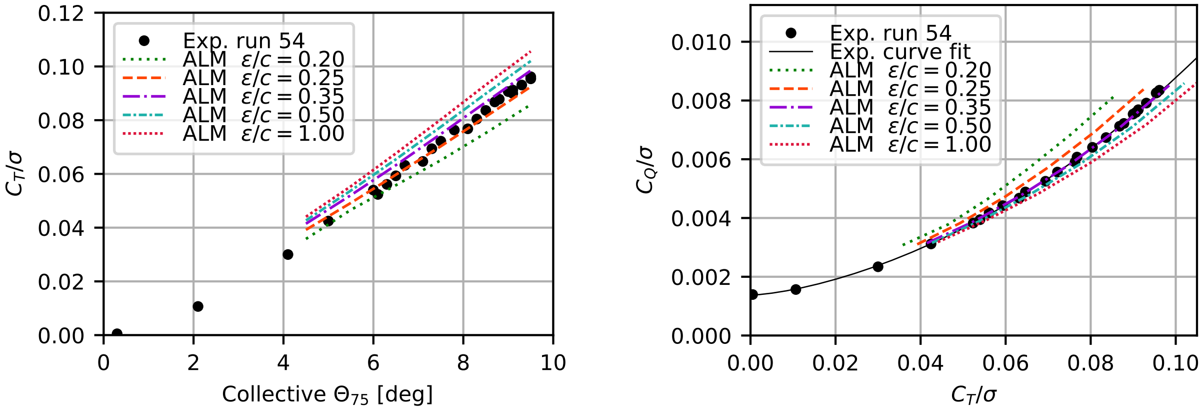

(a) Thrust Coefficient

(b) Torque Coefficient

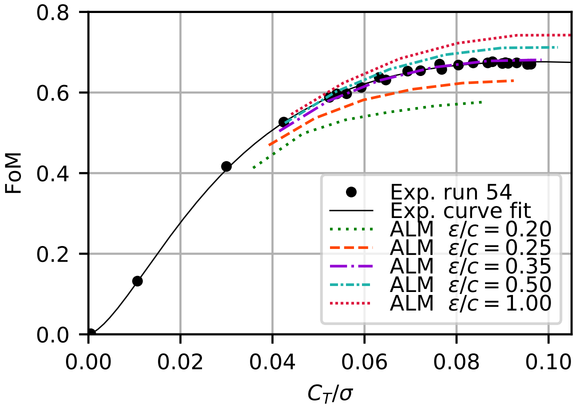

(c) Figure of Merit

Figure 3.6 Integrated performance coefficients for the ALM on the Coarse II mesh

ALM simulations are caused by the differences of the tip vortex structure created by the different force smearing coefficients. Small ϵ values create tighter tip vortices which in turn create a more realistic induced velocity at the rotor yielding a more accurate drop off of the thrust blade loading near the tip without having to resort to a tip-loss function that would artificially bring the tip loading down. This behavior is in tune with what is observed in [136] where the ALM simulations with an $\epsilon/c > 0.25$ need correction whereas values $\epsilon/c \approx 0.25$ produce the most accurate results. The different tip vortex structure not only has an effect on the tip, but also across the whole span of the blade. When considering the inflow angle across the span (not shown), the smaller values of ϵ cause a larger inflow angle. This in turn creates a larger torque loading that is mainly due to induced drag through the rotation of the lift vector by the inflow angle as per BET. The torque loading in Figure 3.7 therefore shows a higher torque for the smaller kernel sizes up to 80% blade span. Towards the tip, the BVI described previously changes the shape of the loading compared to the reference B-R case and creates higher drag and torque. Because of the discrepancy created by the BVI that is not properly captured in the tip region, it becomes difficult to decipher which Gaussian smearing produces the best results in this region.

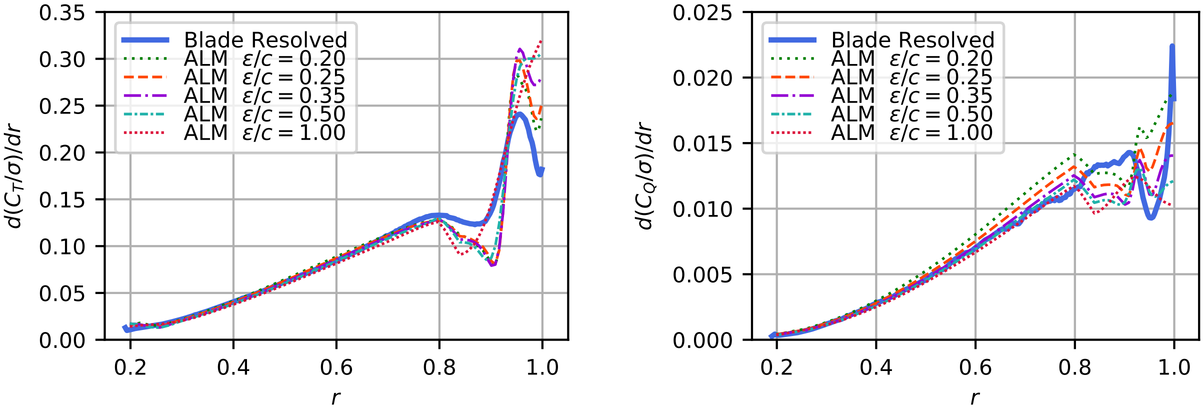

(a) Thrust Loading

(b) Torque Loading

Figure 3.7 Sectional blade loading of the ALM at $C_T/\sigma = 0.0723$ for different ϵ and B-R at $\Theta_{75} = 7.5^o$

Tip Vortex Characteristics

The helical vortex wake is of prime importance for the accurate prediction of the rotor loads. The meshes used in this section are quite coarse which is not ideal when comparing tip vortices as they tend to diffuse quickly. Nonetheless, the vortex positions can be identified for up to a rotor revolution whereas the tip vortices radius and circulation are identified for the early wake ages up to approximately 150^o where the tip vortex leaves the ALM refinement zone. Because all ALM simulations are on the same mesh, they can at least be compared to each other on a qualitative basis. The results for the B-R simulation are added for reference purposes only for the vortex locations as their properties would not be comparable to the ALM because of the different meshes used. More specifically, the mesh in the close vicinity of the rotor disk for the B-R simulations is significantly coarser than the ALM resulting in increased diffusivity. A quantitative analysis of the tip vortex structure and characteristics on a refined mesh is presented in the following section.

Figure 3.8 presents the evolution of the tip vortex positions over one rotor revolution at a trimmed thrust state of $C_T/\sigma = 0.0723$. The slopes at the top of Fig. 3.8 represent the radial contraction of the vortices whereas the ones at the bottom of the graph are the vertical advection below the rotor. In addition, the results of the Kocurek and Tangler empirical model [30] are displayed for reference. All the ALM simulations agree very well and are consistent with both the B-R and empirical model especially for the radial contraction. The axial displacement below the rotor shows a greater variability where the tip vortices from smaller kernels tend to be advected slower. They also better follow the B-R results. Recall that these results are trimmed and thus do not have the same collective settings which varies considerably. Should the same collective of $\Theta_{75} = 7.5^o$ be used, the kernel of $\epsilon/c = 0.25$ would perform the best as its thrust is better predicted across the whole collective sweep without the need of a trim.

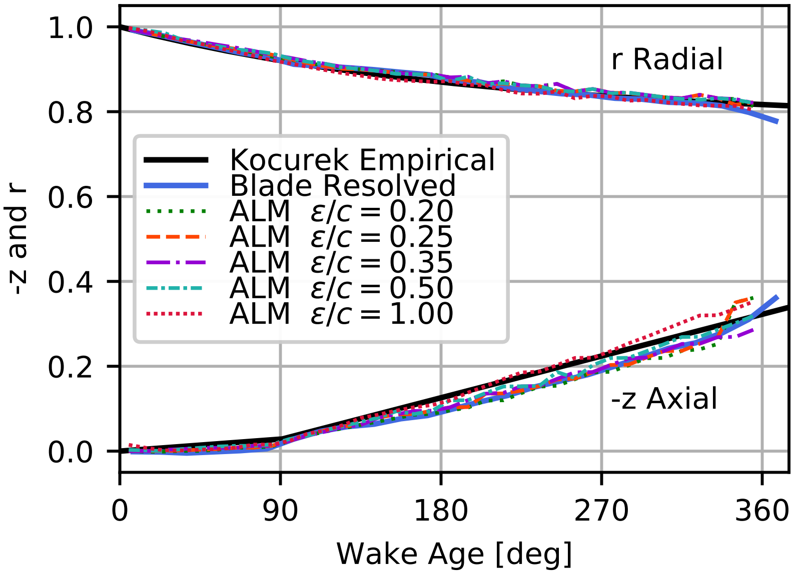

Figure 3.8 Tip vortex positions for the ALM at $C_T/\sigma = 0.0723$ and B-R at $\Theta_{75} = 7.5^o$

The viscous core radius and the circulation of the different tip vortices are presented in Figs. 3.9a and 3.9b for wake ages before 150 degrees. The ALM solutions show a general tendency to have a larger vortex core and circulation as ϵ is increased as a consequence of the higher blade loading near the tip for the different ϵ. The only outlier is the ALM with $\epsilon/c = 1.0$ which shows an excessively large vortex core radius and circulation in the first 40.0 degrees of wake age which then settles to a steadier and more realistic value. This difference is caused by the high blade loading as well as the truncation-normalization of the Gaussian kernel near the tip which further loads the region at the source term level. This results in a highly elliptical tip vortex in the early wake ages that settles back to a circular profile as the wake age grows. This elliptically shaped tip vortex is not properly captured by the present vortex extraction methodology and empirical vortex model which causes the high values of the core radius and circulation. The preceding observations are further reflected in Fig. 3.9c which shows the average tangential velocity profile of the extracted vortex cores at 35.0^o wake age. The position of the maximum tangential velocity of the viscous cores grows as ϵ gets larger. The peak velocity value is highest for $\epsilon/c = 0.20$ and decreases as ϵ is increased.. The circulation is computed further along the core which is where the average velocity gets higher with higher Gaussian kernel sizes, thus explaining the values seen in Fig. 3.9b. Finally, the shape of the tangential velocity profile for $\epsilon/c = 1.0$ does not fit with the rest of the results nor with the empirical model because it is still recovering from its highly elliptical shape.

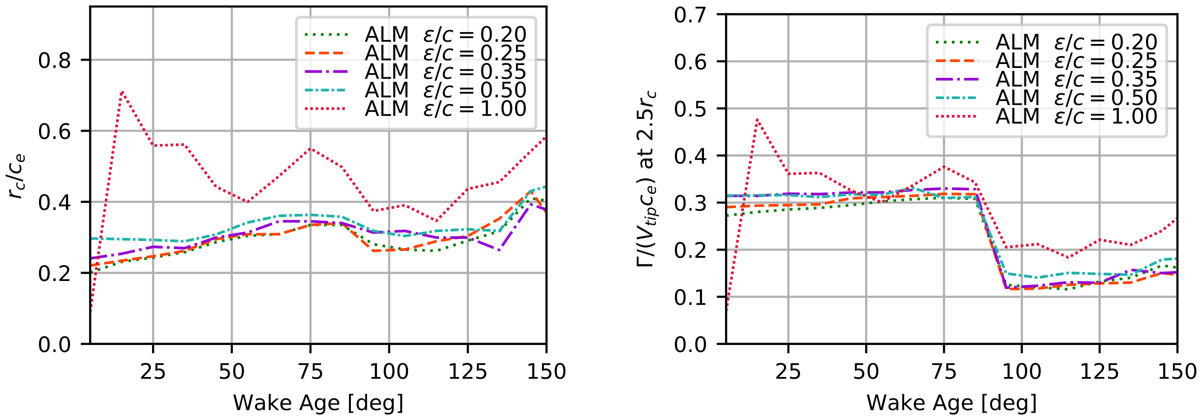

(a) Viscous core radius

(b) Vortex circulation

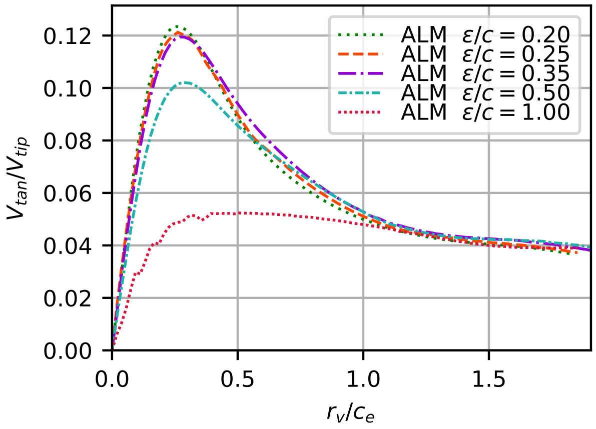

(c) Average tangential velocity profile at 35.0^o wake age

Figure 3.9 Vortex core characteristics in the early wake ages

3.5.2 Detailed Comparison

Section 3.5.1 shows that lower values of the Gaussian smearing coefficient near the value of $\epsilon/c \approx 0.25$ yield more accurate results as suggested in [89, 93]. More specifically, $\epsilon/c = 0.25$ provides better thrust predictive capabilities at a given collective without prior knowledge of the solution thus preventing the necessity to trim simulations excessively. The value $\epsilon/c = 0.35$ provides an excellent prediction of the torque coefficient and Figure of Merit for trimmed solutions. It should be noted that the better agreement of these two integrated coefficients is not a direct consequence of a better blade torque loading from this Gaussian smearing value, but rather from a fortuitous averaging of the BVI disturbed torque loading near the tip. Therefore, this section focuses on a more detailed and quantitative study of the ALM with a selected kernel size of $\epsilon/c = 0.25$ since we value the better thrust predictive capabilities of the method for future applications as well as being consistent with previously published results in the literature. The ALM simulations are run on a similar mesh with respect to their B-R counterparts. The integrated performances plots are generated with their respective Medium meshes whereas the blade loading and tip vortex characteristics are run on the Tip Vortex refined mesh at a collective trimmed to yield a $C_T/\sigma = 0.09$.

Integrated Performance Coefficients

The integrated performances plots of the B-R and ALM are presented in Fig. 3.10. The blade resolved results show excellent agreement with the experimental data especially at higher collective. For the lowest collective setting, the thrust is slightly over-predicted as well as the torque. This results in a slightly lower figure of merit. The ALM on the Medium mesh performs similarly to the Coarse mesh presented in the preceding section. The thrust curve follows a linear trend that overestimates its reference value at lower collective while a slight under-prediction is present at the higher collective angles. The torque curve is over-estimated across the whole range. When comparing the ALM values to the experimental curve fit of torque coefficient at a given thrust coefficient, the relative error is fairly constant at a value of about 7%. Again, this in turn reflects on an under-prediction of the figure of merit with a constant relative error of about -6.5% compared to the experimental curve fit. For reference, the B-R solutions showed a figure of merit relative error of -2.74% to 0.9% from the lowest to the highest collective respectively.

Blade Loading

The simulations are run at a trimmed state of $C_T/\sigma = 0.09$ which corresponds to a collective angle of $\Theta_{75}^{ALM} = 9.27^o$ and $\Theta_{75}^{BR} = 9.14^o$ for the ALM and B-R simulations respectively. The results for the blade loading are presented in Fig. 3.11. In trimmed conditions, the excellent agreement between the two methods for the thrust loading is again shown for the first 80% of the blade span. Then the Blade Vortex Interaction at around 92% blade span occurs. The ALM over-predicts both the up and downwash of this direct hit compared to the B-R case, thus causing the discrepancy. It is fortuitous to see that the loss and increase in thrust on both sides of the BVI cancel each other out when integrated to recover $C_T/\sigma = 0.09$. The torque loading follows a similar trend, but displays a slight over-prediction of torque from span sections $r = 0.5$ to 0.8. The torque loading is again disturbed by the BVI which causes a rise in sectional induced drag both sides of the vortex impact point. This results in the

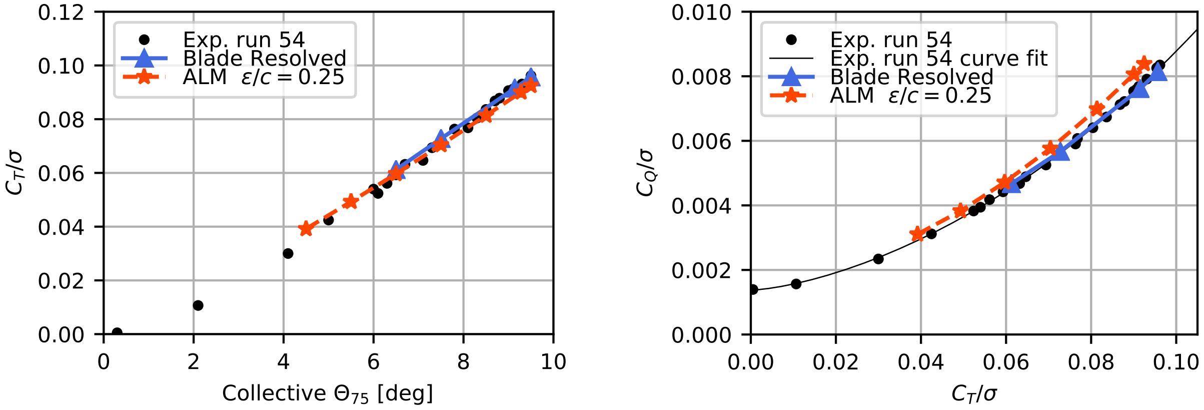

(a) Thrust Coefficient

(b) Torque Coefficient

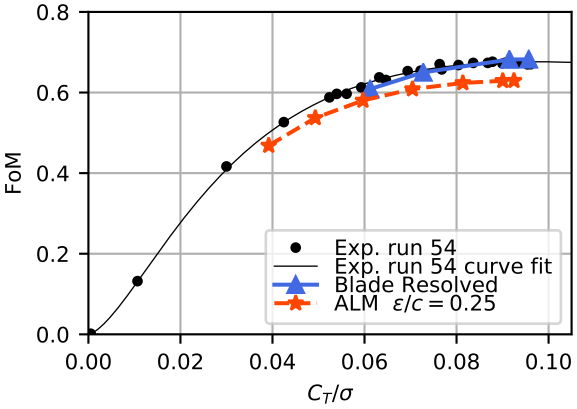

(c) Figure of Merit

Figure 3.10 Integrated rotor performance coefficients for the ALM and B-R on the Medium mesh

higher integrated torque coefficient seen in the performance plots.

Tip Vortex Characteristics

The use of the Tip Vortex mesh for both the blade resolved and ALM simulations allows for a more accurate resolutions and quantification of the tip vortex structure and characteristics. Figure 3.12 shows the positions of the tip vortices over the first rotor revolution. The radial contraction of the two methods are superposed on top of each other as well as the empirical model. The axial advection of the two models is also similar and in good agreement with the prescribed wake model. The slope of the two simulations are usually lower than the

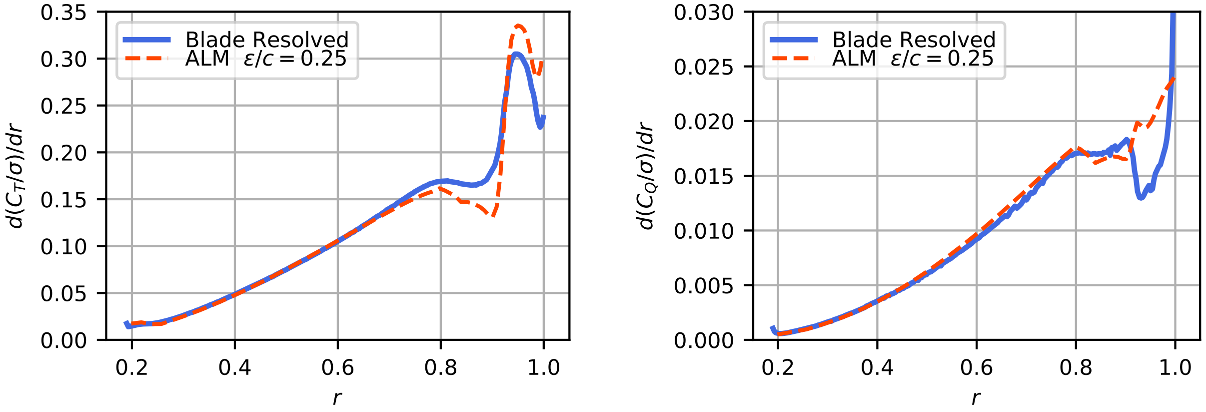

(a) Thrust Loading

(b) Torque Loading

Figure 3.11 Sectional blade loading at $C_T/\sigma = 0.09$ for the Blade Resolved and ALM on the T.V. mesh

empirical reference, but they both retain the characteristic dual slope before and after the first blade passage with the B-R tip vortex being slightly more advected from 125^o to 325^o of wake age. Figure 3.13 presents a qualitative assessment of the wake of the two methods at an iso-level of Q-criterion. The two wakes are very similar in their structure of tip and root vortices whereas the B-R seems to remain cleaner as a consequence of the smaller time step this simulation uses. A small difference is observed at the first blade passage where the BVI splits the tip vortex of the preceding blade in two. The split vortices have their secondary branch differ as the B-R one is more concentrated and is advected towards the center of the rotor faster than the ALM.

The vortex core properties are presented in Fig. 3.14 with the vortex core radius on the left and the circulation on the right. The ALM produces a very similar vortex core size to the B-R until the first blade passage where both methods start with a nondimensional vortex core size of 16% and steadily grow to 26%. After this event, the core radius drops down and starts growing again rapidly caused by the second-order scheme employed and its diffusive nature. The circulation follows a similar pattern as the two methods start around a normalized Γ of 0.3 and grow slightly until the first blade passage prior to dropping significantly and almost halving. Then the vorticity starts to grow again, but remains more constant than the vortex core radius. The difference between the two slopes prior to the first blade passage is attributed to the higher peak blade loading the ALM has over the B-R solution. Figure 3.15 shows the average tangential velocity plots of the two methods for wake ages under the first two blade passages. They complement the preceding figure by showing the core velocity

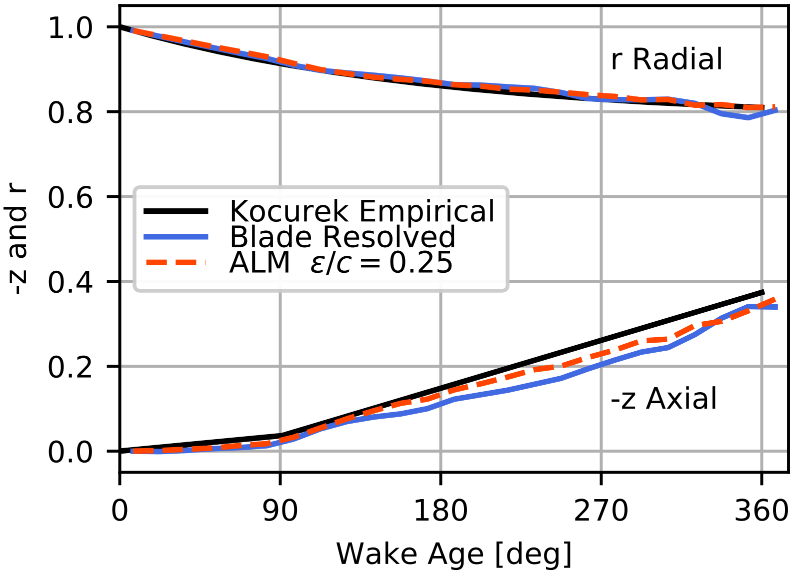

Figure 3.12 Tip vortex positions at $C_T/\sigma = 0.09$ for the ALM and B-R on the T.V. mesh

profile is higher for the B-R at the center of the core radius even though the circulation of the ALM is stronger for the first 90 degrees of wake age. That peak velocity decays faster in the case of the B-R solution in that interval. Then after the first blade passage, the BVI considerably reduces the circulation of the vortices with the ALM being less affected. After the BVI, vortex core of the blade resolved grows at a faster rate than the ALM.

The growing discrepancies between the two methods after the first blade passage is explained by the different response the two methods have towards the BVI. Figure 3.16 presents the vorticity magnitude in slices from the extraction planes at wake ages 2.5^o prior and 5^o, 10^o, 15^o after the first blade passage. At 87.5^o, both methods are similar with the ALM showing a slightly higher vorticity peak. Then, at 5 degrees past the blade passage, the two methods show a secondary vortical structure that is also present in Fig. 3.13. In both cases, the vorticity and size of the primary vortical structure decreases from prior to the BVI. The secondary vortex between the two methods differs as the ALM creates a weaker and larger vortex compared to the B-R. Then the two vortices evolve differently as the secondary vortex of the blade resolved simulation tends to be advected towards the center of the rotor faster than its ALM counterpart. As already mentioned in Section 3.5.1, the ALM projects the force is a porous manner and has no means to enforce a non penetrating boundary conditions, thus leading to a different response when a BVI occurs.

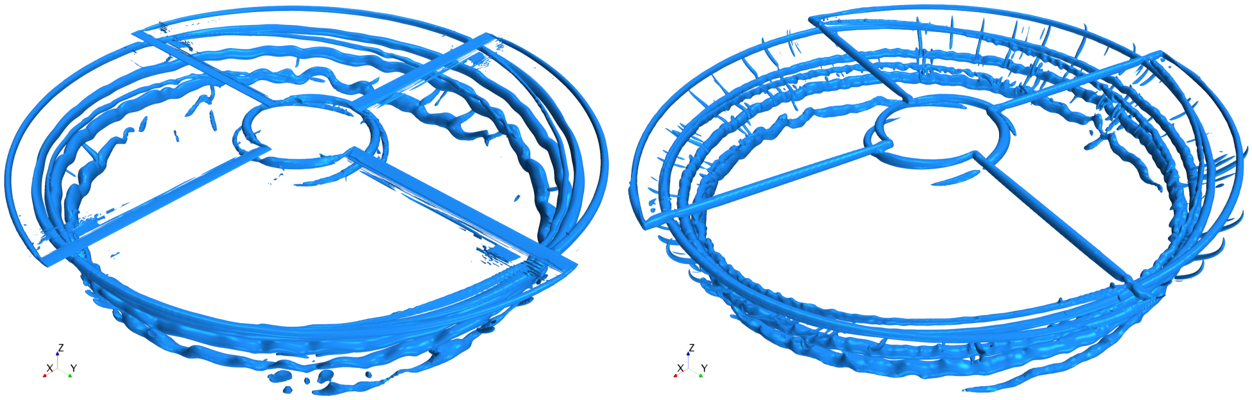

(a) B-R

(b) ALM

Figure 3.13 Q-criterion at iso-level Q=25000 for $C_T/\sigma = 0.09$

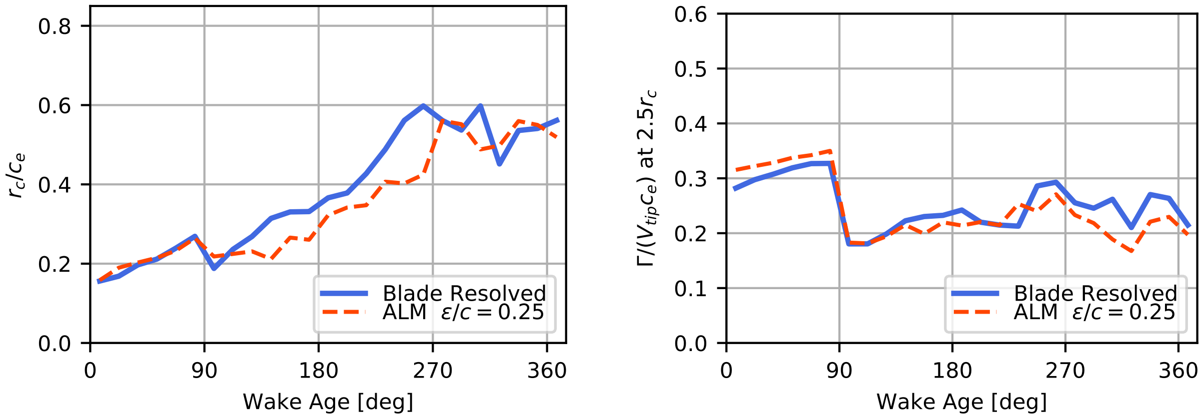

(a) Viscous Core Radius

(b) Vortex Circulation

Figure 3.14 Vortex core characteristics over one rotor revolution at $C_T/\sigma = 0.09$

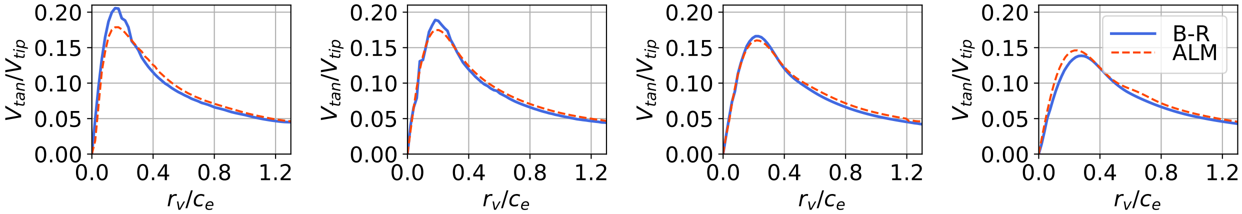

(a) 7.5 deg (b) 32.5 deg (c) 57.5 deg (d) 87.5 deg

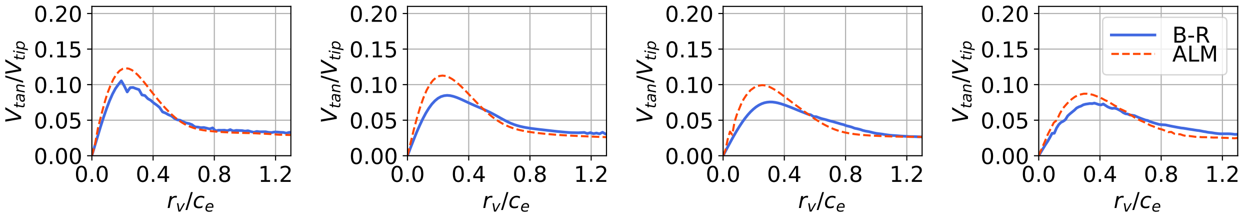

(e) 97.5 deg (f) 122.5 deg (g) 147.5 deg (h) 177.5 deg

Figure 3.15 Vortex core velocity profiles over two blade passages at $C_T/\sigma = 0.09$

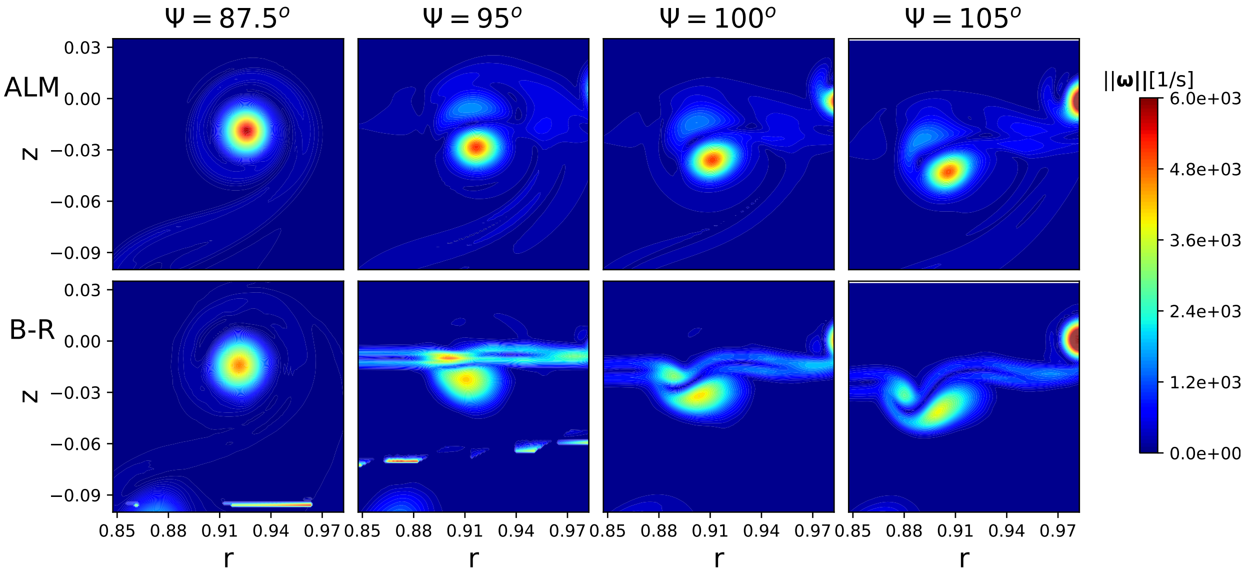

Figure 3.16 Vorticity magnitude slices at $C_T/\sigma = 0.09$

Computational Time

The parallel scaling efficiency of the two methods is presented in Fig. 3.17. This strong scaling study (same mesh, varying amount of cores) is run on the Béluga cluster of Compute Canada which features 40 cores nodes composed of two Intel Xeon Gold 6148 processors each. The compute times of the two methods are measured as the average time over 300 iterations then normalized on a CPUtime[s]/(iteration × Nb_{cell}) basis. The compute times are compared to their respective one node reference time. The B-R on the Coarse mesh and the ALM on the Medium mesh are used. The Speed-Up curves are presented as a function of the number of cores used. Because the two methods have a different amount of mesh cells, an additional metric is included. The amount of mesh cells per core is presented on a secondary and tertiary x-axes as they offer a more representative evaluation of performances. The blade resolved simulations quickly lose their parallel efficiency as the curves drops below 75% at 75000 cells per core as a consequence of the poor scaling capabilities of the moving overset module. The ALM on the other hand is run on a single mesh and sees its speed-up scale much better with a parallel efficiency of 80% up to 10500 cells per core which is comparable to StarCCM+ run on a single mesh region.

Table 3.4 reports the computational times of the two methods over the four meshes used in this study as well as the speed-up the ALM has with respect to the B-R. The total compute times are averaged over the span of the whole simulation and transformed in CPU time per revolution. As seen by the results, the ALM is on average 3 to 4 times quicker than an equivalent blade resolved simulation on similar background meshes. These time improvements are largely attributed to the advantageous mesh size an ALM simulation has over the B-R solution.

Table 3.4 Compute time averaged for one revolution and speed-up

	CPU time per revolution [hr]			
	Coarse	Med	Fine	TV
B-R	1219.8	2321.5	7362.0	23813.5
ALM	284.8	741.9	1771.5	5192.5
Speed-up	4.3	3.1	4.2	4.6

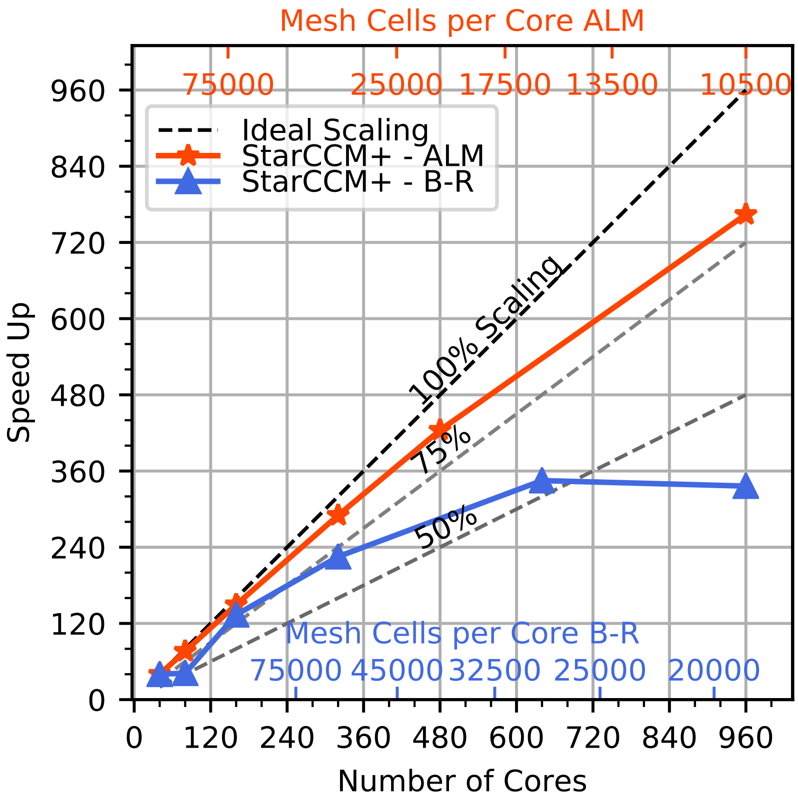

Figure 3.17 Parallel scaling efficiency of the ALM and blade resolved codes on Béluga

3.6 Conclusions

An Actuator Line Model implementation has been developed and adapted for helicopter rotor flow simulations in hover. Key improvements to the method include a modified Gaussian kernel that is truncated and normalized leading to a more consistent force projection at smaller ϵ smearing values. The hyperbolic tangent span discretization enables finer details to be captured at the tip while the force under-relaxation and ramp start increase the stability and convergence of the method substantially.

Proper selection of the kernel width ϵ is explored with a parametric sweep around its optimal value of $\epsilon/c = 0.25$. It is shown that the optimal kernel produces the best overall results and manages to naturally recover a proper behavior of the blade loading at the tip which is often not the case with other ALM implementations that use larger kernel sizes and and rely on tip-loss functions. The larger kernels produce larger tip vortex cores and higher circulation which in turn changes the induced velocity the blade sees resulting in higher blade loading near the tip and higher thrust coefficients at a given collective. Furthermore, the different inflow creates different induced drag characteristics across the span of the blade where smaller kernels see a higher drag resulting in higher torque.

When trimmed to an identical thrust value on equivalent background meshes, the ALM produces similar results compared to its blade resolved counterpart. The only outstanding issue is the over-prediction of the induced velocity a perpendicular blade vortex interaction causes as the porosity of the ALM force projection does not allow the same interaction between the blade and the vortex when compared to the blade resolved case. Fortuitously, the thrust under and over-estimation near the blade tip region cancels out when looking at integrated thrust results, but it causes an increase in drag resulting in torque coefficient and figure of merit curves with an offset. The tip vortex trajectories and core characteristics are in good agreement.

Finally, the computational efficiency of the ALM is showcased. The excellent scalability and 3-4x speed-up across all meshes shows its potential in simulations where main flow features and rotor response is of interest and computational efficiency needed.

CHAPTER 4 AXIAL FLIGHT: VERTICAL CLIMB AND DESCENT

The previous chapter presented the implementation of the ALM for a hovering rotor with the validation being performed on the well-known S-76 rotor. This chapter presents the same numerical model applied to the case of axial flight in climb and in descent. The climb condition, especially at low climb rates, is important because it is closely related to hovering performances which can sometimes prove elusive to accurately measure experimentally. Small climb rates produce well-behaved flowfields that tend to be more periodic in addition to linearly varying FoM values that can be extrapolated to predict hover conditions accurately as explored by Caradonna [142]. Descent on the other hand gives rise to more complex flow conditions namely the vortex wake state (or vortex ring state, VRS) and turbulent wake state which give rise to unsteadiness in the flowfield and reduced manoeuvrability and performances [3,19]. In this chapter, Section 4.1 defines the test case and geometry, Sec. 4.2 presents the numerical setup whereas the results in terms of hover baseline performance, integrated rotor coefficients, blade loading, and wake topology are analyzed in Sec. 4.3.

4.1 Test Case & Rotor Geometry

The selected geometry for this chapter is the four-bladed rotor used by Felker and McKillip [143]. The rotor has been used for various application and was Froude-scaled which results in low tip speeds compared to other similar rotors. This causes equally low Mach and Reynolds numbers at the blade tips. The main rotor characteristics are summarized in Table 4.1. An other particularity of the test rig was the use of the Princeton Long Track. To simulate the climb and descent conditions, the rotor and measurement apparatus were put into motion on a sled atop a 225m long track. The rotor thus moved in still air with large distances to the walls. This results in a turbulence-free freestream with minimal blockage effects. The rotor is rigid and hinge-less. The collective was fixed to a constant value for each test run along with no cyclic variation. Axial velocities in the range of $V_c/V_{ind}^{hov} = [-1.0, 1.0]$ were tested. For the present study, only the highest collective of 10.9° is simulated along with the axial velocities in the range $V_c/V_{ind}^{hov} = [-0.75, 0.75]$.

Parts of this chapter have been presented in Ref. [141]

Table 4.1 Axial flight rotor characteristics

Rotor		**Blade**	
Nb. Blades (N_b)	4	Airfoil Profile, constant	NACA0015
Rotor Radius (R)	1.2192 m	Reference Chord (c_{ref})	0.0635 m
Collective, fixed (Θ_{75})	9.3°, **10.9°**	Linear Twist	-8°
Rotational Speed (Ω)	430.78 RPM	Tip Velocity (V_{tip})	55 m/s
Solidity (σ)	0.0633	Tip Mach number (M_{tip})	0.157
Aspect Ratio (AR)	19.2	Tip Reynolds number (Re_{tip})	212000

4.2 Numerical Setup

A similar setup to the rotor in hover presented in Section 3.3 is used to model the axial flight case. The near wake refinement region extends $0.4R$ above and $0.8R$ below the rotor plane whereas the wake refinement is bounded by a cylinder that extends $0.75R$ above and $1.5R$ below the rotor plane. The mesh cell sizes in these regions are respectively $15\%c_{ref}$ and $30\%c_{ref}$ for the two wake refinement levels whereas the ALM has a further refinement of $7.5\%c_{ref}$ in a region that extends $1.0c_{ref}$ away from the rotor disk. The background meshes contain about 20 million cells. B-R blades are meshed in a similar fashion to the Hover case with each blade region containing about 8.1 million cells. Boundary and initial conditions are set at the same value and correspond to the experimental climb/descent speeds of $V_c/V_{ind}^{hov} = \{-0.75, -0.25, 0.0, 0.25, 0.75\}$. As a result of the low tip Mach number, a segregated SIMPLE [144] solver is used still providing second-order accuracy in both time and space. A similar time-step equivalent to 1^o of azimuthal rotation is used. From the analysis of the Gaussian smearing width presented in the previous chapter, the two values of $\epsilon/c = \{0.25, 0.35\}$ produced excellent results in terms of integrated performance coefficients with $\epsilon/c = 0.25$ performing best at low collective/thrust setting whereas $\epsilon/c = 0.35$ performed better at higher collectives. Both have been tried for the present axial flight case and $\epsilon/c = 0.35$ produced better results when compared to the B-R simulations due to the high collective used. Only $\epsilon/c = 0.35$ results are shown as $\epsilon/c = 0.25$ results would require a trim to be compared to B-R simulations directly.

4.3 Results

4.3.1 Hovering Condition

Table 4.2 presents the integrated performance coefficients of the two numerical methods, B-R and ALM, along with their relative error when compared to the average experimental hover conditions at a collective of $\Theta_{75} = 10.9^o$. For consistency with the rest of the thesis, the two methods use the $k-\omega$ SST turbulence model for the three dimensional flowfield and the sectional 2D database in spite of the low Reynolds present along the blade span. For the hover condition, an additional set of simulations is conducted with the $\gamma - Re_\theta$ transition model. For the fully turbulent case, the two numerical methods are in excellent agreement with each other having only 0.2% thrust discrepancy and about 1.4% difference in terms of torque and figure of merit. Compared to experimental data, there is a marked deficiency in thrust of the order of 5% and an underestimation of the figure of merit which is indicative of excess torque for a given thrust level. Switching to the transitional case, a clear increase of thrust is present, but the numerical results overshoot the experimental data in terms of thrust whereas the FoM is much better approximated in both cases. The increase in thrust can be explained by the non-linear lift increase observed on some airfoil profiles at low angles of attack around nominally transitional Reynolds numbers. The two numerical methods however do not produce similar thrust levels as it was the case for the fully turbulent case which might be caused by the meshing discrepancy between the 3D blade resolved profile and the 2D database in addition to the possible modelling differences present between the 2D and 3D transitional model implemented in the flow solver. With the 3D overset mesh movement taking into account centrifugal and Coriolis effects, which is suspected to have a greater effect transition modelling than for a fully turbulent set up. To avoid the necessity to trim one of the two numerical methods to match the other would the transitional model be selected, the fully turbulent model is kept for the remaining of the axial flight study. Results, once normalized to the hover reference values, should behave similarly.

Table 4.2 Rotor performance coefficients in hover ($V_c/V_{ind}^{hov} = 0$) at $\Theta_{75} = 10.9^o$

		Coefficients					
Type	Turbulence	C_T/σ	Δ[%]	C_Q/σ	Δ[%]	FoM	Δ[%]
ALM	Turbulent ($k-\omega$ SST)	0.0877	-5.0%	0.0078	-1.4%	0.608	-6.2%
B-R	Turbulent ($k-\omega$ SST)	0.0876	-5.2%	0.0078	-0.1%	0.599	-7.6%
ALM	Transition ($\gamma - Re_\theta$)	0.0986	6.8%	0.0088	11.5%	0.641	-1.1%
B-R	Transition ($\gamma - Re_\theta$)	0.0948	2.7%	0.0084	6.5%	0.633	-2.3%
Exp.	-	0.0924	-	0.0079	-	0.648	-

4.3.2 Integrated Performance Coefficients

Moving from a rotor in hover to a climbing condition, the additional freestream velocity effectively increases the inflow velocity above the rotor disk thus reducing the effective angle of attack at a given collective causing a reduction in thrust output. Furthermore, according to momentum theory, the power required for a rotor in climb corresponds to the sum of hover induced power and the climb induced power. Over the blades, this additional power is represented as additional induced drag. One can therefore expect a linear trend for the figure of merit as a function of the climbing velocity [142]. Figure 4.1 presents the thrust coefficient and figure of merit, normalized by their respective hover values, as a function of the climb velocity V_c normalized by the hover induced velocity V_{ind}^{hov}. The reduction in thrust is captured by both numerical methods and agree well between them along with a fair agreement with the experimental data. The linear trend in figure of merit variation is otherwise excellent. However, the two methods fail to accurately capture the proper behaviour in descent. The experimental data presented in Felker and McKillip [143] reports highly unsteady loads and the presence of vortex ring state around the rotor. Both methods at $V_c/V_{ind}^{hov} = -0.75$ still show near-steady converged thrust signals with no apparent presence of VRS around the rotor. However, the far-wake shows some asymmetry which might be indicative of VRS onset.

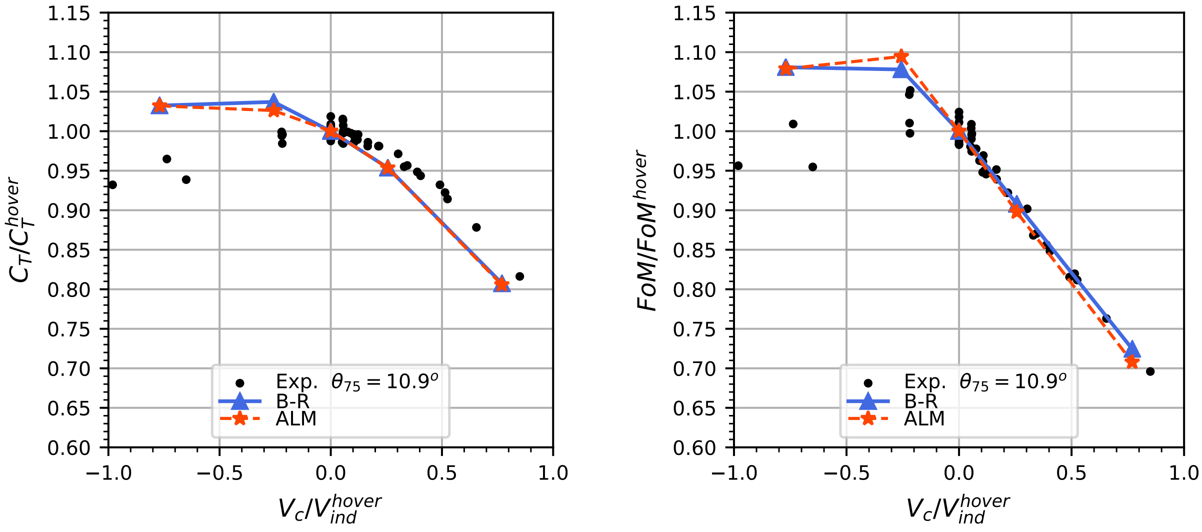

(a) Thrust Coefficient

(b) Figure of Merit

Figure 4.1 Integrated rotor performance coefficients for the ALM and B-R in axial flight

4.3.3 Blade Loading

Looking at the blade loading the two methods produce, a similar behaviour as in Sections 3.5.1 and 3.5.2 is found. The thrust and torque loading are well approximated until about 80% blade span with the BVI from the previous blade causing additional up and downwash in the ALM case. Note that this behaviour is, for the most part, negated by the case in climb with only a small thrust over-prediction present near the blade tip as the tip vortices tend to be advected quickly downwards with the additional freestream velocity and do not cause a BVI phenomenon.

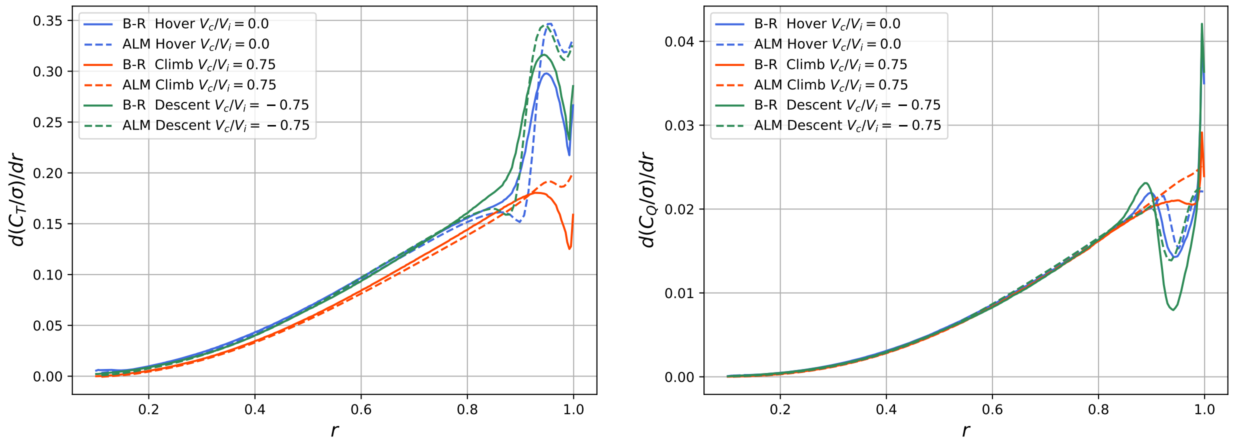

(a) Thrust Loading

(b) Torque Loading

Figure 4.2 Sectional blade loading at $\Theta_{75} = 10.9^o$ for the ALM and B-R in axial flight

The ALM allows direct extraction of the effective angle of attack and inflow angle as required by BET as represented in Fig. 4.3. This is not possible for B-R simulations. The additional freestream velocity in climb is directly represented as a reduction of relative angle of attack and inflow angle increase across the blade span when compared to the hover baseline. The case in descent at an identical descent velocity is not as affected especially in the 50% to 90% span locations region where very similar α_{eff} and ϕ_i are observed. Momentum theory would suggest an equally distributed induced velocity along the blade where the linearity of the wake makes it possible to simply add and subtract velocities. However, for the present simulations, the stronger induced velocity near the blade tips is stronger than the descent rate and acts as a "shield" against the opposite direction freestream. The BVI observed in hover and in descent is also noticeable near the tip with the latter case being of stronger magnitude.

4.3.4 Wake Topology

Figure 4.4 presents the locations of the tip vortices for the two methods in different axial flight conditions. First, in hover, the two methods are in excellent agreement with each other and with the empirical prescribed wake model of Kocurek and Tangler [30]. Although there is a slight lag in the axial velocity between the second and fifth blade passage. In climb at

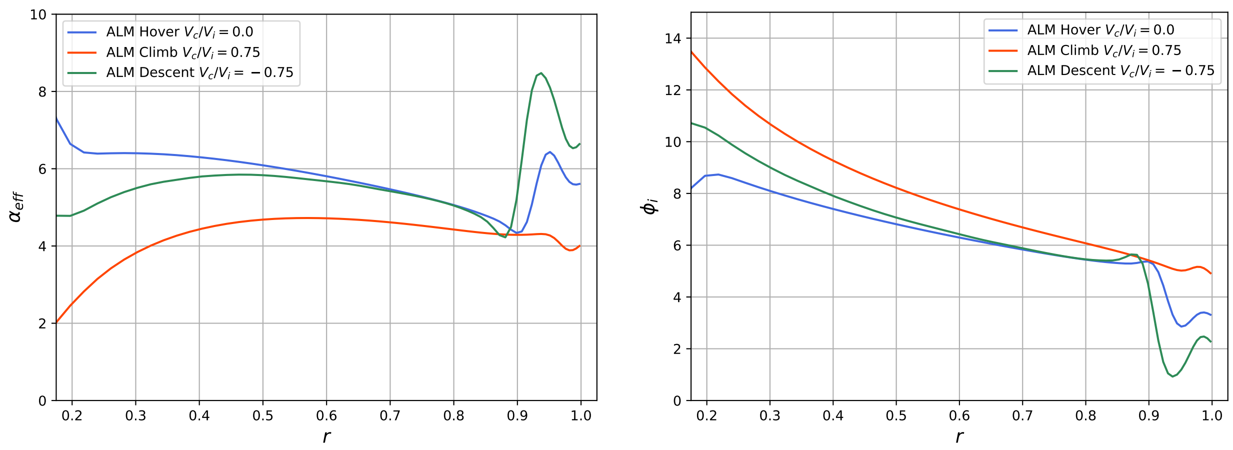

(a) Effective angle of attack

(b) Inflow angle

Figure 4.3 Sectional blade angles at $\Theta_{75} = 10.9^o$ for the ALM and B-R in axial flight

$V_c/V_{ind}^{hover} = 0.75$, the added downward velocity advects the tip vortices faster than in hover despite the loss of thrust (and therefore loss of hover induced velocity). The radial contraction is also considerably reduced. The two numerical methods are nearly indistinguishable from each other. Finally, in descent at $V_c/V_{ind}^{hover} = -0.25$, the wake is less stable resulting in a tip vortex extraction stopped after four blade passages only. As intuition might suggest, the trend is opposite to the climbing case with the wake contracting more than in hover along with a slower axial advection. The wake topology can also be qualitatively assessed in Fig. 4.5 where the ALM appears to create a more stable and better preserved wake than the B-R case in climb and in hover.

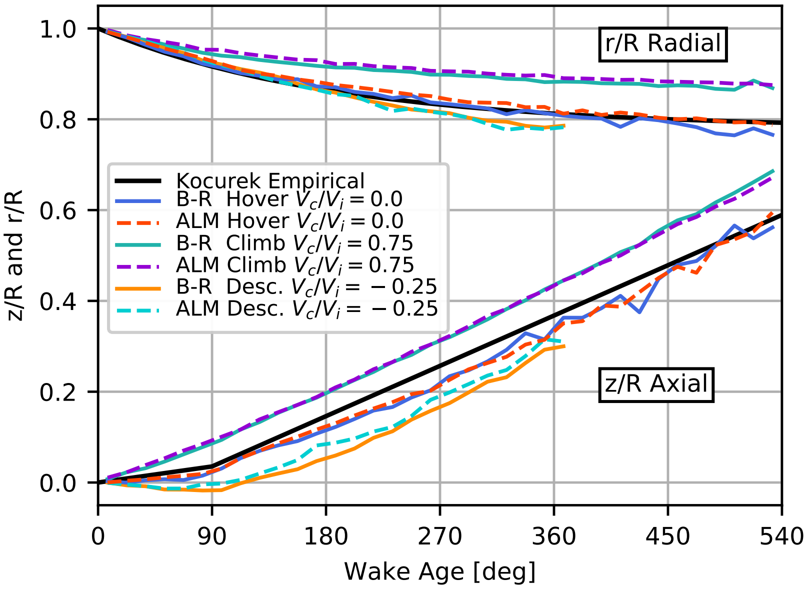

Figure 4.4 Tip vortex positions at for the ALM and B-R in axial flight

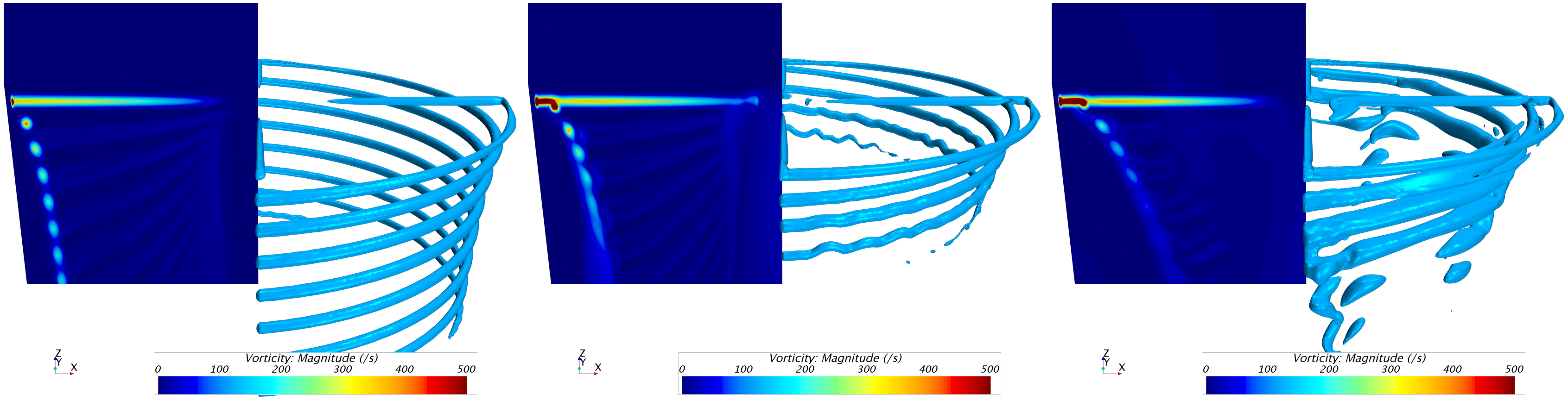

(a) ALM $V_c/V_{ind}^{hov} = 0.75$ - Q-crit=2500 (b) ALM $V_c/V_{ind}^{hov} = 0.00$ - Q-crit=2500 (c) ALM $V_c/V_{ind}^{hov} = -0.75$ - Q-crit=100

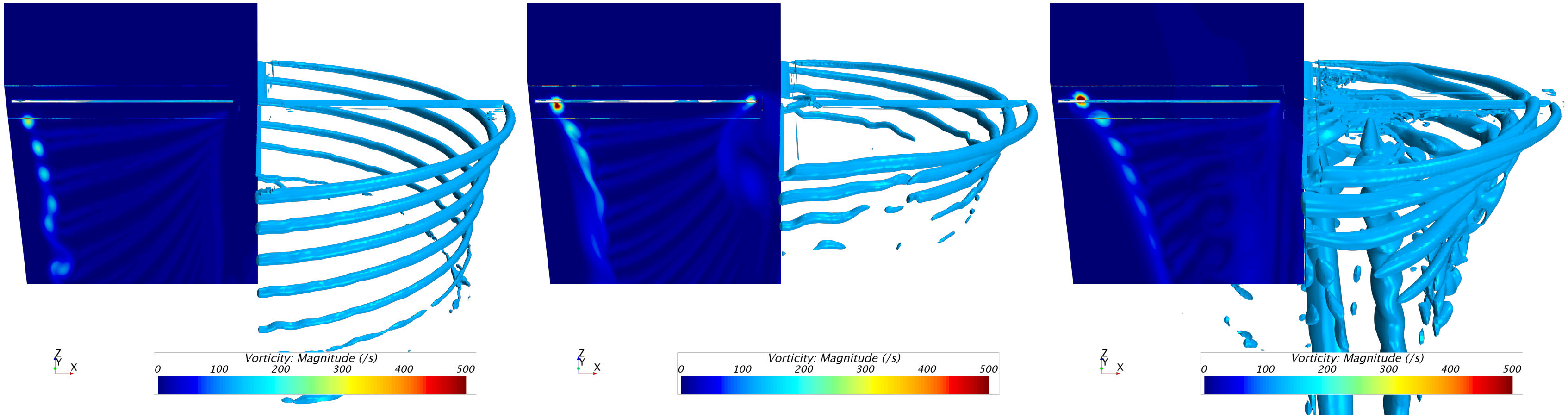

(d) B-R $V_c/V_{ind}^{hov} = 0.75$ - Q-crit=2500 (e) B-R $V_c/V_{ind}^{hov} = 0.00$ - Q-crit=2500 (f) B-R $V_c/V_{ind}^{hov} = -0.75$ - Q-crit=100

Figure 4.5 Axial flight wake topology through vorticity magnitude plane and Q-Criterion tip vortices

4.4 Conclusion

This chapter presented the application of the ALM towards a helicopter in axial flight with comparisons made with equivalent B-R solutions and experimental data. Despite a gap with respect to the experimental data, the ALM performed similarly to the B-R case in terms of global flowfield and integrated performance coefficient trends. The main difference between the ALM and B-R is again the blade loading that is affected from the previous blade BVI resulting in the over-estimation of the vortex-induced velocity and ensuing torque over-prediction. Overall, the ALM correctly captures the thrust reduction of a rotor in climb along with an excellent agreement in the linear trend of the figure of merit. The ALM, unlike the B-R, is also capable of directly extracting the blade effective angle of attack and inflow angle thus allowing potential direct comparison to momentum theory or vortex-based models. These two angles are inherent two-dimensional flow concepts that get lost in traditional blade resolved 3D U-RANS simulations. The ALM is also in excellent agreement with the B-R when comparing the tip vortex wake location in the three axial flight cases. Finally, the two numerical methods do not capture the vortex ring state that is said to occur experimentally. The wake topology at the highest descent rate is however non-symmetrical with unsteady features which might be indicative of VRS onset.

CHAPTER 5 ARTICLE 2: NUMERICAL SIMULATIONS OF A ROTOR IN CONFINED AREAS INCLUDING THE PRESENCE OF WIND

Merabet, R., and Laurendeau, E., Numerical simulations of a rotor in confined areas including the presence of wind, *Submitted to* Aerospace Science and Technology, June 2021. [145]

Abstract

This work explores the high fidelity numerical aerodynamic computations of a helicopter rotor placed in various confined areas including the presence of wind. Two numerical methods, fully blade resolved CFD and the actuator line method (ALM), are compared against each other and experimental data in terms of global rotor loads including thrust, torque, pitching and rolling moments. A detailed assessment of the two methods outside-of-ground effect (OGE) is performed covering blade loading, rotor inflow, wake geometry and fuselage surface pressure coefficient. Excellent agreement and consistency are found between the two numerical methods. Both are able to accurately predict the trends of the experimental rotor in most cases. However, some conditions remain challenging from either a modelling or computational standpoint. The overall agreement of the two numerical methods with the experimental data demonstrates their capabilities in accurately predicting rotor flows in challenging confined areas and the appropriateness of the ALM to replace more costly fully blade resolved simulations.

5.1 Introduction

Due to its hovering and manoeuvring capabilities, the helicopter is currently one of the most versatile flying machines in operation for air transport. This aircraft is capable of flight in challenging conditions such as in rescue scenarios over variable terrain, near city sky-rises, landing atop buildings or even operating in the close vicinity of naval vessels. All these scenarios involve complex geometries that can interact with the flowfield created by the helicopter rotor in addition to the already complex flowfield the obstacles produce by themselves in presence of wind. The disturbed flowfield has a strong influence on the performances and handling characteristics of the helicopter.

A well-studied example of handling degradation is the operation of a helicopter at sea performing a landing manoeuvre near a ship as described by Hoencamp et al. [13] from a pilot's perspective. This problem has also been documented in multiple experimental [146–149] and numerical [16, 50, 51, 64, 150] studies on numerous specific ship and helicopter geometries.

In addition to this very complex type of interaction, there is also an interest in studying the performances of helicopters in simpler settings such as in "confined areas" (i.e. where the helicopter sees its displacement restricted in at least one direction due to terrain or obstacles). This particular issue was the focus of the GARTEUR Action Group project HC/AG-22 [151] which produced multiple experimental databases that pertain to the analysis of small scale helicopter models in interaction with different obstacles [125, 152–154] and the effects of the helicopter on the obstacle surface loads. The analysis of rotors in confined areas is also a field of interest for Micro Air Vehicles (MAV) which has been investigated both experimentally and numerically [155, 156]. One motivation behind such studies is to gain phenomenological understanding of the operation of helicopters on simplified geometries. In addition, these simplified geometries are well suited for Computational Fluid Dynamics (CFD) code validation.

Simulating the aerodynamic performances of helicopters and rotors in complex environments can be done by a multitude of techniques. Simpler cases in-ground-effect or in advancing flight could be simulated through Blade Element Theory (BET) and Blade Element Momentum Theory (BEMT) [3] approaches given proper modelling considerations and calibration. As the level of complexity of the flowfield increases, these low fidelity models quickly become unable to predict rotor performances in these situations and increasingly rely on empirical laws derived from experimental data or higher fidelity models, such as CFD, for their calibration. Increasing in level of fidelity we find singularity based methods such as Vortex Lattice Methods (VLM) [5,26,126,127] and Panel Methods (PM) [152] which can handle simple geometries in an inviscid way. In recent years, these two methods have been coupled to Vortex Particle Methods (VPM) for the evaluation of the rotor wake, including viscous effects, and possible interaction with geometries such as a ground, box and even ships [113, 114, 150, 157]. Finally, mesh-based CFD methods have been used extensively for the simulation of rotors ranging from relatively simpler cases of ground effect in advancing flight cases through increasingly complex environment such as the fully coupled rotor-ship dynamic interface [64, 158, 159]. These high fidelity methods usually offer better predictive capabilities as a result of a more complete description of the flowfield through the modelled equations and the explicit inclusion of geometries within their computational framework. However, this increased level of fidelity and accuracy comes at the cost of additional computational time.

A common trend in the study of helicopters and rotor in complex environment within a high fidelity framework is to use rotor replacement techniques. These simplifications remove the geometry of the rotor blades and thus their associated meshes. The compute time of the simulation is significantly reduced by the economy in mesh size but comes as a trade-off in accuracy, however. The effect of the rotor is replaced by momentum source terms in the (Unsteady) Reynolds-Averaged-Navier-Stokes ((U)-RANS) equations and exert force on the flowfield resulting in similar flow characteristics. The simplest form would be an Actuator Disk (AD) [47, 98, 99, 128] which averages the rotor blade loads azimuthally, and sometimes radially. This approach yields a good prediction in average surface loads on a fuselage but loses the time accuracy and the distinct tip vortex wake. The AD has recently been used by Shi et al. [49–51] in the study of the helicopter/ship dynamic interface for a case with two rotors near a ship landing deck as well as in an investigation of the influence of passive/active flow control on the dynamic interface. An evolution of the AD would be to use an Unsteady Actuator Disk (UAD) as introduces by Boyd [97] with recent developments and different modelling strategies presented in Barakos et al. [160]. Oruc et al. [16, 161] used the model in the study of the interaction between a rotor and a Ship Frigate in a simulation coupled with a flight dynamic model whereas Chirico et al. [129] used it to investigate the interaction between a rotor and a generic box-shaped obstacle. A further evolution is the Actuator Line Method (ALM), as introduced by Sørensen and Shen [80] in the Wind Energy sector, that has been one of the most used computational method for horizontal axis wind turbines in the past two decades but is seldom used in the helicopter community. The ALM represents the rotor blades as rotating lines of momentum source terms whose magnitudes are computed using a BET approach coupled to the 3D RANS flowfield. This method, unlike the AD, produces distinct tip vortices. A modified ALM was used by Alpman et al. [108] in addition to a helicopter flight dynamic model for the computation of rotor load time histories for a rotor placed behind a hangar with incoming wind as well as a rotor behind a ship frigate to evaluate different coupling procedures. Forsythe et al. [110] used a swept version of the ALM to achieve larger time steps towards applying it to a helicopter landing on a ship. Delorme et al. [112] used the ALM to compute rotor noise in a Large Eddy Simulation (LES) framework through the use of a Ffowcs Williams-Hawkings acoustics analogy model. Then the ALM has recently been validated in hovering conditions on the S-76 rotor by Merabet and Laurendeau [12]. Finally, a further variation of the ALM would be to consider a chord-wise distribution of the sectional force with either constant loading or with a distribution mimicking the blade surface pressure coefficient and possibly skin friction coefficient. This Actuator Surface Method (ASM), as introduced by Shen and Sørensen [70] and Sibuet-Watters and Masson [74–76] in the wind turbine industry, was recently used by Linton et al. [106, 107, 162] to simulate a helicopter rotor in hover, forward flight, in a tandem configuration and in interaction with a ship wake for the evaluation of the dynamic interface.

An outstanding issue in the study of helicopters in complex or confined environment, in particular for the study of rotor-ship dynamic interface, is the lack of proper validation data for CFD purposes. For the specific case of rotor-ship dynamic interface, several experimental studies have been performed in the past [146–148, 163–166], with some only using a ship geometry without a rotor whereas others, that did include a rotor, contained complex and or proprietary ship/fuselage geometries. In the context of CFD validation of the complex flowfield of a helicopter in a confined area, it is desirable to simplify the geometry as much as possible. Through the GARTEUR AG22 project, the experimental database of Zagaglia et al. [167] achieves this goal. The obstacle is a well-defined parallelepiped with sizes of the order of 1 to 3 rotor radius. The fuselage is simple, minimalist and does not contain small intricacies whereas the rotor is simplified through the use of well-defined airfoil profiles, fixed collective, no cyclic variation and a rigid rotor. Although these modifications produce a helicopter that is untrimmed and do not reproduce accurately the dynamics of a real helicopter, the authors of the study believe that the main features of the wake are still representative of a real helicopter. Furthermore, on a CFD simulation standpoint, it is simpler to model a helicopter rotor with a fixed geometry that is known *a priori* as it eliminates possible errors and modelling that pertain to blade motions. The study of Zagaglia et al. covers multiple flight conditions in increasing level of complexity ranging from hovering in and out-of-ground-effect, with and without wind (advancing flight) and with the presence of a box-shaped obstacle with the rotor placed at different positions relative to it. Measurements of the rotor thrust, torque, rolling and pitching moments, Particle Image Velocimetry (PIV) and pressure loads on the obstacle are performed to form the database. However, only the rotor loads are reported in their published study, which is plentiful for an initial effort in validation of computed rotor loads through CFD. Consequently, this work uses the database as a validation test case.

For the numerical simulation tools, two methods are considered, starting with a fully Blade-Resolved (B-R) CFD using the Overset Mesh technique within a U-RANS framework. This high fidelity simulation will allow an assessment of the current state of the art for this class of simulation tool against a recently published dataset as well as provide a benchmark for the rotor replacement technique. The second method considered is the ALM and comes as an evolution of actuator disks, which are typically used for this kind of simulations. In fact, as reported above, higher fidelity rotor replacement techniques (i.e. ALM and ASM) are starting to get traction in the helicopter community especially with the aim of tackling complex problems of rotor in confined areas or the rotor-ship dynamic interface. The ALM will therefore be benchmarked against the B-R solutions on identical meshes and simulation templates in order to assess the performance of the method for rotors in confined areas.

In this work, a helicopter rotor is simulated in multiple flight conditions starting with a comprehensive assessment of the hovering and forward flight performances outside of ground effect including detailed performance coefficients evaluation, blade loading, inflow, wake geometry and fuselage surface pressure. Then, for both these conditions, the in-ground-effect (IGE) configuration is studied. It is followed by the addition of the obstacle placed upstream of the rotor with the latter performing a vertical sweep to assess the effects of the obstacle on the ground effect.

5.2 Numerical Methodology

The flow solver used in this work is Star-CCM+ 12.06 [120] which is a general purpose finite volume, unstructured, cell centred, multi-physics flow solver. All computations are done with a segregated approach using the SIMPLE [144] algorithm with an unsteady dual time-stepping scheme with 2^{nd} order accuracy in both time and space. The time step used for all simulations in this work corresponds to an equivalent of 1^o of azimuthal rotation. All the simulations in this work are solved with the $k - \omega$ SST turbulence model [122]. The ALM adds momentum and energy source terms to the U-RANS equations to simulate the effects of the rotor. The implementation is performed through the User Coding framework of Star-CCM+. Both the B-R and ALM solutions use the same simulation template in terms of numerical setup and meshes for a fair comparison between the two methods. It should be noted that the ALM is considerably less sensitive to mesh coarsening than the B-R and would produce accurate results in terms of performance coefficients on coarser meshes as explored in Ref. [12] for hovering conditions. The flowfield, however, would appear somewhat different as a result of the loss in mesh definition.

Blade resolved simulations are modelled through the Overset mesh technique. The rotating blades are individually meshed and interfaced with a static background grid for communication between the different meshes in the hierarchy with the interpolation between the different levels being done with an inverse-distance weighted approach. The mesh regions around the blades are either cylindrical or prismatic shaped and extend $\sim 1.25c_{ref}$ and $\sim 0.375c_{ref}$ away from the blade geometry respectively. The larger cylinder overset mesh region is used for isolated rotor simulations whereas the tighter prismatic mesh region is used when a fuselage is introduced in order for the blade mesh to clear the additional geometry. For both cases, the cell mesh size at the surface of the overset regions approximately matches the background grid.

5.2.1 ALM Modelling

By removing the blades geometry and their associated meshes, the ALM replaces the physical representation of the rotor by source terms in the fluid flow equations. These equations are summarised in their generic integral form, omitting any turbulence model, by Eqs.(5.1-5.3), as per Ref. [120]:

$$\frac{\partial}{\partial t}\int_V \rho\, dV + \oint_A \rho \mathbf{v}\cdot d\mathbf{a} = 0 \tag{5.1}$$

$$\frac{\partial}{\partial t}\int_V \rho \mathbf{v}\, dV + \oint_A \rho \mathbf{v}\otimes\mathbf{v}\cdot d\mathbf{a} + \oint_A p\mathbf{I}\cdot d\mathbf{a} = \oint_A \mathbf{T}\cdot d\mathbf{a} - \int_V \mathbf{f_{alm}}\, dV \tag{5.2}$$

$$\frac{\partial}{\partial t}\int_V \rho E\, dV + \oint_A \rho H \mathbf{v}\cdot d\mathbf{a} + \oint_A \mathbf{q}\cdot d\mathbf{a} = \oint_A \mathbf{T}\cdot\mathbf{v}\, d\mathbf{a} - \int_V \mathbf{f_{alm}}\cdot\mathbf{v}\, dV \tag{5.3}$$

where V is the control volume of a cell and $\mathbf{a}$ its outward area vector. Flow properties are represented by the density ρ, the velocity vector $\mathbf{v}$, the pressure p, the viscous stress tensor $\mathbf{T}$, the heat flux $\mathbf{q}$, and the total energy and enthalpy E and H, respectively. The body force needed for the modelling of the ALM is expressed by $\mathbf{f_{alm}}$ which is treated as any other volumetric body force. The negative signs indicate that the forces to be applied on the flowfield are of equal strength, but opposite direction of the rotor forces. The removal of the blade meshes produces substantial savings in terms of grid size yielding up to 3-4x speed-up in compute time as well as faster set-up time and increased parallel scalability [12].

Through a BET approach, the $\mathbf{f_{alm}}$ source term is modelled by considering the individual rotor blades as rotating lines that are discretised in sections along their span axis located on the quarter chord of the profile of the blade. Each section is considered radially independent from its neighbours and has its velocity sampled along its centre. Through the use of the integral velocity sampling [95,110], the sampled velocity $\mathbf{U_s}$ represents only the wake induced velocity and is void of any bound circulation induced velocity. As per BET, a local effective freestream velocity $\mathbf{U_{rel}}$ and angle of attack α_{rel} is reconstructed through Eqs. (5.4-5.7) and illustrated in Fig. 5.1.

$$\mathbf{U_T} = \Omega(r\cdot R) - \mathbf{U_{s,y}} \tag{5.4}$$

$$\mathbf{U_P} = -\mathbf{U_{s,z}} \tag{5.5}$$

$$\mathbf{U_{rel}} = \mathbf{U_P} + \mathbf{U_T} \tag{5.6}$$

$$\phi = \arctan\left(U_P/U_T\right) \tag{5.7}$$

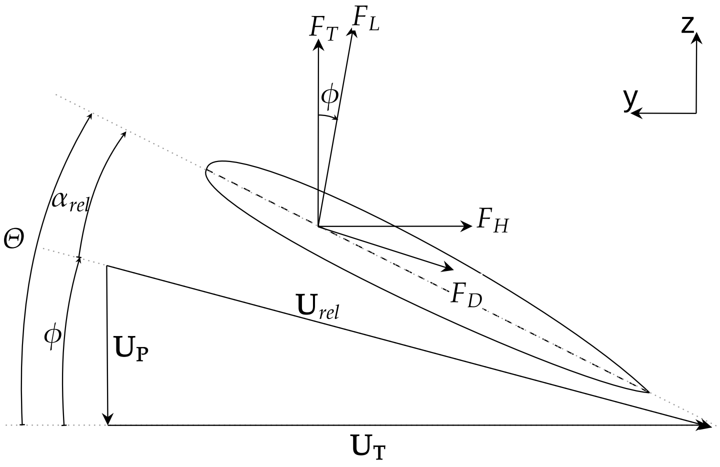

Figure 5.1 Blade element representation of a blade section from [12]

With the freestream velocity and angle of attack computed, the ALM uses pre-computed values from a 2D viscous database to identify local lift, drag and moment coefficients. The lift and drag forces of Eqs.(5.8) and (5.9) are then projected onto the flowfield. The database is evaluated on 6 blade sections along the span with local Mach and Reynolds numbers over an angle of attack range of 0^o to 20^o as a result of the symmetric airfoil geometry.

$$\Delta L = \frac{1}{2}\rho \|\mathbf{U_{rel}}\|^2 C_l(\alpha_{\mathrm{rel}}, \mathrm{Re}, M)c\Delta R \tag{5.8}$$

$$\Delta D = \frac{1}{2}\rho \|\mathbf{U_{rel}}\|^2 C_d(\alpha_{\mathrm{rel}}, \mathrm{Re}, M)c\Delta R \tag{5.9}$$

The computed lift and drag forces from a particular ALM segment are projected into the flowfield through a Gaussian kernel, represented in Eq.(5.10), that spreads the force radially from the collocation point over several grid cells. The extent of the spreading is controlled by the ϵ term which is typically scaled by the local chord with values around $\epsilon \sim 0.25c$ showing better predictive agreement as explored in Refs. [89, 93, 118, 136]. For the present study, the value of $\epsilon = 0.225c$ is used as it produced marginally better results than $\epsilon = 0.25c$. The ALM force source term $\mathbf{f_{alm}}$ is then reconstructed by summing every individual ALM segment contribution as in Eq.(5.11):

$$g(x, y, z) = \frac{1}{\epsilon^3 \pi^{\frac{3}{2}}} \exp\left(-\frac{(x - x_0)^2 + (y - y_0)^2 + (z - z_0)^2}{\epsilon^2}\right) \tag{5.10}$$

$$\mathbf{f_{alm}} = \sum_i \cdot g_{\mathrm{i}} \cdot (\Delta L_i \mathbf{e_{L,i}} + \Delta D_i \mathbf{e_{D,i}}) \tag{5.11}$$

The source term used in this work is also radially truncated to respect the geometrical limits of the span of the rotor blade and normalised. More details about the method and its adaptation to helicopter rotors can be found in Ref. [12].

5.3 Test Cases and Geometry

5.3.1 Experimental Test Case Description

The experimental study of Zagaglia et al. [167] is used to validate the performances of the two numerical methods for a helicopter in confined areas. The main characteristics of the helicopter rotor are summarised in Table 5.1. In addition, the experimental setup featured a reduced-scale fuselage based on a MD500 geometry. The motor and load measuring devices were embedded inside the fuselage which was held in place by a rear sting exiting the fuselage tail boom. The internal balance was fixed in such a way that it only measured the rotor loads, without the forces acting on the fuselage. Multiple configurations were studied including the presence of a box-shaped obstacle geometry and wind. The obstacle had dimensions of 1 m x 0.45 m x 0.8 m (W x H x L) whereas the Politecnico di Milano wind tunnel test section was 13.84 m x 3.84 m x 38 m (W x H x L). The wind was blowing at about 5.07 m/s which corresponds to an advance ratio of $\mu = 0.05$. As the ground was stationary, a boundary layer (BL) at the centre of the test section is present with a thickness of 0.18 m. This height corresponds to 40% of the obstacle height and a rotor normalised height of $Z/R = 0.48$. As such, the boundary layer influences the flowfield around the obstacle, but marginally affects the rotor as it was never placed lower than $Z/R = 1.0$ (double the BL height). Multiple tests were performed both in the presence ($\mu = 0.05$) and absence ($\mu = 0.0$) of wind with the rotor isolated from the obstacle (T0), placed above the obstacle (T1), performing a horizontal sweep above an edge of the obstacle (T2) and performing a vertical ground effect sweep centred (T3) and offset (T4) behind the obstacle.

Table 5.1 Model rotor characteristics

Rotor		**Blade**	
Nb. Blades (N_b)	4	Airfoil Profile, constant	NACA0012
Rotor Radius (R)	0.375 m	Reference Chord (c_{ref})	0.032 m
Collective, fixed (Θ_{75})	10°	Linear Twist	0°
Aspect Ratio (AR)	11.72	Tip Mach number (M_{tip})	0.3
Solidity (σ)	0.10865	Tip Reynolds number (Re_{tip})	220000
Rotational Speed (Ω)	2580 RPM		

5.3.2 Numerical Setup, Meshes and Simplifications

For the present study, the test cases of interest are: hover in-ground-effect T0-μ=0.0, advancing flight in-ground-effect T0-μ=0.05, hovering in-ground-effect with obstacle T3-μ=0.0 and in windy conditions in-ground-effect with obstacle T3-μ=0.05. As such, different modelling strategies are used to accommodate the different setups and flow regimes. Most simulations only consider an isolated rotor with a root cut-out at 20% span. In cases where a fuselage is present, the main body shell is modelled along with the hub cap and all surfaces have 25 cells in their BL surface mesh and a $y^+_{wall} \sim 1.0$. No hub or linkages, rear sting and support structure are considered. For cases without the obstacle (T0, with and without wind), the floor is assumed to be inviscid as the modelling of the floor BL was tested and did not impact the rotor performance coefficients. For cases with the obstacle, both it and the floor have their boundary layer meshed and modelled with a height that captures the wind tunnel BL and a near-wall spacing that ensures $y^+_{wall} \sim 1.0$. The modelling of the obstacle and wind tunnel floor BL allowed a qualitative assessment between the present T3-μ=0.05 test case, with the rotor removed, and both the experimental work of Martinuzzi and Tropea [168] and numerical work of Hwang and Yang [169] and Lim et al. [170]. All numerical simulations are performed in a computational domain that represents the PoliMi wind tunnel test section. Mesh refinement zones are placed in the near wake region of the rotor. An additional volumetric refinement zone is added around the obstacle when present. B-R blade meshes have a near wall spacing of $5e^{-5}c$ and 35 BL cells which ensures a $y^+_{wall} \leq 1.0$. Figure 5.2 illustrates an example of the mesh template used for the flow domain and B-R blade. Table 5.2 presents the total mesh size for both methods with and without the obstacle in a configuration near the ground and one in OGE. The decrease in mesh size for configurations closer to the ground is due to the reduction in size of the wake refinement region as it extends from a fixed height above the rotor to the ground. In all present cases, the ALM has mesh sizes roughly half of the B-R.

Table 5.2 Mesh cell count in different configurations

		Cell count (M)	
Config.	Z/R	**B-R**	**ALM**
T0	1	25.6	12.2
	4	30.0	16.7
T3	1	28.9	13.9
	4	32.9	18.0

Experimental data points were sampled over a 5 seconds averaging window that followed a 10 seconds flow development/stabilisation period. This time interval corresponds to a total

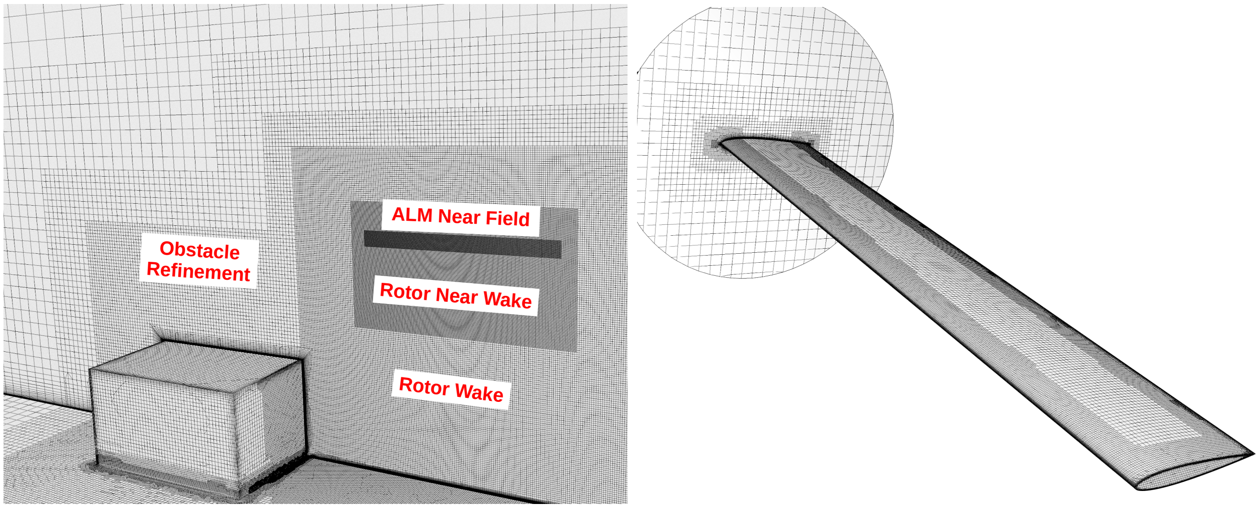

(a) Domain mesh T3 (b) Blade surface mesh

Figure 5.2 Computational mesh template

of 645 rotor revolutions, which represents an exorbitant amount of computational resources in a U-RANS framework if the numerical simulations were to match the number of rotations. Therefore, simpler cases (i.e. T0) are run for a total of 30 to 45 revolutions with the performance values averaged over the last 10 revolutions. Harder cases with the obstacle are run over a longer period of time ranging from 45 up to a maximum of 100 revolutions with the averaging performed over the last 30 revolutions in order to capture the greater flow unsteadiness effect over the rotor performances.

5.4 Results

5.4.1 Reference Conditions OGE

First, the results of the reference cases for the two numerical methods with no obstacle and out-of-ground-effect (T0, Z/R=4) in both wind conditions are assessed. These reference values will be used to normalise the results from other test conditions in the presence of the ground and the obstacle. Numerical results, along with experimental data, of the integrated performance coefficients, are presented in Tables 5.3 and 5.4 for the wind-off and wind-on cases respectively. For the case in hover, the thrust, torque and figure of merit of both numerical methods are in good agreement with the experimental data with relative errors of the order of one percent. The values of the moment coefficients in both axes for both numerical methods are almost negligible (less than 0.15% of the OGE torque value) which is expected due to the axisymmetric nature of the flowfield in hover when only the main rotor is modelled. The slightly higher value observed for the experimental data could be explained by the presence of the fuselage in the physical experiment which breaks the axisymmetric hypothesis. Due to their small magnitudes, the relative errors of the moment coefficients is over-inflated and should not be considered. Next, the addition of wind causes an increase in the thrust, reduction in torque and hence an improved figure of merit as reported in Table 5.4. Both numerical methods show consistent trends when compared to the experimental data with an increase of 4% to 5% in thrust when compared to the hovering case. But the B-R slightly over-predicts the thrust and under-predicts the torque thus resulting in a larger FoM error. The two numerical methods correctly capture the signs of the moments in both axes, indicating a tendency of the rotor to pitch up in the rotor y-axis and a negative rolling moment towards the port side of the helicopter in the x-axis. The magnitudes of the individual axis components present a large error when compared to the experimental data, especially for the rolling moment. However, when looking at the total moment magnitude and the angle it makes in the rotor plane, the magnitude of both methods is better represented when compared to the experimental data with an angle shift of 25^o to 35^o for the B-R and ALM respectively. This shift could be explained by the differences between the simplified numerical models and the more complex physical experimental setup. These values represent the reference conditions from which the remaining results in this work will be normalised.

Table 5.3 Rotor performance coefficients OGE $\mu = 0.00$

	Exp.	**B-R**	**Δ**	**ALM**	**Δ**
C_T^{oge}	7.268e-3	7.171e-3	-1.3%	7.193e-3	-1.0%
C_Q^{oge}	7.804e-4	7.714e-4	-1.1%	7.742e-4	-0.8%
FoM^{oge}	0.561	0.557	-0.9%	0.557	-0.8%
C_{Mx}^{oge}/C_Q^{oge}	0.0086	-0.0005	*-105.5%*	0.0004	*95.8%*
C_{My}^{oge}/C_Q^{oge}	-0.0033	-0.0007	*-78.6%*	-0.0014	*-58.9%*

Table 5.4 Rotor performance coefficients OGE $\mu = 0.05$

	Exp.	**B-R**	**Δ**	**ALM**	**Δ**
C_T^{oge}	7.550e-3	7.577e-3	0.4%	7.500e-3	-0.7%
C_Q^{oge}	7.626e-4	7.411e-4	-2.8%	7.596e-4	-0.4%
FoM^{oge}	0.608	0.629	3.5%	0.606	-0.4%
C_{Mx}^{oge}/C_Q^{oge}	-0.143	-0.625	*337.8%*	-0.668	*367.9%*
C_{My}^{oge}/C_Q^{oge}	1.212	0.996	*-17.9%*	0.745	*-38.5%*
C_{Mtot}^{oge}/C_Q^{oge}	1.221	1.176	-3.7%	1.001	-18.0%
$\Psi_{C_{Mtot}}^{oge}$	96.7^o	122.1^o	25.4^o	131.9^o	35.2^o

Hover Validation

With the global performance coefficients of both numerical methods in good agreement with the experimental data, let us now consider a more detailed investigation of the two numerical methods compared to each other. This data is not present in the experimental database of Zagaglia et al. [167], but will serve as a more comprehensive validation of the actuator line method benchmarked against the fully blade resolved computations. The thrust and torque blade loading distributions are presented in Fig. 5.3 for the case in hover with no wind. The two methods are in excellent agreement in the first 80% to 90% of the blade span for both the thrust and torque distributions. Then, at 91.7% the thrust loading curves intersect, which coincides with the radial position of the tip vortex shed from the preceding blade, resulting in a stronger up and down-wash velocity for the ALM and therefore causing the discrepancy observed in terms of thrust loading. This behaviour has previously been observed in [12] due to the porous nature of the source terms used by the ALM. Despite this difference in loading near the tip, once integrated over the span, the difference in thrust and torque coefficients between the two methods corresponds to about 0.3% magnitude.

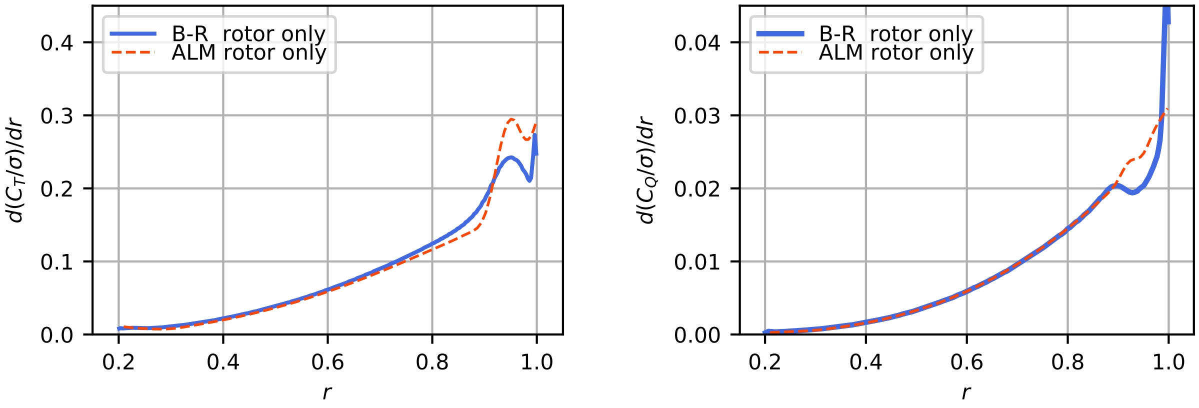

(a) Thrust distribution

(b) Torque distribution

Figure 5.3 Blade loading distribution in hover

Next, the inflow velocity on a plane located 4cm (5.33% D) above the rotor disk, normalised by their respective momentum theory hover-induced velocity V_{ind}^{oge}, is considered. The velocity is sampled on two lines corresponding to the x and y rotor axes and averaged over two full rotor revolutions. Positive x values correspond to the fore part of the helicopter whereas positive y values correspond to the starboard side. Results are presented in Fig. 5.4 for the two cases of hover and advancing flight out-of-ground-effect. In the wind-off case of Fig. 5.4a, the inflow distribution is symmetrical regardless of the axis or direction as expected from the almost nil pitching and rolling moments. From 30% blade span outwards, the two methods produce inflows that are almost identical to each other. In the centre of the rotor disk, the ALM produces a lower inflow than the B-R case due to a slightly weaker root vortex structure and the porous nature of the force. Moving to the wind-on case presented in Fig. 5.4b, the inflow distribution no longer is symmetrical. The addition of incoming wind modifies the flowfield around the rotor by reducing the induced velocity fore of the rotor centre (upwind) whereas it is increased in the aft direction (downwind). This longitudinal asymmetry is consistent with the experimental data presented in [171] and explains the strong positive (nose-up) pitching moment reported in Table 5.4 as a reduction in inflow velocity increases the effective angle of attack experienced by the blade in the fore position. Consequently, the thrust of this section will be larger and create the nose-up pitching moment. A similar inflow curve has also been experimentally measured by Taymourtash et al. [147] on the same helicopter model in similar operating conditions again with an associated strong nose-up pitching moment. Laterally, the counter-clockwise rotation of the rotor (viewed from the top) causes the advancing blade on the starboard side to see a greater freestream velocity, and therefore greater thrust, than on the port side. This lateral thrust imbalance causes the negative rolling moment towards the port side which in turn causes a larger inflow magnitude on the starboard side (advancing blade) of the rotor.

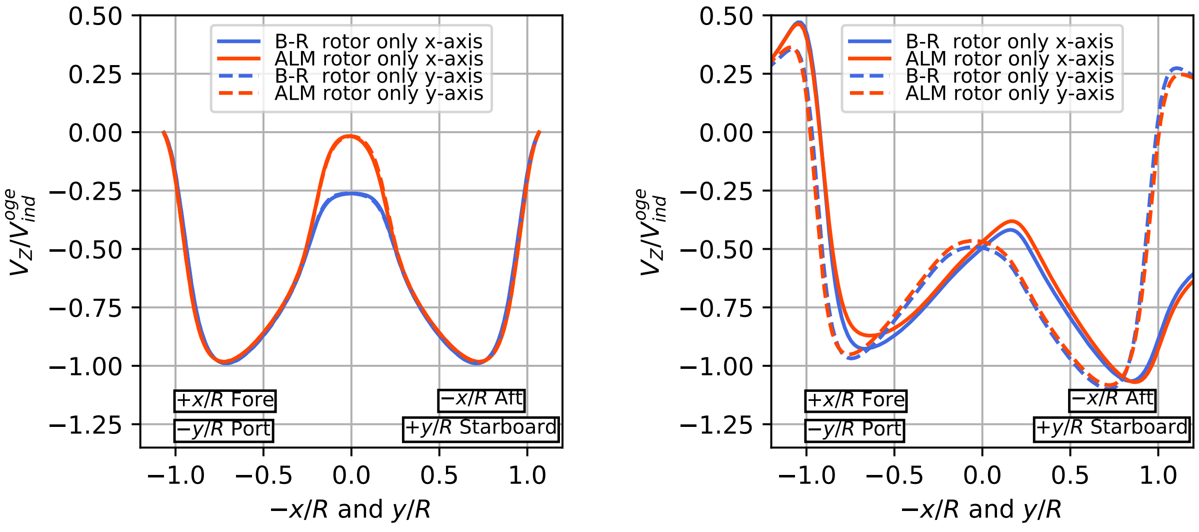

(a) $\mu = 0.00$

(b) $\mu = 0.05$

Figure 5.4 Inflow velocity along x and y axes 4cm above rotor disk

Figure 5.5 presents the tip vortex positions of the two methods averaged over their respective four rotor blades over 1.5 rotor revolutions in wake age. In addition, the empirical model of Kocurek and Tangler [30] is added for reference purposes. The curves at the top of the figure represent the radial contraction of the wake whereas the ones at the bottom are the axial advection of the tip vortices. Both methods are in excellent agreement with each other and the empirical model. The ALM tends to produce a wake that is ever so slightly more outboard than the B-R solution. Both methods experience some increased scattering in the positions of their tip vortices past 360^o of wake age which is due to the degradation of the wake attributed to the dissipative nature of the employed mesh and numerical method.

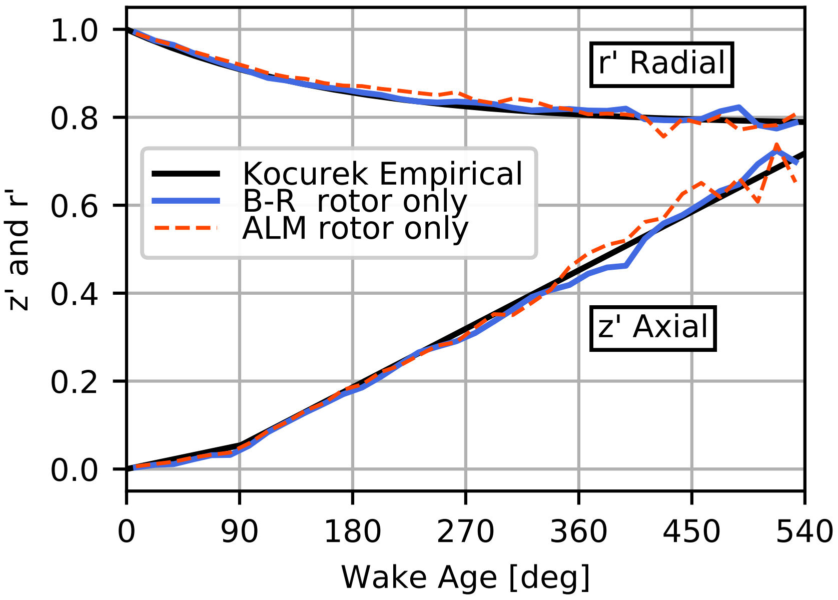

Figure 5.5 Tip vortex trajectories in hover OGE

Fuselage Effects

The experimental model featured a fuselage which, amongst other geometric features, has been neglected thus far in the simulations. The effects of the fuselage and the hub cover on the measured rotor loads are thus assessed in Table 5.5. In the wind-off case, the addition of the fuselage and hub cover slightly improve the thrust prediction of both methods when compared to the experimental data. However, the torque predictions for the B-R simulation is slightly degraded with an excess of torque which in turn causes a larger FoM error. The ALM on the other hand produces more consistent results with marginal errors. Both methods see their moment coefficients increase being on the order of 1% to 2% of the torque value which is more representative of the experimental roll moment, but too large for the pitching moment. Again, the relative errors are large due to the small value of the experimental data upon which they are normalised. For the wind-on case, a similar trend is present with an increase in both thrust and torque coefficient compared to the rotor only case. The moment coefficients do not show significant change for both numerical methods when considering the total moment coefficient and its relative angle. The ALM simulation once again shows less sensitivity to the inclusion of the fuselage and produces slightly better overall integrated results. Nevertheless, both methods are very close to the experimental data and comparable to the rotor only case.

Table 5.5 Rotor performance coefficients with fuselage

	$\mu = 0.00$				$\mu = 0.05$			
	B-R	Δ	**ALM**	Δ	**B-R**	Δ	**ALM**	Δ
C_T^{oge}	7.235E-3	-0.5%	7.268E-3	0.0%	7.679E-3	1.7%	7.533E-3	-0.2%
C_Q^{oge}	7.908E-4	1.3%	7.790E-4	-0.2%	7.662E-4	0.5%	7.613E-4	-0.2%
FoM^{oge}	0.550	-2.0%	0.562	0.2%	0.621	2.1%	0.608	0.0%
C_{Mx}^{oge}/C_Q^{oge}	0.0092	*7.1%*	0.0112	*30.5%*	-0.603	*322.5%*	-0.658	*360.7%*
C_{My}^{oge}/C_Q^{oge}	-0.0280	*747.9.7%*	-0.0173	*424.1%*	0.969	*-20.1%*	0.755	*-37.7%*
C_{Mtot}^{oge}/C_Q^{oge}	-	-	-	-	1.142	-6.5%	1.002	-18.0%
$\Psi_{C_{Mtot}}^{oge}$	-	-	-	-	121.9^o	25.2^o	131.1^o	34.3^o

The addition of the fuselage modifies the inflow distribution of both methods as shown in Fig. 5.6. In the wind off case, there is a clear asymmetry present, most noticeable near the rotor centre and the aft direction on the x-axis due to the tail boom geometry present in the area. The addition of the fuselage, and more specifically the rotor hub cover, negates the tendency of the ALM inflow near the centre to be underestimated compared to the B-R solution. With the presence of wind, the two methods see their distribution slightly modified compared with the rotor only case with most of the differences present near the centre for both axes and in the fore direction of the x-axis. The addition of the fuselage increases the agreement, in terms of overall inflow, between the two numerical methods along both axes in both wind conditions.

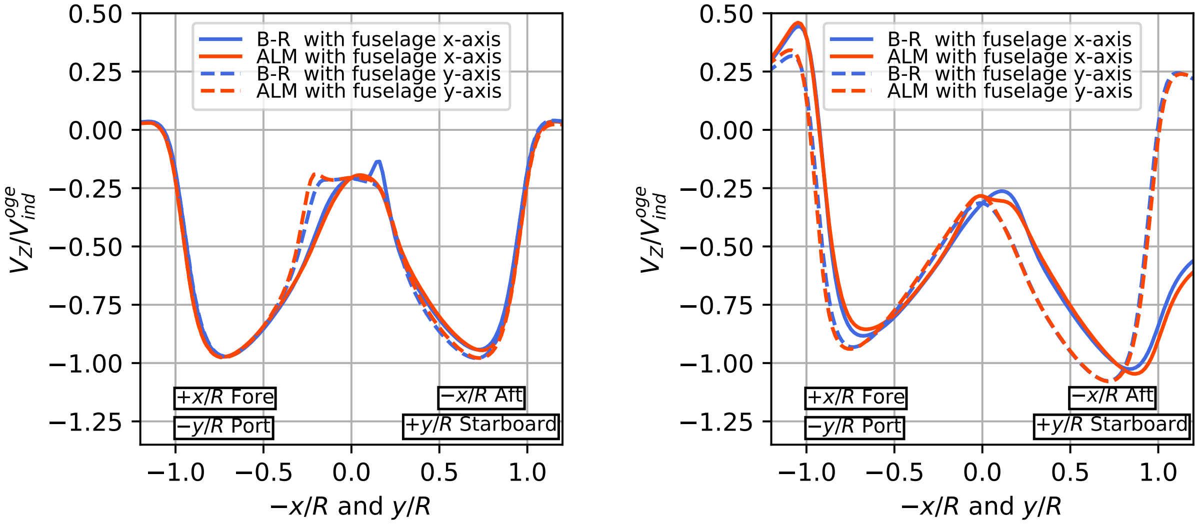

(a) $\mu = 0.00$

(b) $\mu = 0.05$

Figure 5.6 Inflow velocity along x and y axes 4cm above rotor disk with fuselage

The average pressure coefficient, normalised by the hover induced velocity, on the fuselage top centre-line is presented in Fig. 5.7. For their respective wind condition, the two methods show similar predictions with some portions of the pressure profiles being indistinguishable from each other. In the wind-off case, there is a marked influence of the rotor induced velocity on the tail boom culminating in a sharp increase in pressure coefficient at around 85% blade span which coincides with the position of the tip vortex. Adding wind skews the wake in the aft direction making both fore and aft tip vortices flow around the nose of the fuselage and the tip of the tail boom respectively. The increased pressure coefficient over the nose of the fuselage comes from the outboard section of the rotor induced velocity of the skewed wake. The tail boom receives an induced velocity more evenly distributed from the aft section of the rotor.

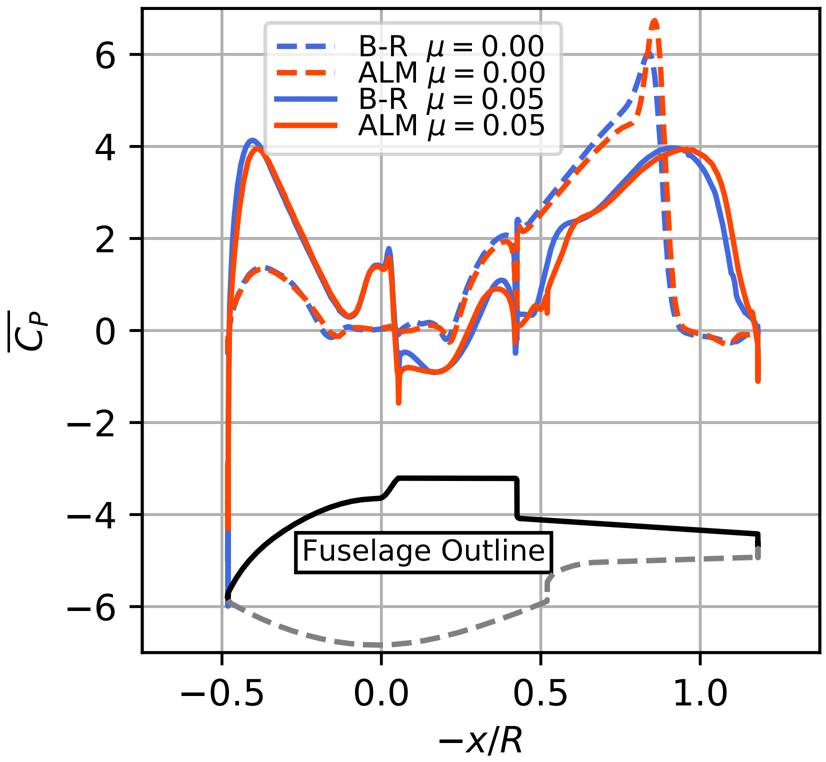

Figure 5.7 Average pressure coefficient along fuselage top centre-line

Figure 5.8 presents the surface pressure coefficient over the whole fuselage with a translucent Q-criterion representation of the tip vortex wake. In addition to the aforementioned observations, we can observe a slight asymmetry between the starboard and port side of the fuselage due to the counterclockwise rotation of the rotor. Most notably, the peak pressure coefficient near the nose is shifted slightly over the starboard side.

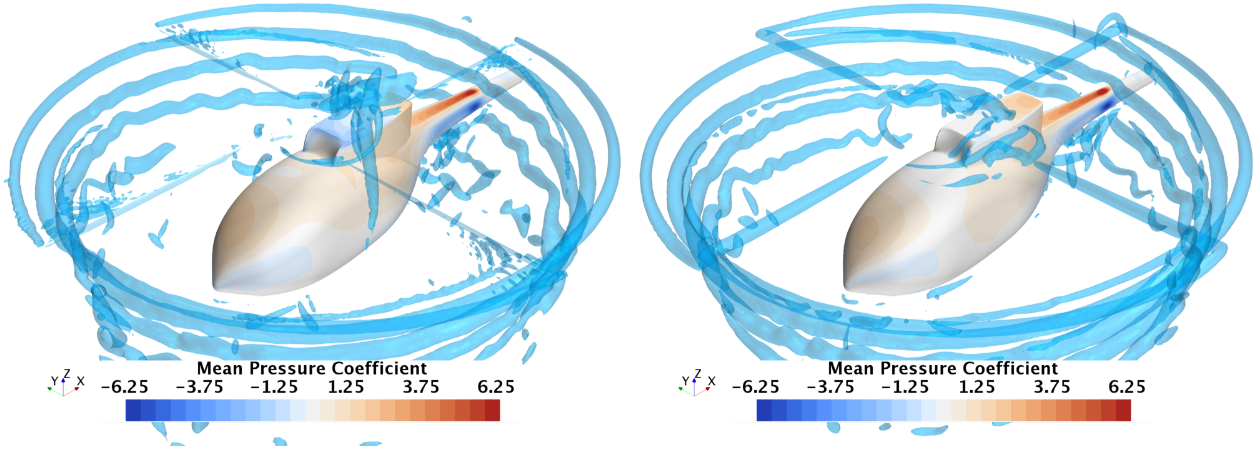

(a) B-R OGE $\mu = 0.00$ (b) ALM OGE $\mu = 0.00$

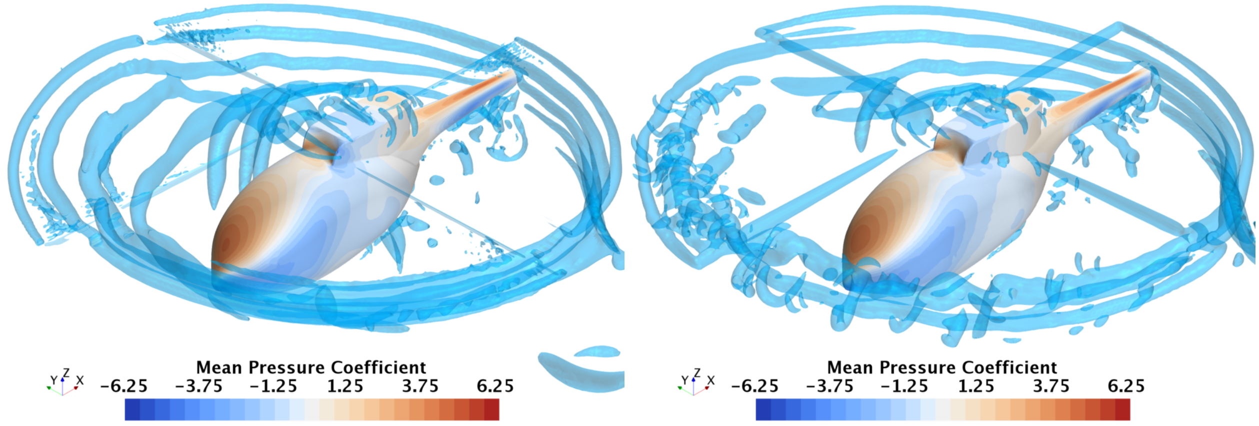

(c) B-R OGE $\mu = 0.05$ (d) ALM OGE $\mu = 0.05$

Figure 5.8 Average surface pressure coefficient and Q-criterion contour at Q=75000

5.4.2 In-Ground-Effect - No Obstacle

Hovering

In the experimental dataset [167], the ground effect in hover without the obstacle of the model scale helicopter is evaluated in Test 0 $\mu = 0.00$. Results are presented in Fig. 5.9 for the ALM, B-R and experimental data. Due to their high computational costs, the numerical methods are evaluated at only 3 heights corresponding to $Z/R = \{4.0, 2.0, 1.0\}$ with the highest corresponding to the reference OGE condition. The same plots as the original article are used with a preference to showcase the torque coefficient ratio instead of the figure of merit ratio. The FoM is dominated by the variation of the thrust and would yield an almost identical graph as the thrust ratio with a different scale. Therefore, both the thrust and torque coefficients of the helicopter rotor are normalised by their respective OGE values presented in Section 5.4.1 whereas the moment coefficient is presented as a difference to the OGE condition, normalised by the torque coefficient $(C_M - C_M^{oge})/C_Q^{oge}$. For this case, the thrust presented in Fig. 5.9a sees an increase related to the ground effect from $Z/R = 3.0$ for the experimental data whereas the computed points at $Z/R = 2.0$ also indicate a thrust increase for both methods that are more in line with the empirical model of Cheeseman and Bennett [172]. Decreasing the height to $Z/R = 1.0$ all data showcase a sharp rise in thrust as ground effect becomes more prevalent. The B-R and ALM solutions still slightly underpredict the thrust ratio by about 4% when compared to the experimental data whereas the Cheeseman model is lower by an additional 4%. It should be noted that the empirical model was derived from an assumption of constant power, which is not the present case. Overall, both numerical methods tend to underestimate the thrust coefficient rise when compared to the experimental data which has already been observed numerically by Gibertini et al. [173] in the case of an Actuator Disk model and Schmid [174] for an Unsteady Panel Method on the same geometry. The torque presented in Fig. 5.9b also presents an increase as the rotor is lowered with the two numerical methods also well capturing the trend and lying within the error bars of the experimental data. A similarly good agreement of the torque coefficient ratio was also found in Refs. [173, 174] although their assessment of C_Q^{oge} was not as precise as the one in this work.

The moment coefficients in both the rotor x and y-axis are presented in Fig. 5.9c where little variations are present for all cases. Moments corresponding to about 2-4% of C_Q^{oge} are present for the numerical methods at $Z/R = 1.0$ caused by a less stable wake topology of the root vortices present in-ground-effect causing asymmetry in the flowfield in particular near the rotor centre with a fountain-like effect causing unsteady upward velocities.

Figure 5.10 presents an open view of the tip-vortex wake topology and the instantaneous axial velocity in the X-Z plane. The two methods appear to be in excellent agreement both in terms of wake topology and axial velocity for a height of $Z/R = 4$. Close to the ground at $Z/R = 1$, the two methods produce a similar tip vortex wake topology in the outboard section of the rotor. However, the B-R produces a more constant downwash profile, especially near the rotor blade root. The resulting upward jet-like effect at the rotor centre is also stronger for the B-R case.

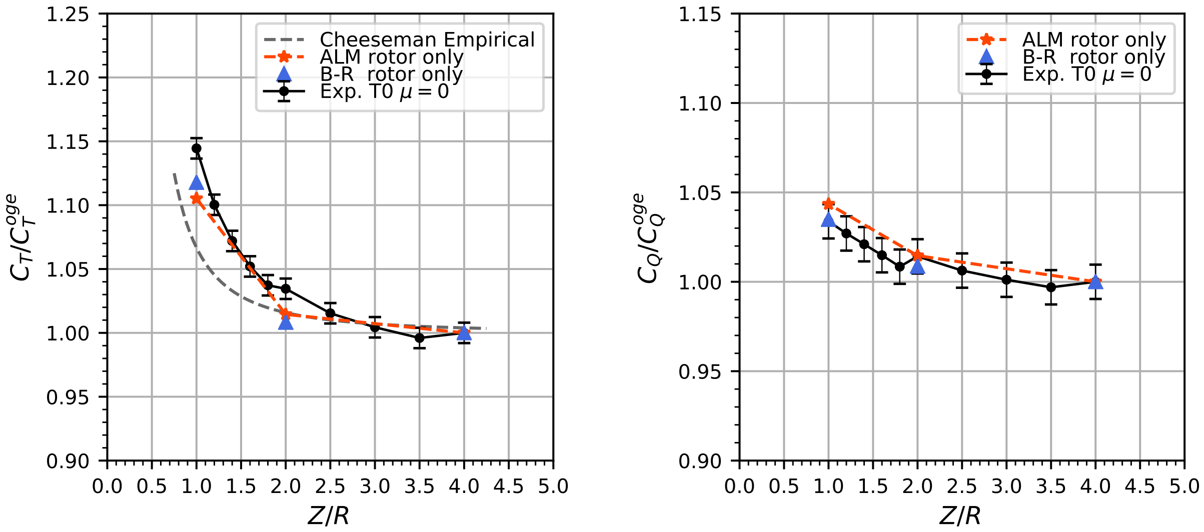

(a) Thrust coefficient ratio

(b) Torque coefficient ratio

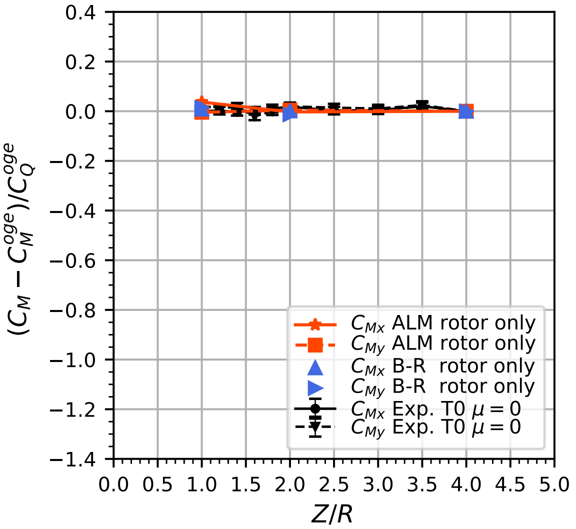

(c) Moment coefficients variation

Figure 5.9 Helicopter in IGE ($\mu = 0.00$) - performance coefficients comparison

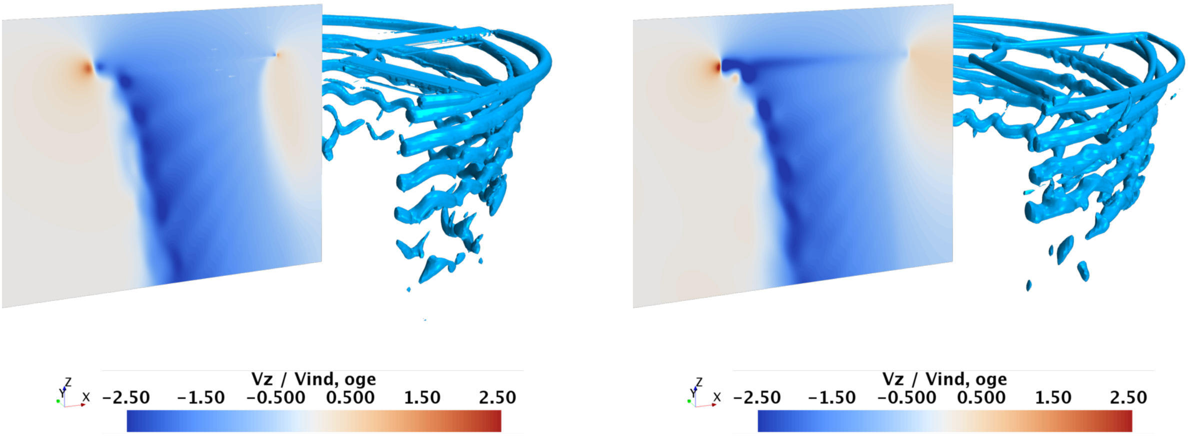

(a) B-R T0 $\mu = 0.00$ $Z/R = 4$ (b) ALM T0 $\mu = 0.00$ $Z/R = 4$

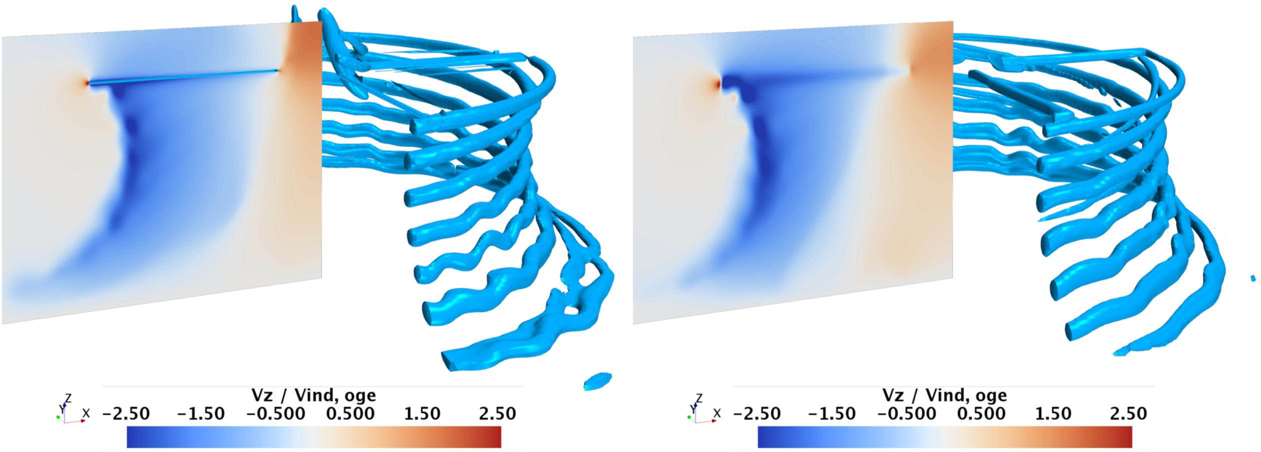

(c) B-R T0 $\mu = 0.00$ $Z/R = 1$ (d) ALM T0 $\mu = 0.00$ $Z/R = 1$

Figure 5.10 Instantaneous axial velocity and Q-criterion contour at Q=25000

Advancing Flight

As observed in Fig. 5.11, the presence of wind in-ground-effect delays the increase in thrust and torque coefficients observed in the previous section to rotor heights closer to the ground. The ALM captures well the slight thrust increase present at $Z/R = 2.0$, but underestimates the thrust value at $Z/R = 1.0$. An additional simulation with the fuselage geometry modelled is performed and improves the underestimated thrust to be more in-line with the Cheeseman and Bennett model as well as the B-R simulations (with and without the fuselage). The B-R solutions also underestimate the thrust ratio compared to the experimental data, but are in line with the empirical model and show less sensitivity to the addition of the fuselage in this case by reducing slightly the predicted thrust ratio. The torque coefficient ratio augmentation is again well captured with the rotor-only ALM despite the thrust coefficient ratio underprediction. The other B-R and ALM simulations are also in fair agreement with values just below the experimental error bars. Looking at the moment coefficients in Fig. 5.11c, the negative difference in rolling moment compared to the OGE reference condition for the experimental data indicates an increase in the value as the reference is already negative. All the simulations predict a near-constant value with a small positive increase in the difference, thus a slight reduction compared to the OGE moment. The dominant pitching moment has a negative variation with its OGE value which translates to a reduction of its magnitude as the rotor is brought closer to the ground. The numerical methods in this case have their predictions forecasting the right trend, but experience more scatter. The addition of a fuselage has the effect of slightly diminishing the pitching moment reduction trend.

Figure 5.12 presents a qualitative assessment of the wakes for both methods. In OGE conditions depicted in Figs. 5.12a and 5.12b, the two methods produced near-identical wake structures with the typical flatten appearance and tip vortex roll-up into trailing supervortices. At $Z/R = 1$, we can observe the formation of a lingering ground vortex slightly upstream of the intersection of fore part of the skewed wake and the ground. This regime corresponds to the “ground vortex regime" identified by Brown and Whitehouse [159] at an identical rotor height above the ground and similar thrust normalised advance ratio. Their observations also suggest that this horseshoe-shaped ground vortex is less stable over the retreating blade region which is most noticeable for the ALM as illustrated in Fig. 5.12d.

Although indicative of the performances of the rotor in terms of roll and pitch attitude, Fig. 5.11c does not correctly take into account the relative magnitude between the two moments and the offset between the experimental data and the simulations in OGE conditions reported in Section 5.4.1. A more insightful way of looking at the data is to compare the relative change of the total moment coefficient to its OGE reference value and the shift in its orientation. Figure 5.13a presents a polar plot of the total moment relative magnitude and its orientation. Experimental data, B-R and the ALM results are presented in tones of grey, blue and orange respectively. The bolder/darker colours represent OGE conditions whereas the lighter tone gradient represents a rotor reducing its distance from the ground. To reduce clutter on the graphs, the rotor-only B-R and ALM simulations are presented. In all cases, a similar trend is observed for the reduction in total moment magnitude and shift in orientation across the simulated height range. Note that the polar plot moment at $Z/R = 2.0$ is indistinguishable from the OGE value as the ground effect does not yet play a major role at that height. Figure 5.13b presents the numerical values of the moment ratio reduction and the orientation shift of the total moment with respect to the OGE condition. Both numerical methods correctly capture the overall trend accurately with a total moment reduction ratio of about 70% of the OGE value and orientation shift around 15^o.

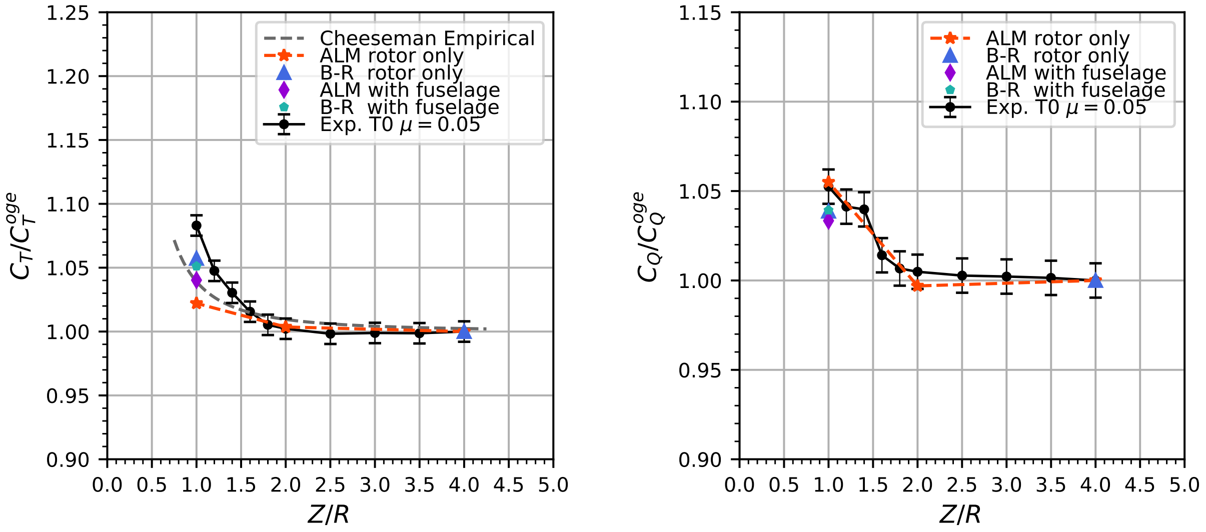

(a) Thrust coefficient ratio (b) Torque coefficient ratio

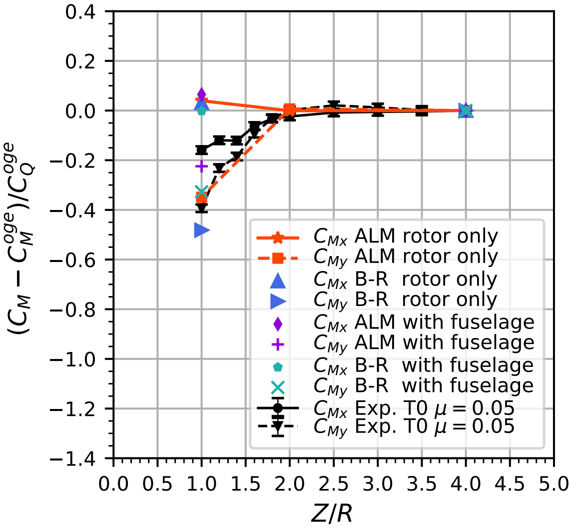

(c) Moment coefficients variation

Figure 5.11 Helicopter in IGE ($\mu = 0.05$) - performance coefficients comparison

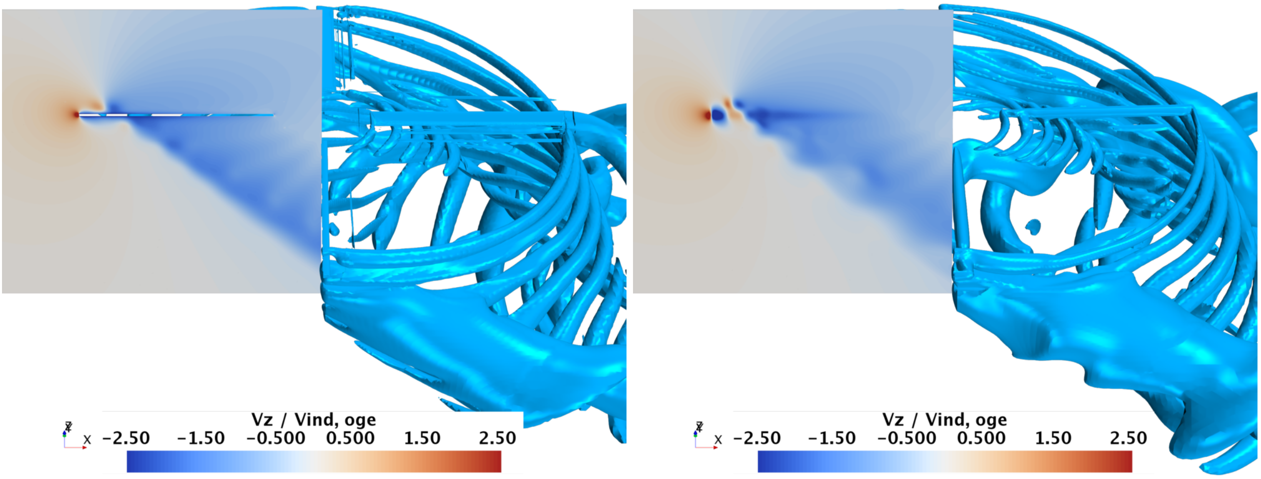

(a) B-R T0 $\mu = 0.05$ $Z/R = 4$ (b) ALM T0 $\mu = 0.05$ $Z/R = 4$

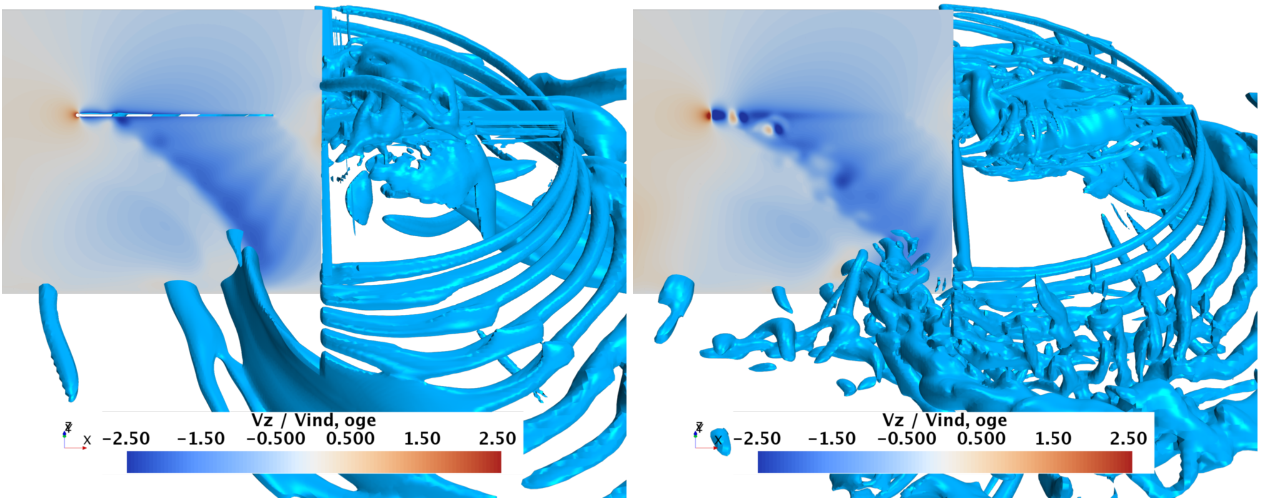

(c) B-R T0 $\mu = 0.05$ $Z/R = 1$ (d) ALM T0 $\mu = 0.05$ $Z/R = 1$

Figure 5.12 Instantaneous axial velocity and Q-criterion contour at Q=7500

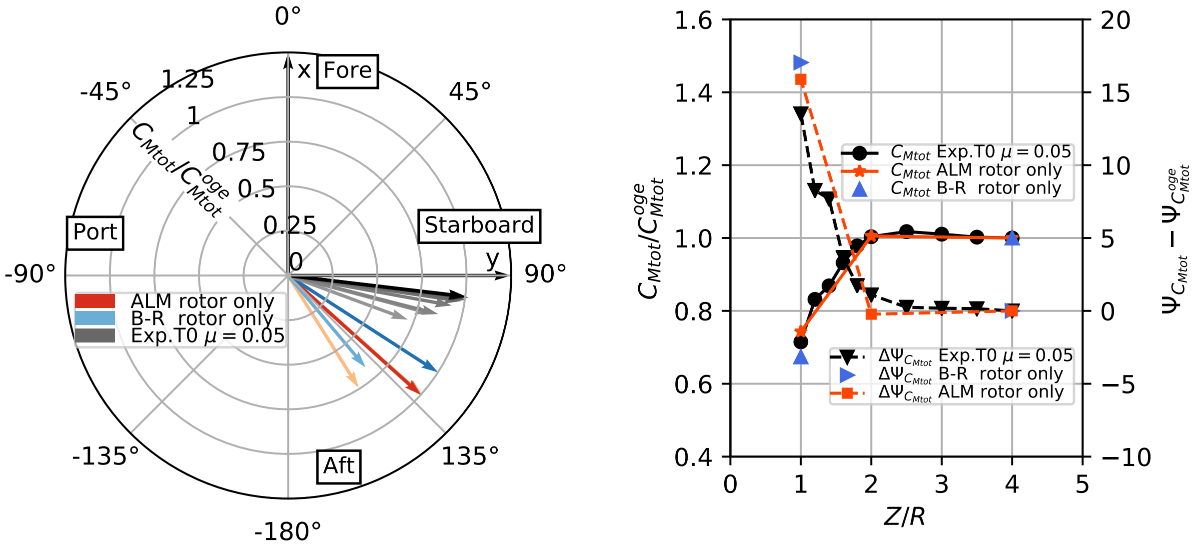

(a) Total moment coefficient ratio polar plot

(b) Total moment coefficient ratio and orientation shift

Figure 5.13 Helicopter in IGE $\mu = 0.05$ - total moment coefficient ratio and phase

5.4.3 In-Ground-Effect - With Obstacle

Hovering

The prismatic obstacle is added fore of the helicopter rotor, with the latter centred along the width of the obstacle, at a horizontal distance of $2R$ downstream. This configuration corresponds to Test 3 in the experimental database which features a sweep in the Z axis to evaluate the ground effect. Numerical results are computed at rotor heights of $Z/R = \{4.2, 2.7, 1.45, 1.0\}$ corresponding to experimental datapoints that showcased the largest variations. Both numerical methods consider the rotor-only configuration. Results are presented in Fig. 5.14. According to the experimental data, this configuration features a flow re-circulation region initiated by the ground and then the vertical wall of the obstacle streaming the rotor downwash upwards that is then re-ingested by the rotor as shown in Fig. 5.15. The flow re-circulation is most present and well-defined for rotor heights $Z/R \leq 1.5$ and causes a significant reduction in thrust in-ground-effect compared to the No-Obstacle case as observed in Fig. 5.14a.

As the re-circulation is asymmetrical and is mostly present fore of the rotor, the increased inflow creates a local deficit in thrust which in turn becomes the observed nose-down pitching moment as explained in [167] and illustrated in Fig. 5.14c. These two values are well captured by the numerical methods for heights near the ground. In that region, the torque coefficient shows a consistent trend with the experimental data, but is slightly over-estimated, in particular for the blade resolved case. For heights $Z/R \geq 1.5$, the two numerical methods show very low variation when compared to the no obstacle case presented in Section 5.4.2 whereas the experimental data features a noted lower thrust and torque and the presence of both rolling and pitching moment on the order of 15% to 20% of C_Q^{oge} even when it is positioned at the maximum height of $Z/R = 4.2$. The presence of roll and pitch moments is probably due to a more complex re-circulation pattern that reaches and interacts with the rotor despite the significant height. As the experiment was run for a total of 15 seconds (10s flow stabilisation followed by 5s data acquisition) which corresponds to a total of 645 rotor revolutions, we believe this flowfield is initiated over a much longer time period than the current simulation framework allows. The present simulations are run up to 75 to 100 revolutions until they are stopped due to excessive computational resources requirements of U-RANS based methods. The fully developed wakes of the simulations are represented in Fig. 5.15 where there is a clear re-circulation region that interacts with the rotor inflow for heights $Z/R \leq 1.5$ whereas for higher heights, the upward velocity region of the re-circulation is still located below the rotor disk and is not re-ingested by the rotor. The simulations at the higher heights are therefore stopped at about 75 revolutions as the rotor loading signals showed minimal or no variations with respect to OGE conditions. For reference, 75 revolutions corresponds to compute times of 9.27 days on 560 CPU cores for the B-R case whereas the ALM would require 4.6 days on the same amount of CPU cores. Reaching the full 675 revolutions as is done in the experiment would require a 9x increase in computational resources per data point which are already substantial.

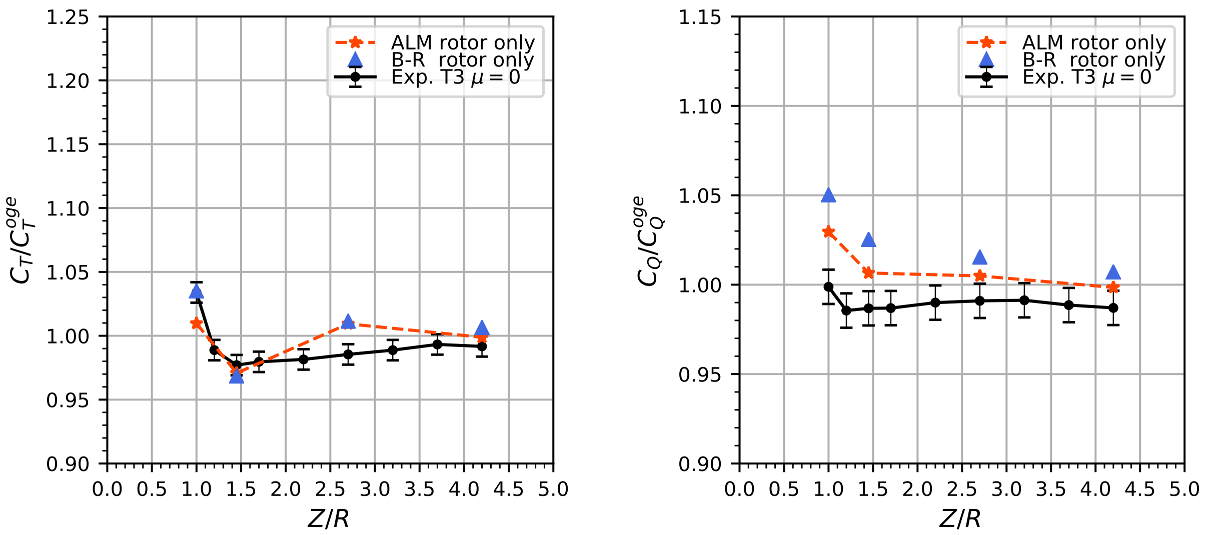

(a) Thrust coefficient ratio

(b) Torque coefficient ratio

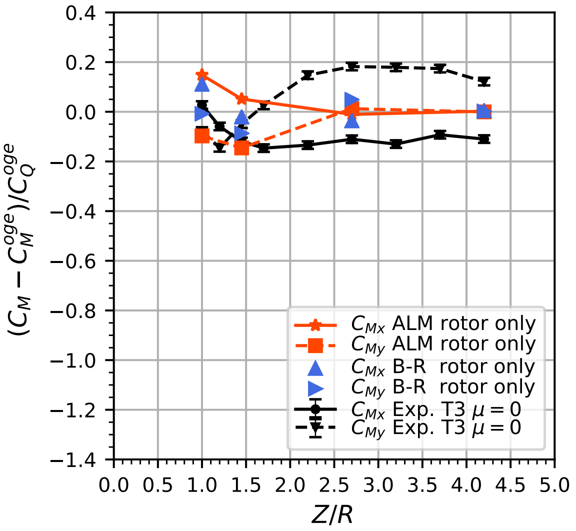

(c) Moment coefficients variation

Figure 5.14 Helicopter in IGE ($\mu = 0.00$) behind obstacle - performance coefficients comparison

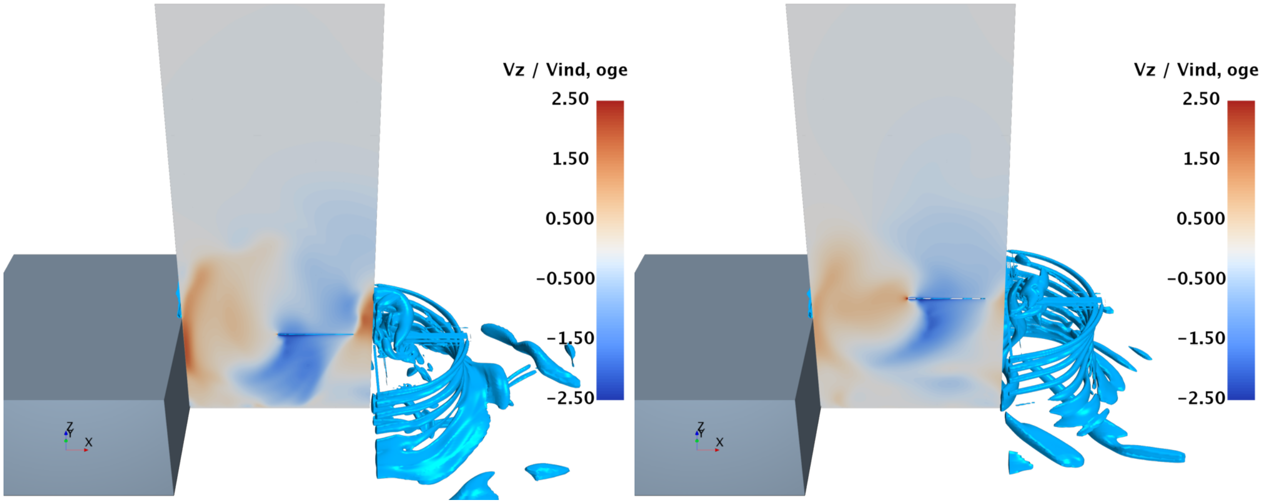

(a) B-R T3 $\mu = 0.00$ $Z/R = 1.00$ (b) B-R T3 $\mu = 0.00$ $Z/R = 1.45$

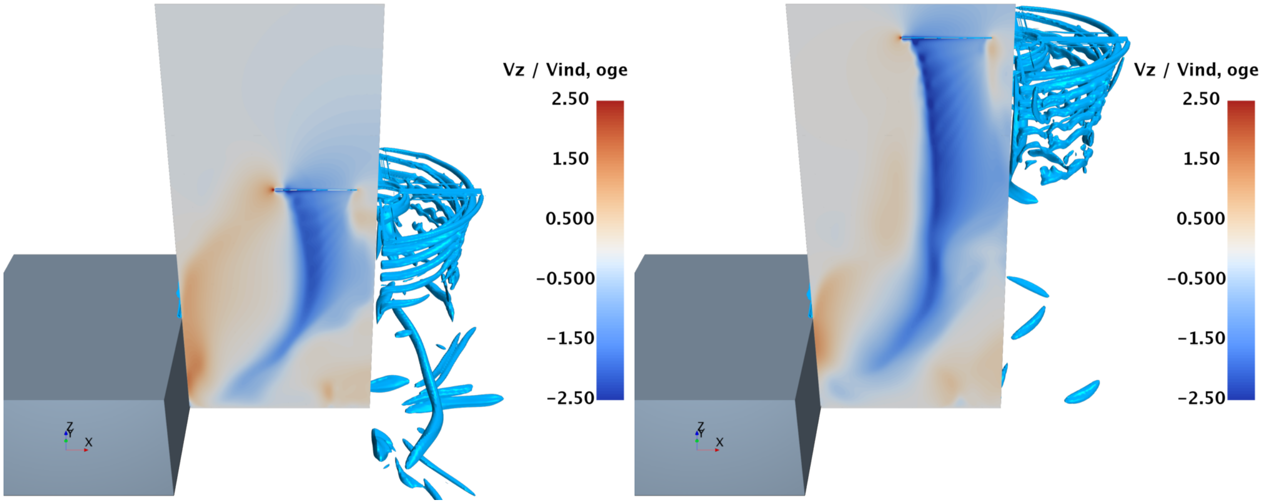

(c) B-R T3 $\mu = 0.00$ $Z/R = 2.70$ (d) B-R T3 $\mu = 0.00$ $Z/R = 4.20$

Figure 5.15 Instantaneous axial velocity and Q-criterion contour at Q=7500

In the Presence of Wind

Adding wind, the rotor is now placed in the wake of the obstacle. Due to the strong wake unsteadiness of the bluff body, an additional flow stabilisation period is simulated for 10s at a larger time step of 0.01s with only the obstacle modelled and the rotor removed from the simulation. The added simulation time allows a fully developed wake to form downstream of the obstacle where the rotor is then placed. For this configuration, only the ALM is considered due to the high computational resources required as the simulations are again run up to 100 revolutions. Performance coefficients are presented in Fig. 5.16. Contrary to the wind-off case presented in Section 5.4.3, the two points simulated above $Z/R = 2.0$ correctly represent the experimental data. In this case, there is less influence coming from the rotor-induced recirculating wake as the freestream and the obstacle wake dominate and transport the rotor wake downstream before it has a chance to re-circulate into the rotor. The flowfield is represented in Fig. 5.17, with the addition of line integral convolution, where the rotor at $Z/R = 2.70$ is positioned at the edge of the obstacle separated wake. The rotor at $Z/R = 4.20$ is positioned well above this region and is essentially subject to freestream conditions. Then, for heights $Z/R \leq 1.5$, the rotor is inside the detached wake of the obstacle which acts as a shield from the freestream for the rotor. As the rotor is brought closer to the ground, there is a decrease in thrust and a sharp drop in pitching moment that the ALM correctly captures when compared to the experimental data. This behaviour is explained by the formation of a rotor-induced re-circulation region similar to the wind-off case and illustrated in Figs. 5.17a and 5.17b. Although the variation of C_{Mx} of the experimental data and the ALM might seem to diverge in Fig. 5.16c, the two tend towards a similar value of $C_{Mx}/C_Q^{oge} = 0.25$ to 0.3 as the rotor height is lowered. The diverging trend is caused by the different OGE values reported previously. Finally, the moments are presented on a polar plot and in terms of ratio and orientation shift in Fig. 5.18. Again, the numerical method correctly captures the trends and the magnitudes of the total moment ratio reduction and the orientation shift.

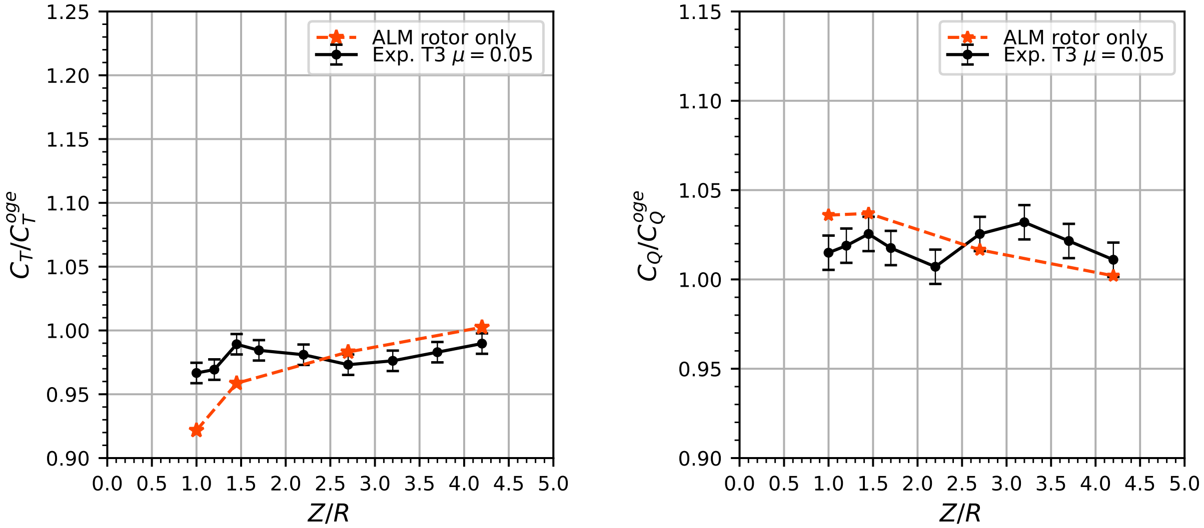

(a) Thrust coefficient ratio

(b) Torque coefficient ratio

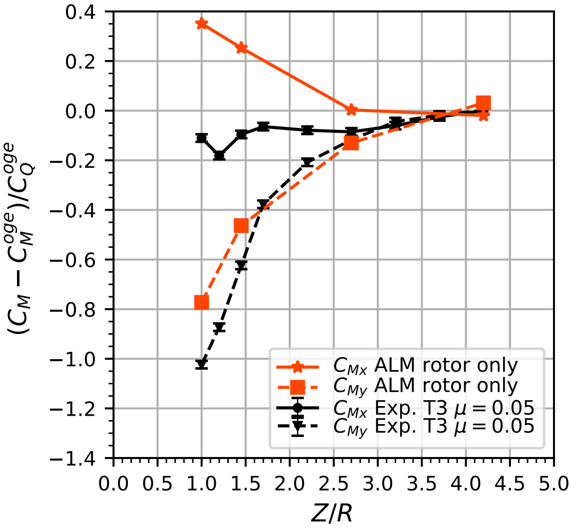

(c) Moment coefficients variation

Figure 5.16 Helicopter in IGE ($\mu = 0.05$) behind obstacle - performance coefficients comparison

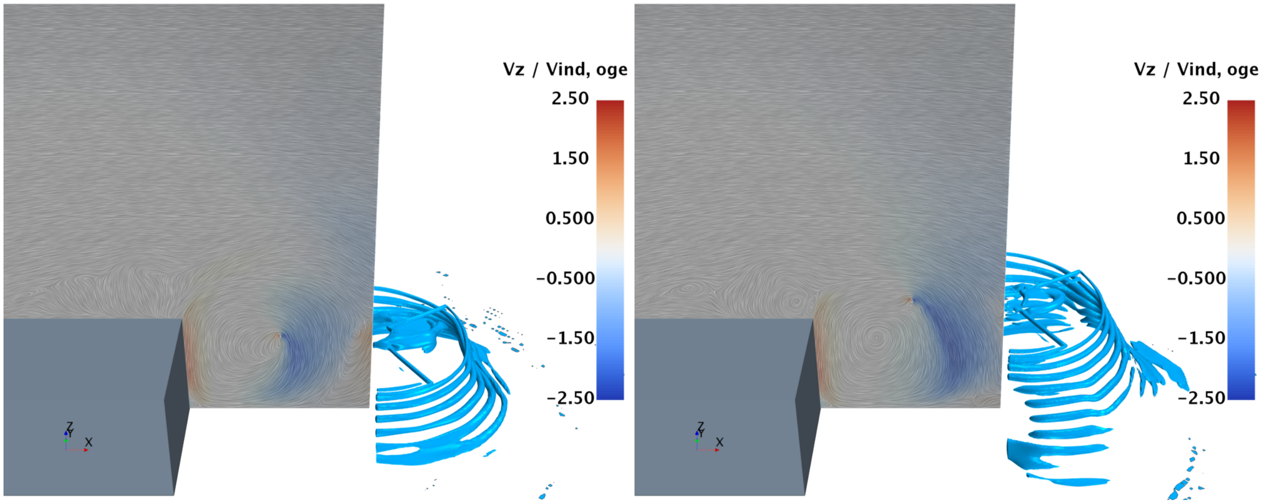

(a) ALM T3 $\mu = 0.05$ $Z/R = 1.00$

(b) ALM T3 $\mu = 0.05$ $Z/R = 1.45$

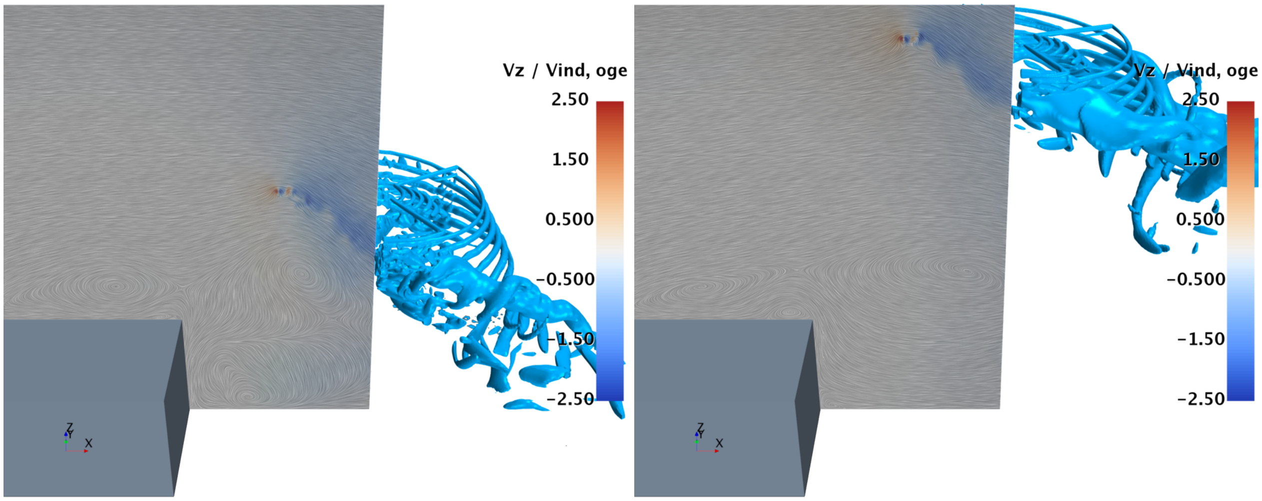

(c) ALM T3 $\mu = 0.05$ $Z/R = 2.70$

(d) ALM T3 $\mu = 0.05$ $Z/R = 4.20$

Figure 5.17 Instantaneous axial velocity with total velocity vector superimposed through line integral convolution and Q-criterion contour at Q=7500

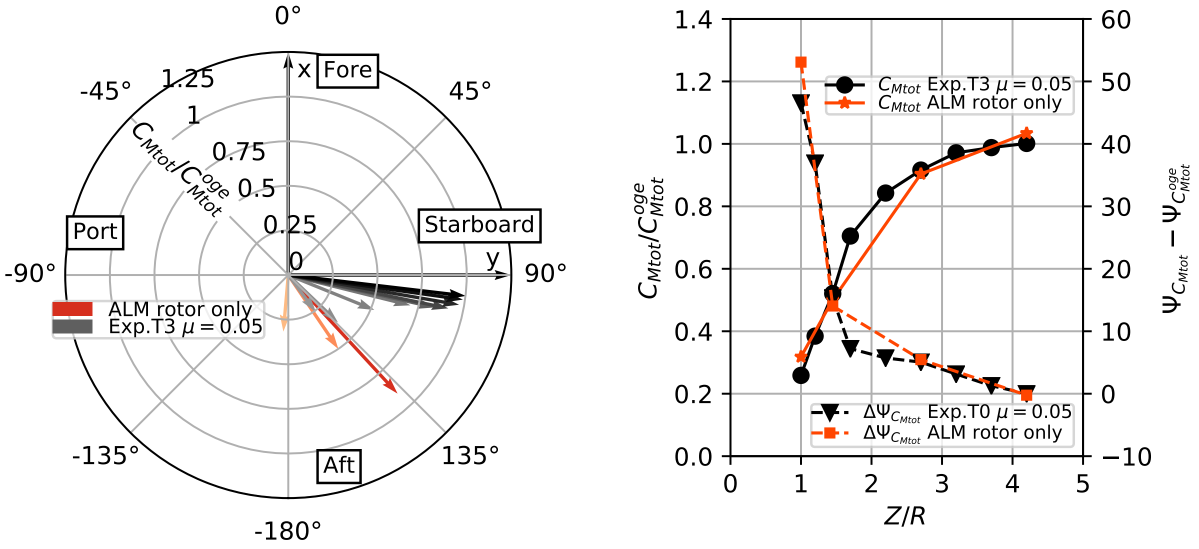

(a) Total moment coefficient ratio polar plot

(b) Total moment coefficient ratio and orientation shift

Figure 5.18 Helicopter in IGE ($\mu = 0.05$) behind obstacle - total moment coefficient ratio and phase

5.5 Conclusions

In this work, high fidelity CFD tools are used to assess their efficacy for the computation of a rotor in confined areas. Through a recently published experimental dataset, several key challenging helicopter flight conditions in ground effect including hovering, in forward flight, in the presence of a low-rise obstacle with and without the influence of wind are studied. Both fully Blade Resolved simulations and the Actuator Line Method are used as numerical methods and are benchmarked against each other. The principal conclusions are:

- Outside of ground effect, the two numerical methods accurately predict the main rotor coefficients with the exception of the moments, most notably the rolling moment, when compared to experimental data. Between them, the agreement of the ALM and B-R solutions over performance coefficients, blade loading, wake geometry, inflow and surface pressure coefficients are excellent.

- Through the reduction in mesh size from the removal of the rotor geometry, the ALM requires less computational resources than the B-R. For the present rotor geometry and test cases, the computational cost of an ALM simulation is about half of a B-R case and is directly proportional to the total mesh cell count.

- Hovering in-ground-effect, the two methods correctly capture the trends of the experimental data with a slight under-prediction of thrust whereas the torque and both moments are accurately captured.

- For the advancing flight case in-ground-effect, a similar trend is present as the thrust in-ground-effect is under-predicted and the torque increase is well captured. Accounting for the mismatch in rolling and pitching moments in OGE conditions, the variation in total moment magnitude ratio and orientation shift is well captured.

- The addition of an obstacle for a hovering rotor causes flow re-circulation that is captured for rotors placed near the ground. Simulations with rotors placed higher could not achieve a sufficiently developed flowfield for the given computational resources and therefore did not accurately capture a proper behaviour in terms of thrust and moments.

- The presence of wind with the ground obstacle is well captured overall, however, thrust is under-predicted for rotors placed near the ground.

CHAPTER 6 GENERAL DISCUSSION

6.1 Modelling

To address the ambiguities in terms of velocity sampling and Gaussian kernel width distribution the ALM presents, Chapter 2 performs a parametric study on a simplified 2D ALM model followed by an extension to a simple 3D finite aspect ratio wing. This chapter also serves to bridge the gap in terms of modelling adaptation for an ALM to be suitable for helicopter rotor simulations and not only for wind turbines with a focus on near-field flow-field performances and blade loading. First, some baseline is established in terms of mesh requirement for converged results with a dependency on both the Gaussian smearing width ϵ and the mesh cell size Δ_g. However, as some researchers pointed out in the past, ϵ also has a physical significance in terms of flow allure in the near-field of the force. In accordance with previous research, a chord-scaled value of $\epsilon/c \approx 0.25$ produces adequate flowfield results in 2D which is observed in the developed framework. In terms of velocity sampling, the main techniques are tested against each other with the integral velocity sampling proving superior both in terms of performances, and framework integration. However, simulations with extremely high drag, very low Reynolds numbers and considerable compressible effects all degrade the velocity sampling for all methods. The extension for finite aspect ratio wings shows the applicability of the conclusions obtained in 2D to a more realistic case. Again, $\epsilon/c \approx 0.25$, and in particular the novel truncated Gaussian kernel detailed later in Chapter 3, along with the integral velocity sampling showed superior performances in terms of wing span loading and general flowfield agreement. However, there persists a wing loading overestimation near the tip due to inaccurate near-range tip vortex induced downwash when compared to a fully resolved simulation.

Chapter 3 studies the ALM model in hovering conditions. The ALM is benchmarked against an equivalent fully blade resolved simulation on near-identical solvers and meshes therefore offering a fair comparison between the two methods on a model accuracy standpoint. Two novel improvements of the method are properly introduced as the hyperbolic tangent spanwise distribution and the truncated and normalized Gaussian kernel distribution.

The former allows a more gradual and controllable ALM segment discretization along the blade/wing span with a tip refinement suitable for rotor flows which typically see most of the loading variation in the last 15% of the blade span. The distribution allows an economy on the number of ALM points when compared to a constant linear distribution. In addition, the *tanh* discretization provides a less aggressive tip refinement and root coarsening than a cosine distribution.

The latter has already been discussed and used at the end of Chapter 2 and showed much improved lift distribution in the tip region with an ever-present over-prediction, however. In hover, the over-prediction is overshadowed by the presence of a perpendicular BVI trailing from the preceding blade tip-vortex. Due to its porous nature, the ALM does not handle the interaction adequately when compared to the B-R reference which ends up in an over-estimation of the vortex-induced velocity causing greater up and down-wash on each side of the BVI location point. This results in lower and higher thrust loading on each side of the BVI that eventually averages out when the global thrust coefficient is integrated. The torque coefficient presents an overestimation of induced drag mainly present in the outboard-most section of the blade span after the BVI. This is caused by the over-prediction of thrust in that particular region.

The Gaussian width is also studied on the hovering case with the general tendency observed in the fixed wing application being maintained in terms of tip thrust (or lift for the fixed wing) loading. Values near $\epsilon/c \approx 0.25$ better predict the tip loading behaviour whereas higher ϵ values do not show the characteristic tendency of a diminishing circulation nearing the tip. This is caused in part by the tendency of larger $\epsilon/c \geq 0.5$ values to produce different tip vortex wake characteristics with, notably, larger vortex core radius. Ultimately, this results in $\epsilon/c \approx 0.25$ producing the best integrated results coefficients for a given collective therefore reducing the necessity to trim an ALM solution to match the B-R equivalent, thus making the method with properly tuned Gaussian width a better predictive tool.

Inserting the rotor in vertical flight in Chapter 4 allows a modification of the tip vortex wake geometry. In particular, the climb condition features a much faster axial advection and less radial contraction of the tip vortex system through the additional downward directed freestream helping their advection. When comparing the blade loading of the climbing case to the baseline hover loading, the under/over-predictions in thrust loading usually caused by the BVI is removed because of the farther location of the tip-vortex. Only the signature of the simple blade/wing tip over-prediction is observed as in the fixed wing application.

6.2 Physical Representation of Rotor Flows

Chapter 2 first compares the general flowfield characteristics for a fixed wing application. The different selected Gaussian widths are benchmarked against the fully resolved reference. Again, $\epsilon/c \approx 0.25$ produces the best results this time in terms of flowfield agreement through similar induced velocity in the plane and wing tip vortex structure. The simple fixed wing application is also able to predict a complete lift polar.

In hover, the ALM with a properly sized Gaussian is capable of accurately predicting the thrust coefficient for a wide collective sweep with a predictable slight over-predictions in torque coefficient and ensuing under-prediction if figure of merit due to the BVI caused blade-tip drag over-prediction. The overall trends are otherwise in excellent agreement. The tip vortex wake shape and core profiles between the ALM and B-R solutions are also in good agreement except at the first blade passage due to the BVI.

In axial flight, the ALM produces near identical results when compared to the reference blade resolved simulations. Both methods captured a fair agreement in the reduction in thrust in climb whereas the linear reduction trend for the figure of merit is well captured. For descent, the two methods fail to accurately capture the trends when compared to the experimental data. The authors from the experimental study suggest the rotor quickly enters a vortex ring state (VRS) in descent thus explaining the allure of the integrated results. However, the two numerical methods show no signs of VRS with well-behaved flowfields and near steady thrust signals. At the highest descent rate, the far-wake did however show some signs of asymmetry which might be indicative of VRS onset.

Finally, in Chapter 5, the ALM, and an equivalent B-R set of simulations are evaluated in confined areas. In terms of general flowfield agreement such as wake topology, inflow, fuselage surface pressure coefficients, the two methods produce similar results, and in some cases near identical. In terms of global loads, the agreement is also excellent and is in line with the experimental data. The thrust and torque rise in ground effect (both in hover and forward flight) are well captured whereas the pitch and roll moments showcase an offset. This offset, first noticed when evaluating the baseline out of ground effect results, is present for both methods in similar magnitude. When correcting for the offset by considering the relative change in total moment magnitude and orientation shift, the two methods produce an excellent prediction trend when compared to the experimental results. Adding a box shaped obstacle, the ground effect thrust rise is negated through rotor wake re-circulation patterns. This flow pattern is slow to develop which causes rotor simulations placed at mid-heights above the ground to slightly over-predict the thrust. At last, adding wind with the box shaped obstacle creates a large separated wake region behind the obstacle. The ALM rotor placed in such a challenging flowfield showed qualitative agreement with the experimental data in terms of thrust and torque and an excellent agreement in terms of moment coefficient ratio and shift.

6.3 Computational Time

The end goal of developing and adapting the ALM to rotor flows, or any other rotor replacement technique, is to save on computational time when compared to traditional blade resolved simulations through mesh reduction. Table 6.1 presents the total mesh count and ratio for three selected test cases from Chapters 3 to 5. In addition, the associated computational time and corresponding speed-up is assessed. As expected, the ALM has a computational speed-up proportional to its mesh reduction ratio. In fact, the speed-up is greater than the mesh ratio as a result of the superior parallel efficiency of the ALM when compared to the B-R case that relies on the overset technique significantly hindering parallel performances.

Table 6.1 Mesh ratio, compute time and speed-up comparison

	Mesh Size [Millions]		
	Hover	Axial Flight	Confined Areas
B-R	28.7	47.1	32.9
ALM	10.1	20.4	18.0
Ratio	2.84	2.31	1.83
	CPU time per revolution [hrs]		
	Hover	Axial Flight	Confined Areas
B-R	2321.5	2504	1661.2
ALM	741.9	880.0	824.3
Speed-up	3.1	2.84	2.02

As an assessment of the limited overset scaling capabilities, the computational time per revolution results presented in Table 6.1 for the B-R Axial Flight case have been run on 480 CPU cores. The same mesh running on 1000 cores has a CPU time per revolution of 3758 hrs, a clear loss in parallel efficiency due to poor scaling. The ALM on the other hand would produce a better scaling past 1000 cores on its given mesh. This behaviour is also echoed by the strong scaling plot presented in Sec. 3.5.2. Most blade resolved simulations are constrained to run on a reduced core count in order to maximize parallel efficiency. As a rule of thumb, this work typically runs B-R simulations in the range of 75 000 to 100 000 mesh cells per CPU cores thus yielding parallel efficiencies in the range of at least 75-80% while maintaining reasonable total compute time in the order of slightly under a week for hover and multiple weeks for longer running confined area cases. The ALM on the other hand benefits from a much improved parallel efficiency that is on par with single region fixed wing applications. Even on a similar amount of CPU cores, with respect to a corresponding B-R case, the ALM still enjoys well above 90% parallel efficiency and produces an adequate 80% scaling up to 10 000 cells per cores. Therefore, ALM is not only faster due to lesser mesh sizes, but also allows greater scalability and the opportunity to run full helicopter CFD simulations in order of hours/days, given sufficient compute resources. By opposition, overset blade resolved simulations are typically constrained to run over several days or weeks as they are curtailed to run on lower core counts in order to satisfy some minimum computational efficiency target to minimize compute time allocation waste. Furthermore, although not fully explored in this thesis, the ALM is much less sensitive to mesh coarsening than B-R solutions. In Chapter 3, Table 3.3 presented much less variation for the ALM in terms of global rotor performances than the B-R. Therefore, ALM simulations could be run on coarser meshes further increasing the total computational time advantage the method provides.

Finally, to provide insight on the convergence characteristics of the ALM when compared to an equivalent fully resolved case, Figure 6.1 presents the time history convergence of the thrust signals of the three rotor geometries considered in this thesis. The thrust signals are normalized by their respective average thrust coefficient. A zoom on the last few revolutions gives an idea of the averaging window. The numerical values for these cases are presented in Tables 3.3, 4.2 and 5.5 as well as Fig. 4.1 and in all cases, the two methods present similar averaged results. In the three cases, the ALM shows similar convergence characteristics as the B-R with the exception of the starting two rotor revolutions. The ALM has a force ramp-up over these first two revolutions whereas the B-R performs an impulse start resulting in a thrust peak. After roughly 5 revolutions, the two methods behave similarly. In the S76 case, both show a low amplitude oscillation corresponding to less than 1% in amplitude with a frequency on the order of 1/rev. In the descending case of the Felker and McKillip geometry, as already mentioned in the text, the two numerical simulations face some asymmetries in the rotor wake resulting in thrust signal unsteadiness over longer periods in addition to a clear 4/rev frequency content with a 3% variation in amplitude. Finally, the geometry of Zagaglia et al. is presented with the inclusion of a fuselage. The addition of the geometry creates a clear 4/rev signal as the rotor passes over the fuselage tail boom. The two methods again have similar convergence characteristics. Therefore, the efficiency gains the ALM has in terms of computational time are preserved by having the method reaching convergence in a similar fashion as the fully resolved case in addition to being able to capture the thrust signal variations accurately.

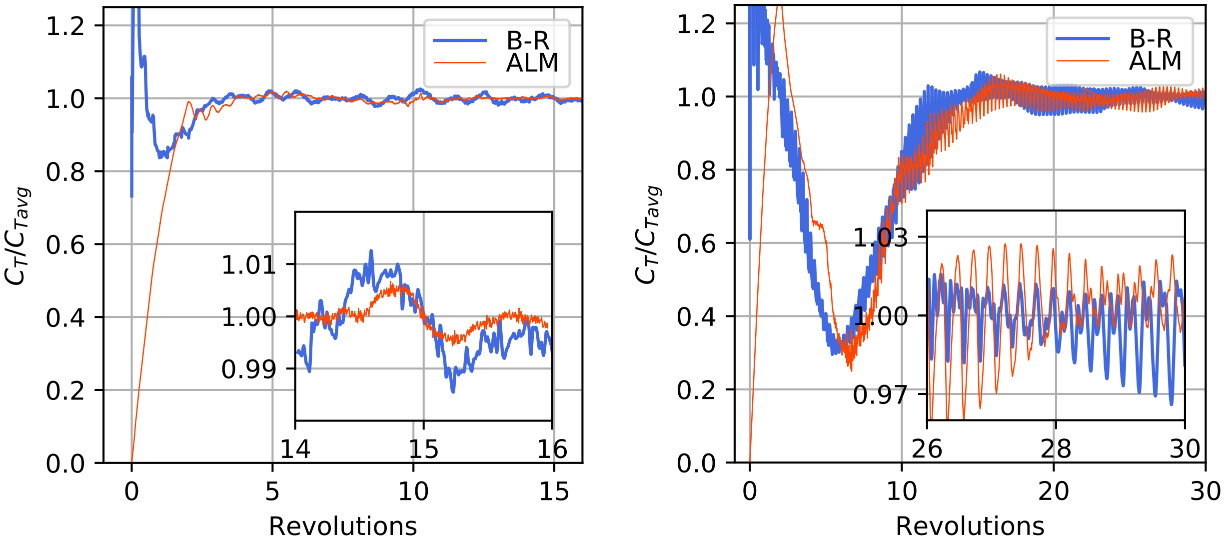

(a) Hover, S76, $\Theta_{75} = 7.5^o$

(b) Descent, $V_c/V_{ind}^{hov} = -0.75$

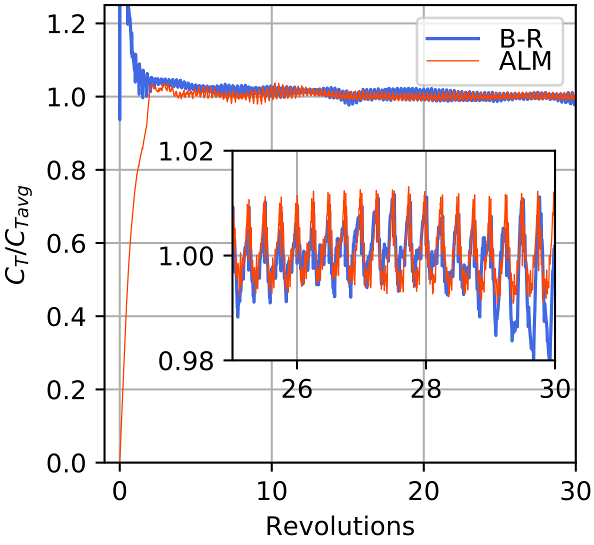

(c) Hover, with fuselage, Z/R=4

Figure 6.1 Thrust signal convergence

CHAPTER 7 CONCLUSION AND RECOMMENDATIONS

This thesis investigates the application of a rotor replacement technique, namely the Actuator Line Method, in a high-fidelity flow solving U-RANS framework. The ALM is most widely used in the wind energy sector for the evaluation of wind turbine wakes.

In order to adapt the method and make it suitable for the more challenging helicopter rotor flows, a parametric study is performed in a simplified framework. In a two-dimensional setting, the better performing integral velocity sampling method is identified along with other model sensibilities. Then, a simple extension in 3D for a fixed wing application shows the appropriateness of the method in handling 3D flows although with a small loading discrepancy near the wing tip.

Applying the model for a rotor in hover, a properly tuned truncated-normalized Gaussian kernel with $\epsilon/c \approx 0.25$ showed superior results in terms of integrated coefficient prediction capabilities. The ALM also produced a similar tip vortex wake when compared to an equivalent blade resolved simulation.

The method is then applied to an axial flight case where the predictive capabilities of the ALM model are near identical when compared to the fully resolved reference. The ALM is also capable of predicting the linear decrease in figure of merit for a rotor in climb with great accuracy. In descent, both methods fail to accurately capture the mentioned vortex ring state present in the experimental results.

Finally, the ALM is tested in increasingly difficult flow conditions including hovering in ground effect, forward flight in ground effect, in ground effect in interaction with a box-shaped obstacle both with and without incoming wind. In all cases, the ALM is capable of predicting global flow trends with a small misprediction of thrust in the most extreme ground effect states. The method is also capable of predicting the relative magnitude and orientation change of the moment coefficient. The ALM otherwise agrees well with the reference B-R simulations.

Revisiting the specific objectives from Section 1.5, they have all been achieved in this thesis:

1. The developed unsteady rotor replacement technique presents computational speed-ups in the order of 2x to 4x when compared to equivalent fully resolved simulations. The speed-up mainly comes from the computational mesh advantage the ALM has by not modelling the blade meshes. The ALM also offers superior parallel efficiency and is much less sensitive to mesh coarsening than B-R simulations.

2. Through the robust and versatile integral velocity sampling and the newly proposed truncated-normalized Gaussian kernel at a width of $\epsilon/c \approx 0.25$, the ALM produced excellent thrust predictive capabilities. However, perpendicular BVIs cause an over-prediction of torque and an associated under-prediction in figure of merit of the order of 5%-7%. Overall trends are otherwise well captured.
3. The ALM has been validated on a wide set of operating conditions.

The ALM therefore showed its value in being an additional analysis tool available for complex rotorcraft interactional aerodynamics that runs significantly faster than traditional fully resolved simulation while having similar performance predictive capabilities within a high fidelity framework.

7.1 Limitations

The method however has some limitations with the most critical ones listed below:

- The blade loading is over-estimated in the tip region because of a different induced flow profile of the trailing tip vortices when compared to a fully resolved simulation. Additionally, for a hovering rotor, the preceding blade tip vortex causes a BVI that is not well captured due to the porous nature of the force. This in turn causes a misprediction on blade loads near the tip.
- Only rectangular blade tips have been studied in this thesis. However, different tip geometries exist (swept, tapered, anhedral) and are widely used on helicopter blades that help the rotor to overcome compressible effects in this region.
- The selected forward flight case is relatively simple in terms of operating conditions and the same ALM model used in hover proved sufficient. However, more complex configurations at higher advance ratios and tip speed would require additional models to take into account the unsteady aerodynamics caused by parallel BVIs as done in [17]. In addition, reverse flow and dynamic stall near the root should be accounted for by the use of correction models. Airfoil databases should also include the effects of possible highly variable Mach and Reynolds numbers, angle of attack and cross-flow variation the different airfoil sections undergo through a rotor revolution.
- The presented simulations and test cases all featured fixed collective simulations with no lead-lag motion, flapping or cyclic pitch variation. To expand on other common test cases with more realistic rotor aero-mechanical behaviour, rotor simulations should be

able to handle at the very least these blade movements in an imposed fashion and ideally a trim routine must be implemented for automatic rotor coefficient trimming.

- Although the selected commercial solver used allowed a relatively easy simulation process of fully resolved blades, the implementation of the momentum source terms through user-coding has not been as straightforward. The solver served as a black box CFD code with limited access to variables and no available documentation. The source term implementation would therefore greatly benefit from an implementation in a solver with access to the source code where better integration, parallelization, memory access patterns and management could be achieved ultimately leading to better performances and development time.

7.2 Recommendations

To address some of the aforementioned limitations, further research paths and solution leads are:

- While retaining the integral velocity sampling, move towards other projection kernels than the isometric Gaussian kernel. Although still porous, a more compact kernel in the airfoil thickness direction [95] would tend to produce better perpendicular BVI interactions.
- The perpendicular BVI over/under-estimation issue could also be solved by implementing a simple numerical-empirically derived correction model.
- Distributing the force in a more representative way when compared to the airfoil pressure distribution. Without going as far as a highly detailed actuator surface [70], other smooth probability density functions could be explored with a Weibull distribution coming to mind to better mimic the pressure distribution of an airfoil. The drag force could also be projected by a different function as in [93].
- Furthermore, the gross assumption of distributing the total force evenly between the pressure and suction side of the airfoil can be revisited by introducing a bias towards the pressure side. Over a real airfoil, this section typically produces 65% to 90% of the total lift. The bias could be as simple as a tuning parameter or could consider the pressure side lift and suction side lift separately in the tabulated database. Splitting the force this way is more realistic and could result in better tip vortex characteristics and ultimately better tip loading.

- Due to its ties to lifting line and BEMT methodologies, further physical models could be taken from these vastly researched approaches and easily implemented in ALM frameworks for added physical modelling such as dynamic stall.

Globally, the ALM proved to be a suitable model in helicopter rotor-based applications for the study of a wide range of flight conditions with fully predictive capabilities at a fraction of the computational cost of B-R methods. The method is also being explored in other rotor-based or propeller-based aerospace applications. It would show great promises for the simulation of new eVTOL, urban air mobility and multi-copter drone applications.

REFERENCES

[1] A. Conlisk, “Modern helicopter rotor aerodynamics,” *Progress in Aerospace Sciences*, vol. 37, no. 5, pp. 419–476, 2001.

[2] S. Wagner, “Flow-Structure Interactions on Helicopter Rotors in Forward Flight,” *GAMM-Mitteilungen*, vol. 28, no. 1, pp. 7–36, 2005.

[3] W. Johnson, *Helicopter Theory.* New York: Dover Publications, 1994.

[4] R. B. Gray, “An Aerodynamic Analysis of a Single-Bladed Rotor in Hovering and Low Speed Forward Flight as Determined from Smoke Studies of the Velocity Distribution in the Wake,” Princeton University, New Jersey, Aeronautical Engineering Report 356, 1956.

[5] C. Ferlisi, “Rotor Wake Modelling Using the Vortex-Lattice Method,” Master’s thesis, Ecole Polytechnique Montreal, Montreal, Canada, Apr. 2018.

[6] S. Wagner, “Flow Phenomena on Rotary Wing Systems and their Modeling,” *ZAMM - Journal of Applied Mathematics and Mechanics*, vol. 79, no. 12, pp. 795–820, Dec. 1999.

[7] J. G. Coder, “OVERFLOW Rotor Simulations Using Advanced Turbulence and Transition Modeling,” in *55th AIAA Aerospace Sciences Meeting.* American Institute of Aeronautics and Astronautics, Jan. 2017.

[8] M. Dietz, M. Kessler, and E. Krämer, “Advanced Rotary Wing Aeromechanics,” in *High Performance Computing in Science and Engineering’ 05.* Springer, Berlin, Heidelberg, 2006, pp. 198–208.

[9] R. Steijl and G. N. Barakos, “Computational Study of Helicopter Rotor-Fuselage Aerodynamic Interactions,” *AIAA Journal*, vol. 47, no. 9, pp. 2143–2157, Sep. 2009.

[10] N. Hariharan, A. Wissink, M. Potsdam, and R. Strawn, “First-Principles Physics-Based Rotorcraft Flowfield Simulation Using HPCMP CREATE-AV Helios,” *Computing in Science & Engineering*, vol. 18, no. 6, pp. 19–26, 2016.

[11] B.-Y. Min and L. N. Sankar, “Hybrid Navier-Stokes/Free-Wake Method for Modeling Blade-Vortex Interactions,” *Journal of Aircraft*, vol. 47, no. 3, pp. 975–982, May 2010.

[12] R. Merabet and E. Laurendeau, “Hovering Helicopter Rotors Modeling Using the Actuator Line Method,” *Under Review by Journal of Aircraft*, Feb. 2021.

[13] A. Hoencamp, T. van Holten, and J. V. R. Prasad, “Relevant Aspects of Helicopter-Ship Operations,” in *Proceedings of the 34th European Rotorcraft Forum ERF34*, vol. 1. Liverpool, United Kingdom: Royal Aeronautical Society, Sep. 2008, pp. 578–588.

[14] A. Matus-Vargas, G. Rodriguez-Gomez, and J. Martinez-Carranza, “Ground effect on rotorcraft unmanned aerial vehicles: a review,” *Intelligent Service Robotics*, vol. 14, no. 1, pp. 99–118, Mar. 2021.

[15] N. S. Hariharan, R. P. Narducci, E. Reed, and A. Egolf, “AIAA Standardized Hover Simulation: Hover Performance Prediction Status and Outstanding Issues,” in *55th AIAA Aerospace Sciences Meeting.* American Institute of Aeronautics and Astronautics, Jan. 2017.

[16] I. Oruc, J. F. Horn, S. Polsky, J. Shipman, and J. Erwin, “Coupled Flight Dynamics and CFD Simulations of the Helicopter / Ship Dynamic Interface,” in *American Helicopter Society 71st Annual Forum.* Virginia Beach, Virginia: AHS International, May 2015.

[17] D. Linton, “A Hybrid Computational Fluid Dynamics Method for Unsteady Simulation of the Ship-Helicopter Dynamic Interface,” Ph. D. Thesis, University of Sydney, Sydney Australia, Jul. 2020.

[18] S. Polsky, “Progress Towards Modeling Ship/Aircraft Dynamic Interface,” in *2006 HPCMP Users Group Conference (HPCMP-UGC’06).* Denver, CO, USA: IEEE, Jun. 2006, pp. 163–168.

[19] J. M. Seddon, *Basic Helicopter Aerodynamics.* BSP Professional Books, 1990.

[20] R. C. Strawn, F. X. Caradonna, and E. P. Duque, “30 years of rotorcraft computational fluid dynamics research and development,” *Journal of the American Helicopter Society*, vol. 51, no. 1, pp. 5–21, 2006.

[21] N. M. Komerath, M. J. Smith, and C. Tung, “A Review of Rotor Wake Physics and Modeling,” *Journal of the American Helicopter Society*, vol. 56, no. 2, pp. 22 006–2 200 619, Apr. 2011.

[22] N. Hariharan, M. Potsdam, and A. Wissink, “Helicopter Rotor Aerodynamic Modeling in Hover Based on First-Principles: State-of-the-Art and remaining Challenges,” in *50th Aerospace Sciences Meeting.* AIAA, 2012.

[23] N. S. Hariharan, T. A. Egolf, and L. N. Sankar, “Simulation of Rotor in Hover: Current State, Challenges and Standardized Evaluation,” in *52nd Aerospace Sciences Meeting.* American Institute of Aeronautics and Astronautics, Jan. 2014.

[24] W. Johnson, “CAMRAD/JA: A Comprehensive ANalytical Model of Rotorcraft Aerodynamics and Dynamics,” Johnson Aeronautics, Palo Alto, California, Tech. Rep., 1988.

[25] M. J. Bhagwat, “Optimum Loading and Induced Swirl Effects in Hover,” *Journal of the American Helicopter Society*, vol. 60, no. 1, pp. 1–14, Jan. 2015.

[26] D. A. Griffiths, S. Ananthan, and J. G. Leishman, “Predictions of Rotor Performance in Ground Effect Using a Free-Vortex Wake Model,” *Journal of the American Helicopter Society*, vol. 50, no. 4, pp. 302–314, Oct. 2005.

[27] G. H. Vatistas, V. Kozel, and W. C. Mih, “A simpler model for concentrated vortices,” *Experiments in Fluids*, vol. 11, no. 1, pp. 73–76, Apr. 1991.

[28] M. Parenteau, F. Plante, E. Laurendeau, and M. Costes, “Unsteady Coupling Algorithm for Lifting-Line Methods,” in *55th AIAA Aerospace Sciences Meeting*, ser. AIAA SciTech Forum. Grapevine, Texas: American Institute of Aeronautics and Astronautics, Jan. 2017.

[29] A. J. Landgrebe, “The wake geometry of a hovering helicopter rotor and its influence on rotor performance,” *Journal of the American Helicopter Society*, vol. 17, no. 4, pp. 3–15, 1972.

[30] J. D. Kocurek and J. L. Tangler, “A Prescribed Wake Lifting Surface Hover Performance Analysis,” *Journal of the American Helicopter Society*, vol. 22, no. 1, pp. 24–35, Jan. 1977.

[31] A. J. Landgrebe, R. C. Moffitt, and D. R. Clark, “Aerodynamic Technology for Advanced Rotorcraft-Part I,” *Journal of the American Helicopter Society*, vol. 22, no. 2, pp. 21–27, 1977.

[32] W. J. McCroskey, “Vortex wakes of rotorcraft,” in *33th Aerospace Sciences Meeting and Exhibit, Reno, NV, January*, 1995, pp. 9–12.

[33] W. Johnson, “A General Free Wake Geometry Calculation For Wings and Rotors,” in *Helicopter Society 51st Annual Forum*, Fort Worth, Texas, May 1995, pp. 1–17.

[34] J. Zhao and C. He, “A Viscous Vortex Particle Model for Rotor Wake and Interference Analysis,” *Journal of the American Helicopter Society*, vol. 55, no. 1, pp. 12 007–1 200 714, Jan. 2010.

[35] P. Singh and P. P. Friedmann, “Application of Vortex Methods to Coaxial Rotor Wake and Load Calculations,” in *55th AIAA Aerospace Sciences Meeting*. American Institute of Aeronautics and Astronautics, Jan. 2017.

[36] N. Hariharan and L. Sankar, “High-Order Essentially Nonoscillatory Schemes for Rotary-Wing Wake Computations,” *Journal of Aircraft*, vol. 41, no. 2, pp. 258–267, Mar. 2004.

[37] J. Blazek, Ed., *Computational Fluid Dynamics: Principles and Applications*, 1st ed. New York: Elsevier, 2001.

[38] P. L. Roe, “Approximate Riemann solvers, parameter vectors, and difference schemes,” *Journal of computational physics*, vol. 43, no. 2, pp. 357–372, 1981.

[39] N. Yeshala, A. Egolf, R. Vasilescu, and L. Sankar, “Application of Higher Order Spatially Accurate Schemes to Rotors in Hover,” in *24th AIAA Applied Aerodynamics Conference*. San Francisco California USA: American Institute of Aeronautics and Astronautics, Jun. 2006.

[40] N. S. Hariharan, R. P. Narducci, and T. A. Egolf, “Helicopter Aerodynamic Modeling of S-76 Rotor with Tip-Shape Variations: Review of AIAA Standardized Hover Evaluations,” in *54th AIAA Aerospace Sciences Meeting*. American Institute of Aeronautics and Astronautics, Jan. 2016.

[41] J. Steinhoff and D. Underhill, “Modification of the Euler equations for “vorticity confinement”: Application to the computation of interacting vortex rings,” *Physics of Fluids*, vol. 6, no. 8, pp. 2738–2744, Aug. 1994.

[42] R. Steijl, G. Barakos, and K. Badcock, “A framework for CFD analysis of helicopter rotors in hover and forward flight,” *International Journal for Numerical Methods in Fluids*, vol. 51, no. 8, pp. 819–847, 2006.

[43] A. Jimenez Garcia and G. N. Barakos, “Accurate Predictions of Rotor Hover Performance at Low and High Disc Loadings,” *Journal of Aircraft*, vol. 55, no. 1, pp. 89–110, 2018.

[44] R. Steijl and G. Barakos, “Sliding mesh algorithm for CFD analysis of helicopter rotor-fuselage aerodynamics,” *International Journal for Numerical Methods in Fluids*, vol. 58, no. 5, pp. 527–549, Oct. 2008.

[45] V. K. Lakshminarayan, T. S. Kalra, and J. D. Baeder, “Detailed Computational Investigation of a Hovering Microscale Rotor in Ground Effect,” *AIAA Journal*, vol. 51, no. 4, pp. 893–909, Apr. 2013.

[46] R. Marpu, L. Sankar, T. A. Egolf, and N. S. Hariharan, “Analysis of a Rotor in Hover using Hybrid Methodology,” in *52nd AIAA Aerospace Sciences Meeting*. American Institute of Aeronautics and Astronautics, Jan. 2014.

[47] R. G. Rajagopalan and S. R. Mathur, “Three Dimensional Analysis of a Rotor in Forward Flight,” *Journal of the American Helicopter Society*, vol. 38, no. 3, pp. 14–25, Jul. 1993.

[48] D. M. O’Brien Jr and M. J. Smith, “Understanding the physical implications of approximate rotor methods using an unstructured CFD method,” in *31st European Rotorcraft Forum*, Florence Italy, 2005.

[49] Y. Shi, Y. Xu, K. Zong, and G. Xu, “An investigation of coupling ship/rotor flowfield using steady and unsteady rotor methods,” *Engineering Applications of Computational Fluid Mechanics*, vol. 11, no. 1, pp. 417–434, Jan. 2017.

[50] Y. Shi, G. Li, D. Su, and G. Xu, “Numerical investigation on the ship/multi-helicopter dynamic interface,” *Aerospace Science and Technology*, vol. 106, p. 106175, Nov. 2020.

[51] Y. Shi, D. Su, and G. Xu, “Numerical investigation of the influence of passive/active flow control on ship/helicopter dynamic interface,” *Aerospace Science and Technology*, vol. 106, p. 106205, Nov. 2020.

[52] A. Jimenez Garcia and G. Barakos, “Numerical simulations on the ERICA tiltrotor,” *Aerospace Science and Technology*, vol. 64, pp. 171–191, May 2017.

[53] F. De Gregorio, “Flow field characterization and interactional aerodynamics analysis of a complete helicopter,” *Aerospace Science and Technology*, vol. 19, no. 1, pp. 19–36, Jun. 2012.

[54] M. Biava and L. Vigevano, “Simulation of a complete helicopter: A CFD approach to the study of interference effects,” *Aerospace Science and Technology*, vol. 19, no. 1, pp. 37–49, Jun. 2012.

[55] B. M. Kutz, F. Bensing, M. Keßler, and E. Krämer, "CFD Calculation of a Helicopter Rotor Hovering in Ground Effect," in *New Results in Numerical and Experimental Fluid Mechanics VIII*, A. Dillmann, G. Heller, H.-P. Kreplin, W. Nitsche, and I. Peltzer, Eds. Berlin, Heidelberg: Springer Berlin Heidelberg, 2013, vol. 121, pp. 297–304.

[56] K. Mulleners, K. Kindler, and M. Raffel, "Dynamic stall on a fully equipped helicopter model," *Aerospace Science and Technology*, vol. 19, no. 1, pp. 72–76, Jun. 2012.

[57] T. Renaud, M. Costes, and S. Péron, "Computation of GOAHEAD configuration with Chimera assembly," *Aerospace Science and Technology*, vol. 19, no. 1, pp. 50–57, Jun. 2012.

[58] M. Biava, W. Khier, and L. Vigevano, "CFD prediction of air flow past a full helicopter configuration," *Aerospace Science and Technology*, vol. 19, no. 1, pp. 3–18, Jun. 2012.

[59] R. Steijl and G. Barakos, "CFD analysis of complete helicopter configurations – lessons learnt from the GOAHEAD project," *Aerospace Science and Technology*, vol. 19, no. 1, pp. 58–71, Jun. 2012.

[60] A. Antoniadis, D. Drikakis, B. Zhong, G. Barakos, R. Steijl, M. Biava, L. Vigevano, A. Brocklehurst, O. Boelens, M. Dietz, M. Embacher, and W. Khier, "Assessment of CFD methods against experimental flow measurements for helicopter flows," *Aerospace Science and Technology*, vol. 19, no. 1, pp. 86–100, Jun. 2012.

[61] A. Kyrkos and J. A. Ekaterinaris, "Assessment of an unstructured mesh approach for CFD predictions of the NH90 fuselage rotor," *Aerospace Science and Technology*, vol. 19, no. 1, pp. 77–85, Jun. 2012.

[62] E. W. Quon, M. J. Smith, G. R. Whitehouse, and D. Wachspress, "Unsteady Reynolds-Averaged Navier-Stokes-Based Hybrid Methodologies for Rotor-Fuselage Interaction," *Journal of Aircraft*, vol. 49, no. 3, pp. 961–965, May 2012.

[63] A. Filippone, R. Bakker, P. M. Basset, B. Rodriguez, R. Green, F. Bensing, and A. Visingardi, "Rotor wake modelling in ground effect conditions," in *37th European Rotorcraft Forum*, Vergiate, Italy, 2011, pp. 29–40.

[64] C. Crozon, R. Steijl, and G. N. Barakos, "Numerical Study of Helicopter Rotors in a Ship Airwake," *Journal of Aircraft*, vol. 51, no. 6, pp. 1813–1832, Nov. 2014.

[65] M. Jones and E. G. Paterson, "Evolution of the propeller near-wake and potential energy in a thermally-stratified environment," in *OCEANS 2016 MTS/IEEE Monterey*. Monterey, CA, USA: IEEE, Sep. 2016, pp. 1–10.

[66] D. Whitfield and A. Jameson, “Three-dimensional Euler equation simulation of propeller-wing interaction in transonic flow,” in *21st Aerospace Sciences Meeting.* Reno,NV,U.S.A.: American Institute of Aeronautics and Astronautics, Jan. 1983.

[67] D. Pelletier, A. Garon, and R. Camarero, “Finite element method for computing turbulent propeller flow,” *AIAA Journal*, vol. 29, no. 1, pp. 68–75, Jan. 1991.

[68] T. C. A. Stokkermans, N. van Arnhem, T. Sinnige, and L. L. M. Veldhuis, “Validation and Comparison of RANS Propeller Modeling Methods for Tip-Mounted Applications,” *AIAA Journal*, vol. 57, no. 2, pp. 566–580, Feb. 2019.

[69] D. D. Apsley, T. Stallard, and P. K. Stansby, “Actuator-line CFD modelling of tidal-stream turbines in arrays,” *Journal of Ocean Engineering and Marine Energy*, vol. 4, no. 4, pp. 259–271, Nov. 2018.

[70] W. Z. Shen, J. H. Zhang, and J. N. Sørensen, “The Actuator Surface Model: A New Navier–Stokes Based Model for Rotor Computations,” *Journal of Solar Energy Engineering*, vol. 131, no. 1, p. 011002, 2009.

[71] B. Sanderse, S. Pijl, and B. Koren, “Review of computational fluid dynamics for wind turbine wake aerodynamics: Review of CFD for wind turbine wake aerodynamics,” *Wind Energy*, vol. 14, no. 7, pp. 799–819, Oct. 2011.

[72] C. Leclerc and C. Masson, “Wind Turbine Performance Predictions Using a Differential Actuator-Lifting Disk Model,” *Journal of Solar Energy Engineering*, vol. 127, no. 2, p. 200, 2005.

[73] C. S. Watters and C. Masson, “Recent advances in modeling of wind turbine wake vortical structure using a differential actuator disk theory,” *Journal of Physics: Conference Series*, vol. 75, p. 012037, Jul. 2007.

[74] C. Masson and C. S. Watters, “Moving actuator surfaces: a new concept for wind turbine aerodynamic analysis,” in *Proceedings of the International Conference on Renewable Energies and Power Quality (ICREPQ08).* Santander, Spain, 2008.

[75] C. Sibuet Watters and C. Masson, “Modeling of lifting-device aerodynamics using the actuator surface concept,” *International Journal for Numerical Methods in Fluids*, vol. 62, pp. 1264–1298, 2009.

[76] C. Sibuet Watters, S. Breton, and C. Masson, “Application of the actuator surface concept to wind turbine rotor aerodynamics,” *Wind Energy*, vol. 13, no. 5, pp. 433–447, Dec. 2009.

[77] I. Dobrev, F. Massouh, and M. Rapin, "Actuator surface hybrid model," *Journal of Physics: Conference Series*, vol. 75, Jul. 2007.

[78] R. Mikkelsen, "Actuator disc methods applied to wind turbines," PhD Thesis, Technical University of Denmark, 2003.

[79] L. Martinez, S. Leonardi, M. Churchfield, and P. Moriarty, "A Comparison of Actuator Disk and Actuator Line Wind Turbine Models and Best Practices for Their Use," in *50th AIAA Aerospace Sciences Meeting*. American Institute of Aeronautics and Astronautics, Jan. 2012.

[80] J. N. Sørensen and W. Z. Shen, "Numerical Modeling of Wind Turbine Wakes," *Journal of Fluids Engineering*, vol. 124, no. 2, pp. 393–399, 2002.

[81] N. Troldborg, "Actuator Line Modeling of Wind Turbine Wakes," PhD Thesis, Technical University of Denmark, 2008.

[82] S. Sarmast, A. Segalini, R. F. Mikkelsen, and S. Ivanell, "Comparison of the near-wake between actuator-line simulations and a simplified vortex model of a horizontal-axis wind turbine," *Wind Energy*, vol. 19, no. 3, pp. 471–481, Mar. 2016.

[83] S. Ivanell, T. Leweke, S. Sarmast, H. U. Quaranta, R. F. Mikkelsen, and J. N. Sørensen, "Comparison between experiments and Large-Eddy Simulations of tip spiral structure and geometry," *Journal of Physics: Conference Series*, vol. 625, no. 1, p. 012018, 2015.

[84] P. K. Jha, "Characterization of wake turbulence in a wind turbine array submerged in atmospheric boundary layer flow," Ph.D. dissertation, The Pennsylvania State University, 2015.

[85] J. Nathan, A. R. Meyer Forsting, N. Troldborg, and C. Masson, "Comparison of OpenFOAM and EllipSys3D actuator line methods with (NEW) MEXICO results," *Journal of Physics: Conference Series*, vol. 854, p. 012033, May 2017.

[86] L. A. Martínez-Tossas, M. J. Churchfield, and S. Leonardi, "Large eddy simulations of the flow past wind turbines: actuator line and disk modeling: LES of the flow past wind turbines: actuator line and disk modeling," *Wind Energy*, vol. 18, no. 6, pp. 1047–1060, Jun. 2015.

[87] A. Wimshurst and R. H. J. Willden, "Extracting lift and drag polars from blade-resolved computational fluid dynamics for use in actuator line modelling of horizontal

axis turbines: Extracting lift and drag polars from blade-resolved computational fluid dynamics," *Wind Energy*, vol. 20, no. 5, pp. 815–833, May 2017.

[88] W. Z. Shen, M. O. L. Hansen, and J. N. Sørensen, "Determination of the angle of attack on rotor blades," *Wind Energy*, vol. 12, no. 1, pp. 91–98, Jan. 2009.

[89] M. Shives and C. Crawford, "Mesh and load distribution requirements for actuator line CFD simulations," *Wind Energy*, vol. 16, no. 8, pp. 1183–1196, Aug. 2012.

[90] J. Schluntz and R. H. J. Willden, "An actuator line method with novel blade flow field coupling based on potential flow equivalence: An actuator line method with novel blade flow field coupling," *Wind Energy*, vol. 18, no. 8, pp. 1469–1485, Aug. 2015.

[91] T. Kim, S. Oh, and K. Yee, "Improved actuator surface method for wind turbine application," *Renewable Energy*, vol. 76, pp. 16–26, Apr. 2015.

[92] A. Mittal, K. Sreenivas, L. K. Taylor, and L. Hereth, "Improvements to the Actuator Line Modeling for Wind Turbines," in *33rd Wind Energy Symposium.* American Institute of Aeronautics and Astronautics, Jan. 2015.

[93] L. A. Martinez-Tossas, M. J. Churchfield, and C. Meneveau, "Optimal smoothing length scale for actuator line models of wind turbine blades based on Gaussian body force distribution," *Wind Energy*, vol. 20, no. 6, pp. 1083–1096, Jun. 2017.

[94] P. K. Jha, M. J. Churchfield, P. J. Moriarty, and S. Schmitz, "Guidelines for volume force distributions within actuator line modeling of wind turbines on large-eddy simulation-type grids," *Journal of Solar Energy Engineering*, vol. 136, no. 3, pp. 031 003–1 – 031 003–11, 2014.

[95] M. J. Churchfield, S. J. Schreck, L. A. Martinez, C. Meneveau, and P. R. Spalart, "An Advanced Actuator Line Method for Wind Energy Applications and Beyond," in *35th Wind Energy Symposium.* American Institute of Aeronautics and Astronautics, Jan. 2017.

[96] W. Khier, "Time-accurate versus actuator disk simulations of complete helicopters," *High Performance Computing in Science and Engineering'05*, pp. 209–220, 2006.

[97] D. D. Boyd Jr, "Rotor/fuselage unsteady interactional aerodynamics: a new computational model," PhD Thesis, Virginia Tech, 1999.

[98] F. Le Chuiton, "Actuator disc modelling for helicopter rotors," *Aerospace Science and Technology*, vol. 8, no. 4, pp. 285–297, Jun. 2004.

[99] D. M. O'Brien Jr and M. J. Smith, "Analysis of rotor-fuselage interactions using various rotor models," *43rd AIAA Aerospace Sciences Meeting*, vol. 468, 2005.

[100] C. Lynch, D. Prosser, and M. Smith, "An efficient actuating blade model for unsteady rotating system wake simulations," *Computers & Fluids*, vol. 92, pp. 138–150, Mar. 2014.

[101] Y.-H. Kim and S.-O. Park, "Navier-Stokes simulation of unsteady rotor-airframe interaction with momentum source method," *International Journal of Aeronautical and Space Sciences*, vol. 10, no. 2, pp. 125–133, 2009.

[102] Y. H. Kim and S. O. Park, "Unsteady Momentum Source Method for Efficient Simulation of Rotor Aerodynamics," *Journal of Aircraft*, vol. 50, no. 1, pp. 324–327, Jan. 2013.

[103] T. Kim, S. Oh, and K. Yee, "Novel Actuator Surface Method for Helicopter Rotor Analysis," *Journal of Aircraft*, vol. 53, no. 6, pp. 1947–1952, Nov. 2016.

[104] D. Linton, G. Barakos, R. Widjaja, and B. Thornbern, "A New Actuator Surface Model with Improved Wake Model for CFD Simulations of Rotorcraft," in *American Helicopter Society 73rd Annual Forum.* Fort Worth, Texas: AHS International, May 2017.

[105] D. Linton, G. Barakos, R. Widjaja, and B. Thornber, "Coupling of an Unsteady Aerodynamics Model with a Computational Fluid Dynamics Solver," *AIAA Journal*, vol. 56, no. 8, pp. 3153–3166, Aug. 2018.

[106] D. Linton, R. Widjaja, and B. Thornber, "Simulations of Tandem and Coaxial Rotors using a CFD-coupled Rotor Model," in *21st Australasian Fluid Mechanics Conference*, Adelaide, Australia, Dec. 2018, pp. 1–4.

[107] D. Linton and B. Thornber, "An Actuator Surface Method for Ship-Helicopter Dynamic Interface Simulations," in *AIAA Scitech 2021 Forum.* Virtual Event: American Institute of Aeronautics and Astronautics, Jan. 2021.

[108] E. Alpman, L. N. Long, D. O. Bridges, and J. F. Horn, "Fully-Coupled Simulations of the Rotorcraft / Ship Dynamic Interface," in *American Helicopter Society International 63rd Annual Forum.* Virginia Beach, Virginia: AHS International, May 2007, pp. 1367–1382.

[109] S. Schmitz and P. K. Jha, "Modeling the Wakes of Wind Turbines and Rotorcraft Using the Actuator-Line Method in an OpenFOAM - LES Solver," in *American Helicopter Society 69th Annual Forum.* Phoenix, Arizona: AHS International, May 2013.

[110] J. R. Forsythe, E. Lynch, S. Polsky, and P. Spalart, "Coupled Flight Simulator and CFD Calculations of Ship Airwake using Kestrel," in *53rd AIAA Aerospace Sciences Meeting.* American Institute of Aeronautics and Astronautics, Jan. 2015.

[111] R. Stanly, Y. T. Delorme, and S. H. Frankel, "Computational Assessment of Actuator Line Model for Large Eddy Simulation of Rotor Noise," in *AIAA Scitech 2020 Forum.* Orlando, Florida: American Institute of Aeronautics and Astronautics, Jan. 2020.

[112] Y. Delorme, R. Stanly, S. H. Frankel, and D. Greenblatt, "Application of Actuator Line Model for Large Eddy Simulation of Rotor Noise Control," *Aerospace Science and Technology*, vol. 108, p. 106405, Jan. 2021.

[113] D.-G. Caprace, P. Chatelain, and G. Winckelmans, "Lifting Line with Various Mollifications: Theory and Application to an Elliptical Wing," *AIAA Journal*, vol. 57, no. 1, pp. 17–28, Jan. 2019.

[114] ——, "Wakes of rotorcraft in advancing flight: A large-eddy simulation study," *Physics of Fluids*, vol. 32, no. 8, p. 087107, Aug. 2020.

[115] N. Sezer-Uzol, "Unsteady flow simulations around complex geometries using stationary or rotating unstructured grids," PhD Thesis, Georgia Institute of Technology, 2006.

[116] D. M. O'Brien Jr, "Analysis of computational modeling techniques for complete rotorcraft configurations," PhD Thesis, Georgia Institute of Technology, 2006.

[117] J. N. Abras, "Enhancement of aeroelastic rotor airload prediction methods," Ph. D. Thesis, Georgia Institute of Technology, Atlanta Georgia, Mar. 2009.

[118] R. Merabet and E. Laurendeau, "Parametric Study on the Velocity Sampling Techniques for the Actuator Line Method in 2D," in *AIAA SciTech 2019 Forum.* San Diego, California: American Institute of Aeronautics and Astronautics, Jan. 2019.

[119] W. Z. Shen, M. O. Hansen, and J. N. e. Sørensen, "Determination of angle of attack (AOA) for rotating blades," in *Proceedings of the Euromech Colloquium - Wind Energy.* Springer, 2005, pp. 205–209.

[120] "STAR-CCM+ Documentation," Siemens PLM Software, User Manual Version 12.06, 2016.

[121] J. M. Weiss, J. P. Maruszewski, and W. A. Smith, “Implicit Solution of Preconditioned Navier-Stokes Equations Using Algebraic Multigrid,” *AIAA Journal*, vol. 37, no. 1, pp. 29–36, Jan. 1999.

[122] F. R. Menter, “Two-equation eddy-viscosity turbulence models for engineering applications,” *AIAA Journal*, vol. 32, no. 8, pp. 269–289, Aug. 1994.

[123] S. J. Hodge, S. J. Zan, D. M. Roper, G. D. Padfield, and I. Owen, “Time-Accurate Ship Airwake and Unsteady Aerodynamic Loads Modeling for Maritime Helicopter Simulation,” *Journal of the American Helicopter Society*, vol. 54, no. 2, pp. 022 005–01 – 022 005–016, Apr. 2009.

[124] D. M. Roper, I. Owen, G. D. Padfield, and S. J. Hodge, “Integrating CFD and piloted simulation to quantify ship-helicopter operating limits,” *The Aeronautical Journal*, vol. 110, no. 1109, pp. 419–428, Jul. 2006.

[125] D. Zagaglia, M. Giuni, and R. B. Green, “Rotor-Obstacle Aerodynamic Interaction in Hovering Flight: An Experimental Survey,” in *American Helicopter Society 72nd Annual Forum.* West Palm Beach, Florida: AHS International, May 2016.

[126] R. Quackenbush, K. Chua, D. A. Wachspress, and H. Boschitsch, “Computation of Rotor Aerodynamic Loads in Forward Flight Using a Full-Span Free Wake Analysis,” NASA, NASA CR 177611, Oct. 1990.

[127] J. Katz and A. Plotkin, *Low-Speed Aerodynamics*, 2nd ed. New York: Cambridge University Press, 2001.

[128] W. Khier, “Time-Accurate versus Actuator Disk Simulations of Complete Helicopters,” in *High Performance Computing in Science and Engineering’ 05*, W. E. Nagel, M. Resch, and W. Jäger, Eds. Berlin/Heidelberg: Springer-Verlag, 2006, pp. 209–220.

[129] G. Chirico, D. Szubert, L. Vigevano, and G. N. Barakos, “Numerical modelling of the aerodynamic interference between helicopter and ground obstacles,” *CEAS Aeronautical Journal*, vol. 8, no. 4, pp. 589–611, Dec. 2017.

[130] S. L. Wood, J. G. Coder, and N. S. Hariharan, “Fundamental Investigation of Grid Resolution on Wake Fidelity Submitted to the APATC Special Session: Simulation of Rotor in Hover,” in *2018 AIAA Aerospace Sciences Meeting.* Kissimmee, Florida: American Institute of Aeronautics and Astronautics, Jan. 2018.

[131] D. T. Balch and J. Lombardi, “Experimental Study Of Main Rotor Tip Geometry And Tail Rotor Interactions in Hover Vol 1 - Text and Figures,” National Aeronautics And Space Administration, NASA CR 177336, 1985.

[132] ——, “Experimental Study Of Main Rotor Tip Geometry And Tail Rotor Interactions in Hover Vol 2 - Run Log and Tabulated Data,” National Aeronautics And Space Administration, NASA CR 177336, 1985.

[133] W. G. Bousman, “Aerodynamic Characteristics of SC1095 and SC1094 R8 Airfoils,” Defense Technical Information Center, Fort Belvoir, Virginia, NASA TP 212265, Dec. 2003.

[134] N. A. R. N. Mohd and G. N. Barakos, “Computational Aerodynamics Of Hovering Helicopter Rotors,” *Jurnal Mekanikal*, vol. 34, pp. 16–46, Jun. 2012.

[135] B. A. Vieira, M. P. Kinzel, and M. D. Maughmer, “CFD Hover Predictions Including Boundary-Layer Transition,” in *55th AIAA Aerospace Sciences Meeting.* American Institute of Aeronautics and Astronautics, Jan. 2017.

[136] L. A. Martinez-Tossas and C. Meneveau, “Filtered lifting line theory and application to the actuator line model,” *Journal of Fluid Mechanics*, vol. 863, pp. 269–292, 2019.

[137] J. Nathan, C. Masson, and L. Dufresne, “Optimal distribution width for ALM in LES for (NEW) MEXICO experiment,” *Journal of Physics: Conference Series*, vol. 1037, pp. 072 026–1 – 072 026–6, Jun. 2018.

[138] R. Jain, “Hover Predictions on the S-76 Rotor with Tip Shape Variation Using Helios,” *Journal of Aircraft*, vol. 55, no. 1, pp. 66–77, Jan. 2018.

[139] ——, “Sensitivity Study of High-Fidelity Hover Predictions on the Sikorsky S-76 Rotor,” *Journal of Aircraft*, vol. 55, no. 1, pp. 78–88, Jan. 2018.

[140] A. Goerttler, J. N. Braukmann, T. Schwermer, A. D. Gardner, and M. Raffel, “Tip-Vortex Investigation on a Rotating and Pitching Rotor Blade,” *Journal of Aircraft*, vol. 55, no. 5, pp. 1792–1804, Sep. 2018.

[141] R. Merabet and E. Laurendeau, “Actuator Line Method for Helicopter Rotors Computations in Various Flight Conditions,” in *CASI Aero 2021.* Online: Canadian Aeronautics and Space Institute, Jun. 2021, p. 15.

[142] F. Caradonna, “Performance Measurement and Wake Characteristics of a Model Rotor in Axial Flight,” *Journal of the American Helicopter Society*, vol. 44, no. 2, pp. 101–108, Apr. 1999.

[143] F. F. Felker and R. M. McKillip, “Comparisons of Predicted and Measured Rotor Performance in Vertical Climb and Descent,” in *American Helicopter Society 50th Annual Forum*. Washington D.C. USA: AHS International, May 1994.

[144] J. H. Ferziger and M. Perić, *Computational methods for fluid dynamics*, 3rd ed. Berlin ; New York: Springer, 2002.

[145] R. Merabet and E. Laurendeau, “Numerical simulations of a rotor in confined areas-including the presence of wind,” *Submitted to Aerospace Science and Technology*, Jun. 2021.

[146] R. G. Lee and S. J. Zan, “Wind Tunnel Testing of a Helicopter Fuselage and Rotor in a Ship Airwake,” *Journal of the American Helicopter Society*, vol. 50, no. 4, pp. 326–337, Oct. 2005.

[147] N. Taymourtash, D. Zagaglia, A. Zanotti, G. Gibertini, and G. Quaranta, “Wind Tunnel Investigation of a Helicopter Model in Shipboard Operations,” in *45th European Rotorcraft Forum*, Warsaw, Poland, Sep. 2019, pp. 1–13.

[148] N. Taymourtash, V. Muscarello, and G. Quaranta, “Gust and Inflow Model Identification from Wind Tunnel Tests for Rotorcraft-Obstacle Interaction,” Rome, Italy, Sep. 2019, pp. 1981–1989.

[149] N. Taymourtash, D. Zagaglia, A. Zanotti, V. Muscarello, G. Gibertini, and G. Quaranta, “Experimental study of a helicopter model in shipboard operations,” *Aerospace Science and Technology*, p. 106774, May 2021.

[150] J. F. Tan, T. Y. Zhou, Y. M. Sun, and G. N. Barakos, “Numerical investigation of the aerodynamic interaction between a tiltrotor and a tandem rotor during shipboard operations,” *Aerospace Science and Technology*, vol. 87, pp. 62–72, Apr. 2019.

[151] A. Visingardi, F. D. Gregorio, T. Schwarz, M. Schmid, R. Bakker, S. Voutsinas, Q. Gallas, R. Boisard, G. Gibertini, D. Zagaglia, G. Barakos, R. Green, G. Chirico, and M. Giuni, “Forces on Obstacles in Rotor Wake – A GARTEUR Action Group,” in *43rd European Rotorcraft Forum*, Milan, Italy, Sep. 2017, pp. 1–14.

[152] Q. Gallas, R. Boisard, J.-C. Monnier, J. Pruvost, and A. Gilliot, “Experimental and numerical investigation of the aerodynamic interactions between a hovering helicopter and surrounding obstacles,” in *43rd European Rotorcraft Forum*, Milan, Italy, Sep. 2017, pp. 1–6.

[153] D. Zagaglia, G. Gibertini, M. Giuni, and R. B. Green, “Experiments on the Helicopter-Obstacle Aerodynamic Interference in Absence of External Wind,” in *42nd European Rotorcraft Forum*, Lille France, Sep. 2016.

[154] D. Zagaglia, M. Giuni, and R. B. Green, “Investigation of the Rotor–Obstacle Aerodynamic Interaction in Hovering Flight,” *Journal of the American Helicopter Society*, vol. 63, no. 3, pp. 1–12, Jul. 2018.

[155] T. Jardin, S. Prothin, and C. G. Magaña, “Aerodynamic Performance of a Hovering Microrotor in Confined Environment,” *Journal of the American Helicopter Society*, vol. 62, no. 2, pp. 1–7, Apr. 2017.

[156] S. Prothin, C. Fernandez Escudero, N. Doué, and T. Jardin, “Aerodynamics of MAV rotors in ground and corner effect,” *International Journal of Micro Air Vehicles*, vol. 11, pp. 1–13, Jan. 2019.

[157] J. F. Tan, J. G. Cai, G. N. Barakos, C. Wang, and M. Q. Huang, “Computational Study on the Aerodynamic Interference Between Tandem Rotors and Nearby Obstacles,” *Journal of Aircraft*, vol. 57, no. 3, pp. 456–468, May 2020.

[158] T. S. Kalra, V. K. Lakshminarayan, and J. D. Baeder, “CFD validation of micro hovering rotor in ground effect,” in *American Helicopter Society 66th Annual Forum*. Phoenix, Arizona: AHS International, May 2010, pp. 1–22.

[159] R. E. Brown and G. R. Whitehouse, “Modelling Rotor Wakes in Ground Effect,” *Journal of the American Helicopter Society*, vol. 49, no. 3, pp. 238–249, Jul. 2004.

[160] G. Barakos, T. Fitzgibbon, A. Kusyumov, S. Kusyumov, and S. Mikhailov, “CFD simulation of helicopter rotor flow based on unsteady actuator disk model,” *Chinese Journal of Aeronautics*, vol. 33, no. 9, pp. 2313–2328, Sep. 2020.

[161] I. Oruc, J. F. Horn, and J. Shipman, “Coupled Flight Dynamics and Computational Fluid Dynamics Simulations of Rotorcraft/Terrain Interactions,” *Journal of Aircraft*, vol. 54, no. 6, pp. 2228–2241, Nov. 2017.

[162] D. Linton, R. Widjaja, and B. Thornber, “Validation of an Actuator Surface Model with CFD-convected Wake Model for Hover and Forward Flight,” in *7th Asian/Australian Rotorcraft Forum*, Jeju Island, Korea, Oct. 2018, pp. 1–8.

[163] S. J. Zan, “Experimental Determination of Rotor Thrust in a Ship Airwake,” *Journal of the American Helicopter Society*, vol. 47, no. 2, pp. 100–108, Apr. 2002.

[164] R. G. Lee and S. J. Zan, “Unsteady aerodynamic loading on a helicopter fuselage in a ship airwake,” *Journal of the American Helicopter Society*, vol. 49, no. 2, pp. 149–159, 2004.

[165] C. H. Kääriä, Y. Wang, G. D. Padfield, J. S. Forrest, and I. Owen, “Aerodynamic Loading Characteristics of a Model-Scale Helicopter in a Ship’s Airwake,” *Journal of Aircraft*, vol. 49, no. 5, pp. 1271–1278, Sep. 2012.

[166] C. H. Kääriä, Y. Wang, M. D. White, and I. Owen, “An experimental technique for evaluating the aerodynamic impact of ship superstructures on helicopter operations,” *Ocean Engineering*, vol. 61, pp. 97–108, Mar. 2013.

[167] D. Zagaglia, A. Zanotti, and G. Gibertini, “Analysis of the loads acting on the rotor of a helicopter model close to an obstacle in moderate windy conditions,” *Aerospace Science and Technology*, vol. 78, pp. 580–592, Jul. 2018.

[168] R. Martinuzzi and C. Tropea, “The Flow Around Surface-Mounted, Prismatic Obstacles Placed in a Fully Developed Channel Flow (Data Bank Contribution),” *Journal of Fluids Engineering*, vol. 115, no. 1, pp. 85–92, Mar. 1993.

[169] J.-Y. Hwang and K.-S. Yang, “Numerical study of vortical structures around a wall-mounted cubic obstacle in channel flow,” *Physics of Fluids*, vol. 16, no. 7, pp. 2382–2394, Jul. 2004.

[170] H. C. Lim, T. Thomas, and I. P. Castro, “Flow around a cube in a turbulent boundary layer: LES and experiment,” *Journal of Wind Engineering and Industrial Aerodynamics*, vol. 97, no. 2, pp. 96–109, Feb. 2009.

[171] J. W. Elliott and S. L. Althoff, “Inflow measurement made with a laser velocimeter on a helicopter model in forward flight. Volume I: Rectangular Planform blades at an advance ratio of 0.15,” National Aeronautics And Space Administration, NASA TM 100541, Apr. 1988.

[172] I. C. Cheeseman and W. E. Bennett, “The Effect of the Ground on a Helicopter Rotor in Forward Flight,” Aeronautical Research Council, London UK, A.R.C. Technical Report 3021, Sep. 1955.

[173] G. Gibertini, G. Droandi, D. Zagaglia, P. Antoniazza, and A. O. Catelan, “CFD Assessment of the Helicopter and Ground Obstacles Aerodynamic Interference,” in *42nd European Rotorcraft Forum*, Lille France, Sep. 2016, pp. 1–13.

[174] M. Schmid, “Simulation of Helicopter Aerodynamics in the Vicinity of an Obstacle using a Free Wake Panel Method,” in *43rd European Rotorcraft Forum*, Milan, Italy, Sep. 2017, pp. 1–14.